Stochastic seismic interpretation of salt bodies: detection, sampling and impact on seismic imaging

Nicolas Clausolles

Stochastic seismic interpretation of salt bodies: detection, sampling and impact on seismic imaging

Interprétation sismique stochastique des corps salifères : détection, échantillonnage et impact sur l'imagerie sismique

THÈSE

présentée et soutenue publiquement le 5 mars 2020
pour l'obtention du grade de

Docteur de l'Université de Lorraine

Spécialité Géosciences

par

Nicolas Clausolles

Composition du jury:

Présidente du jury:	Prof. Mary Ford	Université de Lorraine, France
Rapporteurs:	Prof. Amilcar Soares	IST Lisbonne, Portugal
	Prof. Florian Wellmann	RWTH Aachen, Allemagne
Examinateurs:	Prof. Virginie Gaullier	Université de Lille, France
	Dr. Pierre Thore	Total SA, France
Directrice de thèse:	Dr. Pauline Collon	Université de Lorraine, France
Co-directeur de thèse:	Prof. Guillaume Caumon	Université de Lorraine, France
Invité:	Dr. Xinming Wu	USTC, Chine

GeoRessources - UMR 7359
Université de Lorraine – CNRS
École Nationale Supérieure de Géologie
2 rue du Doyen Marcel Roubault - BP 10162
54505 Vandœuvre-lès-Nancy, FRANCE

Résumé

La création d'un modèle numérique 3D du sous-sol nécessite d'intégrer des données éparses et ambigües. Les corps salifères développent des formes compliquées et des singularités topologiques spécifiques à la tectonique salifère. Modéliser leurs géométries est donc difficile, mais important puisqu'ils introduisent de larges contrastes de propriétés physiques dans le sous-sol. L'imagerie sismique est couramment utilisée pour cartographier le sel et obtenir des informations sur sa géométrie. Il s'agit toutefois d'un processus itératif long nécessitant de nombreuses phases d'interprétation. Ces interprétations sont sujettes à des incertitudes qui se propagent à travers le processus d'imagerie et impactent la compréhension du sous-sol et les modèles qui en sont faits. Prendre en compte ces incertitudes est donc crucial, et nécessite d'être réalisé automatiquement étant donné le caractère itératif de l'imagerie sismique. Dans cette thèse, je m'intéresse en particulier à l'estimation des incertitudes structurales liées à l'interprétation d'images sismiques ambigües dans des environnements de tectonique salifère.

La principale contribution de cette thèse est une méthode numérique de modélisation stochastique des enveloppes de corps salifères et de leur connectivité. La modélisation se base sur une définition *a priori* des incertitudes, sous forme d'une zone tampon autour de l'enveloppe du sel. L'enveloppe est définie par la combinaison d'un champ scalaire de référence, calculé à partir de la zone tampon, et d'un champ aléatoire spatialement corrélé servant de perturbation. Cette formulation implicite permet de simuler à la fois des géométries et des topologies variables, tout en assurant la validité des enveloppes simulées. Lorsque plusieurs corps déconnectés sont simulés, une suture est simulée pour les connecter. Sa position est déterminée à partir du champ scalaire représentant l'enveloppe de sel afin d'assurer sa cohérence avec les corps salifères simulés. La méthode est automatique et permet d'intégrer des informations ponctuelles (données de puits, pointés sismiques, etc.) et, dans une certaine mesure, des connaissances géologiques *a priori*.

Cette méthode est utilisée pour caractériser les incertitudes structurales liées à l'imagerie d'un jeu de données sismiques 2D synthétique. À partir d'une zone tampon grossière, un ensemble d'interprétations possibles de l'enveloppe du sel est simulé. Ces interprétations sont utilisées pour définir des modèles de vitesse de migration, qui servent à générer autant d'images sismiques. L'analyse statistique de ces images, directement ou via des attributs sismiques permet de mettre en évidence les régions les plus sensibles aux variations de vitesse de migration, et fournit des indications sur la nature des corps salifères imagés.

Ces contributions ouvrent de nouvelles perspectives pour la quantification des incertitudes dans le cadre de la mise à jour automatique du modèle de vitesse en imagerie sismique.

Abstract

Building a numerical 3D model of the subsurface requires to integrate sparse and ambiguous data. Due to salt tectonics specificities, salt bodies have complex shapes and may present topological singularities. Modeling their geometries is, therefore, difficult, but important as they introduce large physical property contrasts in the subsurface. Seismic imaging is commonly used to map salt and get information about its geometry. Nevertheless, building a seismic image is a long and iterative process, which requires numerous interpretation phases. These interpretations are prone to uncertainties, stemming from the limits of data acquisition and resolution and the assumptions underlying their processing. These uncertainties propagate through the imaging process and impact our understanding and models of the subsurface. Taking them into account is, therefore, crucial during seismic interpretation and requires to be done automatically given the iterative nature of seismic imaging. In this thesis, I am interested in the assessment of structural uncertainties related to the interpretation of ambiguous seismic images of salt tectonics environments.

The main contribution of this thesis is a numerical method for stochastically modeling variable shapes of salt bodies and their connectivity. The modeling is based on an *a priori* definition of the uncertainties, represented as a buffer zone encompassing the salt boundary. The boundary is defined as the combination of a reference scalar field, computed from the buffer zone, and a spatially correlated random field that is used as a perturbation. This implicit formulation allows for the simulation of both varying salt geometries and topologies while ensuring the validity of the simulated boundaries. When the simulated diapir is a bulb detached from its pedestal, a weld is simulated to connect them. The position of the weld is determined from the scalar field representing the salt boundary, to ensure its consistency with the simulated salt bodies. The method is automatic and proposes to integrate punctual information (e.g., well data or manual seismic picks) and, to some extent, prior geological knowledge.

The second contribution of this thesis is an application of this method to the characterization of structural uncertainties underlying seismic imaging on a 2D synthetic data set. Starting from a rough buffer zone, I simulate a set of possible interpretations of the salt boundary. I use these interpretations to define a set of equiprobable migration velocity models, that are used in turn to generate as many seismic images. The statistical analysis of this image set, both directly and from derived seismic attributes, permits to highlight the image parts which are most sensitive to migration velocity variations, and provides insights on the

nature of the imaged salt bodies.

These contributions open new perspectives for uncertainty quantification in an automatic velocity model updating framework in seismic imaging.

Résumé étendu

La création d'un modèle numérique 3D du sous-sol nécessite d'intégrer des données éparses et ambigües. Les corps salifères ont des formes compliquées et peuvent présenter des singularités topologiques issues des spécificités de la tectonique salifère. La modélisation de leurs géométries est donc difficile [Collon et al., 2016], mais importante puisqu'ils introduisent de larges contrastes de propriétés physiques dans le sous-sol.

L'imagerie sismique est une méthode couramment utilisée pour cartographier le sel et obtenir des informations sur sa géométrie. Toutefois, la construction d'une image sismique est un processus itératif long, nécessitant de nombreuses phases d'interprétation [Brown, 2011]. Ces interprétations sont sujettes à des incertitudes émanant à la fois des limites d'acquisition et de résolution des données sismiques et des hypothèses faites lors de leur traitement. Ces incertitudes se propagent à travers le processus d'imagerie et impactent la compréhension du sous-sol et les modèles qui en sont faits. Leur prise en compte lors de l'interprétation sismique est donc cruciale pour éclairer les processus décisionnels futurs.

Dans cette thèse, je m'intéresse en particulier à l'estimation des incertitudes structurales liées à l'interprétation d'images sismiques ambigües dans des environnements de tectonique salifère. L'estimation des incertitudes structurales comporte trois volets distincts et complémentaires [Wellmann and Caumon, 2018] : leur caractérisation, leur échantillonnage et leur quantification. La caractérisation consiste à identifier les sources d'incertitudes et à les paramétriser (par exemple, en termes de position, intensité, orientation et corrélation spatiale) afin de définir un espace des incertitudes. Cet espace décrit l'ensemble des interprétations et modèles qui peuvent être attendus compte tenu de l'incertitude sur les données disponibles. L'échantillonnage consiste à tirer aléatoirement des modèles dans l'espace des incertitudes afin d'obtenir un sous-ensemble de modèles dont la variabilité soit représentative des incertitudes. Enfin, la quantification consiste à évaluer la variabilité de l'échantillonnage de telle sorte que cette information soit utilisable pour une prise de décision ultérieure.

Les quatre chapitres de cette thèse s'articulent autour de ces trois axes - caractérisation, échantillonnage, quantification - et se focalisent sur certains aspects spécifiques à l'interprétation des corps salifères à partir d'images sismiques. Le chapitre 1 établit un état de l'art des récents développements autour des méthodes d'interprétation sismique automatiques, et discute leur intérêt et leur intégration au sein d'une approche permettant la prise en compte des incertitudes lors de l'interprétation. Le chapitres 2 et 3, qui constituent la principale contribution de

cette thèse, proposent une méthode numérique de modélisation stochastique des enveloppes de corps salifères et de leur connectivité. La modélisation se base sur une définition *a priori* des incertitudes, sous forme d'une zone tampon autour de l'enveloppe du sel, pouvant être obtenue à partir des travaux décrits dans le premier chapitre. Enfin, le chapitre 4 présente une application de cette méthode pour caractériser et quantifier l'impact des incertitudes d'interprétation structurale lors de l'imagerie sismique d'un jeu de données synthétiques en 2D.

Interprétation sismique automatique des corps salifères

Historiquement, l'interprétation d'images sismiques est basée sur la capacité humaine à observer et développer des concepts pour expliquer ces observations [Herron, 2011]. Néanmoins, avec l'avènement des campagnes d'acquisition sismique en 3D, cette tâche est devenue plus compliquée puisque la vision humaine ne permet pas d'appréhender convenablement l'information volumique. D'autre part, le volume grandissant des jeux de données sismiques et le temps souvent limité pouvant être consacré à leur interprétation sont autant de facteurs supplémentaires qui viennent limiter la fiabilité des interprétations. Ces différents arguments ont justifié le développement de méthodes d'interprétation sismique automatiques dont une partie, depuis une vingtaine d'années, s'intéresse plus particulièrement aux corps salifères. Ces méthodes comportent généralement deux aspects complémentaires : d'une part, la mise en avant des objets d'intérêt dans l'image (c'est-à-dire le sel ou sa limite), et d'autre part, l'extraction à proprement parler de ces objets. Ces deux aspects ont grandement bénéficié des avancées réalisées dans les domaines du traitement d'image et de l'apprentissage automatique, dont nombre de méthodes ont été testées pour interpréter le sel.

Dans le premier chapitre de cette thèse, je dresse un état des lieux des différentes méthodes qui ont été proposées pour l'interprétation sismique automatique de corps salifères. Cet état des lieux propose une classification des méthodes en fonction de la stratégie d'interprétation mise en œuvre et de la famille d'algorithme utilisé, permettant de mettre en relief les différentes méthodes les unes par rapport aux autres. Si ces méthodes peuvent déjà atteindre une très bonne précision, il faut cependant garder à l'esprit qu'elles ont avant tout pour but l'extraction du "meilleur" prédicat possible de l'enveloppe de sel, et que ce prédicat reste une approximation de la réalité. Or, la question de la validation des interprétations obtenues via ces méthodes sur des données réelles (c'est-à-dire où la solution n'est pas connue) n'est jamais traitée dans la littérature et est laissée à la charge de l'interpréteur. Un élément crucial en vue de cette validation est le sens géologique qui est associé à l'interprétation. Considérer l'interprétation sismique comme un problème de traitement d'image classique limite fortement les liens réalisables entre structures interprétées et scénario géologique associé. La discussion associée à l'état des lieux proposé se concentre sur les possibilités qu'offrent les différentes familles de méthodes pour intégrer de la connaissance géologique dans l'interprétation.

Les principaux éléments de cette discussion ont servi de base à l'élaboration

d'une méthode d'interprétation sismique automatique combinant interprétation multi-attributs et multi-échelle. Cette méthode a été développée dans le cadre du projet de Master de Capucine Legentil, et est présentée en annexe de cette thèse [Legentil, 2019].

Modélisation stochastique des corps salifères

La principale limite des méthodes automatiques, à mes yeux, est qu'elles sont fondamentalement déterministes, se focalisant sur l'extraction du "meilleur" prédicat possible de l'enveloppe de sel. Cette vision de l'interprétation rend très difficile la caractérisation et la quantification des incertitudes liées à l'interprétation, ce qui est le cœur de cette thèse. Ceci m'a motivé à m'intéresser aux approches stochastiques. Elles sont en particulier développées en géomodélisation, où elles permettent d'échantillonner des géométries et des topologies variables d'horizons et de failles par exemple [Mallet, 2002]. Les méthodes existantes ne sont cependant pas adaptées aux spécificités des corps salifères, qui peuvent présenter des formes particulièrement complexes et des singularités topologiques (des sutures) [Collon et al., 2016].

Les chapitres 2 et 3 proposent une méthode numérique de modélisation stochastique des enveloppes de corps salifères et de leur connectivité. La modélisation des enveloppes s'inspire des travaux de Lecour et al. [2001] sur la perturbation géométrique de modèles surfaciques explicites à partir de champs de probabilités [P-fields, Srivastava, 1992], et de la méthode de modélisation de corps géologiques complexes par perturbation de la distance au squelette proposée par Henrion et al. [2010].

La méthode se base sur une caractérisation *a priori* des incertitudes, sous forme d'une zone tampon délimitant l'ensemble des positions possibles de l'enveloppe du sel [Bistacchi et al., 2008, Li et al., 2015]. Cette zone définit donc l'espace des incertitudes à échantillonner, et peut être générée à partir des méthodes d'interprétation automatiques discutées dans le chapitre 1. La modélisation repose sur une formulation implicite (utilisant directement la grille sismique), ce qui permet de simuler des géométries et des topologies variables tout en assurant la validité des enveloppes de sel simulées. La position de l'enveloppe dans la zone tampon est définie comme la surface de niveau 0 du champ scalaire $D_{pert} = D - \varphi$, où D est un champ scalaire de référence et φ un champ scalaire aléatoire spatialement corrélé servant de perturbation.

Le champ de référence D peut être considéré comme la probabilité *a priori* de chaque cellule de la zone tampon d'être dans les sédiments. Il est calculé à partir de la zone tampon : sa valeur est imposée à 0 au contact avec le sel déjà interprété, à 1 au contact avec les sédiments déjà interprétés, et le restant des valeurs est ensuite interpolé. La perturbation φ est décrite par un modèle de distribution et un modèle de corrélation spatiale. Le modèle de distribution contrôle à quel point l'enveloppe du sel peut s'éloigner de sa position de référence, et plus globalement le volume total de sel simulé. Le modèle de corrélation spatiale contrôle localement la forme de l'enveloppe.

Comme précisé, la méthode proposée permet de simuler des topologies variables de corps salifères. Lorsque le résultat de la simulation est un diapir dont le bulbe est déconnecté du piédestal, cela introduit une singularité topologique appelée suture dans le modèle qui nécessite d'être prise en compte et doit être représentée à part. J'ai donc proposé une extension à la méthode décrite ci-dessus, permettant de détecter automatiquement les modèles présentant une suture et de modéliser cette suture. Lorsque deux corps salifères différents sont simulés (un bulbe et un piédestal), il existe dans le champ scalaire D_{pert} une arête de valeurs minimales les reliant. Cette arête est utilisée pour définir la position de la suture à modéliser, ce qui permet d'assurer la cohérence de la suture avec les corps salifères simulés. Cette position est isolée en utilisant un algorithme de segmentation par ligne de partage des eaux [Cousty et al., 2009], couplé à un algorithme de filtrage des extrema locaux [Najman and Couprie, 2006]. Le résultat de cette segmentation est une partition binaire du modèle définissant une surface semi-infinie contenant la suture. La position exacte de la suture est ensuite définie en appliquant des critères de visibilité [Moës et al., 2002] calculés à partir des corps salifères simulés.

La quasi-totalité de la méthode de modélisation des corps salifères proposée est automatique. Elle permet d'autre part d'intégrer des informations ponctuelles dans la modélisation, telles que des données de puits et des pointés sismiques manuels de l'enveloppe du sel et/ou de la suture. Une sélection méticuleuse des paramètres de modélisation permet également d'introduire une connaissance *a priori* lors de la modélisation et de reproduire des structures géologiques spécifiques (contacts avec des séquences halocinétiques, diapirs en sapin de Noël, sutures incomplètes et partielles).

Impact des incertitudes structurales sur l'imagerie sismique

Dans le dernier chapitre de cette thèse, j'applique la méthode décrite ci-dessus à la caractérisation et la quantification de l'impact des incertitudes d'interprétation structurale au cours d'une itération de la boucle d'imagerie sismique. Plutôt que de proposer un unique scénario, je définis une zone tampon relativement grossière autour de la position de l'enveloppe du sel, et je génère stochastiquement une centaine d'interprétations structurales possibles de l'enveloppe. Ces interprétations sont couplées à un modèle de vitesse adaptatif représentant les structures sédimentaires en arrière-plan pour créer autant de modèles de vitesse de migration. Les modèles de vitesse sont utilisés pour remigrer les données sismiques (migration par renversement temporelle) et obtenir une collection d'images sismiques plus ou moins perturbées.

Je propose d'évaluer l'impact des incertitudes structurales sur l'imagerie à partir de la variabilité des images de cette collection. L'estimation de la variabilité peut se faire simplement par analyse statistique des images. Le calcul de l'image sismique "moyenne" permet de mettre en évidence les portions de l'image dans lesquelles les modèles de vitesse ont une réponse similaire de celles où la réponse est disparate (le principe est identique à celui de la sommation de traces

sismiques). Le calcul de l'écart-type permet d'apporter une information quantitative supplémentaire, et de distinguer, dans les portions d'images où l'amplitude est quasi-nulle, celles correspondant à une forte disparité de réponse sismique du modèle de vitesse et de celles où le signal est systématiquement faible.

Le calcul de ces statistiques (moyenne et écart-type) directement sur les images sismiques n'est possible, cependant, que grâce aux hypothèses faites lors de la création du jeu de données (en particulier, l'utilisation d'un modèle de vitesse exact dans les sédiments). Ces conditions "idéales" ne sont jamais rencontrées dans la réalité, et il est nécessaire de prendre également en compte l'incertitude du modèle de vitesse dans les sédiments. Pour que la description statistique de la collection d'images soit plus robuste aux variations introduites par les changements de vitesse, je propose de réaliser l'analyse statistique sur des attributs sismiques calculés à partir des images perturbées. Comme décrit dans le chapitre 1, de nombreux attributs ont été proposés et utilisés dans la littérature pour faciliter l'interprétation sismique. J'illustre cette proposition avec deux attributs issus de la matrice de co-occurrence des niveaux de gris [GLCM, Haralick et al., 1973] : le contraste et l'énergie. La GLCM est un descripteur de la texture locale de l'image autour d'un pixel. L'analyse statistique réalisée sur des attributs qui en sont dérivés permet de mettre en avant la variabilité locale de texture au sein de la collection d'image. Celle-ci est beaucoup plus robuste aux variations du modèle de vitesse que ne l'est la position des réflections dans l'image.

La comparaison des résultats obtenus en utilisant le même ensemble d'interprétations structurales sur deux jeux de données sismiques synthétiques différents (un diapir connecté à la couche de base du sel et un diapir déconnecté) met en évidence le fait que la méthode proposée permet également de fournir une information géologique sur la nature des corps salifères imagés.

Perspectives

La méthode de modélisation proposée dans cette thèse et son application ont produit des résultats intéressants sur des jeux de données synthétiques relativement simples. Cependant, plusieurs questions restent à aborder afin de pouvoir appliquer la méthode à des jeux de données réels.

La principale piste de recherche à aborder, selon moi, concerne la modélisation des structures sédimentaires associées aux corps salifères : les "mini-bassins" et leurs structures internes, telles les séquences halocinétiques [par exemple, Giles and Lawton, 2002, Giles and Rowan, 2012]. Ces structures ne sont pas gérées à l'heure actuelle par les logiciels de modélisation puisqu'elles correspondent à des strates sédimentaires qui sont à la fois conformes au centre des bassins et non-conformes à leur extrémités. De telles structures sont importantes à prendre en compte pour deux raisons. D'une part, elles peuvent fournir des informations importantes par rapport à la géométrie des enveloppes de sel sur les images sismiques. D'autre part, je me suis focalisé dans cette thèse sur les erreurs de vitesse liées au sel, mais il est primordial de prendre également en compte les erreurs de vitesse dans les sédiments lors de l'évaluation des incertitudes structurales.

La question de la création et de la mise à jour de la zone tampon modélisant les incertitudes structurales *a priori* reste également ouverte. De nombreux travaux décrits dans la littérature peuvent présenter d'intéressantes pistes de réflexion pour mener à bien cette tâche. Cette question et la limitation du coût de calcul sont deux points importants à prendre en compte pour aller vers une procédure de mise à jour automatique du modèle de vitesse de migration en imagerie sismique.

Remerciements

Merci ! (plein plein plein de fois) à Pauline et Guillaume, mes directrice et co-directeur de thèse, pour ces trois années et quelques. J'ai énormément appris à vos côtés, et votre contribution à cet ouvrage est plus que conséquente. En particulier, merci à toi Pauline pour ta disponibilité et ton encadrement au quotidien, sans lequel j'aurais passé mon temps à me heurter à des murs imaginaires. Et merci à toi Guillaume pour toutes les discussions qui apportent toujours de nouvelles façons d'appréhender ses travaux et ceux des autres. Vous avez formé une paire d'encadrants très complémentaire, c'est exactement ce dont j'avais besoin.

Merci aux membres du jury : Mary Ford, Amilcar Soares, Florian Wellmann, Virginie Gaullier, Pierre Thore et Xinming Wu, pour avoir accepté d'évaluer mon travail. J'ai eu droit à une toute belle équipe pour ma soutenance, et à des discussions très chouettes ! La preuve : c'est la première soutenance à laquelle j'assiste intégralement (questions comprises) et où je ne me suis pas ennuyé une seule seconde. Un merci tout particulier à Virginie et Xinming qui ont suivi mes travaux d'un peu plus près au travers des comités de suivi, et à Mary qui a accepté d'intégrer le jury au dernier moment et sans qui la soutenance n'aurait peut-être pas pu avoir lieu.

Merci aux sponsors du consortium RING-GOCAD pour avoir financé cette thèse et à l'ASGA, nommément Maryse, Armelle, Elisabeth et Nicole, qui en assure la gestion et nous protège au quotidien des questions administratives.

Merci à RING, parce qu'en plus d'être balèze c'est humain et convivial ! Et c'est important, parce que revoir ses copains, c'est bien plus motivant pour monter au bureau le matin que la pensée de la pile de bugs ou de biblio en retard qui nous y attend. Merci aux permanents : Guillaume, Pauline, Paul C, Fifi, Christophe, Mustapha et Christine, qui tiennent la boutique et font que ce petit monde perdure. Merci aux anciens thésards et post-docs qui m'ont recueilli il y a bien des années : Gautier, Benj, Jon, Marion, Antoine, Gaby, Pierre, Margaux, Modeste et Julien. Merci à Nico M et aux petits nouveaux qui m'ont permis de devenir sereinement un vieux con : Melchior, Yves, Coco, Paul B, Capucine, et Zoé. On a beau avoir des sujets complètement différents, je crois bien que tout le monde à RING m'a aidé au moins une fois dans ma thèse (des dizaines et des dizaines de fois pour ceux que j'ai le plus exploités...), que ce soit pour de l'expertise scientifique, de l'aide technique ou administrative, des conseils sur des présentations, des relectures d'articles... C'est chouette, vraiment ! Et bien sur, merci à Fatima,

Sophie et Nageoi qui ont su transformer les questions administratives inévitables en divertissement bienvenu. Pour finir, il faut reconnaître - très objectivement - que j'ai eu le bureau le plus cool du monde pendant 3 ans. Alors plein de bisous à Benj, Marion, Pierre, Julien, Zoé et Capu !

Le problème une fois sorti de RING, c'est qu'on se retrouve à Nancy. Et quand on n'a pas l'habitude, Nancy peut paraître austère, tendance astringent. Alors merci à toute la communauté des géologues férus de littérature qui a transformé ma morne vie nancéienne en aventure truculente ! Des débuts à la BU John Milton et aux Dockumentalistes jusqu'aux nocturnes de la Little Auditorium Bibliothèque, en passant par les BUs de plein air de Charles III et de Saint-Epvre, que de temps passé à bouquiner et refaire le monde avec vous. Et si les thésards de RING m'ont toujours supporté avec ferveur dans cette saine activité, il serait par trop d'aspects inique d'oublier les collègues de GeoRessources et du CRPG. Alors merci également à Yann, Boss, Josy, Seb, Pierric et toute l'équipe des bars doctorants : Julien P, Lucas, Laurie, Martin, Sylvain et notre chef d'orchestre Anne-Sylvie. Et puisque la littérature ne se vit pas seulement dans les bibliothèques, un grand merci à tous ceux qui m'ont ouvert leurs collections privées : Fifi, Julie, Arthur, Thomas, Benoit, Pauline, Paul C, Christine, Denis, Guillaume, les pelletées de thésards, etc. Si pendant 3 ans je n'ai pas eu à me soucier de découvrir l'écosystème local, c'est grâce à vous tous !

Pour finir, quelques remerciements pêle-mêle : à Capu, Léonore, Pierre et Thomas, pour leurs travaux et tout ce que j'ai pu apprendre au cours de leurs projets ; à Christine, Paul C, Guillaume, Pauline et Helmut, pour m'avoir permis de m'essayer à l'enseignement ; à Gautier, Benoit, Julien C, Pauline et Nico M, les forçats de la grimpe qui m'ont traîné derrière eux ; à Philippe, Mattia, et leurs collègues suisses et italiens, des (vrais) géologues qui nous ont montré des (vrais) cailloux ; à la Sainte-Barbe et aux copains sudistes pour les bouffées d'air pur ; et enfin à ma famille, parce que je ne leur dis pas souvent merci mais que j'ai toujours pu faire ce que je voulais, et qu'à la fin des "études" c'est l'occasion.

Bisous les copains !

Nancy, le 19/03/202X

Contents

Introduction

Drawing an accurate representation of the subsurface organization, and especially of its heterogeneities, is a key step toward the understanding of the solid Earth processes. This requires to have information about the subsurface, and a framework to support this information. The framework is called a geological model (or *geomodel*), and the different sources of information are obtained by answering the following questions: What can we see? What do we already know? What is left? What we observe or measure on the field are *data*, the already available information forms our empirical *prior knowledge*, and what goes beyond the scope of data and knowledge forms the *uncertainties*. The accuracy of our vision of the subsurface depends first and foremost on our ability to characterize these uncertainties, that is to say to determine up to which extent our predictions may be wrong.

Structural uncertainties: sources and assessment

Sources of uncertainties

Subsurface data are fundamentally incomplete, due to limited resolution and spatial distribution [e.g., Bond, 2015]. Geology provides direct observations and lab analyses of outcrops and core samples, that is to say precise punctual information. Geophysics provides information about otherwise inaccessible locations, through indirect measurement methods which can either be relatively precise and local (e.g., well logging) or have a global coverage and a poor resolution (e.g., potential and seismic methods). Uncertainties related to data can be considered as objective [Bond, 2015].

To overcome data scarcity and ambiguity, geologists strongly rely on the empirical knowledge they have built over time [Frodeman, 1995]. This knowledge is made of geological rules and concepts, analog data, and numerical and analog modeling experiments. Except for the controversies, that are inherent to geology, the uncertainties underlying this knowledge are *per se* objective and negligible. A major source of uncertainty resides, however, in the combination of data and knowledge, that is to say in how knowledge can be used for the *data interpretation* and the interpolation/extrapolation of the geology away from the data [Wellmann and Caumon, 2018]. Interpretation uncertainties are subjective, and affect both the geometry (i.e., the position and the shape) and the topology (i.e., the number, the nature and the connectivity) of the subsurface structures.

From a general point of view, a specific source of uncertainty can be characterized according to several criteria [e.g., Thore et al., 2002]: its position (its surface or subsurface localization), its magnitude (that relates to "maximum" possible error), its direction

(uncertainties are often anisotropic and larger along specific directions), and its spatial correlation (i.e., up to which extent it affects the uncertainty of its neighborhood). In some cases, and especially for interpretation, it is also possible to characterize the uncertainties in terms of conceptual model, that is, which specific knowledge is used to explain the data.

Uncertainty assessment

In geomodeling, two categories of uncertainties are usually considered: the structural uncertainties and the petrophysical uncertainties [e.g., Caumon, 2018]. Structural uncertainties are related to the position and the connectivity of structures represented in the geomodel (e.g., horizons, folds and faults). The petrophysical uncertainties relate to the distribution of the rock petrophysical properties in the subsurface (e.g., porosity and permeability). During my PhD, I focused on the study of structural uncertainties. Their assessment usually consists of two steps: sampling the uncertainty space (the set of all possible models given the uncertainties), and quantifying the variability of this sampling.

Sampling of the uncertainty space Sampling the uncertainty space is exactly what geologists naturally do when maintaining multiple hypothetical scenarios explaining their observations, and updating, refining, and disposing of them when new data are available [Chamberlin, 1890, Frodeman, 1995, Bond, 2015]. It provides insights on the variability of interpretations and models that can be expected given the data. When done by a geologist, this task is usually limited to the consideration of different conceptual models (i.e., different model topologies), as sampling variable model geometries requires generating a large set of models. Two solutions have been considered for this: asking for a large set of persons to interpret a single data set [e.g., Bond et al., 2007, 2012, Schaaf and Bond, 2019], and stochastically generating multiple geomodels [e.g., Caumon et al., 2007, Caumon, 2018, Wellmann and Caumon, 2018]. The first approach allows for the quantification of subjective interpretation uncertainties, but cannot be used in practice due to the large amount of persons it requires.

A central element for sampling uncertainties resides in the formalization of the "geological knowledge" into a set of applicable rules [Frodeman, 1995, Bond, 2015]. First, it allows for the invalidation of interpretations and models that would not satisfy with geological reasoning [Bond, 2015], and thus for the reduction of the uncertainty space. Secondly, this formalization is necessary for the development of numerical modeling methods [Caumon, 2018, Wellmann and Caumon, 2018]. In the frame of geomodeling, the uncertainty space sampling can be performed by perturbing the data [e.g., Wellmann et al., 2010, Lindsay et al., 2012], the way data are associated [e.g., Godefroy et al., 2019] or a reference structural model [e.g., Lecour et al., 2001, Caumon et al., 2007]. An interesting perspective about the formalization of geological knowledge and its numerical implementation is that it paves the way to the development of systematic and automatic interpretation methods [Caumon, 2010], which are a way to reduce subjective interpretation uncertainties and especially the potential human biases illustrated by Bond et al. [2007].

Quantification of the uncertainties The question of structural uncertainty quantification can be seen under two perspectives. The first one is from a structural point of view. Variable strategies can then be used to characterize the structural variability. For example, various authors have proposed to compute indicator functions monitoring the variations between models, especially based on stratigraphic information [e.g., Wellmann et al., 2010, Lindsay et al., 2012, Wellmann and Regenauer-Lieb, 2012]. The second aspect that can be considered is from the model application point of view. Indeed, all the structural details do not have the same impact on the subsurface processes [e.g., Anquez, 2019, Raguenel, 2019]. In particular, topological details may play a prominent role as compared to geometric variations [e.g., Thiele et al., 2016b, Wellmann and Caumon, 2018]. Therefore, various authors have also proposed to quantify the structural uncertainties based on the results of forward physical simulations [e.g., Manzocchi et al., 2008, Lindsay et al., 2013, Julio et al., 2015] or geophysical inversion [e.g., Lindsay et al., 2014, Giraud et al., 2017].

General problem and context

One of the major questions underlying the integration of uncertainty management into the geomodeling workflow is how to numerically formalize the structural interpretation process and its evaluation, in order to update an *a priori* knowledge model of the subsurface and assess the reliability of the *a posteriori* model. This question raises more elementary questions, such as: How to numerically translate an expert knowledge based on experience? How to assess the uncertainty related to an interpretation or a set of interpretations? How to integrate this uncertainty into an updating procedure of the *a priori* subsurface model?

In this thesis, I consider the global question of structural uncertainty assessment on a specific application: the interpretation of seismic reflection images in salt tectonics environments. I therefore work in a context where data have a global coverage but limited resolution, and with specific geological concepts derived from salt tectonics.

Salt tectonics

Evaporitic rocks are crystalline rocks resulting from the precipitation of minerals rich in chlorides, sulfates, and alkali and alkaline earth metals during the evaporation of brines. The most common of them is known as *salt*. This term initially referred to rocks composed exclusively of halite mineral (NaCl), but is now used in a broader sense including all evaporitic rocks mainly composed of halite (that is, salt may have a composite nature and include for example gypsum and anhydrite) [e.g., Hudec and Jackson, 2007]. Following the common usage, I use the term salt in this manuscript in its broad acceptation, without specific reference to pure halite.

Evaporitic rocks have so specific physical properties and rheological behavior, as compared to other (sedimentary) rocks, that a branch of geology is specifically dedicated to their study, namely salt tectonics. Salt tectonics encompasses all the deformations that occur in sedimentary basins under the effect of salt displacement [e.g., Jackson and Hudec, 2017]. It therefore includes the mechanisms behind salt displacement, the

salt and surrounding sediment structures that result from this displacement, and the relations with regional tectonic.

Salt physical properties

The most peculiar property of evaporites is their rheological behavior. For example, at geological time scale, salt behaves like a viscous fluid. When submitted to stress, it deforms with a creeping behavior (i.e., viscoplastic deformation), developing complex structures (termed *salt bodies*) and inducing deformation of the surrounding sediments [e.g., Jackson and Hudec, 2017]. From a general point of view, the deformations implied in salt tectonics are termed brittle-ductile as they depend on the ductile behavior of evaporites and the brittle behavior of surrounding sediments.

Among the physical properties of interest for seismic imaging, evaporites are almost incompressible (due to their crystalline structure) and have high seismic wave velocities and relatively low densities (e.g., respectively about 4500 $m.s^{-1}$ (for P-waves) and 2.15 $kg.m^{-3}$ for slightly impure halite) [e.g., Baar, 1977].

Several other salt properties underpin specifically the interest of the petroleum industry. First, salt is an impermeable rock. Combined with the complex structures that salt develops, this property makes salt structures potential seals to form hydrocarbon traps. In addition, salt has a high thermal conductivity (about 6.7 $W.m^{-1}.K^{-1}$) [e.g., Jackson and Hudec, 2017]. It therefore plays a key role in the hydrocarbon maturation process, as temperature is one of the most crucial factors impacting this maturation [e.g., Hudec and Jackson, 2007].

Mechanisms controlling salt tectonics

Salt flow is driven by differential loading, that is to say it flows as a reaction to a gradient of load in order to accommodate it [e.g., Hudec and Jackson, 2007]. This loading can have three different origins: gravity forces, tectonic forces, and thermal effects. Gravitational loading includes the gravity forces acting within salt bodies and the effect of the salt overburden weight. It results in the lateral expulsion of salt from an initial source. Displacement loading occurs during tectonic deformation when a forced displacement is applied to one of the salt boundaries. Thermal loading is induced by gradients of temperature within the salt body and can trigger convective intrasalt flows.

Some forces resist to salt flow, explaining why not all the salt bodies undergo deformation: the overburden strength, and boundary drag [Jackson and Hudec, 2017]. For salt to move, the overburden must undergo deformation. In the absence of differential loading, this requires damaging the overburden, which is less likely to happen when the overburden compaction and thickness increase (e.g., with depth). Boundary drag corresponds to the viscous forces opposed to flow at the contact between salt bodies and the surrounding sediments. These forces are linked to the thickness of the salt body: the thinner the salt body, the stronger the viscous forces are. This effect implies that salt is unlikely to be completely expelled from a location, without the intervention of external phenomena (e.g., dissolution).

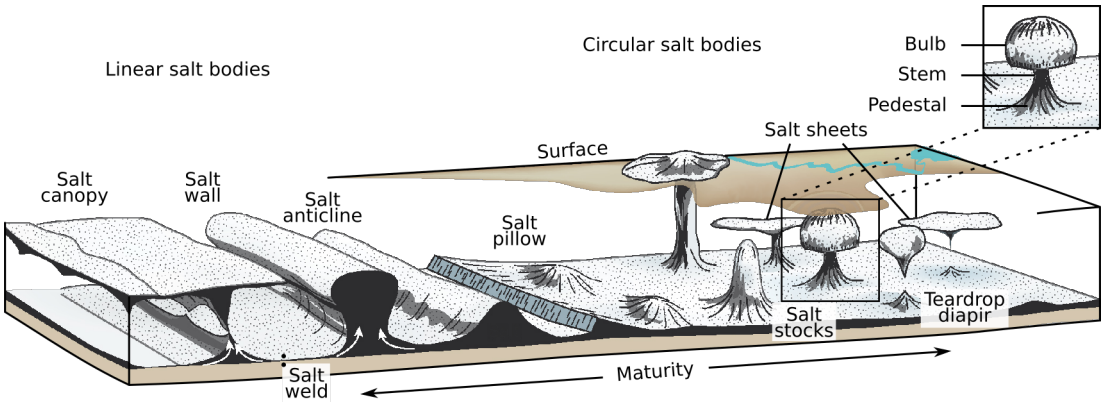

Figure 1 – Nomenclature of salt bodies. The structure maturity increases toward the image boundaries. Salt welds are highlighted by pairs of dots. Image from Fossen [2016]. Reproduced with permission of Cambridge University Press through PLSclear.

Atlas of salt structures

When moving, salt forms a wide variety of structures whose shapes and growth mechanisms are strongly related to the geological context (figure 1). The aim is not to exhaustively review here all the mechanisms involved in the formation of salt bodies, but rather to provide the reader with an overview of the diversity of structures that can develop in salt tectonics environments. For an in-depth state of the art, the readers can refer to the book of Jackson and Hudec [2017]. In the following, we present the different structures according to their "maturity", which is the order in which they develop.

Salt pillows and anticlines When salt begins to move, its overburden forms gently folded structures cored with salt. Depending on the context, these folds can be either circular or elongated, and the associated salt structures are termed respectively salt *pillows* and salt *anticlines*. They develop within salt layers, either *autochthonous* (i.e., salt that has not significantly moved and thus remains on the strata it deposited on) or *allochthonous* (i.e., salt that has moved and formed second generation layers on top of younger sediments, presented and properly defined later).

Salt stocks and walls If the salt supply persists, salt can continue flowing into pillows and anticlines, forming more vertical structures grouped under the term of salt *diapirs* (salt masses that discordantly "intrude" their overburden). These are the most widespread types of salt bodies, and those I am primarily interested in. As pillows and anticlines, diapirs can be divided into salt *stocks* and salt *walls* according to their circular or elongated geometry. Salt diapirs can be divided into three parts (figure 1): the *pedestal* (which links the diapir with its source), the *bulb* (the top, often inflated, part of the diapir), and the *stem* (the central part linking the pedestal and the bulb).

Three types of diapir growth mechanisms have been identified: reactively to tectonic extension, actively by "piercing" of a thin overburden, and passively as sediments deposit around the diapir, maintaining a gravitational loading. During their evolution, diapirs can also pinch off (either partially or completely), due to squeezing by regional shortening or gravitational loading.

Concurrently to diapir building, sedimentary *minibasins* develop. These minibasins form on top of thick salt layers and progressively subside within salt. Therefore, they are a source of gravitational loading, and their organization is strongly related to the one of diapirs. Sedimentary minibasins are beyond the scope of my work, but their organization provides interesting information about the diapir history. In particular, sediment packages that deposit in the vicinity of a passively growing diapir develop very specific patterns. These packages are called *halokinetic sequences*, and are separated by unconformities. They provide information about the variations between the diapir rise and sedimentation rates, and can be useful indicators when interpreting diapir boundaries on seismic images.

Salt sheets and canopies It may happen that, during its growth, a diapir reaches the surface (or the sea floor). Due to its viscous behavior and gravity forces, it spreads at the surface over younger sediments, forming an allochthonous salt *sheet*. The initial diapir is then termed the salt *feeder* of the sheet. If sedimentation and diapir building start up again, the salt sheet is buried and forms a salt *wing*. When this happens multiple times, the diapir exhibits stacked wings and is termed a *Christmas tree* diapir.

Different salt sheets can coalesce at the surface, forming a salt *canopy*. The junctions between two sheets are called salt sutures. Depending on the available volume of salt, salt sheets and canopies can themselves serve as source layers for the development of new generations of salt diapirs, sheets and canopies.

Salt welds In many cases, it may happen that salt is completely expelled from a given location and that originally separated sediment strata enter in contact (e.g., due to minibasin subsidence or complete diapir pinch off). The contact zone separating the sediment blocks is called a salt *weld*. Salt welds play major roles in various domains (e.g., basin compartmentalization, deformation mechanisms and thermal transfers). They are the topic of chapter 3, which further develops their properties.

The understanding of salt tectonics mechanisms and structures has long been limited by the paucity of available data. Even though salt basins are widespread across the world [e.g., Hudec and Jackson, 2007], the high solubility of salt entails that outcropping salt bodies are quickly weathered, complicating their observation. In addition, outcrops only allow for the observation of 2D sections through complex geobodies and thus do not provide much information about the 3D architecture of salt bodies. Analog modeling has proven to be a fundamental help in overcoming these limitations and understanding salt tectonics mechanisms and the resulting 3D architectures [e.g., Vendeville and Jackson, 1992, Weijermars et al., 1993]. It is now completed by numerical modeling that provides new insights about model validity and subsurface stress state [e.g., Gemmer et al., 2004, Weijermars et al., 2015]. Nevertheless, when it comes to subsurface exploration, the main source of information to constrain the geomodel structures comes from seismic reflection imaging. Borehole data and geological concepts can then help constrain the models further.

Seismic reflection imaging

Seismic reflection imaging (contracted in *seismic imaging* in the following through common abuse of language) is a geophysical exploration method that uses the echoes of acoustic waves propagating in the subsurface to draw a map of subsurface heterogeneities.

The seismic imaging workflow

Seismic imaging can be divided into three steps: the data acquisition, their processing, and the interpretation of the results. Seismic reflection data consist of a set of recordings of the ground (or water) motion, indicating the travel times and amplitudes of seismic waves traveling between pairs of sources and receivers. Seismic processing aims at transforming this information into a map of the reflection locations into the subsurface (a *seismic image*). The interpretation consists in extracting the geological content of a seismic image, that is to say in assigning a geological meaning to these reflections.

At first sight, it may seem that these three steps are relatively independent. Data acquisition is necessarily upstream and should not much affect the next phases; processing is performed by expert geophysicists who understand the physics of wave propagation; and interpretation is the role of expert geologists that are able to interpret structures and propose scenarios explaining them. In practice, the difficulty to process seismic data does not allow it to be so simple. The aim here is not to enter into all the details about seismic imaging, but to highlight the difficulties which are specifically introduced by the presence of salt bodies. The reader is referred for example to Yilmaz [2001] for further details.

Seismic processing in salt environments The processing of seismic data includes numerous phases, all of which are not necessarily mandatory and are achievable in different manners. Among the necessary steps, the migration is maybe the most important one, as its aim is to reposition the reflections at their correct location in the subsurface. The presence of complex salt bodies is best handled by pre-stack depth migration (PSDM) methods, due to the large lateral velocity contrasts salt introduces in the subsurface. These methods require to define various detailed models of the earth parameters, and especially a velocity model of the subsurface [e.g., Jones, 2015].

The imaging loop The use of incorrect parameter fields during migration results in a somehow distorted image. As an example, if you use a wrong migration velocity model, you cannot correctly estimate the depth of a reflection given its travel time. Yet, it is extremely difficult to derive accurate subsurface parameter fields, due to the few subsurface data available.

As a consequence, seismic imaging is often an iterative process (figure 2). Working on the assumption that a reflection is correctly repositioned if the velocity model above its corresponding reflector is correct (as the waves reaching it only traveled through the correct model part), the aim is to build the velocity model using a top-down approach, fixing the upper model parts first and progressively updating the lower parts [e.g., Dellinger et al., 2017]. This requires to loop over a series of migration, interpretation,

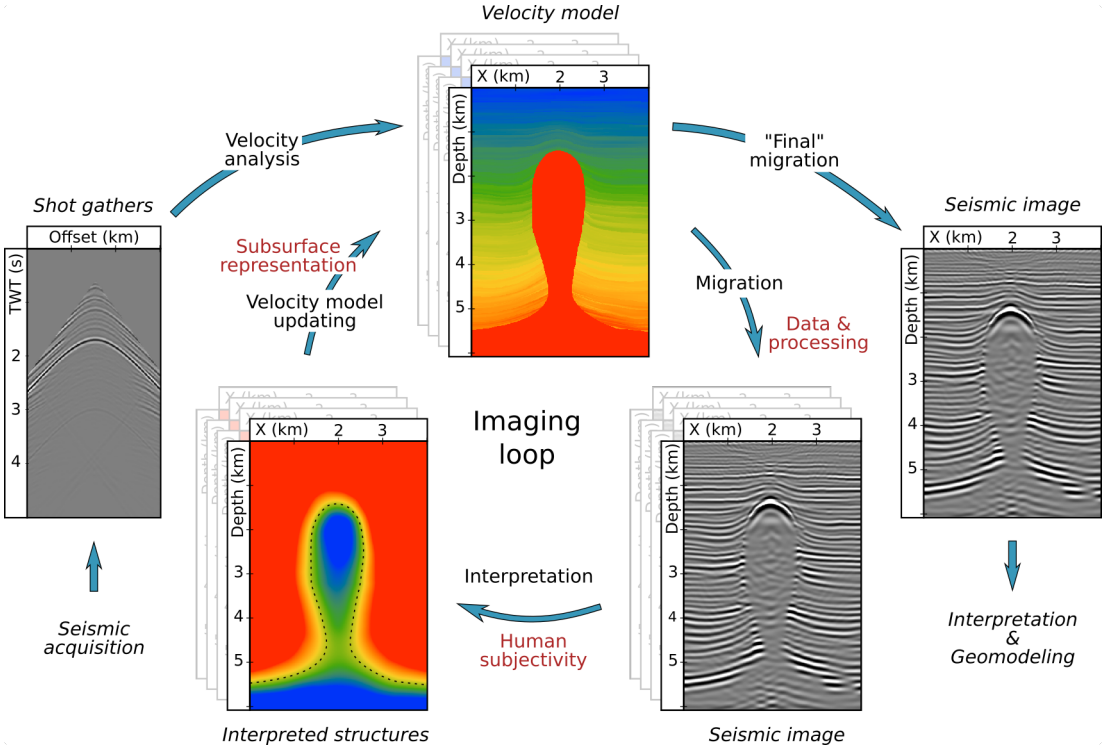

Figure 2 – Overview of the seismic imaging workflow. An initial velocity model is built from velocity analysis. This model is progressively improved by looping over a series of migration/interpretation/updating phases. Once the image is judged satisfactory, it is transfered to the geomodeling workflow. The main sources of uncertainties that take place in the imaging loop are highlighted in red. TWT = two-way travel time.

and updating of the velocity model until obtaining an image with a quality judged sufficiently satisfactory regarding its application.

Structural uncertainties in seismic imaging

It is possible to divide the uncertainties underlying seismic imaging into three categories (figure 2): those related to the data, those related to the processing, and those related to the interpretation.

Data uncertainties The data uncertainties are mainly related to noise and resolution. Numerous processing methods allow for noise reduction (e.g., stacking and demultiple), so its contribution to the overall uncertainty can usually be considered as relatively low. Resolution is inherently related to the wavelength of propagating seismic waves, and thus to the recorded frequencies. It determines the minimum distance necessary between two consecutive reflectors to obtain two separated reflections in the recorded signal, and thus controls the maximum level of detail contained in a seismic image.

Processing uncertainties Processing uncertainties are extremely varied, as each processing step can introduce some errors through its underlying assumptions and sim-

plifications. In addition, uncertainty effects can be difficult to properly track and quantify as processing often involves highly non-linear transforms.

Nevertheless, from a general point of view, a lot of processing uncertainties are related to the time-to-depth conversion due to the difficulty to accurately predict the velocity model [Thore et al., 2002]. When using PSDM methods, this step is included in the migration, which can thus be considered as concentrating most of the processing uncertainties. This uncertainty is amplified by the presence of salt bodies which drastically complicate the subsurface velocity field. Among the difficulties specifically introduced by salt, the complex salt body shapes result in complex wave travel paths and large lateral velocity variations. In addition, they can also introduce low illumination regions [e.g., Jones and Davison, 2014]. The presence of cap rock around salt bodies can also drastically change the local velocity field and thus the final images, as well as an inaccurate anisotropy representation [e.g., Jackson and Lewis, 2012, Jones and Davison, 2014]. These effects, with the usually large velocity contrasts between salt and sediments, make the accurate prediction and modeling of velocity and other parameter fields prone to large uncertainties.

Interpretation uncertainties The uncertainties related to the interpretation of a seismic image, independently from its building, are subjective and related to the choices made by the interpreter [Bond et al., 2007, Schaaf and Bond, 2019]. They are about the geometry and the topology of the interpreted elements, that is to say respectively on the position of the elements in the model, and on the number, type and connectivity of the elements [Wellmann and Caumon, 2018]. An associated source of uncertainty comes from the link between interpretation and velocity model updating, due to the difficulty to conciliate the geological (i.e., geomodel) and geophysical (i.e., parameter fields) visions of the subsurface [Caumon, 2018].

Propagation of the uncertainties As it has already been stated, imaging complex environments requires iterating over multiple interpretation and migration phases. Current practices for interpreting the intermediate images in the imaging loop usually resume to a manual picking of the main interfaces [e.g., Dellinger et al., 2017]. In addition, the even more sophisticated migration algorithms require more and more computational power and time to perform. Due to these time requirements, seismic imaging is most often performed in a deterministic manner. Such approaches leave no chance to propagate the uncertainties between the iterations, and thus make it almost impossible to properly characterize seismic imaging uncertainties.

Contributions

Scientific barriers

Seismic uncertainties have been a long-running topic in geosciences. The statement of Thore et al. [2002] still holds true today: the topic of seismic uncertainty quantification is still treated either from a geophysical point of view [e.g., Osypov et al., 2013, Fomel and Landa, 2014, Weinzierl et al., 2016], a subjective point of view [e.g., Bond et al., 2007, Schaaf and Bond, 2019], or a geostatistical point of view [e.g., Abrahamsen, 1993,

Holden et al., 2003, Caumon et al., 2007], but more general approaches are rare [e.g., Irakarama et al., 2019].

Concurrently, numerous progresses have been achieved in the field of automatic seismic interpretation, and especially in the domain of salt interpretation [e.g., Wu, 2016, Shi et al., 2019]. The proposed methods consider, however, seismic interpretation as a purely deterministic signal processing problem, and lack the possibility to explicitly integrate geological knowledge. In addition, they often assume working with high quality seismic images.

In geomodeling, works have focused on the development of stochastic modeling methods for quantifying structural uncertainties. These methods are designed to perturb specific geological objects (e.g., horizons and faults) [e.g., Caumon et al., 2007]. Most of the time, they are, however, not suited to model salt bodies, due to the complex geometries that salt develops and the necessity to sample variable topologies [Collon et al., 2016].

Approach

I am interested in the assessment of structural uncertainties underlying the interpretation of seismic images. Given the time required to propose and assess different interpretations and *a fortiori* the difficulty to do it in 3D, this task requires to be performed numerically. The overall aim of my work is thus to develop a numerical interpretation method that allows for this uncertainty assessment.

To design such a method, I based my work on several postulates. The first one is that (1) the uncertainties "underlying" seismic interpretation can fundamentally be divided into two categories: the interpretation uncertainties in a strict sense (i.e., the subjective ones related to the interpreter choices) and the image uncertainties (i.e., the objective ones inherent to the seismic image limited quality). This drives the following postulate: (2) different types of uncertainty should not be handled the same way. Subjective uncertainties can be reduced by formalizing the interpretation concepts into a set of rules that can be applied rigorously. Furthermore, formalizing the way these rules are selected permits to reduce even more the human subjectivity contribution to the global interpretation uncertainty. Objective uncertainties cannot be reduced (without control on seismic processing). They therefore require first and foremost an adapted model sampling method. As I am focusing on salt-related structural uncertainties, this method must handle the specific salt geometries and topologies. The last postulates are related to the iterative nature of seismic imaging. As interpretation occurs at each step of the imaging loop, (3) an interpretation method should not rely on a high-quality seismic image. In addition, (4) as uncertainties are propagated throughout the imaging workflow, their definition must allow for their propagation from an iteration to the next one.

With these considerations in mind, my PhD work aimed at designing numerical methods and workflows to address these different problems. This includes the development of new C++ codes, of various shell wrappers and Python tools to make use of existing libraries and automate the procedures, and the testing of the proposed workflow on typical data sets.

Contributions and organization of this thesis

Chapter 1 reviews works which have been performed in the automatic seismic interpretation domain (especially about salt interpretation). The aim is to propose an overview of the existing (deterministic) approaches, in order to assess their potential and discuss their adaptation to uncertainty quantification. This chapter also presents the work performed in the frame of a master project that I supervised [Legentil, 2019], which built upon this review to develop a multiscale interpretation method. The aim of the method is to explicitly introduce a notion of spatial continuity in pixel-base classification methods.

The main contribution of this thesis is a method for stochastically modeling variable shapes of salt bodies and their connectivity from seismic images. The salt body modeling is based on an *a priori* definition of the uncertainties in the form of a buffer zone (supposed to encompass the actual salt body boundary). It allows for the simulation of both varying salt geometries and topologies. It is the topic of chapter 2 and has been published in the journal *Interpretation* [Clausolles et al., 2019a].

Depending on the input configuration, the method can generate teardrop diapirs (i.e., whose bulb is detached and connected to the pedestal by a weld). From a geomodeling point of view, such configurations are not valid if the connectivity (i.e., the weld) is not represented. In chapter 3, I propose an extension of the salt modeling method to detect these configurations and model a salt weld. The entire method is automated, and proposes to integrate punctual data such as manual seismic picks and well data about the salt boundary and weld position.

In chapter 4, I present an application of the modeling method to the characterization of structural uncertainties underlying seismic imaging on a 2D synthetic data set. Starting from a rough uncertainty envelope, I simulate a set of possible interpretations of the salt boundaries that I use to remigrate the seismic data. The statistical analysis of the resulting seismic image set, both directly and from derived seismic attributes, permits to highlight the image parts which are most sensitive to migration velocity variations, and provides insights on the nature of the imaged salt bodies. This chapter concludes with a discussion about the work ahead toward the completion of the overall interpretation and updating loop.

Context of the thesis

Administrative and scientific frame

During this thesis, I was attached to the GeoRessources[1] laboratory, which depends from the University of Lorraine and the french National Center for Scientific Research. The laboratory activity focuses on the subsurface resources (both energy and mineral resources) all along their life cycle, from exploration to the reuse of residues. This activity is divided into three main research themes: geomodels, raw materials and geosystems, around which several research teams are organized.

My research work enters in the frame of the RING[2] (Research for Integrative Numerical Geology) team project, which performs methodological research about the description of the subsurface geometry and heterogeneities consistently with observations and geological concepts. This research combines geosciences, applied mathematics, and computer programming to develop theoretical works and novel technologies in the fields of stochastic structural and stratigraphic modeling, stochastic sedimentary and diagenetic objects description, adaptive gridding and scale management, and investigate their impact on subsurface physical processes.

Research at RING benefits from the support of an international research consortium, the RING-GOCAD consortium, which gathers companies, universities and research institutes interested in the various aspects of subsurface modeling. This consortium, which is managed by ASGA[3] (Scientific Association for Geology and its Applications), financed my PhD work.

Technical frame

As stated, the RING project promotes the development of the technologies supporting its research. Therefore, I have had the opportunity to implement most of the tools and workflows described throughout this thesis.

Most of the developments realized in the frame of this PhD are grouped in a custom plugin (called Goscope) of SKUA-GOCAD™, an industrial geomodeling software suite whose software development kit and application programming interface are complimentary provided by Emerson E&P Software [2019]. Goscope is mainly written in C++ and offers automatic seismic interpretation tools. It has been initially developed by Pierre Jacquemin, who worked on the extraction of faults, horizons and layers. I mainly added image processing algorithms, a salt and velocity modeling workflow, and seismic cube manipulation tools. In the frame of the annual meeting held by the team (the RING Meeting), I also had the occasion to propose trainings for the attendees to test the proposed modeling workflow by themselves.

[1] https://georessources.univ-lorraine.fr/en
[2] https://www.ring-team.org/home
[3] http://asgageol.univ-lorraine.fr/

Communications

Notations: $^{(r)}$*peer-reviewed article,* $^{(o)}$*oral presentation,* $^{(p)}$*poster presentation,* $^{(a)}$*proceeding article,* $^{(e)}$*extended abstract.*

Peer-reviewed article

$^{(r)}$ N. Clausolles, P. Collon, and G. Caumon (2019). Generating variable shapes of salt geobodies from seismic images and prior geological knowledge. *Interpretation*, 7(4): T829–T841, doi: 10.1190/INT-2019-0032.1.

Conferences

$^{(p,e)}$ N. Clausolles, P. Collon, and G. Caumon (2018). A workflow for 3d stochastic modeling of salt from seismic images. In *80th EAGE Conference and Exhibition 2018*. doi: 10.3997/2214-4609.201801272.

$^{(o)}$ N. Clausolles, P. Collon, and G. Caumon (2018). Generating variable shapes of salt geobodies from seismic images. In *19th Annual Conference IAMG 2018*.

RING Meeting

$^{(o,a)}$ N. Clausolles, P. Collon, and G. Caumon (2017). Seismic interpretation of salt geobodies using texture attributes. In *2017 Ring Meeting*, p. 141–154.

$^{(o,a)}$ N. Clausolles, P. Collon, and G. Caumon (2018). Generating variable shapes of salt geobodies from seismic images. In *2018 Ring Meeting*, p. 493–503.

$^{(o,a)}$ N. Clausolles, P. Collon, G. Caumon, and M. Irakarama (2019). Stochastic salt modeling for characterizing seismic imaging uncertainties. In *2019 Ring Meeting*, p. 113–126.

Chapter 1

Seismic interpretation of salt bodies

Contents

Abstract In this chapter, I first review the different approaches which have been proposed in the literature to automatically interpret salt bodies. As these approaches focus on deterministically extracting a "best possible" predicate of the salt boundaries, I discuss in a second time how some of the proposed elements can help incorporate geological knowledge into automatic interpretation and assess interpretation uncertainties. A key element is that these methods should not only focus on segmenting salt from sediments, but also consider the possibility for the interpretation to be too ambiguous to be conclusive, and thus to integrate an uncertain category. These different elements have been integrated into an automatic interpretation method combining multi-attribute and multiscale approaches, in the frame of a master project [Legentil, 2019].

1.1 Introduction

"*Interpretation is telling the geologic story contained in seismic data*" declares Herron [2011] in the opening of his book. This philosophical description of the essence of seismic interpretation is confirmed in practice as interpreters describe their task as extracting geological details from seismic data [e.g., Brown, 2011]. Seismic interpretation is therefore at the interface between geophysics and geology. It requires both to understand how the data were processed (as it defines what we are looking at), and the geological reasoning advocated by Frodeman [1995] (to explain what we observe). Historically, it has relied on the human capacity to observe and develop concepts. Human vision is, however, relatively limited to process 3D seismic data as it cannot handle volume information (it is usually restricted to the visualization of sets of 2D sections). In addition, the ever increasing size of the seismic data sets requires the interpreters to spend more and more time to interpret seismic images.

In practice, there may not be enough time to perform the interpretation in ideal conditions. Moreover, various sources of limitations complicate the task of the interpreter and limit the reliability of the resulting interpretations (e.g., poor data quality, which may leave uninterpretable portions of the data, and potential human biases [Bond et al., 2007]). All these reasons have incited a lot of works dedicated to help seismic interpretation and to automate it [e.g., Wang et al., 2018]. This chapter especially focuses on those related to salt body interpretation. These works aim at developing numerical interpretation methods that characterize the "signature" of the features of interest in seismic images, in order to recognize and extract them automatically [e.g., Schlaf et al., 2005]. These methods offer various advantages as compared to manual interpretation [e.g., Wang et al., 2018]: they are not limited by the size and the dimension of seismic images, they allow for the integration of multiple sources of information, and thus to make a "better use" of seismic data, and finally, they apply their underlying decision

criteria in a systematic way, preventing potential biases that may happen during manual interpretation. Therefore, they outperform manual interpretation in numerous ways.

There is, however, one limitation to their applicability, which is the ambiguous nature of seismic data. To interpret uncertain parts in a seismic image, an interpreter usually relies on his prior knowledge [e.g., Frodeman, 1995, Brown, 2011]. The question of the formalization of the geological knowledge and reasoning into interpretation rules is particularly difficult, and has remained marginal so far. Current automatic methods rather consider the interpretation as a signal processing problem. They build on the recent progresses in the image processing and machine learning domains to improve interpretation accuracy [e.g., Wang et al., 2018]. The strategy consists in automating as much as possible the interpretation of the least ambiguous image parts, and to leave the validation and the most complex parts to interpreters. The automation is, therefore, mainly seen as a tool that help reducing the necessary time spent by interpreters to manually pick the different structures.

This chapter is two-sided. On the one hand, it contains a review of the different methods which have been considered in the literature to automatically interpret salt bodies from seismic images. On the other hand, it presents the outlines of a master project that I supervised which builds on this review conclusions to develop a custom interpretation method integrating the notion of uncertainties [Legentil, 2019].

The review I propose principally considers the classification of the different types of approaches which have been developed for interpreting salt. The discussion focuses on how these different categories may allow for the integration of geological knowledge into the interpretation. I do not compare the methods in terms of results (e.g., accuracy, etc.). For multiple reasons, this comparison is very difficult to perform objectively. The main reasons are: (1) the lack of benchmark data sets containing salt structures (comparing different interpretations requires a reference interpretation), (2) the tuning of each method set of input parameters (which may drastically affect the results, and which is not discussed by authors when comparing their methods to preexisting ones (furthermore, such comparison is not necessarily provided)), and (3) the potentially composite nature of automatic interpretation methods (which often include a feature emphasis step and a feature extraction step, as discussed later in this chapter), which makes the impact of each specific step difficult to investigate.

One of the main conclusions of the review is that the proposed methods consider the automatic interpretation of salt as a deterministic problem whose aim is to extract a "best possible" boundary geometry, leaving the question of the validation to the interpreter. The work performed in the frame of Capucine Legentil's master project [Legentil, 2019] proposes an automatic interpretation method taking into account uncertainties and allowing for the integration, to some extent, of geological knowledge. The main idea is that instead of interpreting a deterministic salt boundary geometry, it aims at defining a buffer zone encompassing the boundary which size depends on the ambiguity of the interpretation.

Section 1.2 introduces some preliminary notions and vocabulary about seismic interpretation which are used throughout this thesis. Sections 1.3 and 1.4 develop the aforementioned review. Section 1.5 provides further elements of discussion about the uncertainty assessment during automatic seismic interpretation and outlines the work

of Legentil [2019].

1.2 Fundamentals of seismic interpretation

1.2.1 Sources of information

Formalizing the interpretation process requires first to clearly identify the nature of seismic data and of the objects we are trying to interpret. Seismic data primarily consist of a series of recordings of the ground acceleration (or water pressure) at different locations during a fixed time window. These recordings (called *traces*) contain the travel times required by seismic waves for traveling from a set of controlled sources to a set of receivers when reflecting on the subsurface objects [e.g., Yilmaz, 2001]. The information contained in seismic data can be divided into four categories [Brown, 2011]: time information (which is mainly about subsurface structures), amplitude information (about stratigraphy and petrophysical properties), frequency information (likewise amplitude), and attenuation (still difficult to interpret). In addition to seismic data, an interpreter can also gain information from any prior knowledge and by assessing the data quality.

1.2.2 The notion of seismic image

Interpretation, in the largest sense of the term, occurs at each step of the seismic imaging workflow. When talking about seismic interpretation, we usually only refer, however, to the interpretation of seismic images. The term "image" refers to the seismic data after stacking, that is, after gathers of recorded traces have been summed according to some criterion (e.g., common midpoint or common depth point) [Yilmaz, 2001]. At this point of the processing, there remains one virtual vertical trace per position at the surface. By considering each trace sample as a pixel (whose gray level value is defined by the seismic amplitude), the set of contiguous seismic traces forms a 2D or 3D "image" of the subsurface reflection amplitude. Depending on the processing, the vertical axis of the image can be expressed either in time or in depth. As I mainly consider PSDM images when imaging salt, the images I study are usually expressed as a function of depth (the stacking is applied after the depth migration) [Yilmaz, 2001].

From a lexical point of view, it is common to distinguish image pixels from image voxels in computer sciences. The only difference is that a pixel is the base element of 2D images when a voxel is the base element of 3D images. As I will often talk about seismic images from a general point of view (i.e., independently from their dimension), I will use the term of image pixel in the general case, and reserve the term voxel when specifically talking of 3D seismic images. The notion of pixel neighborhood is also frequently used throughout the manuscript. The neighborhood of a pixel refers, in a general sense, to a collection of pixels surrounding it (and which often include it). It usually forms a volume (or surface in 2D) of connected pixels of arbitrary shape, without holes, around the pixel.

1.2.3 Feature emphasis and extraction

In the specific case of salt interpretation, automatic segmentation methods applied directly on seismic images can usually provide a relatively reliable solution where the top

salt boundary is well defined, but often struggle to provide adequate results elsewhere [e.g., Lomask et al., 2007]. Most authors therefore perform the interpretation in two complementary (but not mandatory) steps [e.g., Wang et al., 2018]. The first step consists in highlighting the salt boundary or in segregating salt from surrounding sediments in the image. This emphasis is performed by computing seismic attributes (section 1.3). The second step consists in extracting them (section 1.4). It can be done manually by an interpreter that picks the feature boundaries, by using automatic methods, or by a combination of both. The output of the extraction usually consists of three dimensional surfaces delimiting the objects or of a labeling of the pixels indicating to which feature they belong to. The two following sections review the different ways which have been proposed in the literature to respectively approach the problems of highlighting and extracting salt bodies from seismic images.

1.3 Highlighting salt in seismic images

1.3.1 Texture-based description of seismic images

Seismic reflections occur on heterogeneities, revealing the external and internal architecture of subsurface structures. The diversity of processes at the origin of rocks and their deformations results in a variety of signatures on seismic images, called image *textures* [e.g., Schlaf et al., 2005]. An image texture is a general term that refers to any specific pattern that helps isolating a region in an image.

Salt texture Salt has a typical texture on seismic images. As compared to the surrounding layered sediments that appear as packages of planar reflections, salt often appears as relatively smooth, low amplitude bodies that do not present any specific internal organization. This is explained by the massive and crystalline nature of salt bodies [e.g., Jackson and Hudec, 2017]. In addition, salt top boundaries usually correspond to large amplitude reflections that are well captured in seismic images, due to the relatively large impedance contrast between salt and its overburden. On the contrary, salt base and steep diapir flanks are often poorly imaged and may not appear [e.g., Jackson and Hudec, 2017]. This is due to multiple factors, and especially low illumination. Figure 1.1 provides some examples of salt and sediment textures in a real seismic data set.

Seismic attributes The description of image textures (which is the core of many automatic interpretation methods) consists in describing the tonal distribution in an image through a set of metrics, both in terms of intensity variation and spatial distribution [e.g., Gao, 2003]. In seismic interpretation, these metrics are grouped under the notion of seismic *attribute*. The term attribute refers to any measure based on seismic data [Sheriff, 2002]. The overall aim of seismic attributes is to emphasize a specific characteristic of the seismic signal. They have been extremely popular for a long time, and even early proposed attributes, such as the complex seismic trace [Taner et al., 1979], are still widely used today. Regular reviews establish states of the art of existing seismic attributes, their characteristics and classifications [e.g., Brown, 1996,

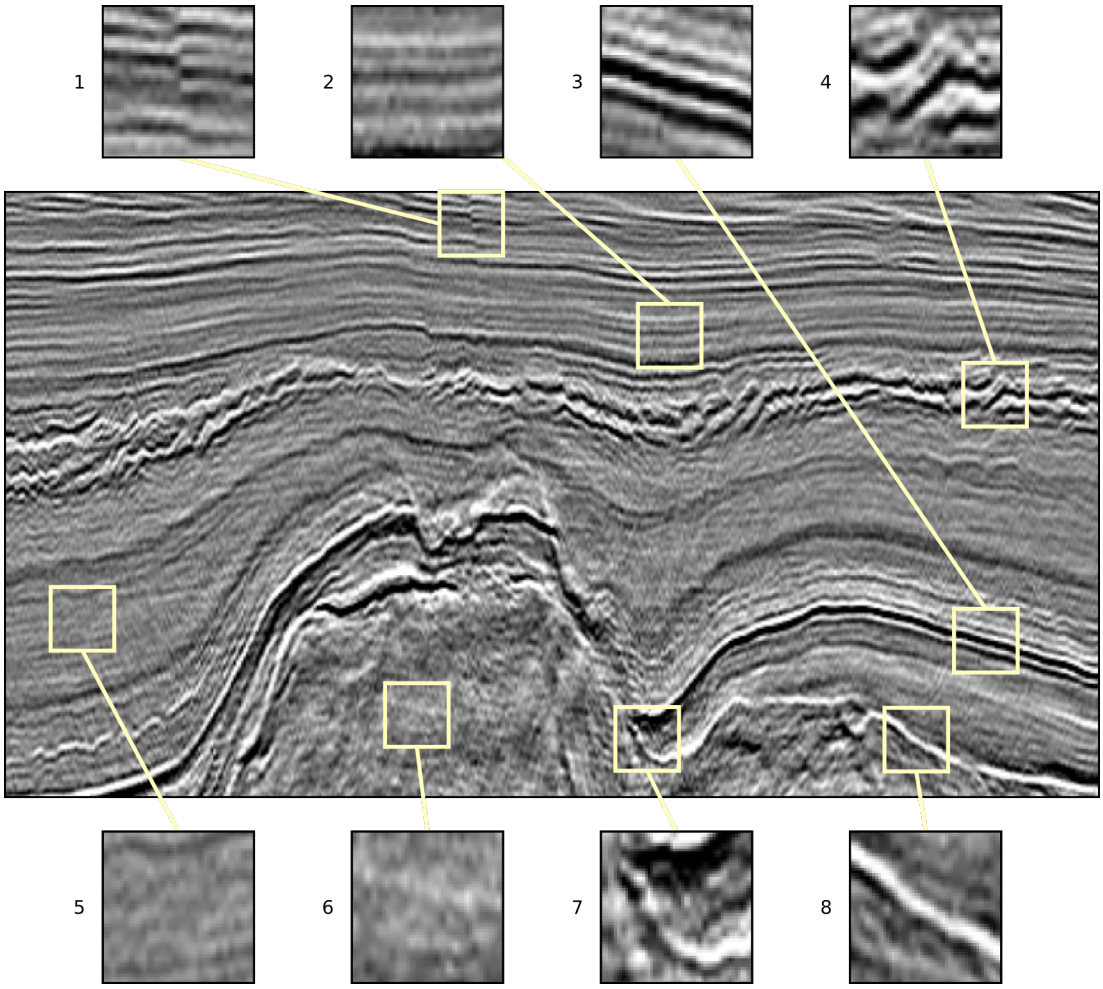

Figure 1.1 – Examples of seismic image textures. The seismic image is a subsection of the F3 block seismic data set, offshore Netherlands [dGB Earth Sciences B. V., 1987]. The different image samples illustrate: (1) a fault; (2) medium amplitude sediment reflections; (3) strong amplitude sediment reflections; (4) strong amplitude chaotic sediment patterns; (5) smooth low amplitude sediment reflections; (6) smooth random internal salt reflections; (7) a termination of a strong sediment reflection against the salt boundary; and (8) a strong amplitude reflection corresponding to the salt boundary.

Chopra and Marfurt, 2005], unnecessary and redundant attributes [e.g., Barnes, 2007] and propose guidances for further works [e.g., Chopra and Marfurt, 2008].

It is interesting to note that the notion of attribute is so large that it includes seismic amplitude (i.e., seismic images), and even the two-way travel time of waves [Herron, 2011]. Other classically used attributes include the coherency [Bahorich and Farmer, 1995], dip and azimuth [Dalley et al., 1989]. Among the variety of attributes that have been used to interpret salt in the literature, some are general metrics imported from the image processing field, some have initially been developed for other seismic interpretation purposes, and some have been specifically developed for interpreting salt. In the remaining of this section, I review the different approaches and attributes which have been proposed according to the image texture characteristics they focus on.

1.3.2 Statistical characterization using generic image descriptors

Image texture analysis takes place in a wide variety of applications. The topic has therefore been investigated for long, and numerous tools and metrics have been proposed independently from the seismic interpretation domain to describe image textures in a generic way (that is, without any prior knowledge of the features contained in the image). These image descriptors usually focus on a statistical description of the pixel relations in the image.

Gray level co-occurrence matrix The Gray Level Co-occurrence Matrix [GLCM, Haralick et al., 1973] is the most widely used generic descriptor in seismic interpretation [e.g., Gao, 2003, Eichkitz et al., 2013, Berthelot et al., 2013]. In its general formulation, it is a two-point statistics method describing for each pixel the probability of finding, in its neighborhood, pixel value pairs spaced out by a given distance in a specific direction. It is worth mentioning that, contrarily to the claim of Haralick et al. [1973], the GLCM does not fully represent the textural information contained in the image: as compared to multi-point statistics, it does not capture the structures and patterns beyond two-point correlations [e.g., Guardiano and Srivastava, 1993].

From the GLCM, various quantities (which are as many potential attributes) can be derived [Haralick et al., 1973]. These quantities highlight either the statistical distribution of the gray levels, their contrast, or their orderliness [Eichkitz et al., 2013]. More details about the computation of the GLCM and its attributes are provided in appendix of this chapter (section 1.6).

Other generic descriptors The GLCM has been for long the only generic descriptor to be used in seismic interpretation. Long et al. [2018] proposed a benchmark of several other local texture descriptors which have been introduced more recently in the image processing community. The benchmark includes, in addition to the GLCM, the local binary patterns (which has been widely used since their introduction) [Ojala et al., 2002], several of their extensions, and the local radius index [Zhai et al., 2013]. The results of Long et al. [2018] show that the use of such generic descriptors usually brings interesting information (and have a relatively similar accuracy) to segregate salt from surrounding sediments.

An interesting characteristic of these descriptors is that, as they are designed to provide a generic statistical description, they provide information both about salt and about the other image features (sediments, etc.). Therefore, they can be used in global labeling approaches [see e.g., the application in Long et al., 2018]. Furthermore, research about generic descriptors is very active in the image processing domain, and regular improvements of the different methods are proposed to make them more robust and invariant to image orientations, method parameters, etc. [e.g., Löfstedt et al., 2019]. This should provide interesting improvement avenues for seismic interpretation methods in the future.

1.3.3 Salt as a discontinuity

Another category of approaches, which also builds upon image processing advances, consists in considering salt interpretation (and especially top salt interpretation) as an edge-detection problem. This is a common topic in image processing, and various solutions have been adapted. As an example, Jing et al. [2007] and Aqrawi et al. [2011] propose to use Sobel edge detectors (respectively in 2D and 3D). The Sobel operator is a classic gradient operator, that is used to capture the high derivative magnitude edges in an image. As it is relatively influenced by the image orientations, Amin and Deriche [2015] propose to consider more scanning directions (i.e., to compute the derivatives also along diagonals) to increase the accuracy of this edge detector. Similarly, Di and Gao [2014] propose to use a Canny edge detector, which couples the gradient computation with a smoothing operation in order to reduce the sensitivity of the gradient operator to noise. Approaches based on frequency filters have also been investigated. For example, Berthelot et al. [2013] use Gabor filters, which are designed to extract features with specific size and orientations.

From a general point of view, approaches based on edge-detection are quickly limited by the quality of seismic data. Indeed, the top of salt is often clearly visible on seismic images [e.g., Mosher et al., 2007], but the base of salt and steep diapir flanks may not be imaged [e.g., Dellinger et al., 2017], and thus not be possible to detect.

1.3.4 Structure anisotropy and salt organization

One of the specificities of salt bodies is that they are often "unstructured" as compared to the surrounding sediments. Particularly, sediments often appear as stacked planar features on seismic images. Attributes distinguishing between salt and sediment organizations have therefore been investigated with particular attention. A first indicator, which was already in use in seismic interpretation, is the reflection dip [e.g., Halpert and Clapp, 2008]. It often efficiently highlights both the salt boundary (which exhibits a different dip than the surrounding non-conformal sediment layers) and the internal salt texture (unorganized and thus having random and quickly varying dips) [e.g., Lomask et al., 2007].

To go further, it is also possible to use a more complete representation of the local structure orientations to characterize the image anisotropy around a pixel. Two relatively similar mathematical operators have been used: the gradient covariance matrix and the structure tensor. Both are defined in the neighborhood of each image pixel.

The gradient covariance matrix is defined as the covariance matrix of the gradient components [e.g., Johnson and Wichern, 2007]. The structure tensor is defined as the smoothed outer product of the gradient [e.g., Van Vliet and Verbeek, 1995]. Their eigendecomposition provides a description of the local anisotropy both in terms of principal directions (through eigenvectors) and magnitude along each direction (through eigenvalues) [e.g., Fehmers and Höcker, 2003]. Based on the eigenvalues, several attributes have been proposed to describe seismic image textures. For example, Randen et al. [2000] and Berthelot et al. [2011] use the chaos attribute, a global indicator discriminating isotropic, linear and planar structures. Hale [2009] proposes individual measurements of each of these characteristics. One of these attributes, the planarity, is interesting for segregating the planar sediment patterns from the "on average" isotropic salt pattern. More details about the planarity and its computation are provided in appendix of this chapter (section 1.6).

Some approaches tend to couple discontinuity detection and texture description, that is to say, to highlight variations in the image texture. For this, Shafiq et al. [2017] propose an attribute they call the "gradient of textures". It is based on a dissimilarity operator, that compares the texture of the neighborhoods on each side of a pixel. By scanning along each image axis, they derive a "magnitude" of local texture variation for each pixel, that is expected to be maximum at the salt boundary. Wu [2016] proposes to use the planarity variations to detect the boundary between salt and sediments. He introduces a "salt likelihood" attribute, defined as variation of planarity orthogonally to the image gradient. As the gradient of texture, it is expected to be maximum at the salt boundary.

An interesting advantage of the methods based on the gradient covariance matrix and the structure tensor is that they provide both a quantitative measure of the local image anisotropy and a description of the principal structure orientations in a pixel neighborhood. This information can be related to relatively simple geological observations. For example, large planarity values are likely to correspond to sediments (that is, stacked planar reflections), whereas low planarity values may indicate salt, linear structure such as channels, chaotic sediment deposits, etc.

1.3.5 Assessment on seismic attributes

Attribute selection In this section, I reviewed the various approaches which have been proposed to highlight salt bodies and boundaries in seismic images. An important question that is raised when designing an interpretation method concerns the selection of the attribute(s) to use. A way to visualize and organize the spectrum of proposed seismic attributes is to distribute them between two poles [Barnes, 2007, Herron, 2011]. The first one is defined by the idea that a seismic attribute should only be used if it concretely helps the interpretation. The second one is defined by the idea that a seismic attribute should only be used if it has a clear physical meaning. According to Herron [2011], there is no "good solution" for the choice of the attributes to use. This choice depends on the interpreter's preferences and the specific case study. I think that this statement is, however, debatable in the frame of automatic interpretation. As stated in the introduction, one of the main challenges that the automation of interpretation faces consists in formalizing the geological knowledge used by an interpreter. Whereas

an interpreter may test a set of attributes to decide which ones are best suited to help interpret a given seismic image, I consider that, when developing interpretation workflows that aim at being applied in a systematic way on any seismic image, the emphasis should be laid on the use of attributes that have a clear meaning relating to some physical or geological property of the subsurface structures. In addition, it is well admitted that well understanding 3D effects is fundamental when interpreting seismic data [Brown, 2011]. Therefore, attributes should be natively computed in 3D, rather than along specific directions. This permits to limit the impact of subsurface structure orientation as compared to data set axes. With these considerations in mind, I think that attributes such as those derived from the GLCM, the planarity, the salt likelihood and the gradient of textures are good candidates for salt interpretation. The appendix of this chapter illustrates the computation of these attributes.

Attribute computation and parameter selection In this section, I only discussed the "philosophy" underlying the different proposed attributes, and not their practical application. This is not the topic of this review, but it is important to mention that most attributes require the definition of a set of parameters to be computed in practice. The choice of these parameters largely influences the resulting attribute values (see e.g., Löfstedt et al. [2019] about the impact of the number of gray-levels used when computing the GLCM and Wu [2016] for the impact of the smoothing when computing the planarity). Moreover, it is often a non-trivial step which is not much discussed in the literature. This is one of the reasons which makes the comparison of different attribute efficiency difficult, even when using a same interpretation workflow. The understanding of attribute parameter impact and their ease of selection might, therefore, also serve as a criterion for attribute selection.

1.4 Extracting salt from seismic images

Once the salt (or its boundaries) has been highlighted, seismic interpretation can be seen as a general image segmentation problem. This problem has been thoroughly studied in computer graphics, and numerous methods have been adapted to salt interpretation. Two types of approaches can be distinguished: the surface-based methods, which aim at defining the position of the salt boundary, and the volume-based methods, which aim at assigning a label (such as "salt" or "sediments") to each image pixel.

1.4.1 Surface-based extraction

The approaches based on edge-detection attributes often rely on the application of a threshold, to preserve only the edges. Various strategies exist to perform this step, such as the application of morphological operators (e.g., successive dilatations and erosions) until connecting the different extracted segments [e.g., Amin and Deriche, 2015].

Most authors prefer, however, using "global" extraction methods, that is, methods that extract at once the salt boundary. This can be performed by using graph partitioning methods. For example, Lomask et al. [2007] and Halpert and Clapp [2008] use the normalized cuts image segmentation algorithm [NCIS, Shi and Malik, 2000], Halpert et al. [2014] use the pairwise region comparison segmentation algorithm [PRC,

Felzenszwalb and Huttenlocher, 2004] and Berthelot et al. [2011, 2013] use the algorithm proposed by Winkler and Liebscher [2002] to extract an optimal path using dynamic programming. The other global approaches generally consist in solving some partial differential equation (PDE) system defining the salt boundaries. Among the various approaches which have been proposed, Ledez [2003], Kadlec et al. [2009], Carlson [2010], Zhang and Halpert [2012] and Haukås et al. [2013, 2017] use methods inspired from level sets [Osher and Sethian, 1988] and active-contour models [Kass et al., 1988]. Wu [2016] adapted a surface reconstruction method and solves a screened Poisson equation [Kazhdan and Hoppe, 2013] to define an implicit salt indicator function whose zero level set is the boundary. Wu et al. [2018] track the salt boundary as an optimal path picking problem [Fomel, 2009] by solving the eikonal equation.

The advantage of "global" extraction methods is that they ensure that the final salt boundary is continuous across the entire image and relatively robust to outlier samples. Methods based on the resolution of PDEs produce relatively smooth boundaries, but they require to build an adequate scalar field, task which may not be trivial. Similarly, graph cut approaches ensure that the cuts cross through the entire domain, but require to define a single indicator function describing the probability for any pair of pixels to belong to two different geobodies. In my opinion, the main drawback of these methods is the necessity to group the entire segmentation information into a single scalar field.

1.4.2 Volume-based classification

The alternative to surface extraction consists in assigning a label to each pixel, that is, in associating each pixel to a predefined category (e.g., salt, sediments or fault). This is a general problem of classification, and numerous methods exist to perform this task. The simplest kind of approach consists in applying a clustering method, such as the k-means clustering [MacQueen, 1967], that aims at finding a somehow optimal set of classes [e.g., Di et al., 2018a, Legentil, 2019]. Such approaches struggle, however, to perform an accurate classification due to the highly ambiguous nature of the seismic signal. Therefore, most authors use methods derived from the machine learning domain, mainly supervised classification algorithms, but not necessarily (e.g., Ramirez et al. [2016] use a sparse dictionary based method). Lots of the models proposed in the machine learning literature have already been tested for salt interpretation. Berthelot et al. [2011, 2013] use a Bayesian classification. Alfarraj et al. [2018], Long et al. [2018] use a support vector machine (SVM) model. Guillen et al. [2015] use random forest (a collection of decision trees). With the recent promises of deep learning, more and more authors use artificial neural networks (ANN), and especially (de)convolutional ones [e.g., Waldeland et al., 2018, Di et al., 2018b, Shi et al., 2019].

Unlike PDE-based and graph partitioning methods, classification methods offer a simple way to integrate multiple sources of information into the interpretation (that is, multiple attributes). They do not ensure, however, that the interpreted bodies are continuous across space (each pixel being labeled independently from its neighbors). Nevertheless, various solutions exist to relieve this limitation and integrate some notion about spatial continuity. A non-negligible drawback of the above classification approaches is that they require to be trained to recognize the different categories to interpret, that is, they must be provided with a large quantity of already interpreted

seismic image samples similar to those that can be found in the image to interpret. Some databases of already interpreted image samples exist, however, and can be used to reduce the necessity on manual labeling [e.g., the LANDMASS-1 data set, CeGP, 2015, for 2D images].

1.4.3 Assessment on extraction methods

As it was stated in the introduction, it is extremely difficult to compare the relative efficiency of different interpretation methods. Therefore, I only discuss here how these different methods may allow for the integration of geological knowledge in the interpretation.

1.4.3.1 Use of multi-attribute classification

As stated during the review, both surface- and volume-based extraction methods have their own advantages and drawbacks. Even though some authors published convincing results using a single attribute [e.g., Wu, 2016], most authors agree on the fact that using multiple attributes during the interpretation helps improving the accuracy of the solution [e.g., Berthelot et al., 2011, 2013, Di et al., 2018a, Shi et al., 2019]. In particular, using multiple attributes permits to explicitly input different sources of knowledge about the structures to interpret rather than concatenating them into a single measure.

Classification approaches offer an ideal framework to integrate multiple attributes at once. Depending on the underlying model (i.e., SVM, ANN, etc.), the complexity of the decision rules may limit, however, their discussion in terms of geological meaning. Another advantage of these approaches is that they often compute, prior to the decision of the label to assign to the pixel, the probability of this pixel to belong to any of the possible labels. When assessing uncertainties, these probabilities are even more important than the final labeling, as they provide a confidence estimation about the final pixel label.

In my opinion, classification approaches should, therefore, be preferred to global segmentation methods. There remains, however, the question of the spatial continuity of the interpretation to discuss, which is the topic on the next section.

1.4.3.2 Spatial continuity in classification approaches

The notion of spatial continuity is primordial in geology. For example, in the case salt interpretation, we expect to interpret large scale salt bodies (e.g., diapirs and canopies) rather than isolated salt lenses scattered in the subsurface. It is necessary to take this information into account during the interpretation, and several ways exist to do so.

Through the use of seismic attributes The most common way for introducing spatial continuity within the automatic interpretation process consists in using seismic attributes. Indeed, most of the attributes used for interpreting seismic images are derived from the seismic amplitude and are computed within a given neighborhood around a pixel (e.g., GLCM attributes, complex trace attributes, planarity, etc.). As compared to the amplitude, the value of such attributes thus contains information about

the pixel neighborhood, and the values of a given attribute at two close pixels sharing part of their neighborhood is, therefore, spatially correlated.

A similar solution consists in directly using the neighborhood of a pixel, that is to extract an image patch around each pixel and to classify the pixel according to this patch [e.g., Di et al., 2018b, Long et al., 2018, Shi et al., 2019]. Given that the definition of a seismic attribute is broad, we can consider that the pixel neighborhood defines a vectorial attribute, and that the use of image patches is thus included into the previous category. These solutions use, however, very large image patches (between 99 and 256 cells per image axis for the cited examples) and therefore require a large computational power, which may represent a limitation.

Through the use of multiscale approaches A solution to explicitly integrate the notion of spatial continuity into seismic interpretation consists in using a multiscale interpretation approach. This can be done in the space domain (using the scale-space theory), or in the frequency domain (using the wavelet theory). Methods based on the analysis of the frequency spectrum are relatively common in seismic interpretation, but have rarely been applied to salt. The few examples include the use of Gabor filter [e.g., Berthelot et al., 2013].

From a geological point of view, I think that space domain methods can provide an interesting way to guide automatic interpretation methods. Indeed, seismic images are prone to noise and the accuracy of automatic interpretation methods is known to be limited. At coarse scales, salt bodies are large enough to be preserved, whereas seismic noise is largely reduced. The most common scale-space representation is the Gaussian pyramid [Adelson et al., 1984]. As far as I know, it is the only representation which has been tested in the literature. Alfarraj et al. [2018] propose a 2D application highlighting moderate improvements of the interpretation as compared to using directly the seismic image, and Alfarraj et al. [2017] present an application to reduce the noise sensitivity of instantaneous attributes (that is, derived from the complex seismic trace).

It is worth mentioning that the use of CNN actually introduces a form of multiscale analysis, as all the convolutional layers do not work at the same level of detail [e.g., Wang et al., 2018]. The relations between the different scale interpretations may, however, be harder to characterize than in an approach like the Gaussian pyramid in which the fusion rule must be explicitly stated.

1.5 Toward the incorporation of uncertainty quantification in automatic seismic interpretation

1.5.1 Assessment about uncertainty characterization in automatic interpretation methods

Current automatic interpretation methods aim at determining the "best possible" salt boundary geometry given the limited quality of seismic data. Therefore, they consider the problem of salt interpretation from a deterministic point of view. Furthermore, whereas some methods provide quantitative indicators about the precision of their interpretations, the question of the validation of an interpretation in a real case (i.e.,

when the exact boundary geometry is not known) has not been broached. The proposed strategy rather consists in using automatic methods to quickly interpret the well defined image parts and to leave the more complex parts and the validation to human interpretation.

In my opinion, this represents the major limitation to the applicability of these approaches: they do not allow for the characterization of the uncertainties underlying seismic interpretation. Nevertheless, as discussed in the review, various elements of these approaches offer interesting tools to integrate the notion of uncertainty characterization into automatic interpretation. In particular, seismic attributes can permit to translate geological knowledge into quantitative indicators, multiscale approaches permit to guide fine scale interpretation using coarse scale observations, and classification approaches, which are often based on the computation of some facies probabilities, could be used to quantify the reliability of the interpretations (e.g., in an automatic validation scheme).

1.5.2 Integration of uncertainty quantification in automatic interpretation workflows

As stated by Haukås et al. [2017], it is unlikely that the imaging conditions provide a perfect seismic image, and a solution to better take this imperfection into account can consist in segmenting the image in three categories: "salt", "sediments", and "uncertain". From another point of view, stochastic methods are commonly used in the geomodeling community to sample structural uncertainties [Wellmann and Caumon, 2018]. They require the definition of the uncertainty space to sample. In the case of complex shapes such as salt bodies, a solution for defining the maximum spatial extent of this space consists in representing it by a buffer zone encompassing all the possible positions of the salt boundary [e.g., Bistacchi et al., 2008, Li et al., 2015].

A solution for integrating the possibility of quantifying structural uncertainties in automatic seismic interpretation workflows can, therefore, consists of two steps: (1) using an automatic interpretation method to segment the image into *Sediments* and *Salt* where the image quality is sufficient, and let the remaining parts classified as *Uncertain* (especially close to the limit between sediments and salt), similarly to Haukås et al. [2017], and (2) using the volume defined by this *Uncertain* region to define a buffer zone in which a stochastic structural modeling method can sample variable salt geometries [e.g., Li et al., 2015].

A non-negligible difficulty may reside, however, in the automatic definition of a suitable buffer zone (which is referred to as *uncertainty envelope* in the following chapters, cf. section 2.2.1). Nevertheless, given the progresses of automatic interpretation methods, I consider that this should not present a major obstacle. Although this topic would require to be further discussed (cf. section 2.4.2 for a discussion specific to this thesis), a first order solution may consist in deterministically extracting the salt boundary, and later define the uncertainty envelope using some distance function (e.g., a fixed distance to the reference boundary, or scaled by the ratio of the classifier probabilities). Note that such approach would, however, not be relevant in highly ambiguous seismic image parts.

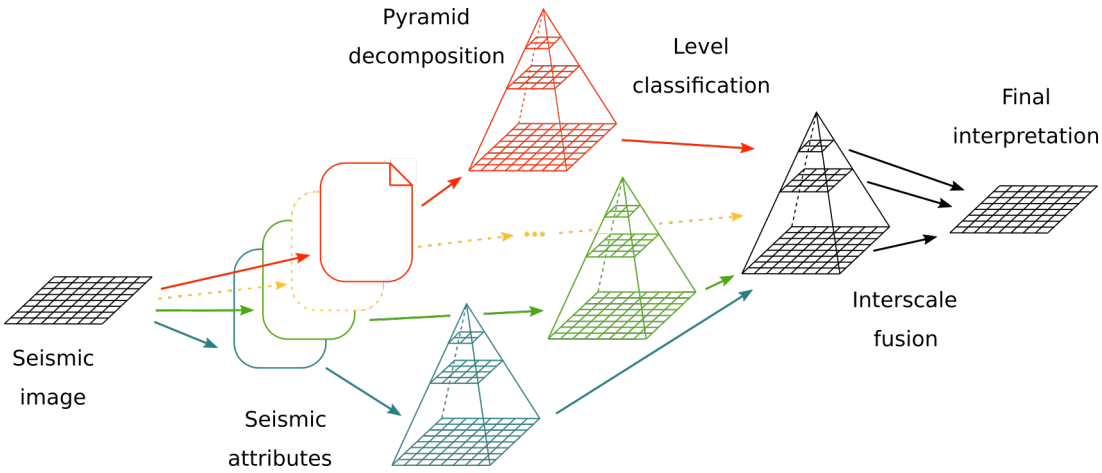

Figure 1.2 – Multiscale and multi-attribute automatic interpretation workflow proposed by Legentil [2019].

1.5.3 An example of automatic interpretation workflow allowing for uncertainty quantification

In order to test the different elements discussed above, I supervised a Master research project on automatic seismic interpretation methods. The project was realized by Capucine Legentil. Her master thesis can be found in appendix A [Legentil, 2019]. It resulted in the development of an interpretation workflow combining multi-attribute and multiscale approaches, which was applied to the characterization of structural interpretation uncertainties. Here, I briefly review the workflow, and present some updated results. The reader may refer to appendix A for further details.

1.5.3.1 Workflow overview

The workflow consists of four steps (figure 1.2): (1) the computation of a set of seismic attributes, (2) their decomposition across several scales, (3) the interpretation of each scale independently from the others, and (4) the fusion of the different scale interpretations to obtain a final interpretation.

Attribute selection Ideally, the selected attributes must emphasize either salt, its boundaries or sediments (cf. section 1.3.5). Depending on the tests, various GLCM attributes were used, together with the planarity, the dip variance and the semblance [a generalization of the coherency, Marfurt et al., 1998]. Each attribute is computed on the initial seismic image.

Pyramid decomposition The attributes are decomposed into a Gaussian pyramid representation [Adelson et al., 1984]. Depending on the tests, Legentil [2019] used four or five levels. The first level (or pyramid base) corresponds to the scale of the initial seismic image. Each of the following levels is obtained by smoothing the lower pyramid level (using a Gaussian smoothing filter) and downsampling it by a factor of two. At this step, we therefore have a collection of Gaussian pyramids, one for each seismic attribute. Note that we do not downsample the amplitude to compute the attributes

later. Indeed, the amplitude being an oscillating signal, applying a low-pass filter would tend to cancel it.

Level classification For each level, all the attributes are given to a K-means clustering algorithm [MacQueen, 1967]. The result of the classifier is a deterministic labeling. In addition to this labeling, we use the K-means clusters to define the probability for a pixel to belong to each of the different classes (the probability is proportional to the inverse of the distance to the clusters, cf. equation 4.11).

Interscale fusion The last step consists in merging the classifications obtained at the different pyramid levels. The idea is that the interpretation at higher levels should guide the interpretation of lower levels, to introduce the notion of spatial continuity. Legentil [2019] used the approach proposed by Kim et al. [2009]. The decision rule for assigning a label to a pixel is defined by the combination of three probabilities: the probability provided by the K-Means clustering algorithm (equation 4.19), a textural continuity prior within the neighborhood of the pixel (equation 4.17), and an interscale dependency with the classification at the upper level (equation 4.15). In practice, these three probabilities are computed independently for each label, and the label assigned to the pixel is the one maximizing the product of the three probabilities (equation 4.20).

1.5.3.2 Application to the characterization of structural uncertainties

Some early results of the proposed workflow are presented in Legentil [2019]. However, some elements in the implementation used to generate these results were incomplete at that time. Here, I present an updated application using the up-to-date implementation of the workflow.

Description The application is similar to the one presented in Legentil [2019]: the proposed workflow is used to segment an input seismic image into three categories (*Sediments*, *Salt* and *Uncertain*). The seismic image is a subset of the F3 block seismic data set, offshore Netherlands [dGB Earth Sciences B. V., 1987], which is restricted to inlines 100 to 699, crosslines 601 to 1250, and timelines 201 to 462. The total grid geometry is thus 600 x 650 x 262 cells. I selected four attributes: the GLCM contrast (equation 1.2), the GLCM energy (equation 1.3), the GLCM standard deviation (equation 1.5), and the planarity (equation 1.6). The reader is referred to figures 1.5 and 1.6 for illustrations and details about the parameters used to compute these attributes. The pyramid decomposition, the K-means classifications and the pyramid fusion follow the steps described in Legentil [2019], except that the K-means clusters are randomly initialized (the same cluster initialization is used for all the pyramid levels).

Results Figure 1.3 illustrates the results obtained when using only the K-Means classifier (top left) and the proposed workflow with different parameter sets (top right and bottom). They are globally in accordance with those of Legentil [2019]. The use of the multiscale approach reduces the number of blobs which are present in the classified cube, and therefore improves the spatial continuity of the interpretation (figure 1.3, top right). This reduction is even more important as the size of the neighborhood used to

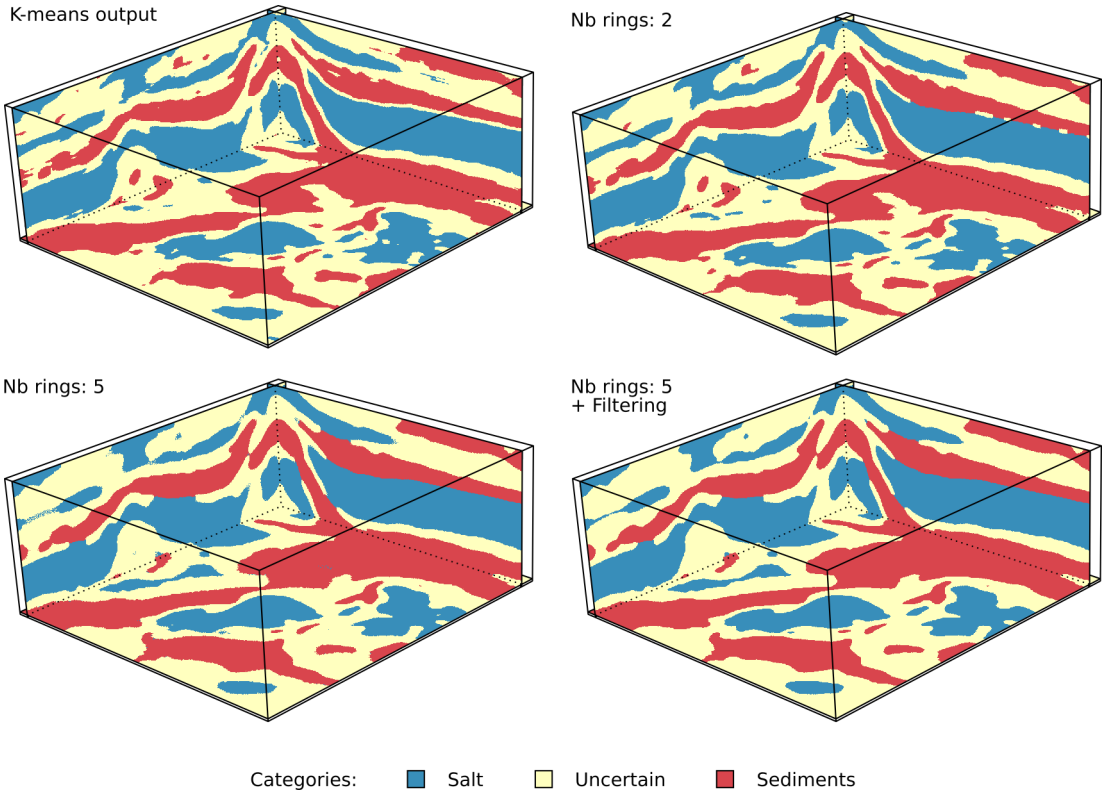

Figure 1.3 – Results of the proposed multiscale classification workflow on the F3 block seismic data set, offshore Netherlands [dGB Earth Sciences B. V., 1987]. Top left: result of the K-means classifier (without multiscale decomposition). Top right: result using a two neighbors ring when computing the textural prior probability (equation 4.17) and the interscale dependency (equation 4.15). Bottom left: result using a five neighbors ring. Bottom right: result using a five neighbors ring and a filtering as post-processing. See section 1.5.3.2 for full details.

compute the different pyramid fusion probabilities is large (figure 1.3, bottom left, cf. equations 4.15 and 4.17). An increasing neighborhood may, however, introduce some pixelated patterns in the interpretation (figure 1.3, bottom left). Their origin is unclear, and due to the lack of time, it was not possible to investigate further this effect. A simple filtering is, however, sufficient to cancel it. An example is presented in figure 1.3 (bottom right). The filter is defined similarly to a median filter. For each pixel, it scans all the pixels in its neighborhood (here, a window of two pixels in each direction) to determine a local distribution of the labels around the pixel, and assigns the mode of the distribution (i.e., the most represented label) to the pixel. The results (and the initial choice of the categories) also highlight the limitations of the K-means clustering algorithm to efficiently segregate salt from low amplitude sediment reflections and the salt boundary from the other high amplitude reflections within the sediments.

In summary Due to the lack of time, it was not possible to perform more tests during the master project and my PhD. Now that all the elements of the workflow have been implemented, it would be interesting to properly test the entire workflow. Future works should first focus on replacing the K-Means clustering by a more reliable classifier (sec-

tion 1.4.2). It was initially selected for its ease of implementation, but it does not allow for the integration of any prior knowledge (it is an unsupervised clustering algorithm, which does not integrate any learning phase). Furthermore, even though some indicators about the accuracy are provided in Legentil [2019] for information, the question of the validation has mainly been treated qualitatively (that is, by visual inspection) due to the absence of reference solution and remains to be thoroughly investigated.

1.6 Conclusion

Automatic seismic interpretation of salt bodies currently focuses on determining the "best possible" geometry of the salt boundaries. Recent developments in image processing and machine learning (and especially about convolutional neural networks) have led major improvements in the accuracy of automatic interpretation methods, and more and more authors investigate these solutions.

In my opinion, these methods suffer from several limitations. First, they require large data sets of image samples for training the algorithms. The absence of open access 3D data bases of already interpreted image samples restricts the applicability to real data sets. Then, even though they can already obtain a very good accuracy, it is highly unlikely that they reach one day the "perfection". The question of their validation in the case of real data (i.e., where the solution is unknown) is, however, never discussed in the literature. Finally, the interpretation of seismic images is known to be prone to large uncertainties where the subsurface was not properly imaged (e.g., due to low illumination or errors in the migration parameter fields). The use of deterministic approaches does not allow, however, for the quantification of these uncertainties, and there is no guarantee that they may provide a satisfying solution in poorly imaged regions.

In order to take advantage of automatic interpretation methods while taking into account interpretation uncertainties, I advocate that automatic interpretation methods should allow for the definition of an uncertainty envelope separating salt and sediments in the vicinity of the boundary. The size of this envelope should vary with the reliability of the interpretation. Various tools, such seismic attributes and multiscale approaches, can provide valuable ways to integrate prior geological knowledge into the interpretation to define this envelope. The structural uncertainties related to the interpretation of the ambiguous salt boundaries can then be quantified by sampling different salt geometries in this envelope. This is the topic of the next chapter, which introduces a method for stochastically modeling variable shapes of salt bodies from this uncertainty envelope.

Appendix 1.A: Examples of seismic attributes

This appendix provides further information about the computation of various attributes which have been implemented and used in this thesis. They are illustrated on a subset of the F3 block seismic data set, offshore Netherlands [figure 1.4, dGB Earth Sciences B. V., 1987, cf. section 1.5.3.2].

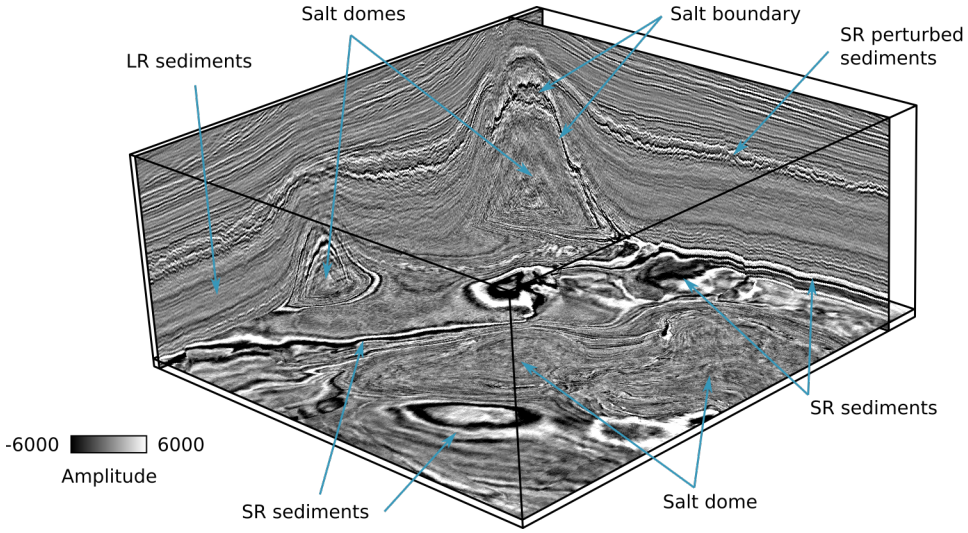

Figure 1.4 – Amplitude sections through a subset of the F3 block data set [dGB Earth Sciences B. V., 1987] used for illustrating the different seismic attributes, and rough manual interpretation. SR = Strong Reflection, LR = Low Reflection.

GLCM attributes In its generic formulation, the GLCM is computed in a given scanning direction and with a specific sampling step. In this thesis, I only consider, however, a single "global" GLCM per pixel. I scan all the pairs of contiguous pixels in the neighborhood of the pixel (i.e., I consider a distance of one pixel in any space direction). This neighborhood is usually defined as a cube of arbitrary size centered around the pixel. Such simplifications are common when using the GLCM in seismic interpretation [e.g., Eichkitz et al., 2013]. The GLCM is defined for discrete gray levels. When using it for a continuous property (such as the seismic amplitude), a preliminary step is required to requantize this continuous signal into a discrete number of gray levels.

Let M_{ij} be the (i, j) entry of the GLCM for a given pixel. As defined above, it describes the number of times that the association of two contiguous pixels p_1 and p_2 having respectively the values i and j was found in the neighborhood N_{global} of this pixel. It can be written as

$$M_{ij} = \sum_{p_1 \in N_{global}} \sum_{p2 \in N_{local}} \begin{cases} 1 & \text{if } p_1 = i \wedge p_2 = j, \\ 0 & \text{else,} \end{cases} \tag{1.1}$$

where N_{local} contains all the pixels contiguous to p_1, that is, sharing a face, an edge or corner with it. Using this definition, the GLCM is a symmetric matrix. In addition, it is often convenient to normalize the GLCM coefficients. Let m_{ij} be the normalized

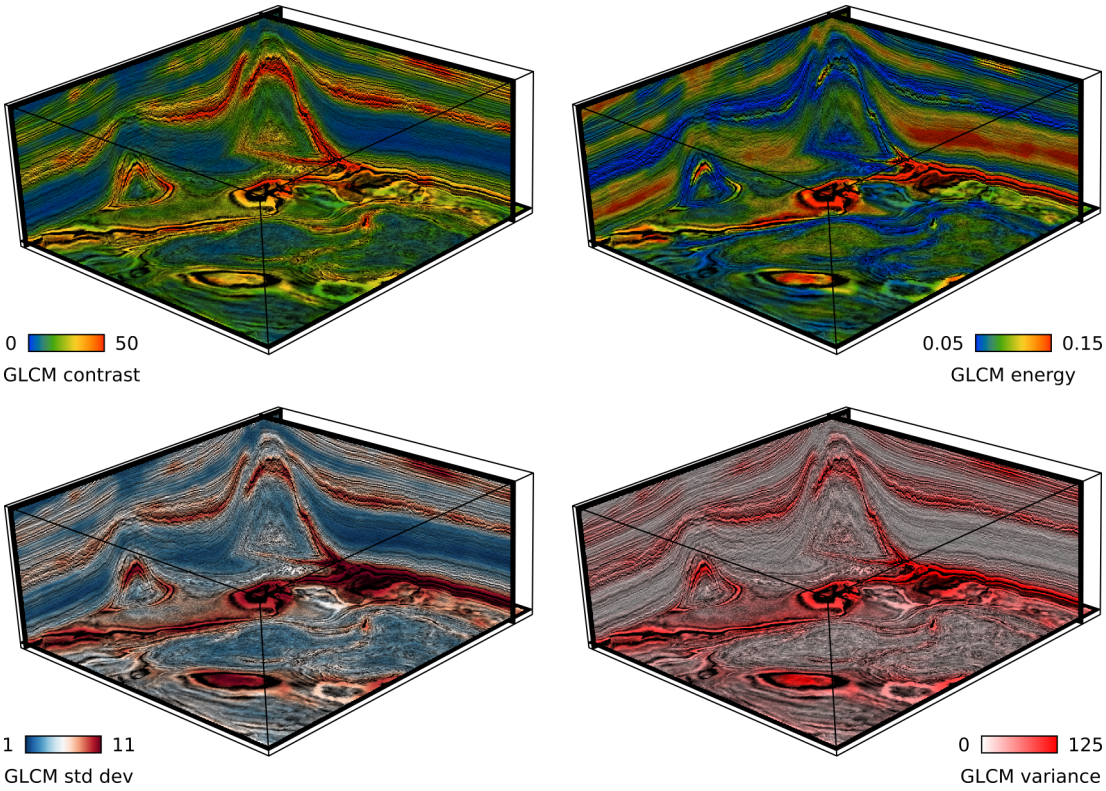

Figure 1.5 – GLCM attributes computed on the F3 block seismic data set and painted above the amplitude. Top left: contrast (equation 1.2), top right: energy (equation 1.3), bottom left: standard deviation (equation 1.5), bottom right: variance (equation 1.4). Input parameters: neighborhood size = 21x21x21 cells, number of gray levels = 32.

version of M_{ij}. It is defined as

$$m_{ij} = \frac{M_{ij}}{\sum_{k=0}^{n_g-1} \sum_{l=0}^{n_g-1} M_{kl}},$$

where n_g is the total number of gray levels. The normalized GLCM describes the joint distribution of the gray level associations in the neighborhood of a pixel. Numerous attributes can be derived from it. All these quantities are often, however, somehow redundant, and it is possible to organize them into three categories [e.g., Eichkitz et al., 2013], depending on the characteristics they emphasize. The contrast group highlights the strong gray level variations between neighboring pixels. The orderliness group highlights the uniformity of the gray level associations (the opposite being the presence of predominant gray level associations). The statistics group characterizes the gray level distribution in the neighborhood (independently of the pair associations).

Among the most commonly used GLCM attributes, the contrast is the only recurrent representative of its group [e.g., Eichkitz et al., 2013, Berthelot et al., 2013, Di et al., 2018a, Long et al., 2018], the angular second moment [e.g., Di et al., 2018a, Legentil, 2019], the energy [e.g., Eichkitz et al., 2013, Di et al., 2018a, Long et al., 2018] and the entropy [e.g., Eichkitz et al., 2013, Berthelot et al., 2013, Di et al., 2018a, Long et al., 2018] belong to the orderliness group, and various statistics about the gray level distributions such as the variance and the standard deviation [e.g., Berthelot et al.,

2013, Di et al., 2018a] are also commonly found. In this thesis, I used the contrast (equation 1.2), the energy (equation 1.3), the variance (equation 1.4) and the standard deviation (equation 1.5). They are illustrated in figure 1.5.

$$GLCM_{contrast} = \sum_{i=0}^{n_g-1} \sum_{j=0}^{n_g-1} (i-j)^2 m_{ij} \tag{1.2}$$

$$GLCM_{energy} = \left(\sum_{i=0}^{n_g-1} \sum_{j=0}^{n_g-1} m_{ij}^2 \right)^{\frac{1}{2}} \tag{1.3}$$

$$GLCM_{variance} = \sum_{i=0}^{n_g-1} (m_i - \mu_i)^2 \tag{1.4}$$

$$GLCM_{std\ dev} = (GLCM_{variance})^{\frac{1}{2}} \tag{1.5}$$

where $m_i = \sum_{j=0}^{n_g-1} m_{ij}$ is the proportion of pixels having a gray level i, and $\mu_i = \sum_{i=0}^{n_g-1} m_i$ is the average gray level.

Planarity The planarity [Hale, 2009] provides an information about the local anisotropy around a pixel. It is computed from the structure tensor (the smoothed outer product of the gradient by itself). Let $\mathbf{g}$ be the image gradient at a given pixel location (computed using e.g., centered finite differences). The structure tensor $\mathbf{T}$ is defined as $\mathbf{T} = \langle \mathbf{g}\mathbf{g}^T \rangle$, where $\langle \cdot \rangle$ is a smoothing operator (such as a Gaussian smoothing filter). The structure tensor is, by construction, a symmetric positive-semidefinite matrix. Its eigendecomposition provides three eigenvalues λ_u, λ_v and λ_w (ordered such that $\lambda_u \geq \lambda_v \geq \lambda_w$) and the associated eigenvectors $\mathbf{u}$, $\mathbf{v}$ and $\mathbf{w}$ which can be related to the local anisotropy of the image in the pixel neighborhood [Fehmers and Höcker, 2003]. The principal directions of anisotropy are given by the eigenvectors: $\mathbf{u}$ describes the direction maximizing the image gradients (i.e., it can be seen as a gradient estimate at the chosen neighborhood scale), $\mathbf{w}$ describes the direction of maximum continuity (i.e., along which the variations are minimal), and $\mathbf{v}$ is the third associated direction. The eigenvalues provide an information about the relative magnitude of the variations along each axis. The planarity p is defined as [Hale, 2009]

$$p = \frac{\lambda_u - \lambda_v}{\lambda_u}. \tag{1.6}$$

When the planarity is close to 1, it means that the image only varies along one direction, and the resulting patterns are thus planar (e.g., the stacked sediment packages). On the contrary, if the planarity is close to 0, it means that the image varies in at least two directions, denoting linear (e.g., channels) or isotropic (e.g., salt) structures. Figure figure 1.6 (left) illustrates an example of planarity attribute.

Reflection strength The reflection strength corresponds to the envelope of the complex seismic trace [Taner et al., 1979]. It is thus computed in 1D (i.e., along a trace and not in a 3D neighborhood). In my sense, it should not be considered as an attribute

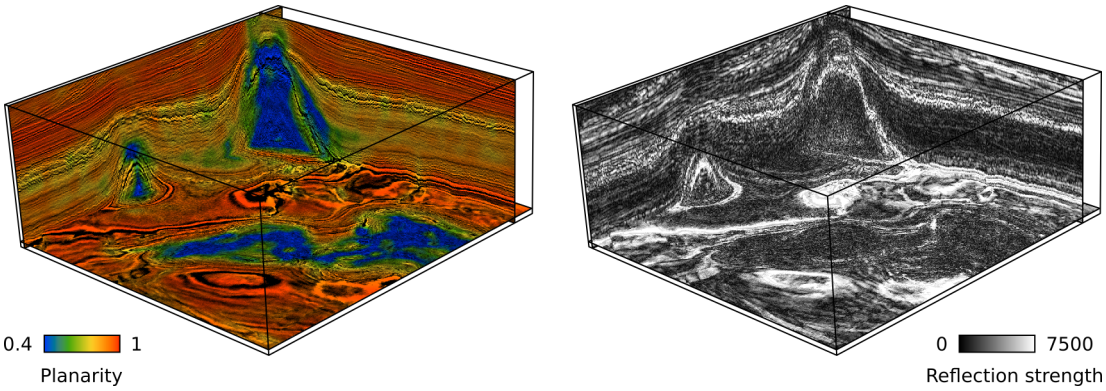

Figure 1.6 – Planarity (left) and reflection strength (right) computed on the F3 block seismic data set. The planarity is painted above the amplitude. Input parameters for the planarity: gradient operator = recursive Gaussian derivative filter (sigma = 1 cell), smoothing operator = recursive Gaussian smoothing filter (sigma = 8 cells), cf. Wu [2016]. Reflection strength was computed using SKUA-GOCAD implementation [Emerson E&P Software, 2019], using default parameters.

in the same sense as the GLCM ones or the planarity, but as an alternative to the seismic amplitude. It allows to get rid of the local phase variations of the seismic trace, while preserving its magnitude. It is illustrated in figure 1.6 (right). This attribute was already implemented in SKUA-GOCAD.

Chapter 2

Stochastic salt modeling - Part 1: Simulating variable shapes of salt bodies

Contents

Abstract This chapter introduces an implicit method to generate multiple possible interpretations of salt top surfaces. It takes as input a rough *a priori* estimate of the uncertainties, represented as a buffer zone encompassing the salt boundary. This buffer zone can be defined from a seismic image using, for example, the approach developed by Legentil [2019] (appendix A). The method is automatic and proposes to integrate punctual information (e.g., well data or manual seismic picks) and, to some extent, prior geological knowledge. The salt boundary is defined as the combination of a reference scalar field, computed from the buffer zone, and a spatially correlated random field that is used as a perturbation. This implicit formulation allows for the simulation of both varying salt geometries and topologies while ensuring the validity of the simulated boundaries.

This chapter was published in the journal *Interpretation* [Clausolles et al., 2019a]. It is reproduced as is in its post-print version.

Abstract (original) We have developed an implicit method to automatically generate several possible models of salt top surfaces with varying geometries and topologies. This method can be conditioned to available data such as well markers and seismic picks. As seismic imaging of salt is prone to velocity uncertainty and Fresnel zone effects, the input of the method is a seismic image that is segmented into three regions: salt, sediments and uncertain. he uncertain region contains the salt boundary and all the further computations focus within this zone. A monotonic scalar field, ranging from zero on the edge of the certain salt body to one on the maximal possible salt boundary, defines the cumulative probability for a point to be outside the salt body. A random scalar field, also bounded between zero and one, is then used as a threshold for the first scalar field. The salt boundary is implicitly defined by the zero isovalue of the difference between the two fields, and can be further extracted using marching cubes. The random field parameters have a geometrical and topological impact on the simulated salt volumes. They can be adapted to reproduce specific geological features, but their inference remains difficult. The application of the method to the reconstruction of diapir boundaries from a set of partly interpreted sections shows that it is well suited to honor numerous constraining data while proposing different possible structural scenarios in the uninterpreted parts.

2.1 Introduction

Recent advances in seismic acquisition methods and processing algorithms enable the imaging of complex geological settings [Jones and Davison, 2014]. The increasing size and quality of the new seismic data sets have motivated numerous works in seismic interpretation, and especially on the development of automatic interpretation methods.

In this global context, a specific attention has been paid to salt tectonics contexts. Salt structures are known, however, to often present challenges for seismic imaging. These challenges stem from three reasons: (1) specific physical properties of evaporites (high velocity and strong acoustic impedance contrasts with surrounding sediments [e.g., Fossen, 2016]), (2) internal heterogeneity of salt bodies [e.g., Jackson and Lewis, 2012], and (3) complex geometries and topologies that develop when salt and surrounding sediments undergo deformation [e.g., Hudec and Jackson, 2007]. This leads to a variety of difficulties for seismic imaging, such as poorly illuminated zones, complex travel paths or anisotropy representation [Jones and Davison, 2014], which raises many challenges and uncertainties during structural interpretation [Dellinger et al., 2017].

Salt interpretation is usually done in two complementary (but not mandatory) steps: the interpreter first tries to highlight the salt geobodies (or their boundaries) in the seismic data, and then extracts the boundaries by creating three dimensional surfaces. The most common way to highlight salt is to compute seismic attributes that are sensitive to the image texture. Some authors [e.g., Gao, 2003, Berthelot et al., 2013, Di et al., 2018a] use pixel-based statistical descriptions such as the Gray-Level Co-occurrence Matrix [Haralick et al., 1973] or the Gradient of Texture [Shafiq et al., 2017]. Other authors focus on characterizing the local feature orientations. This characterization can be achieved by computing the image gradient using either the gradient covariance matrix [Berthelot et al., 2011] or the structure tensor [Wu, 2016], whose eigen decomposition provides a measure of the local image anisotropy. Similarly, the reflection dip provides information on the local strata orientation [e.g., Lomask et al., 2007, Halpert and Clapp, 2008]. It can be computed using numerous methods, such as plane-wave destruction filters [Claerbout, 1992] or the ones previously mentioned for the gradient computation. A third alternative to pixel-based statistical descriptions and local orientations characterization consists in characterizing the salt boundaries by solving an edge detection problem [e.g., Aqrawi et al., 2011, Amin and Deriche, 2015]. As one single attribute may not be sufficient to highlight the salt boundary in the whole seismic cube, many authors now propose to combine a set of attributes [e.g., Halpert and Clapp, 2008, Berthelot et al., 2013, Di et al., 2018a].

Once the choice of the input attribute(s) has been made, the interpretation of the salt boundary can be seen as a general image segmentation problem. Image segmentation consists in partitioning an input image into different subsets of pixels according to some similarity criterion. In other words, it aims at assigning a label to each image pixel, pixels sharing the same label sharing also some characteristics. This problem has been thoroughly studied in the fields of computer vision and image processing, and numerous methods have been adapted to extract salt boundaries. Lomask et al. [2007], Halpert and Clapp [2008] use normalized cuts image segmentation [Shi and Malik, 2000] which is a graph partitioning-based approach. Other authors use methods based on partial differential equations (PDEs) to fit a surface to the salt boundary. Haukås et al. [2013, 2017] use methods inspired from active-contour models [Kass et al., 1988] and level sets [Osher and Sethian, 1988], Wu [2016] solves a screened Poisson equation to compute an implicit salt indicator function and Wu et al. [2018] extract an optimal path by solving the eikonal equation. Finally, several authors have also proposed to use various machine learning algorithms [e.g., Berthelot et al., 2013, Di et al., 2018a, Waldeland et al., 2018,

Shi et al., 2019].

All these methods aim at automatically determining the "best" possible predicate for the salt boundary. But as noted by Long et al. [2018], the interpreter should keep in mind that such automatic labeling process can only lead to a first approximation of the salt boundary and not to the exact surface. Generating a single deterministic salt geometry can lead to biases in velocity modeling, hydrocarbon trap determination, and reservoir gross rock volume assessment. The topic of seismic interpretation uncertainties has been raised for a long time in classic stratigraphic contexts [e.g., Abrahamsen, 1993, Thore et al., 2002, Bond et al., 2007], however only a few papers broach this topic and propose solutions to handle it in the presence of salt. Rojo et al. [2016] discuss the impact of the attribute selection and tuning on seismic noise reduction along salt boundaries. Most authors also propose to integrate manually picked information to guide the interpretation, either directly [e.g., Wu, 2016] or during the training phase for methods relying on classification algorithms [e.g., Berthelot et al., 2013, Di et al., 2018a, Waldeland et al., 2018, Shi et al., 2019]. Finally, Haukås et al. [2017] propose an interesting approach to avoid overinterpreting seismic images: they extract surface patches only in well-defined boundary zones, and then smoothly connect the patches in the poorly resolved image parts. Such approach remains, however, deterministic as one single interpretation is produced in the end.

To tackle the problem of interpretation bias reduction, we propose a general framework for characterizing the uncertainties underlying a seismic image. In practice, it allows for the exploration of different structural scenarios that can be admissible considering the imaging uncertainties. This framework is designed in two parts: the first one consists in identifying the image parts in which the interpretation is ambiguous, and the second one focuses on the generation of salt body boundaries with both variable geometries and topologies. The first part is, therefore, specific to seismic interpretation uncertainty characterization. It has already been investigated by several authors, and numerous works on automatic interpretation can be adapted to address this question (see above references). As it is not the main topic of this paper, we confine the presentation to the strategy we retained to model this uncertainty. The second part of the framework, which represents the main contribution of this paper, is more general and can be applied to the modeling of any type of geobodies (salt geobodies, ore geobodies, igneous intrusions, etc.). It addresses the problem of generating complex geobody boundaries while allowing for the integration of data (e.g., seismic picks and well markers) and prior geological knowledge (e.g., type and connectivity of the structures to interpret).

The paper is organized as follows. We first introduce the workflow on a 2D seismic section to provide the reader with a broad overview of the method and the different elements that take part in the modeling process. We then present various simulation results obtained from 3D synthetic data to illustrate the potential of the method, the impact of the different simulation parameters, and data conditioning. We finally discuss the topics of uncertainty characterization on seismic images, integration of prior geological knowledge and parameter inference from available data.

2.2 Method

The most common approach for sampling structural uncertainties in geomodeling consists of two steps [e.g., Abrahamsen, 1993, Lecour et al., 2001]. First, an explicit reference structural model is built. This reference model can be seen as the "best" possible model considering the limited amount of available data. Then, the different elements of the model (usually horizons and faults) are perturbed around their reference position to sample different possible geometries. This approach presents, however, some limitations. As noted by Caumon et al. [2007], perturbing an explicit reference model only allows for exploring geometrical uncertainties and not topological ones. Moreover, perturbing complex surfaces (such as salt geobody boundaries) introduces the risk of generating self-intersecting surfaces [Wellmann and Caumon, 2018].

To overcome these limitations, we adopt an implicit modeling strategy. Implicit methods are now well-known in geomodeling and have been widely used in a variety of applications. The seismic grid directly serves as modeling support. The geobody boundaries are represented as a level set of a scalar field [Osher and Sethian, 1988]. It prevents classic topological pitfalls, such as self-intersections and invalid contacts, encountered when perturbing explicit models [Wellmann and Caumon, 2018]. It also offers a frame to incorporate conceptual knowledge, and especially locally varying anisotropy, into the modeling [e.g., Martin and Boisvert, 2017]. This last point is addressed later in the paper.

2.2.1 Characterizing the uncertainties

The input of our workflow is a seismic image (figure 2.1.a). The first step consists in identifying the uncertainties in this image. The idea is to discriminate the image parts in which we consider the interpretation as sure from those which require more focus. In practice, we propose to classify each pixel of the image into one of the following three categories (figure 2.1.b): "sediments" (in red), "salt" (in blue), and "uncertain" (uncolored). This type of partitioning has also been used by Haukås et al. [2017] to avoid over-interpreting the image parts in which the seismic signal is too ambiguous. In our application, the pixels classified as "uncertain" form a volume (referred to as "uncertainty envelope") between the "sediments" and "salt" regions that contains the salt boundary.

In the synthetic examples we present after, the uncertainty envelope is manually defined as we do not have associated seismic images. More details about existing methods that can help to automatically generate the uncertainty envelope are provided in the discussion.

2.2.2 Generating salt boundary interpretations

The next step is to generate salt boundary interpretations in the uncertainty envelope. As stated previously, an interpretation is implicitly defined by a level-set of a scalar field. The generation of this scalar field is inspired by the Object-Distance Simulation (ODSIM) method [Henrion et al., 2010, Rongier et al., 2014]. An interpretation is defined by the combination of two scalar fields: a pseudo-distance field D (figure 2.1.c) and a spatially correlated random field φ (figure 2.1.d). The main difference with the

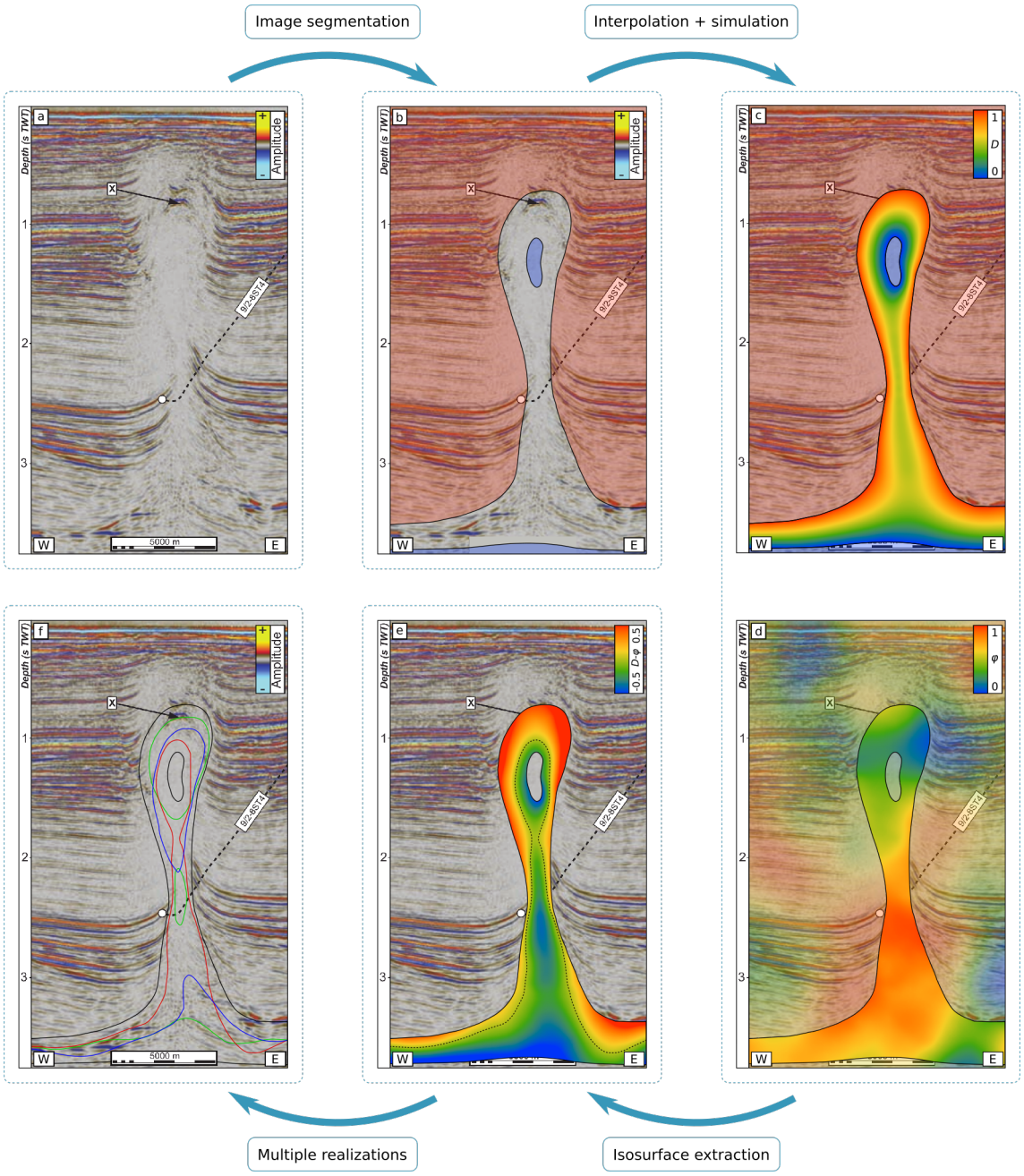

Figure 2.1 – Simulating stochastic interpretations of salt boundaries. The input seismic data [a, image from Jackson and Lewis, 2012] are segmented into three categories (b): sediments (red), salt (blue) and uncertain (uncolored). A normalized "distance" field D (c) and a normalized random field φ (d) are then generated in the uncertain region. The salt boundary S_B (e, dashed curve) is obtained by extracting the zero isovalue of the difference between D and φ. Different salt boundaries (f) can be obtained by generating different random fields (the three realizations share the same distribution and variogram models).

ODSIM method is that we perturb the probability of being in the salt body rather than the actual distance to the salt. This approach offers a way to efficiently explore the solution space, and allows for a control of the geometry and topology of the generated

boundaries while honoring local salt boundary observations.

The pseudo-distance field D (figure 2.1.c) is a monotonically varying scalar field that ranges from 0 at the contact with the "salt" region and the base of sediments, to 1 at the contact with the external "sediments" region. It represents a relative normalized distance of each sample to salt. In other words, it can be seen as the probability for each sample to be located outside the salt boundary (i.e., to be sediments). This scalar field is obtained by: (1) setting to 0 the value of the samples in contact with the "salt" region and the base of sediments, (2) setting to 1 the value of the samples in contact with the "sediments" region, and (3) interpolating the intermediate values in the remainder of the "uncertain" region. In this paper, we use the finite difference-based interpolation method proposed by Irakarama et al. [2018] to generate this scalar field.

The second scalar field φ (figure 2.1.d) is a spatially correlated random field which is applied to the pseudo-distance field D. The values of φ must lie in the same range as the values of D (between 0 and 1). Two parameters control the random field generation: a distribution model and a spatial correlation model. The distribution model describes the repartition of the values that will be drawn (and must therefore be bounded by 0 and 1). The spatial correlation model describes the local variability of the random field. The choice of the random field parameters is mainly expert-driven. In this paper, we use a sequential Gaussian simulation (SGS) to generate this random field φ. The spatial correlation model is thus represented by a variogram model.

Once the two scalar fields D and φ have been generated, we define the salt boundary S_B (figure 2.1.e) as the location of the 0-level surface of the scalar field defined as the difference between D and φ:

$$S_B : \{(t, x, y) \mid D(t, x, y) - \varphi(t, x, y) = 0\}. \tag{2.1}$$

As we want to sample structural uncertainties, we need to generate many realizations. In our case, all the realizations share the same pseudo-distance field D. In order to simulate different salt boundaries, we just need to generate one random field per realization. Figure 2.1.f presents three different salt boundaries generated using the same simulation parameters (i.e., distribution and variogram models).

2.3 Stochastic generation of salt geobodies

The above workflow is based on several elements: the uncertainty envelope, the pseudo-distance field D and the random field φ. Each of these elements requires the definition of some parameters, which raises several questions. How do parameters impact the realizations? Can we introduce conceptual knowledge into the modeling to reproduce specific geological features? Can we infer parameters from data and prior knowledge? And overall, can we appraise the different interpretations we simulate? The remainder of the paper aims at providing elements to answer these questions. In this section, we use an example of 3D synthetic salt diapir to illustrate the impact of the simulation parameters on the geometry and topology of the salt boundaries. Using the same example, we then present two examples illustrating how conceptual knowledge can be introduced by an appropriate selection of parameters to reproduce specific geological features. Finally, we explain how local salt observations or interpretations can be integrated in the

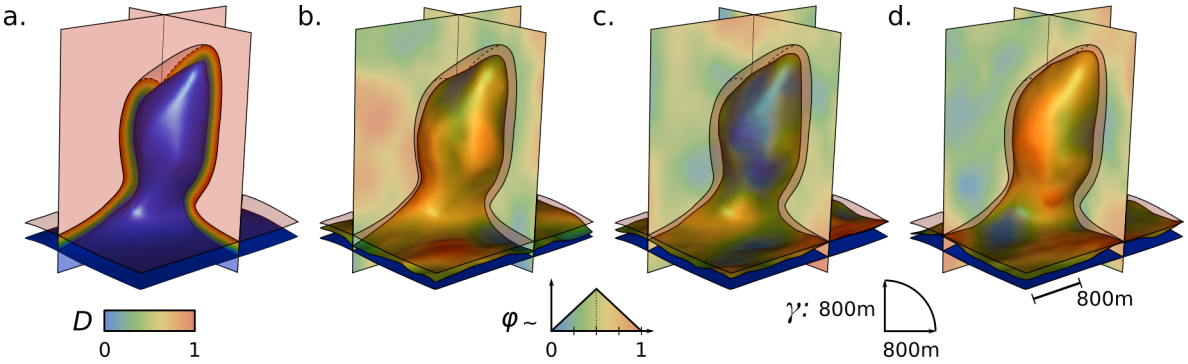

Figure 2.2 – Simulating variable salt top boundary geometries. (a) Input data: the "salt" region (in blue), the "sediments" region (in red) and the "uncertain" region (painted with the pseudo-distance field D). The dashed line represents the contact between the external sediments and the uncertainty envelope on the sections. (b), (c) and (d) Three different simulated salt boundaries painted with their respective random fields φ. φ follows a triangular distribution, and the variogram model γ is isotropic.

process.

2.3.1 Generating variable salt shapes

Figure 2.2 illustrates the generation of different salt boundary geometries. In this example, we consider that the segmentation of the image resulted in a clearly defined salt diapir (below the blue surface in figure 2.2.a). The uncertainties are thus limited to the position of the boundary in the envelope. The distance field D is computed in the uncertainty envelope (figure 2.2.a). The SGS parameters used to generate the random field φ are: (1) a triangular distribution model ranging from 0 to 1, with a mode at 0.5, and (2) an isotropic Gaussian variogram model with a range of 800 meters. These parameters are used as "default" parameters in our applications as they allow for the generation of relatively smooth boundaries (the global model size is about 3000 meters) that are centered within the uncertainty envelope. It is important to note that the generation of the random field φ is intrinsically prone to statistical biases, due to the relatively large variogram ranges as compared to the uncertainty envelope dimensions. Several strategies can therefore be considered to generate it. The one we selected consists in simulating the random field in the whole seismic image, and keep only the sub-sample corresponding to the uncertainty envelope. Three realizations are presented in figures 2.2.b, 2.2.c, and 2.2.d. Depending on the random field values, the simulated boundaries are generated everywhere in the uncertainty envelope and can be either close to salt (blue surface parts) or sediments (red surface parts).

2.3.2 Impact of the simulation parameters

The impact of the parameters used for the simulation of the random field φ is relatively intuitive and can be described in terms of oscillations of the simulated boundary around a reference position. As a reminder, two parameters control the generation of φ: a distribution model and a variogram model.

The mean of the distribution model determines the reference position of the bound-

ary in the envelope. If the mean is close to zero, the boundary will be statistically close to the "salt" region and, conversely, if the mean is close to one, the boundary will be statistically close to the "sediments" region. It controls therefore the total volume of salt that is simulated. For a given spatial correlation model, the standard deviation of the distribution determines the amplitude of the boundary oscillations as compared to its reference position: the higher the standard deviation, the larger the amplitude of the oscillations. The principal ranges of the variogram model control the frequency of the oscillations around the reference position, and thus the smoothness of the boundary: the larger the ranges, the smoother the boundary. Very short variogram ranges may also trigger the apparition of isolated salt blobs. Figure 2.3 summarizes the impact of the parameters on the boundary geometry.

It is important to note that the uncertainty envelope, the spatial correlation model and the distribution model all affect the boundary smoothness: the envelope shape controls the global shape of the distance field D (and thus the reference boundary position and its initial shape), the spatial correlation model range determines the global wavelength of the boundary oscillations within this envelope, and the distribution model standard deviation determines how much the boundary can move away from its reference position.

2.3.3 Generating more complex salt shapes

In geology, it is common to have some prior knowledge about the structures being interpreted. Such knowledge can be inferred from many sources of information, such as available data, global geological context, known field analogs, etc. Therefore, an interpreter may want to tune the simulation parameters in order to reproduce specific features. We present here two examples to illustrate how to select the simulation parameters according to a given target salt boundary shape.

Halokinetic sequences are sedimentary objects that are often associated with salt diapirs. These thin packages of strata are folded upward during the diapir growth, which results in non-conformable relationships between the different packages of strata [Giles and Rowan, 2012], and typical cusp-shaped patterns for the salt boundary. Figure 2.4.a illustrates an example of such an interpreted boundary from Giles and Rowan [2012]. To reproduce these features, we propose to use an anisotropic variogram model, with horizontal ranges higher than the vertical range (figure 2.4.b). The shorter vertical range reduces the vertical correlation and allows the boundary position to vary more rapidly within the envelop, reproducing the cusp-shaped patterns.

Salt Christmas trees are diapirs with very specific shapes. They are characterized by allochthonous salt "wings" located between sediment layers and connected to the diapir stem [Mohr et al., 2007]. These wings usually originate from a former salt glacier stage, when the diapir spread at the surface before being buried again. Figures 2.5.a and 2.5.b illustrate an example of salt glaciers forming such wings around a diapir on seismic sections, extracted from Mohr et al. [2007]. As strata far from the diapir can generally be imaged and interpreted, we propose to use them to build a relative geologic time function [e.g., Mallet, 2004, Wu and Zhong, 2012]. The equipotentials of this function (figure 2.5.c) describe the stratigraphic horizons, but also the diapir wing layout close to the diapir. This information is used during the simulation to locally

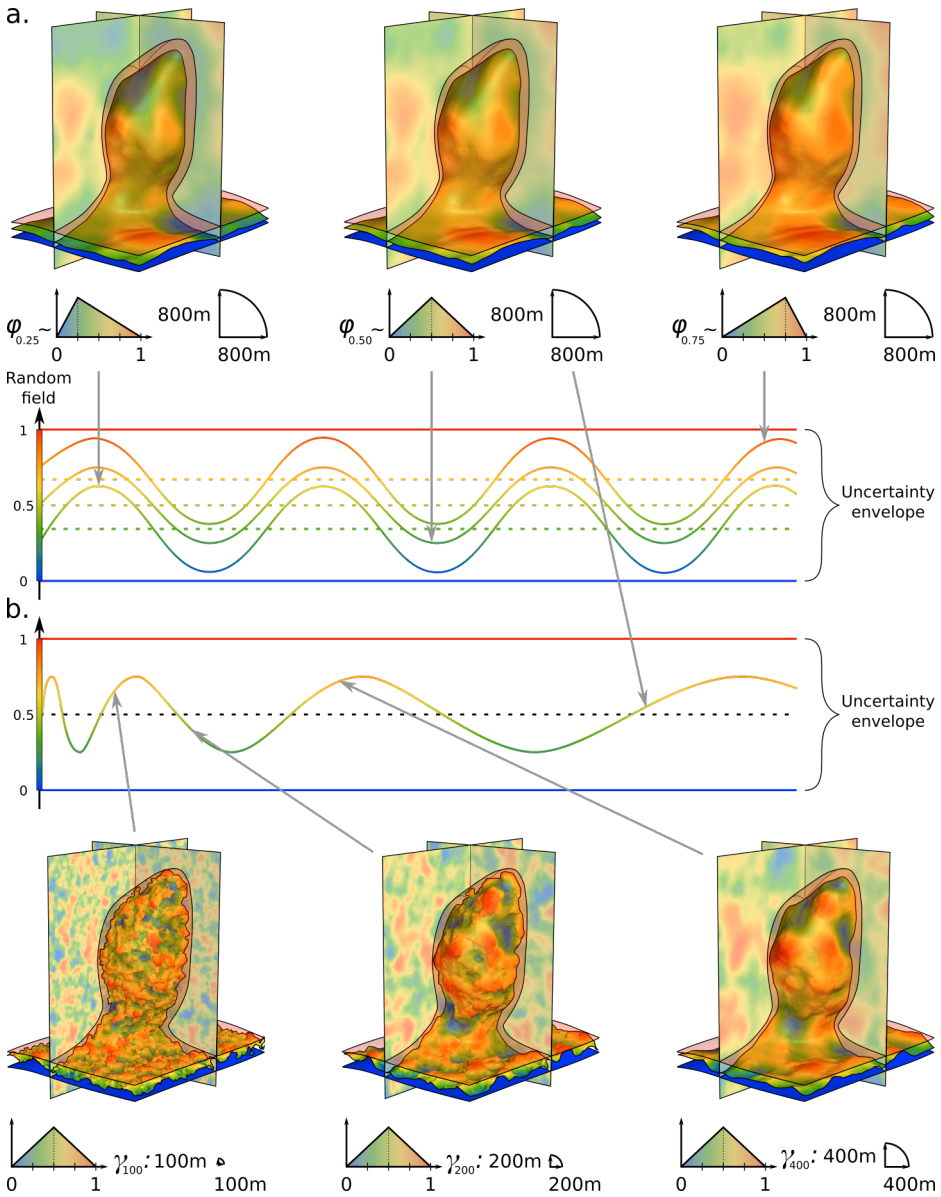

Figure 2.3 – Impact of simulation parameters on the boundary geometry. Each sinusoid represents an idealized boundary within the uncertainty envelope. (a) The distribution model affects the mean position of the boundary. (b) The variogram ranges affect the smoothness of the boundary. The variogram's principal ranges linearly increase from the left to the right of the uncertainty envelope. Input data from figure 2.2.a.

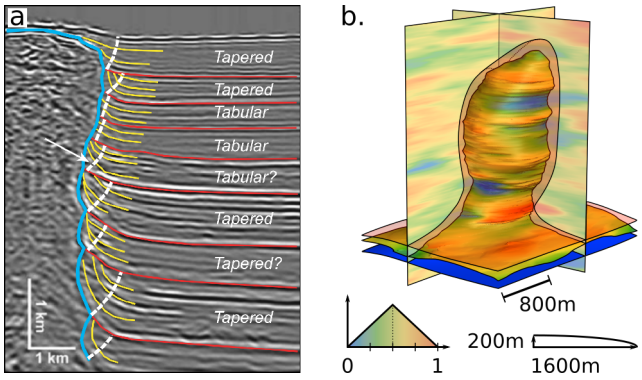

Figure 2.4 – Reproducing halokinetic sequences contact. (a) Example of the typical cusp-shaped patterns observed at the contact between halokinetic sequences (in red) and a salt diapir (in blue). Image and interpretation from Giles and Rowan [2012]. (b) An example of salt boundary generated using a transversely isotropic variogram model with short vertical range. Input data from figure 2.2.a.

orient the variogram model axes and reproduce the deposition of the diapir wings over the sediment layers: the "horizontal" axes are aligned along the equipotential surfaces, and the "vertical" axis along the gradient of the stratigraphic function. Combined with anisotropic ranges (very large horizontal ranges and short vertical range), it allows for the simulation of wing-like patterns along the diapir flanks. Figure 2.5.d presents a realization example of such a Christmas tree salt diapir.

2.3.4 Generating variable salt topologies

For the moment, we have only considered the generation of variable boundary geometries. Depending on the configuration of the regions interpreted during the image segmentation phase, it is also possible to generate salt boundaries with variable topologies. In particular, if the "salt" region is made of one basal part and a top teardrop-like part, then both connected and disconnected salt boundaries can be generated. This is illustrated in figure 2.6.a: the "salt" region contains a basal layer part, and a salt blob has been isolated above. The intermediate part has, however, been classified as uncertain, which allows for the interpretation of either a diapir stem or a weld. Figures 2.6.b, 2.6.c, and 2.6.d present three examples of simulated salt boundaries, generated using the same random fields as in figures 2.2.b, 2.2.c, and 2.2.d. Depending on the random field values, we generate either connected (figure 2.6.d) or disconnected (figures 2.6.b and 2.6.c) salt boundaries, which would need to be connected by a weld.

To characterize the topological changes between realizations, the approach of Thiele et al. [2016a] could be use. They propose a framework for characterizing the topological relationships between the different volume entities of a geomodel. In particular, they distinguish between structural and lithological topologies which describe the relations between respectively the different (structural) volumes of conformable stratigraphic units, and the different lithologies (independently of their spatial location). This classification is not perfectly suited for salt tectonics, as diapirs usually have a limited extent at the model scale (they do not cross the whole model) and halokinetic sequences define complex stratigraphic relations (they can be in the same time conformable in the basin

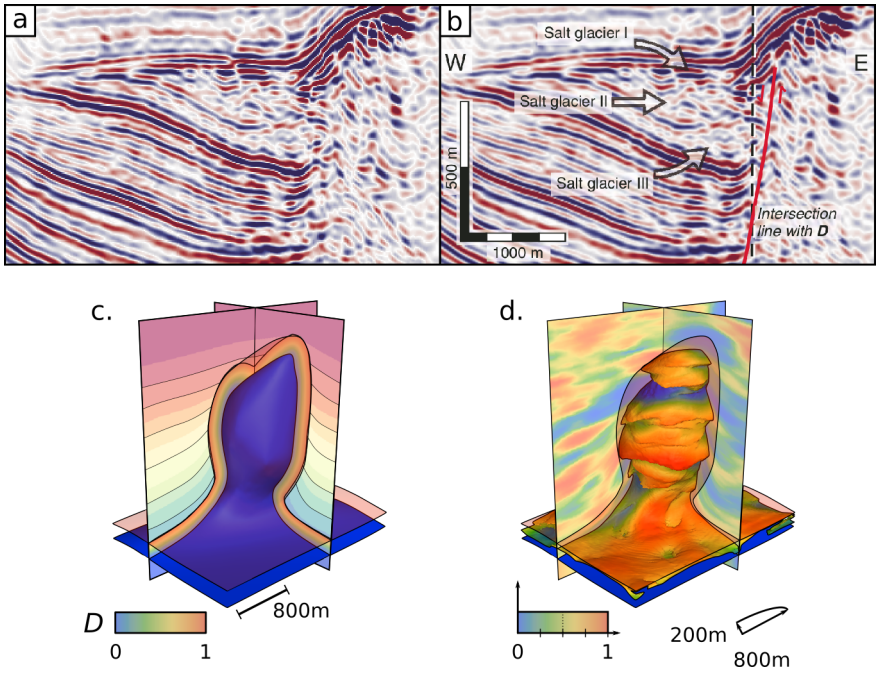

Figure 2.5 – Reproducing Christmas tree-like salt diapirs. Example of a salt Christmas tree diapir wing on uninterpreted (a) and interpreted (b) seismic sections. Image and interpretation from Mohr et al. [2007]. (c) Input data from figure 2.2.a, with the relative geologic time function used to align the variogram axes displayed on the vertical sections. (d) An example of salt boundary generated using a uniform distribution model and a transversely isotropic variogram model, with a short "vertical" range and larger "horizontal" ranges aligned with the relative time function.

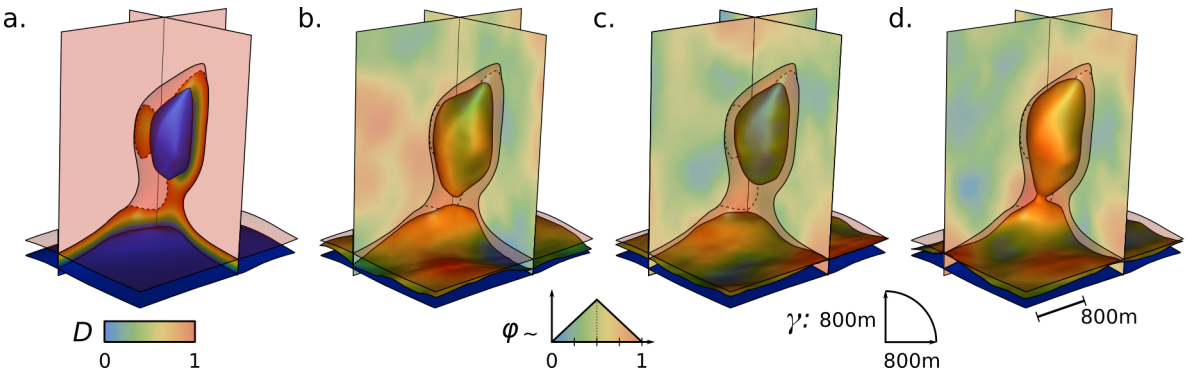

Figure 2.6 – Simulating variable salt top boundary topologies. (a) Input data: the "salt" region (in blue), the "sediments" region (in red) and the "uncertain" region (painted with its pseudo-distance field D). The dashed line represents the contact between the external sediments and the uncertainty envelope on the sections. (b), (c) and (d) Three different simulated salt boundaries, painted with their respective random fields φ.

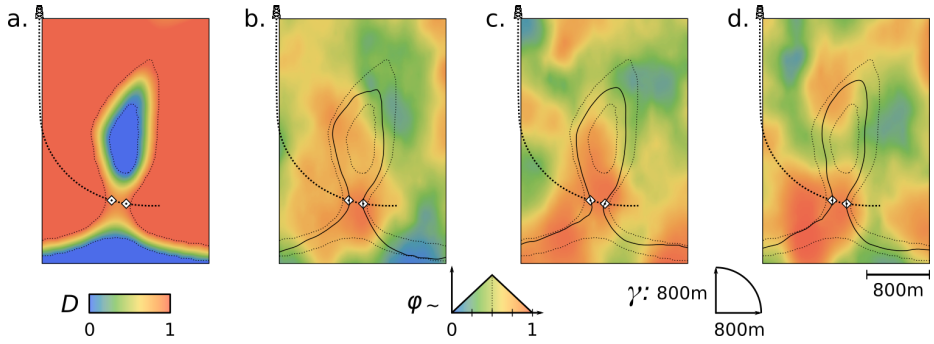

Figure 2.7 – Conditioning the simulations to well data. (a) Input data from figure 2.6.a, with a synthetic well and two markers (white diamonds) indicating the salt boundary position. (b), (c) and (d) Three different simulated salt boundaries (painted with their respective random fields φ) obtained using the same simulation parameters. The boundaries still have variable geometries, but honor the two well markers.

center and unconformable in the diapir vicinity). We consider, however, that it provides an interesting way of describing the different topologies that our method can generate. Our method, in itself, can generate variable structural topologies (depending on whether the simulated bodies are connected or not). It does not generate variable stratigraphic topologies, as we do not model the sediments. Modeling halokinetic sequences would be, however, an interesting extension of the method and would allow for the generation of variable stratigraphic topologies. Indeed, as the salt boundary geometry varies from one realization to another, modeling different disconnected salt bodies implies modeling different welds, and thus modifying the lithological contacts through the weld.

2.3.5 Conditioning to available data

The method proposed in this paper has the advantage of resting on a simple principle. This makes it easy to adjust to more specific purposes. Especially, it can be constrained to honor various types of geological data. The data conditioning is ensured by constraining the random field generation.

The easiest type of data to handle is punctual information on the salt boundary location (e.g., well markers or deterministic seismic picks indicating the boundary). As the salt boundary is defined by the set of points for which the value of the pseudo-distance field D is equal to the value of the random field φ, such observations can directly be treated as conditioning data for the SGS (by setting at data locations the value of the random field φ to the value of the normalized distance field D). Figure 2.7 illustrates this conditioning. Two well markers (figure 2.7.a) are added to the example presented in figure 2.6. The simulated salt boundaries (figure 2.7.b, 2.7.c and 2.7.d) exhibit variable geometries, but honor the two markers.

This type of conditioning does not restrict the number of data points that can be taken into account. Our method can, therefore, be applied in cases where some image parts have been interpreted, to reconstruct the boundary in the missing image parts. Figure 2.8 presents an example that illustrates this application. We consider that a seismic interpreter has made a fast interpretation of a salt diapir. The interpreter picked the salt boundary every twenty lines, in the regions where it is clearly defined

(figure 2.8.a). The top of the diapir and the top of the salt layer away from the diapir, which are generally well imaged, are therefore already interpreted. The diapir flanks are, however, poorly resolved and remain to interpret. Figures 2.8.b, 2.8.c, and 2.8.d present three automatically generated interpretations of the possible diapir boundary, which all honor the manually picked samples but exhibit very variable geometries and topologies.

We can also imagine integrating lithological observations (e.g., punctual well log information like "salt" or "sediments"). We do not illustrate this point here, but Henrion et al. [2010] showed that it only requires the use of a more sophisticated sampling method than direct sampling. They use Gibbs sampling [Geman and Geman, 1984] in their application. The main idea is that the simulated value at conditioning data location should be in accordance with the observation: if we observed salt, the simulated value should satisfy the condition $D - \varphi < 0$, and conversely if we are in sediments (then $D - \varphi > 0$). The Gibbs sampling ensures that the simulated data still verify the spatial correlation model.

2.4 Discussion

In this section, we develop some aspects that have been mentioned above. In particular, (1) we discuss the problem of the definition of the uncertainty envelope and the pseudo-distance field D, and their impact on the topology of the simulated boundaries; (2) we summarize the different elements about integration of prior knowledge and geological concepts in the modeling; and (3) we develop some points about parameter inference.

2.4.1 Workflow applications and anisotropy modeling

A common question that arises when modeling geological structures is the question of anisotropy modeling. Concerning salt modeling, there are two types of anisotropy: the anisotropy related to the large-scale structures (e.g., salt domes, walls, sheets, etc.) and the anisotropy related to the local features of the salt boundary (e.g., smooth, cusp-shaped, with wings, etc.). It is important to note that, depending on the application, we are not interested in integrating the same level of details into the models. As an example, in geomodeling we are interested in building models that integrate as much information as possible (such as precise halokinetic sequence contacts) in order to make predictions on potential hydrocarbon traps, reservoir heterogeneity, well planning, etc. In seismic imaging, using velocity models with such small scale details may, however, lead to more distorted images than using smoother velocity models, as they introduce details that drastically complicate the travel paths. We propose therefore to integrate separately structure-related anisotropy and boundary-related anisotropy into the model. Structure-related anisotropy is handled during the definition of the uncertainty envelope, and boundary anisotropy is controlled by the variogram model.

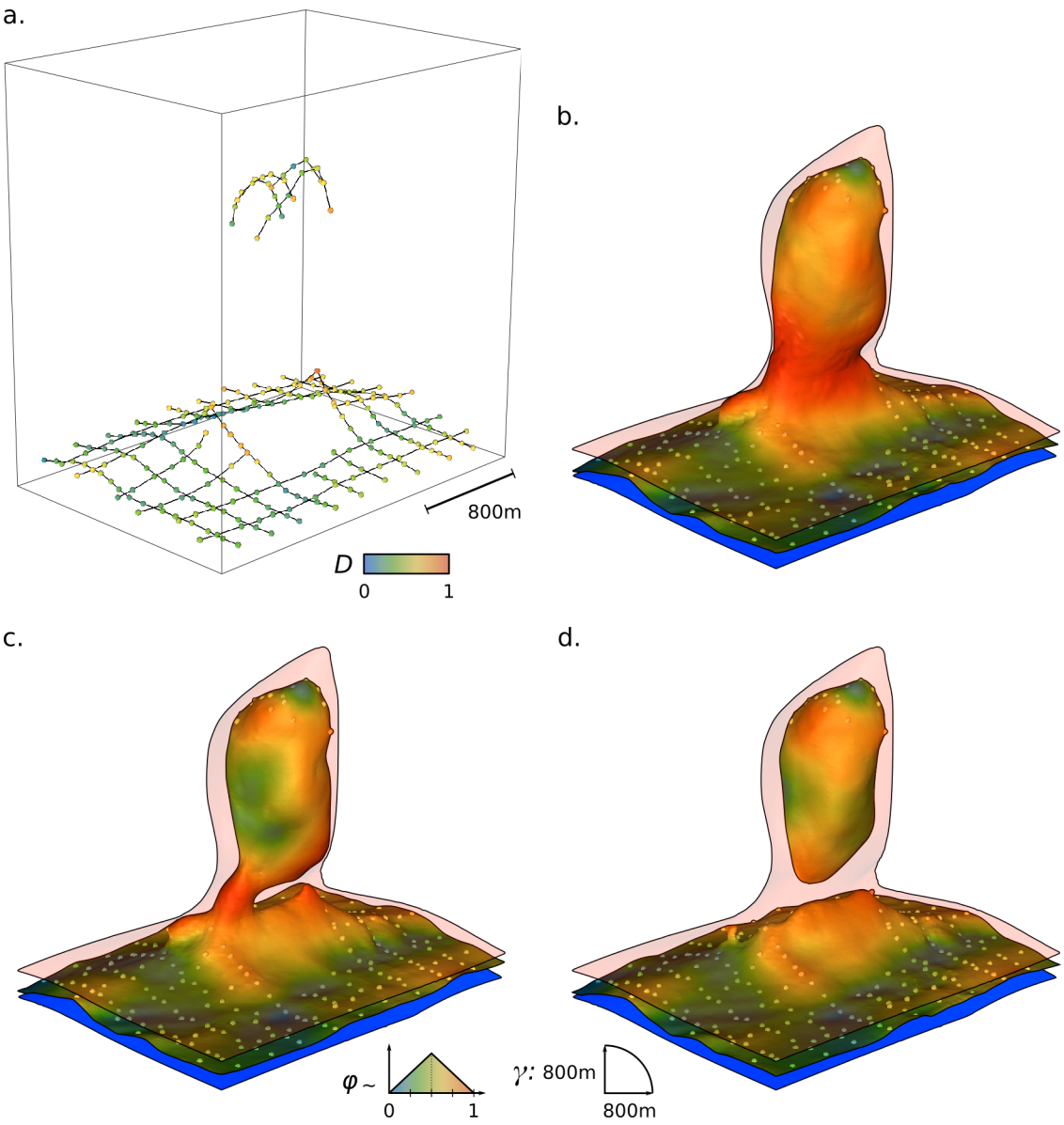

Figure 2.8 – Sampling variable diapir geometries and topologies while honoring incomplete manual interpretation. (a) Manual seismic picks of the salt boundary (painted with the pseudo-distance field D), used as constraints with the input data from figure 2.6. (b), (c) and (d) Three simulated salt boundaries (painted with their respective random fields φ) obtained using the same simulation parameters. The boundaries honor all the seismic picks, but exhibit variable geometries and topologies in the unconstrained part of the diapir.

2.4.2 Generation of the uncertainty envelope and influence on the simulated boundaries

As previously discussed, the topology of the uncertainty envelope impacts the topology of the simulated salt bodies. As a reminder, if the initial image segmentation phase produced several independent "salt" regions, then the simulation may produce one or several distinct geobodies. Otherwise, the simulation will produce one single geobody (provided that the variogram principal ranges are large enough to prevent the apparition of isolated blobs). The shape of the uncertainty envelope also has a direct impact on the geometry of the simulated boundaries, as it controls the shape of the pseudo-distance field D. It introduces a trend in the interpretations as it defines the "reference" boundary position together with the distribution model mean. We estimate, however, that this trend mainly determines the type of structures that will be interpreted (e.g., salt diapirs, salt walls or allochthonous salt sheets). When interpreting seismic images, most of the uncertainties relate to the exact location of the boundaries or the potential salt body connectivities, rather than the type of salt body to interpret. We consider, therefore, that the uncertainty envelope should be as smooth as possible so most of the geometrical properties of the simulated boundary are determined by the simulation parameters rather than the pseudo-distance field D itself.

As it determines the reference position of the boundary, the definition of the uncertainty envelope is a crucial step. Several strategies can be considered to achieve this step[1]. A first solution consists in coupling an automatic interpretation method proposed in the literature (see the introduction review[2]) with a confidence criterion. The most straightforward method could be to use the salt indicator function proposed by Wu [2016] and to define the three different categories by thresholding it. As an example, Haukås et al. [2017] use this type of approach. If enough data points are available (either lithological or boundary observations), it is also possible to consider building the uncertainty envelope directly from these data, using for example the method proposed by Martin and Boisvert [2017]. It would provide a good way to integrate locally varying structural anisotropy. Finally, we can also consider applying velocity uncertainty to this envelope [Thore et al., 2002], or re-migrating it [Osypov et al., 2013, Fomel and Landa, 2014] to account for imaging parameters uncertainty. To go further, it could be interesting to consider methods from the surface reconstruction domain in computer graphics to provide control on the topology of the uncertainty envelope [e.g., Huang et al., 2017].

Despite the above, it may not be easy to generate a smooth uncertainty envelope from automatic image segmentation techniques. To handle envelopes that would be too irregular, we suggest to use a second envelope that encompasses the first one (thus larger, but smoother). This second envelope is used to generate a smooth distance field D, and the points of the second envelope that do not belong to the first one (i.e., those that were first classified as "sediments" and then as "uncertain") can be used as lithological constraints (using a Gibbs sampler) to ensure that the simulated boundaries remain within the initial uncertainty envelope.

Another difficulty a user might face in some configurations consists in generating a

[1] See also section 1.5

[2] More details can be found in sections 1.3 and 1.4

pseudo-distance field D allowing for the interpretation of variable salt topologies. As an example, in figure 2.1 we had to constrain the values of the field D within the diapir stem in order to generate both connected and disconnected salt bodies. Indeed, as we impose its value to 1 on each side of the stem (at the contact with the "sediments" region), the interpolation populates the stem with values extremely close to 1, which makes the probability of simulating a connected salt diapir almost null. To constrain the values within the stem, we manually picked several samples within the stem and imposed the distance field values to be equal to 0.5 at the sample location. It is possible to automate this conditioning, for example by extracting the medial axis of the envelope and imposing its value[3].

To go further, it is possible to impose the topology of the simulated bodies. A potential strategy is to analyze the topology of the pseudo-distance field D to detect the presence of critical points. These points are characterized by a vanishing gradient of D, and identify the locations (and the associated values of D) where topological changes will occur when extracting a level set (i.e., when moving from a single to disconnected bodies). The values of φ can then be adapted to impose a given topology: if $\varphi < D$ at a critical point, disconnected salt bodies are simulated, and conversely if $\varphi > D$ a single salt body is simulated.

2.4.3 Integrating prior knowledge and geological concepts

Knowledge can be integrated either in the uncertainty envelope definition or in simulation process, depending on the type of information. The uncertainty envelope constrains the global shape of the structures. Its definition offers a way to integrate information about regional context, such as the regional structure orientations, the type of structures and their connectivity. The distribution model defines the average volume of salt that is generated, and how much the boundary can move away from its reference position in the uncertainty envelope. The variogram model offers a control on the local shape of the boundary. Depending on the application, a user might choose a long range isotropic variogram (to generate smooth boundaries, figure 2.2), or an anisotropic one to reproduce specific patterns (figure 2.4). Locally varying anisotropy can be introduced (and especially varying orientations) to reproduce, for example, depositional or salt spreading processes (figure 2.5). The choice of the variogram model also determines the influence of punctual data (e.g., well markers ans seismic picks) in the simulation. Choosing a Gaussian model (which is characterized by a large correlation for short distances) ensures that the interpretation in the neighborhood of the data points is consistent with the primary information. The selection of the variogram ranges then offers a way to control the area of influence of the data points.

To go further, it would be interesting to integrate geological concepts in the modeling. The most direct example is maybe the modeling of salt welds[4]. When the simulation produces disconnected salt bodies, we know from a geological point of view that an allochthonous salt body cannot "float" among younger sediments. It has to have been connected to a former salt source through a feeder, whose existence is indi-

[3] A method based on this idea as been implemented since the publication of the article and is presented in appendix of chapter 3

[4] This is the topic of chapter 3

cated by the presence of a weld. Modeling welds should be of interest in the oil and gas industry. They play indeed a major role in basin compartmentalization and in the deformation processes that occur at basin scale, and they can severely affect seismic imaging [Jackson and Hudec, 2017].

2.4.4 Simulation parameter inference

The definition of the simulation parameters is a key step of the workflow. It should take into account both the geometrical and topological specificities of the salt boundaries to interpret, when such characteristics can usually not be observed on seismic images. Therefore, strategies to calibrate the model parameters need to be developed depending on the type of salt geobodies to be simulated. Henrion et al. [2010] discuss some aspects of such model parameter calibration using prior geological knowledge. Among the available sources of information, well data and manual seismic picks can be used to obtain information about the actual salt distribution, geometry and topology. Analogs such as lab experiments [e.g., Vendeville and Jackson, 1992, Dooley et al., 2009], outcrop descriptions [e.g., Ringenbach et al., 2013] or interpreted seismic data sets from similar geological contexts usually represent another source of information, as they can generally be used together with field data to derive some set of model parameters [Guardiano and Srivastava, 1993]. The use of analogs is, however, not directly possible in our method.

This can be explained by considering the mathematical aspects of our problem. Let D_{pert} be the scalar field defined as

$$D_{pert} = D - \varphi. \tag{2.2}$$

From a geostatistical point of view, we have three random fields (D , D_{pert}, and φ) related by a linear combination. Considering that D and φ are independent and intrinsically second order stationary, we can relate their spatial correlation models: $\gamma_D = \gamma_{D_{pert}} + \gamma_\varphi$. This means that, knowing the variogram models γ_D and $\gamma_{D_{pert}}$ of D and D_{pert}, we can deduce a variogram model γ_φ for the simulated field φ. As we know the pseudo-distance field D, we can compute an experimental variogram from it and define an analytical variogram model γ_D. The field D_{pert}, whose variogram model represents the true variability of the salt boundary, is unknown yet (as the field φ is not known). We might consider using some analog to deduce an analytical model $\gamma_{D_{pert}}$. For the analog spatial correlation model (and thus $\gamma_{D_{pert}}$) being consistent with γ_D, we shall define an uncertainty envelope on the analog. Yet, this is not possible on lab and outcrop analogs. On analog seismic data sets, we can generate an uncertainty envelope. It is, however, not straightforward to estimate the analog boundary variability relatively to the envelope, as we only know the zero-level of the analog perturbed distance field, and not this whole field. Moreover, the fields D and D_{pert} are non-stationary and exhibit zonal anisotropy, with varying local principal orientations. In practice, it is, therefore, complex to define variogram models that actually describe these fields. Finally, the spatial distortion effect induced by the varying width of the uncertainty envelope adds another degree of complexity to the variogram model definition.

2.5 Conclusion

The proposed workflow allows for the generation of stochastic interpretations of salt geobody boundaries reflecting seismic imaging uncertainties. It can simulate both connected and disconnected salt bodies while honoring preexisting geological observations, such as manual seismic picks, well markers and lithological observations. The parameters of the method can be calibrated to reproduce specific geological features; however, quantitative parameter inference remains difficult. To address the impact of geometrical and topological salt interpretation uncertainties, further work should focus on appraising the various interpretations we generate with our method to inject them back into the seismic processing chain.

Moreover, the workflow is generic and can be used in other types of applications. In particular, it is well suited for the generation of any type of geological body boundaries (salt bodies, ore bodies, igneous intrusions, etc.), even in the presence of numerous constraining data. As an example, it could be of great use for estimating ore deposit extent in mining applications, where numerous data (and especially drillholes) are available.

Chapter 3

Stochastic salt modeling - Part 2: Modeling of salt body connectivity

Contents

Abstract In this chapter, I introduce a method to simulate and represent secondary salt welds. Welds represent the connectivity between detached salt bulbs and the source salt layer and are therefore necessary to develop valid boundary representation models. The method is almost fully automatic, and enables the integration of punctual information about the weld geometry and content. It takes as input the D_{pert} scalar field representing the salt boundaries. This field already contains all the necessary information for modeling a weld consistently with the simulated salt bodies. The weld position is defined by the minimum ridge located in the "stem" of the uncertainty envelope. This definition is, however, not suited for representing the weld in a geomodel. To represent the weld, I use a combination of Boolean fields. A first field represents a semi-infinite surface crossing through the entire domain and defining a binary partition of the seismic image. This surface contains this actual weld surface. It is obtained by performing a watershed transform to isolate the minima edges in the D_{pert} field. To preserve only the edge corresponding to the weld, I apply a preprocessing to the D_{pert} field. It is a local maxima filtering strategy, which ensures that the watershed transform produces a binary partition of the image. Two other Boolean fields are then used as visibility criteria to define the actual weld extent.

3.1 Introduction

The method presented in chapter 2 focuses on the generation of salt boundaries, i.e., on the geometry of the simulated salt bodies. Whereas the topic of the topology control during the simulations has been broached (section 2.3.4), we have only considered how to preferentially generate salt stocks or teardrop diapirs. We have not discussed, however, about how to actually represent the salt body connectivity when simulating teardrop diapirs. Indeed, as salt bodies are intrusive, they break the continuity within sediment layers when developing. After salt expulsion, discontinuities remain and impact the connectivity between the different layers [Giles and Rowan, 2012]. In order to preserve the model validity when integrating the simulated salt bodies in a geomodel, we therefore need to represent their connectivity. The geological object representing it is called a *salt weld*.

Much like faults, welds are surfaces (or most often thin volumes) resulting from the removal of salt from a former layer or diapir stage [Jackson and Talbot, 1991]. Due to the lack of available data, they are relatively poorly known as compared to other geological objects. Outcropping welds are quickly weathered, and well preserved examples are rare. When available, field data provide knowledge about the geometry and layout of the intermediate scale structures (the weld and the surrounding halokinetic sequences), and help developing geological scenarios about weld formation [e.g., Rowan et al., 2012]. In the subsurface, borehole data provide information on the composition and thickness

of welds [e.g., Jackson et al., 2019], but are most often proprietary and not necessarily published. Seismic reflection images (also often proprietary) and analog modeling help understanding the spatial organization of welds [e.g., Dooley et al., 2009, Ringenbach et al., 2013, Wu et al., 2015, Jackson et al., 2019]. Finally, numerical experiments allow for testing and validating hypotheses about the mechanisms of implementation and development of welds [e.g., Wagner and Jackson, 2011].

Due to their specific properties (detailed thereafter), salt welds play a major role in various processes such as basin compartmentalization (as potential seals), heat flow (as vectors of transport), and deformation mechanisms (as gliding surfaces).

In this chapter, we consider the integration of salt welds into a geomodel, and more specifically into the model provided by the salt modeling workflow presented in chapter 2. The first question it raises is about the determination of the weld position in the model. This choice should be coherent with the geometry of the simulated salt bodies. Furthermore, a weld introduces topological singularities in the model at the contacts with the salt boundaries. Therefore, it cannot be represented using the same scalar field D_{pert} as the salt bodies [e.g., Wellmann and Caumon, 2018]. A second question that we consider in this chapter thus concerns the structure used to represent welds in the model. Section 3.2 introduces some notions about weld nomenclature, classification and properties. Section 3.3 describes how to automatically detect disconnected salt bulbs in D_{pert} and how to define a weld connecting it to its pedestal. Section 3.4 treats specifically the problem of modeling the weld surface. Finally, section 3.5 develops further some elements for introducing prior information into the modeling.

3.2 Origin and classifications of welds

The term of weld refers to an evidence of the former presence of a vanished salt body. In practice, it includes a variety of structures that originate from different processes and in different geological contexts [e.g., Jackson and Hudec, 2017]. Several ways of describing and classifying welds have been proposed in the literature, based on the weld content, the initial salt body geometry and the associated basin structures (figure 3.1).

3.2.1 Weld description and classifications

Using weld content As stated above, welds are not always surfaces. Thin bodies of remnant salt may remain trapped between sediment strata. A first important distinction when describing a weld is based on the weld content [e.g., Jackson and Cramez, 1989, Wagner, 2010, figure 3.1]. If salt has been totally removed from the weld, it is said a *complete weld*. On the contrary, if some salt is trapped (up to 50 meters thick), the weld is said an *incomplete weld*. As the processes of salt removal may vary in space, some parts of a weld can be completely welded, when some others can still contain remnant salt. Such weld is said to be a *discontinuous weld*. It is often difficult to predict whether a weld is complete or incomplete on seismic images, due to limited seismic resolution. Moreover, thin salt layers (thicker than 50 meters) may also appear as single reflections on seismic images. These are referred to as *apparent welds*. Determining the true nature of a weld in the subsurface often requires, therefore, to have access to borehole data.

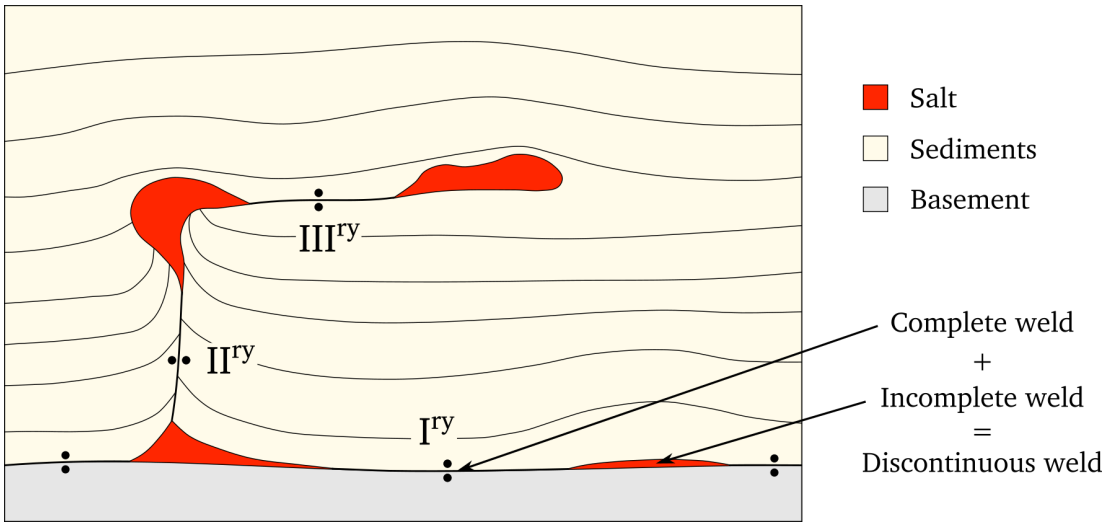

Figure 3.1 – Weld nomenclature and classification. The pairs of dots highlight the presence of a weld. Reproduced after Jackson and Hudec [2017].

Classification using the initial salt geometry The first attempt to classify salt welds, based on the initial geometry of the welded salt body, was proposed by Jackson and Cramez [1989] (figure 3.1). *Primary welds* result from the removal of an autochthonous salt layer, and are therefore often subhorizontal. *Secondary welds* form by shortening of a salt stock or wall, and are usually steeply dipping. *Tertiary welds* encompass all the welds that result from the expulsion of an allochthonous salt body and thus exhibit more variable geometries.

Classification using the geological context Rowan et al. [1999] proposed a modified version of this classification, based on observations from the Gulf of Mexico, in which the secondary and tertiary welds are divided into subcategories according to their geometries and the associated sediment deformations. These welds are also tightly related to the notion of *fault welds*: as salt is much weaker than surrounding sediments, significant displacement can occur between strata on each side of the weld [e.g., Jackson and Hudec, 2017]. This classification provides a better description of the role of each weld at the system scale, but in this thesis we will only consider the classification of Jackson and Cramez [1989] which provides a simple way to describe the different families of welds.

3.2.2 Physical mechanisms

Salt removal can occur following two different processes. First, differential loading can trigger creeping flow in salt bodies, resulting in salt expulsion. Then, salt can also be dissolved due to fluid circulations in the subsurface or meteoric water when exposed at the surface. These two types of process are often complementary. Most information in this section is summarized from the review of Jackson and Hudec [2017].

Welding by viscous flow As stated in the introduction, salt flows in response to differential loading. Depending on the initial salt geometry and the type of loading, dif-

ferent types of welds will form. Primary and most tertiary welds form after gravitational loading due to varying overburden repartition. Secondary welds form by squeezing of a salt diapir due to displacement loading. In the case of fault welds, the relative displacement between the fault blocks can also play a role in the welding by smearing the salt bodies. Analytical and numerical models have been proposed in the literature to try to better characterize and understand the behavior of salt welding by viscous flows [e.g., Wagner, 2010].

Welding by dissolution The second mechanism involved in salt removal is the dissolution that occurs when water circulations enter in contact with a preexisting salt body. Salt often has a high water solubility, e.g., 26.4% at 20°C for halite [Baar, 1977], but dissolving large volumes of salt would require prohibitive volumes of water, especially at depth (see e.g., Wagner [2010] and the discussion in Jackson and Hudec [2017]). Moreover, for the dissolution process to persist with time, it is necessary to constantly renew the circulating fluids to avoid saturation.

Combined effect of viscous flow and dissolution It is admitted that it is difficult to form complete welds by purely viscous flow, due to boundary drag effects [e.g., Jackson and Hudec, 2017]. The remaining thin volumes of salt are, however, likely to be dissolved if they enter in contact with unsaturated fluids, resulting in the formation of complete welds.

3.3 Simulation of secondary salt welds

Given the range of possible weld geometries and the diversity of associated sediment structures [cf. Rowan et al., 1999], defining a single unified approach to weld modeling is a particularly difficult task. In this chapter, we focus on the modeling of secondary welds. Several reasons motivate this choice. First, primary welds do not usually present a particular difficulty to interpret on seismic images. They correspond to subhorizontal stratigraphic surfaces, and result in a vanishing top salt boundary. On the contrary, secondary welds are likely to be difficult to image as they correspond to vertical structures overhung by a salt body. Then, tertiary welds exhibit much more variable geometries than secondary welds. This makes them harder to describe and characterize. Therefore, we chose to focus first on the modeling of secondary welds. It allows for the development of a modeling strategy on a "not too complex" case, which might later be extended to integrate tertiary welds. This is however not discussed in this thesis.

3.3.1 Detection and filtering of the simulated salt bodies

This input of the weld modeling is the already simulated salt bodies, and thus the scalar field D_{pert} (equation 2.2). The first thing to do is to determine whether we need to model a weld or not (i.e., whether the simulation produced a single or multiple salt bodies). This step is a general problem of blob detection in a scalar field.

Before going further, it is necessary to notice that most of the modeling steps discussed in this chapter (the blob detection first) are based on the definition and the manipulation of sets of connected pixels in the image. This has motivated the choice

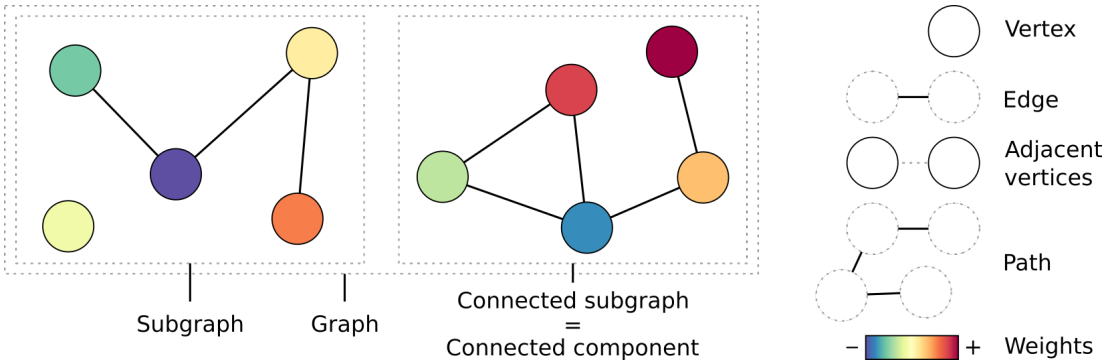

Figure 3.2 – Definitions about graphs.

of using a graph structure to represent an image in this chapter. Graph structures are widely used in image processing, and most of the problems we consider in this chapter have already been discussed in the literature. We introduce here some fundamental definitions about graphs that are used in the following.

Definitions In this thesis, we consider the following definitions (figure 3.2):

- *graph*: a graph $\mathcal{G} = (V, E)$ is a pair composed of a set of vertices V and a set of edges E.
- *edge*: a pair of vertices that are connected in the graph.
- *adjacent*: two nodes are adjacent if they are connected by an edge.
- *subgraph*: a graph $\mathcal{G}_{sub} = (V_{sub}, E_{sub})$ composed of a subset of vertices V_{sub} of V and a subset of edges E_{sub} of E.
- *path*: a sequence of edges joining a sequence of vertices.
- *connected*: a graph is said to be connected if there exists a path between any of its pairs of vertices.
- *component*: a connected subgraph in which it is not possible to add any other vertex while preserving its connected property.
- *vertex weighted graph*: a graph $\mathcal{G}_W = (V, E, W)$ where W is a map associating to each vertex of V a scalar value (a weight).

Link with images Definitions are given for 2D images to ease the reading, but their generalization to 3D images is straightforward. A 2D image of size $N_i \times N_j$ pixels (figure 3.3.a) can be seen as a graph $\mathcal{G} = (V, E)$ (figure 3.3.b) defined as

$$\begin{aligned} V &= \{N_{i,j} \mid (i,j) \in [\![0, N_i[\![\times [\![0, N_j[\![\}, \\ E &= \{(N_{i_1,j_1}, N_{i_2,j_2}) \in V^2 \mid \|i_1 - i_2\| + \|j_1 - j_2\| = 1\}. \end{aligned} \tag{3.1}$$

Each pixel is assigned a scalar or vector value (e.g., its gray-scale or RGBA value). We consider in the following only scalar values. A gray-scale image can therefore

be assimilated to a scalar field and represented by a vertex-weighted graph $\mathcal{G}_{gs} = (V_{gs}, E_{gs}, W_{gs})$ where W_{gs} is the map associating to each vertex the gray-scale value of its corresponding pixel ($W_{gs} : [\![0, N_i[\![\times [\![0, N_j[\![\rightarrow [\![0, 255]\!]$). More generally, any scalar field defined on a (seismic) grid can be represented by a vertex-weighted graph whose vertices and edges are defined by the grid, and the vertex weights by the scalar field.

Detection of the simulated salt bodies We define the vertex-weighted graph $\mathcal{G} = (V, E, D_{pert})$ as the graph defined by the simulated perturbed distance field D_{pert} (equation 2.2). We then define the subgraph $\mathcal{G}_{salt} = (V_{salt}, E_{salt}, D_{pert})$ of $\mathcal{G}$ as the graph containing all the simulated salt pixels and their corresponding edges:

$$\begin{aligned} V_{salt} &= \{N_{i,j} \in V \mid D_{pert}(N_{i,j}) < 0\}, \\ E_{salt} &= \{(N_{i_1,j_1}, N_{i_2,j_2}) \in E \mid (N_{i_1,j_1}, N_{i_2,j_2}) \in {V_{salt}}^2\}. \end{aligned} \tag{3.2}$$

Using the graph $\mathcal{G}_{salt}$, the problem of detecting all the simulated salt bodies is reduced to finding all the connected components of $\mathcal{G}_{salt}$. It can be done easily by using, for example, a depth-first search algorithm (algorithm 1).

Algorithm 1: Computation of connected components in $\mathcal{G}_{salt}$.

Data: $\mathcal{G}_{salt}$ - the vertex-weighted graph defined in equation 3.2
Result: $\mathcal{L}$ - a labeling of V_{salt} indicating the connected components of $\mathcal{G}_{salt}$
Result: *nb_components* - the number of connected components in $\mathcal{G}_{salt}$

```
/* Initialization of the labeling                                    */
foreach v ∈ V_salt do
    L(v) ← 0 ;
end
/* Graph traversal using depth-first search strategy                 */
nb_components ← 0 ;
foreach v ∈ V_salt do
    if L(v) = 0 then
        nb_components ← nb_components + 1 ;
        depth_first_search(L, v, nb_components) ;
    end
end
```

Function *depth_first_search(labeling $\mathcal{L}$, vertex v, label l)*

```
L(v) ← l ;
foreach vertex v_adj adjacent to v do
    if L(v_adj) = 0 then
        depth_first_search(L, v_adj, l) ;
    end
end
```

Filtering of the potential blobs Depending on the choice of the simulation parameters, some blobs may be present in the D_{pert} field (section 2.3.2). Computing the number of connected components of $\mathcal{G}_{salt}$ offers a way to detect these small blobs. To

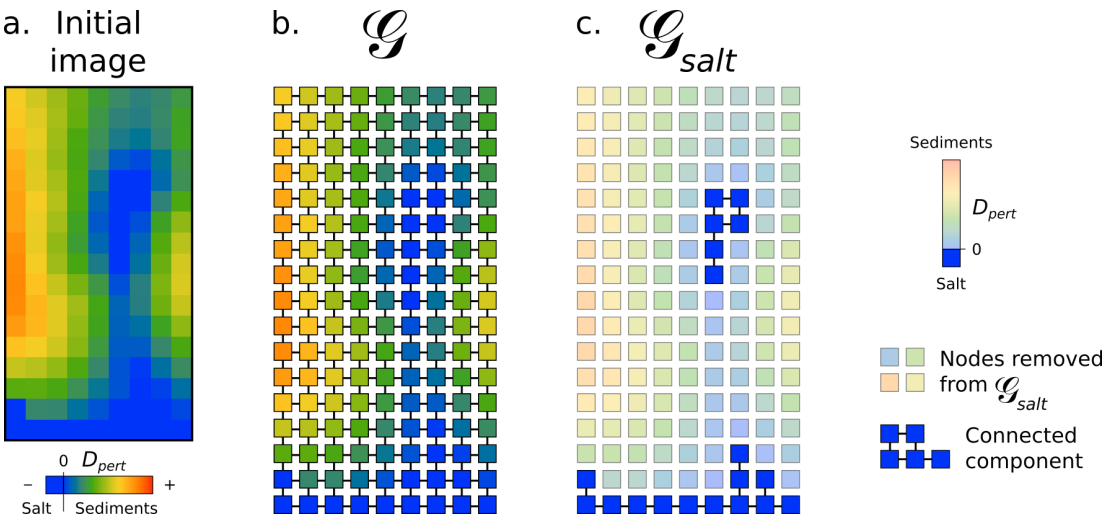

Figure 3.3 – Detection of the disconnected salt bodies. The D_{pert} field (a) is transformed into a graph $\mathcal{G}$ (b) in which each pixel corresponds to a node and contiguous pixels are connected by an edge (equation 3.1). The subgraph $\mathcal{G}_{salt}$ (c) of $\mathcal{G}$ contains all the nodes for which $D_{pert} < 0$ and the edges connecting these nodes (equation 3.2). The number of simulated salt bodies is given by the number of connected components in $\mathcal{G}_{salt}$.

filter out these blobs, we must determine which component in the graph corresponds to the diapir pedestal, and which one corresponds to the diapir bulb. It can be determined by testing the inclusion relations between the $\mathcal{G}_{salt}$ components and the initial *Salt* region: the bulb component in $\mathcal{G}_{salt}$ includes the bulb component of the initial *Salt* region, and the pedestal component includes the pedestal component of the initial *Salt* region.

3.3.2 Definition of the weld surface

As described in section 2.3.2, the scalar field D defines a "reference" position for the salt boundary. It works exactly the same way for the weld (figure 3.4). Its reference position is defined by the medial axis of the uncertainty envelope, or equivalently, by the minimum ridge of D located in the center of the envelope stem (solid line in figure 3.4.a). Perturbing the reference position of the salt boundary thus implies perturbing the reference position of the weld: when we stochastically simulate salt bodies, we simulate in the same time the associated weld. The only thing left to do is thus to extract the weld surface.

3.4 Extraction of the weld surface

At this point, we have detected the necessity of integrating a salt weld in the model and we have already simulated it. Its current representation (a ridge in the scalar field D_{pert}) is, however, not suited for most applications and may have branches. In order to integrate salt welds into a boundary representation model, we have to transform this scalar field ridge into a suitable representation. The branching points between the weld and the salt boundaries introduce singularities in the model. Handling these singularities require to represent the weld separately from the scalar field D_{pert}.

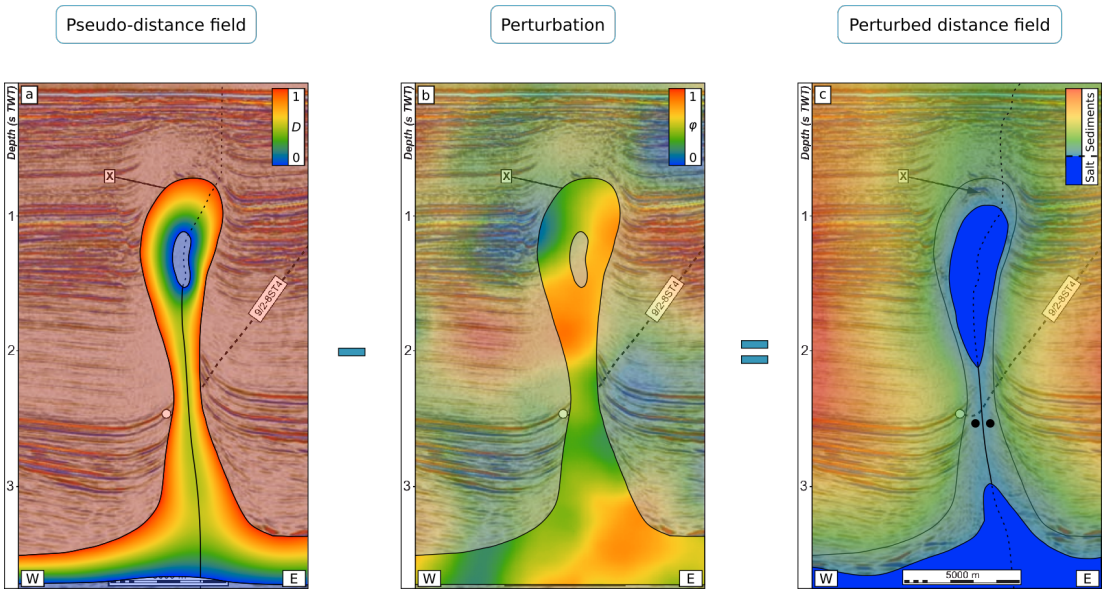

Figure 3.4 – Definition of the weld position. (a) Reference position of the weld defined in the pseudo-distance field D (minimum ridge defined by the black solid line). (b) Perturbation field φ applied to D. (c) Perturbed weld position defined by the D_{pert} field.

To represent the weld in practice, we use Boolean operations on Heaviside basis functions [Moës et al., 2002]. A first Boolean field defines a binary partition of the seismic image. Exactly as it is possible to represent a fault by defining its hanging wall and footwall, we use this partition to define two "weld blocks" isolating the weld surface. As the partition cuts through the whole domain, we then use visibility criteria (other Boolean fields) to define the actual weld extent.

3.4.1 Partitioning of the perturbed distance field

Extracting the minimum ridge in D_{pert} and defining a binary partition that isolates the weld are two different approaches for solving an equivalent problem. Various solutions exist in the image processing literature. We chose is the watershed transform (figure 3.5). This transform was originally introduced by Beucher and Lantuéjoul [1979]. It aims at partitioning an input image into a set of disjoint regions by reproducing the geomorphological notion of drainage basins separated by watersheds. Different formulations have been proposed since. We use the one proposed by Cousty et al. [2009]. It is defined on arbitrary N-dimensional graphs, which makes it independent of the image dimension.

Watershed transform principle We associate a scalar value to each pixel in the image (in this case the D_{pert} field, figure 3.5.a). This value is assimilated to the pixel "elevation". We define one region (a drainage basin) per local minimum in the image. Then, each cell is assigned to a given drainage basin by simulating a stream starting from it. The stream follows the steepest descent on the topography until reaching one of the local minima. The cell is finally associated to the drainage basin it reached. The output of the transform is a categorical field: each pixel is assigned a label determining

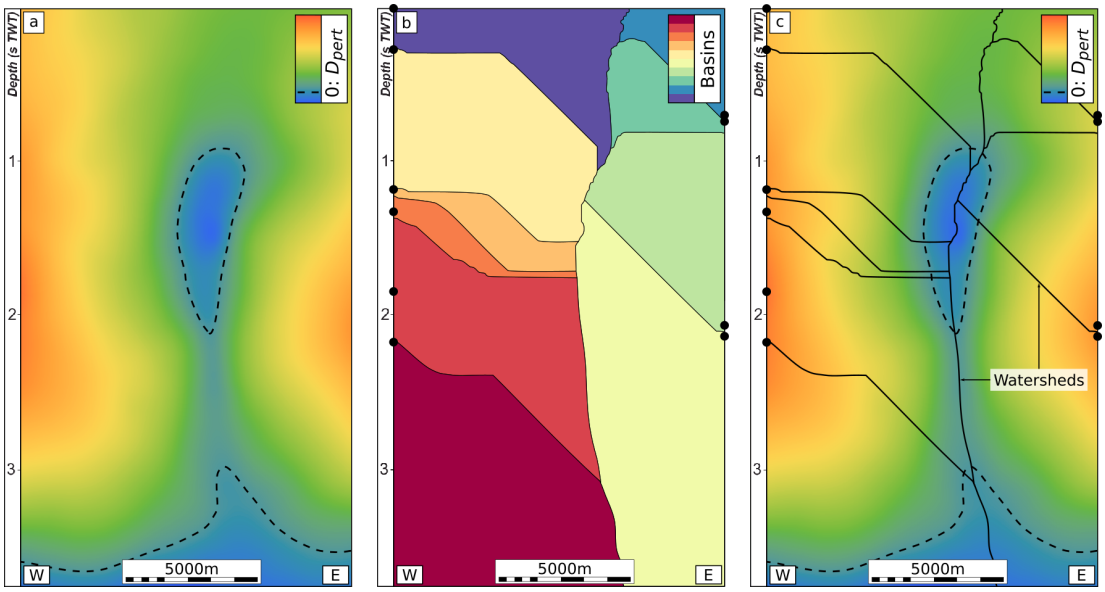

Figure 3.5 – Watershed transform applied to D_{pert}. (a) Perturbed distance field of figure 3.4.c and its corresponding salt boundaries (dashed lines). (b) Result of the watershed transform of D_{pert}: the image is partitioned in ten drainage basins (black dots highlight the position of local maxima). (c) Watershed cuts defined by the transform superimposed on D_{pert}.

the drainage basin it belongs to (figure 3.5.b). Equivalently, it is possible to define the watersheds from the drainage basin contours (figure 3.5.c). Note that this is a simplified explanation of the method proposed by Cousty et al. [2009]. The reader is referred to the paper for full details (and especially to algorithm 2).

In practice As the watershed transform mimics the geomorphological notion of watershed, it segments a scalar field along the maximum value ridges using the local minima. In practice, we want to do the contrary: the weld to segment corresponds to a minimum value ridge (what would be a valley from a geomorphological point of view). To extract the weld from the D_{pert} field, we simply consider the opposite of D_{pert}. By multiplying all the values of D_{pert} by -1, what was a minimum ridge becomes a maximum and we can perform the watershed transform as explained above. Figure 3.5 presents the result of the watershed transform applied to the D_{pert} field presented in figure 3.4.

3.4.2 Filtering of the local minima

The watershed transform creates one region per local minimum. It is not sufficient to define the Boolean field we use to represent the weld. To create a binary partition of the image, we couple the watershed segmentation with a local minima filtering method (figures 3.6 and 3.7). The idea is to detect all the non-significant local topographic minima before computing the watershed transform (figure 3.6.a). These local minima are then "flattened" by modifying their elevation so that water cannot accumulate within them anymore (figure 3.6.c). We use the strategy and the algorithms proposed by Najman and Couprie [2006]. Like the watershed transform proposed by Cousty et al. [2009], the method is defined on arbitrary N-dimensional graphs, making it independent

of the image dimension. As it was initially proposed to filter out local maxima, we slightly adapted the strategy. Here we present the adapted version.

Principle The aim of the method is to determine a ranking of the different local minima. To do so, we will build an alternative representation of the topography (figure 3.6.b). We simulate the progressive flooding of the topographic surface. A lake appears when the water level reaches the elevation of a local minimum. Two lakes merge when the water level reaches the elevation of a local maximum isolating two minima. During the flooding, we monitor the apparition and especially the coalescence of the different lakes.

Mathematical formulation If we consider again the image as a weighted graph $\mathcal{G} = (V, E, D_{pert})$, "lakes" at a given elevation z correspond to the connected components of $\mathcal{C}_{\mathcal{G},z} = (V_{\mathcal{C}}, E_{\mathcal{C}}, D_{pert})$ of $\mathcal{G}$ defined as

$$\begin{aligned} V_{\mathcal{C}} &= \{N_{i,j} \in V \mid D_{pert}(N_{i,j}) < z\}, \\ E_{\mathcal{C}} &= \{(N_{i_1,j_1}, N_{i_2,j_2}) \in E \mid (N_{i_1,j_1}, N_{i_2,j_2}) \in {V_{\mathcal{C}}}^2\}, \end{aligned} \tag{3.3}$$

and each connected component can be uniquely identified by its node having the highest elevation (its representative node).

The inclusion relations between the different components that have been defined during the flooding form a specific graph structure, namely a tree (called *component tree* in the following, figure 3.6.b). The initial components corresponding to local minima form the tree leaves. All the components that appear during the flooding form different levels of branches: when two components merge, a new higher order branch is created in the tree, on which are branched the two initial ones. And the final component which is obtained when the entire surface is flooded corresponds to the tree root. Note that in practice, one component is created per pixel in the image. The reader is referred to Najman and Couprie [2006] for full details about the implementation (and especially to algorithm 2).

Filtering strategies From the component tree, we have a first idea of the relative significance of the different minima (figure 3.6.b). To quantitatively estimate the significance of each minimum, we use different measures: the minimum area (the number of vertices belonging to the lake it defines), its depth (the difference between the surface and bottom elevation of the lake), or its volume (the amount of water that can accumulate within the lake) [Najman and Couprie, 2006]. We assign to each component in the component tree the value of the estimator of its representative node.

Two strategies can then be adopted to filter the least significant minima (figure 3.6.c): either we remove all the components having an estimator value lower than a given threshold, or we keep only a given number of minima, the ones having the highest estimator value. In our case, as we want to create a binary partition of the D_{pert} field, we choose to preserve only the two most significant local extrema (figure 3.7.b). To remove a given component from the component tree, we simply set the D_{pert} value of all the vertices belonging to the component to the elevation of its representative node.

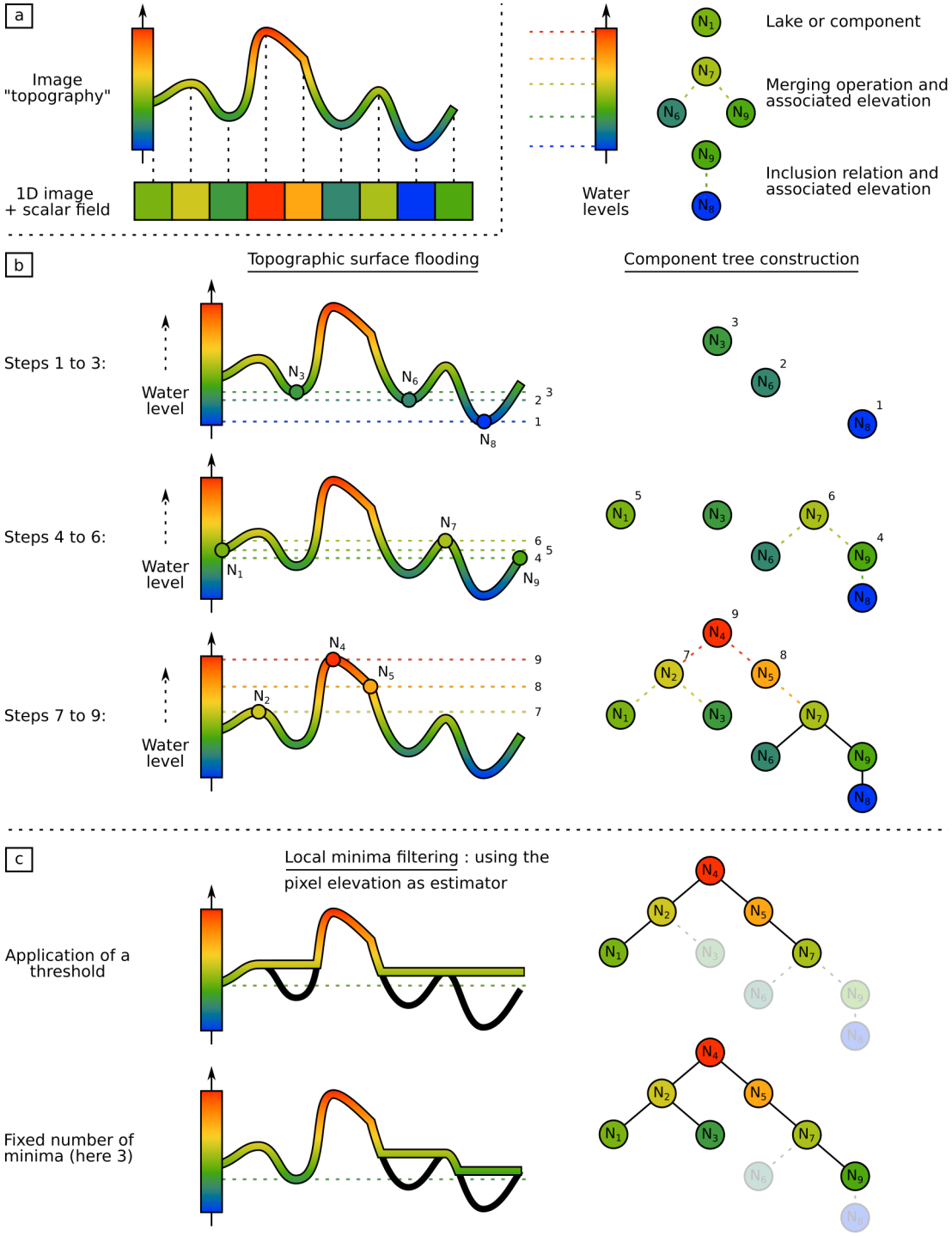

Figure 3.6 – Local minima filtering strategy. (a) Input 1D image and its associated "topography". (b) The component tree is computed by flooding progressively the topography and monitoring the apparition and coalescence of lakes. (c) The "significance" of each image pixel (each component tree node) is estimated using some measure (e.g., the area, depth or volume of the associated lake). Based on this estimator (here the pixel elevation), two filtering strategies can be considered: either removing all the local minima below an estimator threshold or preserving a fixed number of minima (i.e., of component tree leaves).

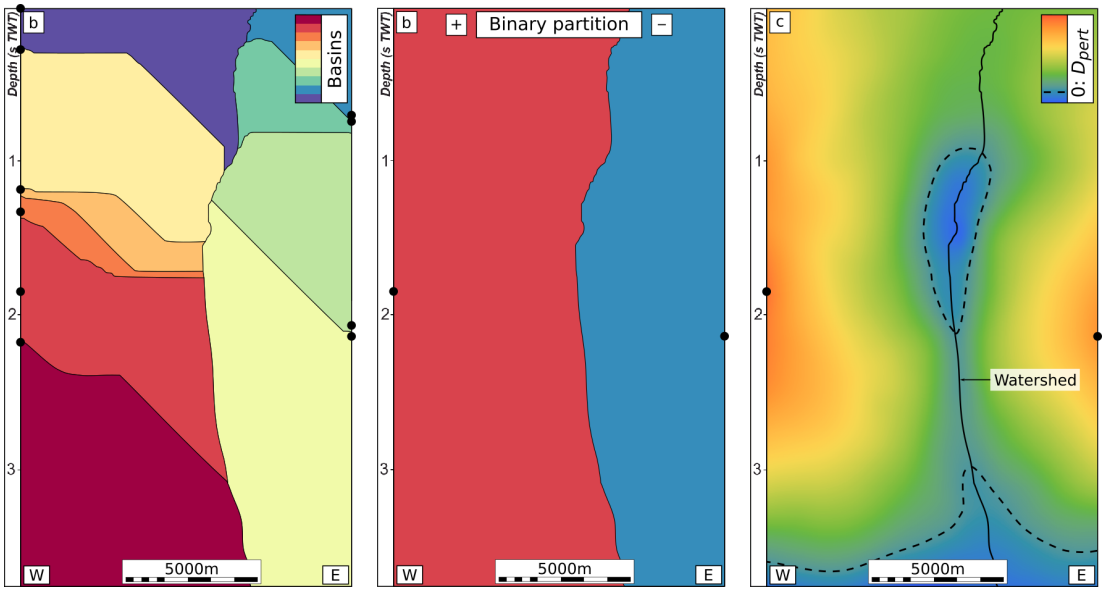

Figure 3.7 – Watershed transform applied to D_{pert} after local maxima filtering. (a) Result without filtering (image from figure 3.5.b). Black dots highlight the local maxima. (b) Result of the watershed transform of D_{pert} after local maxima filtering: a binary partition of the image. Black dots highlight the two most significant maxima preserved (in terms of area). (c) The watershed cut defined by the transform superimposed on D_{pert}, linking the base layer and the salt bulb.

3.4.3 Truncation of the weld surface

At this point, we have a binary partition of the image which defines a semi-infinite surface containing the weld. In order to actually represent the weld, we also need to determine its extent (figure 3.8). To do so, we define two visibility criteria [Moës et al., 2002] that we use to truncate the semi-infinite surface (figure 3.8.b). Each criterion defines a specific binary partition of the space ("visible" and "not visible"), and the final weld extent is defined by the intersection of all the "visible" parts of the partitions. In practice, the truncation is formulated as a set of binary operations applied successively. It is important to note that the criteria developed thereafter are specifically defined for the modeling of secondary welds and are not necessarily relevant for modeling other types of welds.

First criterion: be located between the salt bulb and pedestal In a first time, we limit the vertical and lateral extent of the weld to the subsalt domain. In practice, we formulate it as: a point belongs to the weld if it is located (1) in a trace that crosses both the diapir bulb and the pedestal, (2) below the bulb (figure 3.8.d). This criterion sometimes leads, however, to the apparition of holes in the weld surface. This happens when the surface locally goes over the edge of the salt bulb. Some solutions to overcome this problem are discussed in section 3.5.2.

Second criterion: belong to the uncertainty envelope We expect the weld to be located within the uncertainty envelope. This second criterion is used to laterally refine the initial cut (in the case of a shrinking envelope stem). It can be debatable, as

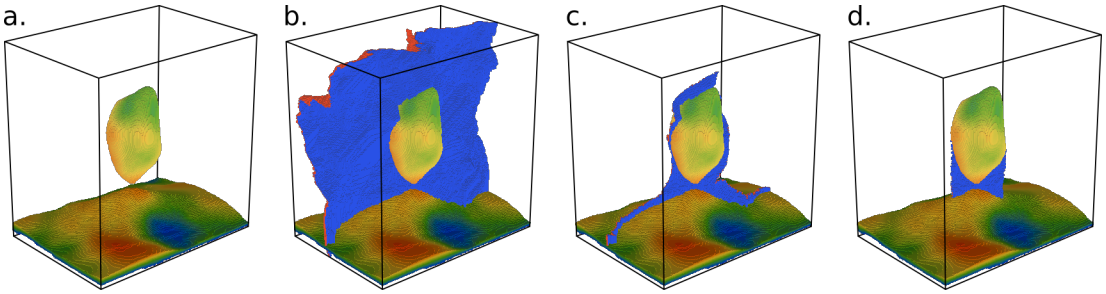

Figure 3.8 – Truncation of the weld surface. (a) Input (simulated) salt bodies. (b) Semi-infinite weld surface resulting from the watershed transform and minima filtering. (c) Intersection of the semi-infinite weld surface with the uncertain envelope. (d) Final weld surface intersected by the traces crossing both the diapir bulb and pedestal.

the weld being an "absence" of salt, it may be classified as "sediments" during the image segmentation phase (section 2.2.1). We consider, however, that in the case of secondary welds, the imaging of the weld beneath the salt bulb is likely to be challenging and that this configuration should therefore not happen (figure 3.8.c).

3.5 Discussion and perspectives

3.5.1 Modeling incomplete and apparent welds

Extracting the weld surface consists in modeling a complete weld. As summarized in section 3.2.1, welds are often discontinuous with patches of remnant salt trapped within. Moreover, as we work with seismic images, it is possible that thin salt layers appear as apparent welds on the images. These salt volumes are important features to take into account in many processes (e.g., reservoir sealing estimation, seismic imaging, stress state prediction).

Principle To simulate a volume around the weld surface, we use the Object-Distance Simulation method proposed by Henrion et al. [2010]: we compute the distance D_{weld} to the weld surface (figure 3.9.b), and we truncate this distance field using a spatially correlated random field φ_{weld} (figure 3.9.c). The final weld is defined by the initial weld surface plus all the pixels for which $D_{weld} - \varphi_{weld} \leq 0$ (figure 3.9.d). These pixels define small volumes of remnant salt located along the weld surface. Depending on the thickness and continuity of the simulated volumes, it is possible to model either incomplete, discontinuous, or apparent welds. The control of the type of simulated welds is provided by the parameters used to generate φ_{weld} (as in section 2.2.2, we use a sequential Gaussian simulation to generate this spatially correlated random field).

Simulation parameter impact The random field φ_{weld} controls the amount and the thickness of remnant salt that is simulated. It can be seen, in a way, as a description of the half width of the weld. In detail, the distribution model controls the probability of simulating a complete weld. In the example of figure 3.9, the distribution model ranges from -30 to 120 (all the quantities used in this paragraph are distances, expressed in meters). Drawing a negative value results in modeling a "negative" weld thickness, which

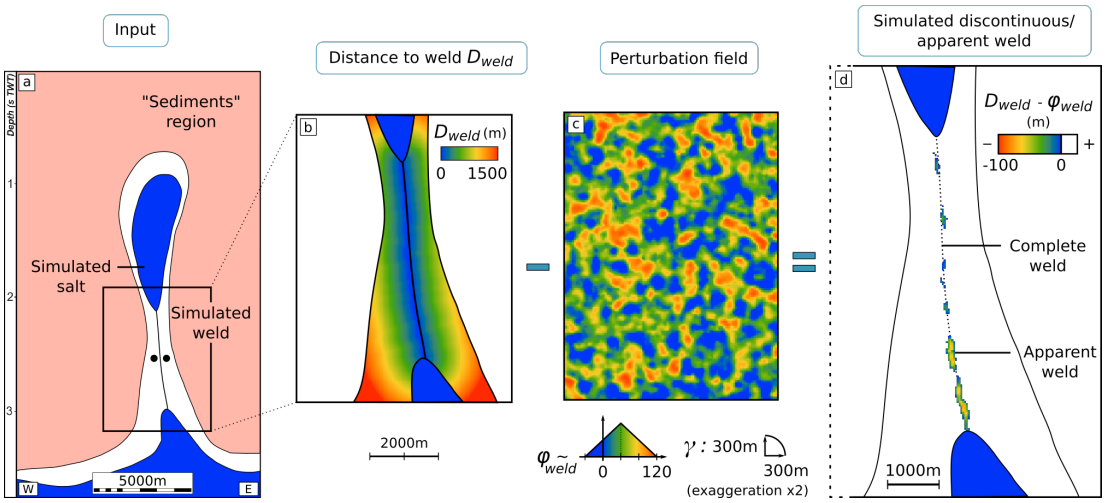

Figure 3.9 – Simulation of discontinuous/apparent welds using the ODSIM method [Henrion et al., 2010]. (a) Input data: the already extracted weld surface. (b) Euclidean distance D_{weld} to the weld surface. (c) Perturbation field φ_{weld} used to truncate D_{weld}. (d) The weld is defined by the initial weld surface and all the pixels for which $D_{weld} - \varphi_{weld} \leq 0$ (which are considered to be salt).

is interpreted as a complete weld. The cumulative probability of drawing a negative value corresponds therefore to the probability of modeling (locally) a complete weld. The mean and range of the distribution then controls the average weld thickness that is simulated. The variogram model controls the spatial continuity of the simulated salt lenses: the larger the variogram ranges, the more continuous the simulated salt lenses.

Simulation parameter choice The choice of the distribution model is relatively straightforward. The ratio between complete versus incomplete weld portions to simulate determines the cumulative probability of drawing respectively a negative or a positive value. Then, the positive value domain is determined depending on the average and maximum weld thickness to simulate. The choice of the variogram model is more difficult and essentially depends on the application the model is intended for. As an example, for seismic imaging applications, it may be interesting to use very large variogram ranges, as the presence of multiple small scale salt lenses can make the wavefield dramatically more complex. On the contrary, for estimating reservoir sealing and potential in place volumes, it is necessary to introduce layer scale details in the model, and thus the variogram ranges may be much shorter. More generally, this problem is similar to the inference of the variogram model of the field φ discussed in section 2.4.4, and the two variogram models should be of similar scale, as they are part of the same model.

The choice of the simulation parameters thus does not present much difficulties. Their inference is, however, not as easy as it would require having data. Seismic imaging is not likely to provide any information about the weld thickness (as we are investigating apparent welds), and when borehole data would be available, it is unlikely to be in a sufficient quantity. Outcrops may eventually provide 1D analog profiles of welds, if their condition is good.

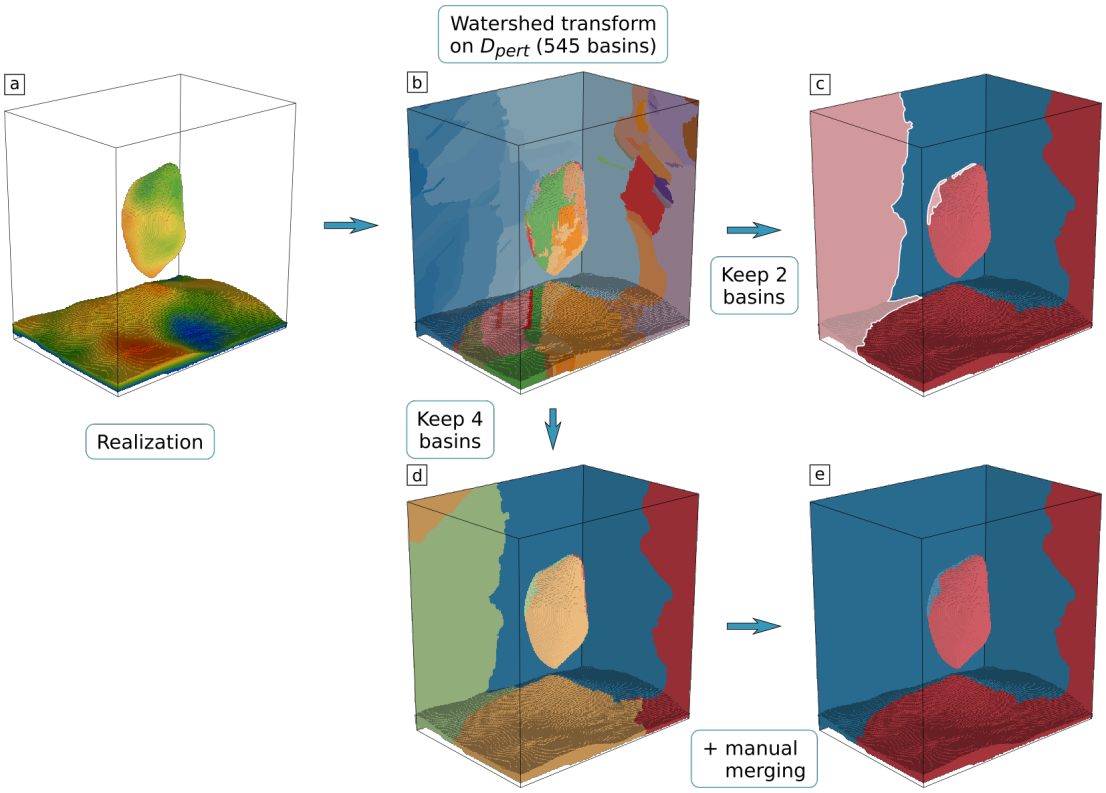

Figure 3.10 – Watershed transform limitations. (a) Input scalar field D_{pert}. Watershed transform (b) without filtering, (c) with filtering preserving only the two most significant maxima (in height), and (d) with filtering preserving the four most significant maxima (in height). The whitened region in (c) is the part of the cube which is not partitioned correctly as compared to the target binary partition (e), obtained after manually merging the 4 basins in (d).

3.5.2 Watershed transform limitations and potential solutions

One of the major drawbacks of the watershed transform is its sensitivity to local variations within an image. We have presented in section 3.4.2 the method introduced by Najman and Couprie [2006] that we use to filter the unwanted local maxima in the D_{pert} field. It is not possible, however, to ensure that the binary partition obtained after filtering actually corresponds to the target minimum ridge (figure 3.10.c). This is due to the very large number of drainage basins introduced by the perturbation φ (e.g., the realization presented in figure 3.8.a contains 545 basins for about 8,3 millions voxels, figure 3.10.b).

Manual editing A first solution to this problem consists in preserving more than two local maxima (figure 3.10.d). Tests on various models have shown that preserving five to ten drainage basins seems sufficient to systematically preserve the weld surface. A quick visual inspection of the model then permits to determine how the last basins should be merged (figure 3.10.e).

Using boundary conditions A close look at figure 3.5.c shows that one of the factors impacting the number of local extrema in the image is the reduced pixel neighborhood

along the image boundaries. Very close pixels can form independent extrema, resulting in independent drainage basins. Therefore, a numerical solution consists in introducing artificial local maxima in the image. By adding a "pixel" with a very high weight to the image graph and connecting it to all the pixels of a given boundary, it is possible to ensure that a single drainage basin will be associated to all the pixels in contact with the boundary. This solution is straightforward in 2D, but some complications arise in 3D: it requires to determine along which cube faces these local extrema should be introduced. In order to solve this problem automatically, we need to introduce some prior information in the segmentation process.

Prior information about weld orientation If some information about the regional tectonic context is available, it can be used to infer the general orientation of the weld (section 3.5.4). In the absence of such prior knowledge, the weld orientation can be estimated using the pseudo-distance field D or the simulated salt bodies. As already stated, the field D defines the reference position of the weld. This field is very smooth (by construction) and much less prone to the presence of local maxima as compared to D_{pert}. Segmenting the field D can thus provide some information about how to merge the different local maxima in D_{pert}. An alternative consists in estimating the principal orientations of the simulated salt body: a principal component analysis of the point cloud defining the salt bulb can provide an information about the *a priori* weld orientation. This information can then be used to separate the seismic image into two parts, defining the merging rules to use for the local maxima.

3.5.3 Imposing the weld position and thickness

It is possible to have some prior information about the weld geometry. First, when well data are available, we potentially have well markers indicating the presence of the weld. Well data can also demonstrate the presence of an incomplete (or apparent) weld. Then, a seismic interpreter may want to impose the position of a weld in a seismic image or incorporate an apparent weld in the model. Such elements can be integrated in the modeling, in two steps: we first determine the weld surface, and then (if necessary) we simulate a salt volume around it.

Imposing the weld position is not as easy as imposing the salt boundary position. This is due to the fact that it is defined as a ridge, and not as a level set, of D_{pert}. We consider that we take as input a point set (which contains the well markers and the manual seismic picks to honor). The aim is to obtain a scalar field with a minimum ridge crossing through each data point. Two solutions can be considered: we can either reinterpolate the D_{pert} field to match these conditions, or define a new scalar field (a Euclidean distance field as presented later).

Reinterpolation of the D_{pert} field When modifying D_{pert}, we do not want to modify the salt boundary. The points defining the salt boundary (i.e., satisfying $D_{pert} = 0$) are therefore used as conditioning data together with the input weld point set. The value of all these points is fixed to 0. Then, we need to "guide" the interpolation and define the polarity of the field. To do so, we fix the 1 level set of D_{pert} (we impose that these points keep their original value). Finally, we impose that all the points that are located

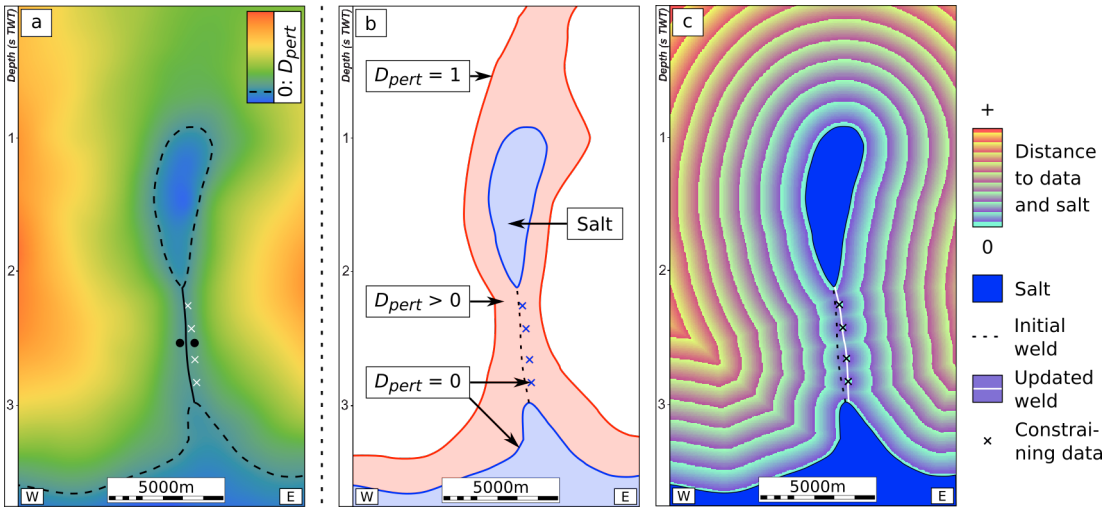

Figure 3.11 – Integration of well markers and seismic picks in weld modeling. (a) Input scalar field D_{pert}, initial weld location (black line), and manually picked samples (white crosses) used to constrain the weld position. (b) Constraints used for updating the D_{pert} field through interpolation. (c) Euclidean distance to the constraining data and the simulated salt bodies, and updated weld position (white line) extracted by watershed transform and maxima filtering.

between the 0 and 1 level sets of D_{pert} have a strictly positive value. This ensures that the points already fixed to zero actually belong to the minimum ridge. Once all these constraints have been set, we interpolate the D_{pert} field [e.g., Mallet, 1992, Irakarama et al., 2018, Renaudeau et al., 2019]. We did not test this approach, due to the lack of time and appropriate tools. Handling inequality constraints requires to solve iteratively the system defined by the interpolation constraints, and the number of iterations tends to increase with the number of constraints to honor.

Definition of a new distance field The second solution is geometric. To obtain a scalar field with minimum values at the constraining data location, we compute the Euclidean distance to the constraining point set (figure 3.11.c). In practice, we compute the distance to the data points and the simulated salt bodies, otherwise the distance field behavior is not properly constrained beyond the last data points. The updated weld surface can then be extracted using the watershed transform. The final weld is no more smooth: it consists of a series of straight lines (or triangular surface patches in 3D), producing results which are geologically less consistent than with the interpolation.

Control of the weld thickness It is not possible to have an exact control on the weld thickness. However, it is possible to integrate lithological information about the presence or absence of salt, and to locally influence the weld thickness. The integration of lithological information in the ODSIM method is described in Henrion et al. [2010]. It consists in adding inequality constraints during the simulation of the perturbation field. As an example, to impose the presence of salt at a given location along the surface, the simulation must ensure that $\varphi_{weld} > D_{weld}$. On the contrary, for locally imposing a complete weld, the simulation must honor the condition $\varphi_{weld} \leq D_{weld}$. Note that the

integration of inequality constraints in the SGS requires the use of a specific sampling method, such as a Gibbs sampler (section 2.3.5). In addition, even if it is not possible to directly impose the weld thickness, it is possible to influence it to match more or less an observation. As stated in section 3.5.1, the scalar field φ_{weld} values approximately represent the half weld thickness along the weld surface, due to the spatial correlation. Imposing the value of φ_{weld} at a given location provides therefore a loose control on the local weld thickness.

3.5.4 Integrating prior geological knowledge

We may want to incorporate other data types than well markers or manual interpretations. Some indirect sources of information can also provide useful constraints during the modeling. As an example, linear salt diapirs (i.e., salt walls) usually develop coherently with the regional tectonic orientations. Similarly, welds are often associated with fault systems [Rowan et al., 1999]. Some knowledge about regional tectonics may therefore be interesting to constrain the weld orientation. The integration of such information in the modeling of welds is, however, not straightforward. It can either be integrated upstream, during the definition of the fields D and φ (as discussed in section 2.4.3), or in the filtering of the watershed drainage basins. This last solution requires, however, to adapt the local maxima filtering strategy .

3.5.5 Definition of a weld surface parameterization

The truncation rules used to limit the weld extension, as defined in section 3.4.3, introduce sometimes holes in the weld surface. This happens when the weld surface locally goes beyond the edge of the salt bulb (i.e., the first criterion is no more respected) or when it locally leaves the uncertainty envelope (i.e., the second criterion is no more respected). It may be possible to define some post-processing to repair these holes, but it seems difficult, *a posteriori*, to define criteria that ensure a proper and automatic truncation of the semi-infinite weld surface.

Another approach that could be considered to define the weld extent consists in defining a parametric surface on the semi-infinite weld surface. Parametric surfaces are well-known in computer-aided design and have already been used in numerous geomodeling applications [e.g., de Kemp, 1999, Lallier and Clausolles, 2017]. A parametric surface is defined by a parametric equation which have the general form $\vec{p}: \mathbb{R}^2 \to \mathbb{R}^3$. In practice, for finite extent surfaces, it is often defined as $\vec{p}: [\![0,1]\!]^2 \to \mathbb{R}^3, (u,v) \to (x,y,z)$. The u and v parameters are built from the already defined semi-infinite weld surface.

Once the (u,v) parameterization is defined, different strategies can be used to define the weld extension. The simplest one consists in defining it as u and v intervals, which is more or less similar to the vertical truncation rule defined by the first criterion on traces (which is rather arbitrary). More generally, using a surface parameterization offers a more formal frame to define the weld visibility rules. We can therefore imagine using concepts from the mathematical morphology field to define weld extent criteria that better reproduce observed weld geometries. This would, however, introduce an explicit structure to handle in the model, which may limit the possibility to perturb later the weld position.

3.5.6 Morphological aspects about the weld modeling

Another morphological aspect about the modeling of welds which has not been treated yet concerns the junction between the weld and the salt bodies. In this chapter, we have mainly considered the modeling of welds as a "by-product" of the salt body modeling: a weld is defined using the scalar field D_{pert}, which is initially used to define the salt boundaries. This definition simulates a weld which is systematically consistent with the simulated salt bodies.

The D_{pert} field is mainly generated, however, depending on the target salt bodies, without considering the potential necessity of integrating a weld. It results in a relatively unrealistic junction between the weld and the base salt layer (see figure 3.8 for example): the base layer is relatively smooth and seems to truncate the weld surface. From a geological point of view, we expect the salt boundary to locally uplift and progressively pinch until transforming into the weld strictly speaking. The same remark holds equally true for the contact with the salt bulb.

A solution to correct this could consist in applying a morphological operator to the salt boundary after having extracted the weld, to locally reshape it. As an example, defining displacement profiles might be a solution. This has already been proposed for providing a kinematic control of the fault displacement during modeling [e.g., Godefroy et al., 2018]. The same approach can be considered in our case, with the definition of "displacement" profiles along and orthogonal to the weld surface to describe the uplifting of the salt boundary along the weld trace.

3.6 Conclusion

I introduced and implemented a method to model secondary salt welds from stochastically simulated salt bodies. Salt welds directly impact the sediment strata connectivity. Their representation is therefore necessary to build a valid boundary representation of the subsurface. Based on the implicit salt body representation proposed in chapter 2, the proposed method automatically detects the invalid scalar field configurations (i.e., the presence of multiple disconnected salt bodies) and determines the weld surface. One step still requires, however, some manual interaction: the definition of the two blocks separated by the weld surface.

The method initially generates complete welds. I presented how to simulate remnant salt along the weld surface to simulate incomplete and apparent welds. As for the modeling of salt bodies (chapter 2), I discussed the integration of prior information, and especially punctual information about the weld presence and content. From a general point of view, integrating prior knowledge is more complex when modeling welds than when modeling salt bodies. This is due to the fact that the weld geometry is constrained by the scalar field representing the salt bodies. Prior information should therefore be introduced during the definition of the pseudo-distance field D, otherwise it may require to update the scalar field D_{pert} or to define a new one.

The definition of the weld extent is based on two simple visibility criteria, which have proven to be limited in use. To improve it, I discuss a way to define more formally the weld surface using a parametric representation. This representation would permit the definition of morphological operators for both defining the weld extent and locally

reshaping the salt bodies near the weld to improve the geometrical consistency of the junction between the weld and the salt bodies. Handling explicit surfaces would, however, limit the flexibility of the modeling as their perturbation is more prone generate local invalid configurations (such as self intersections) than implicit methods.

Appendix 3.A: Constraining the probability of generating disconnected salt bodies automatically

Note: This appendix is an extension of chapter 2, but is presented here as it requires various notions introduced in this chapter.

In section 2.4.2, we discussed the necessity of controlling the values of the scalar filed D within the stem of the uncertainty envelope to influence the probability of generating single or disconnected salt bodies. We propose here a method to automatically impose the D values locally in the uncertainty envelope to honor such probability. Note that the method provides a "weak" control on this probability, as it depends on multiple factors (the D values within the stem, but also the length of the stem for example). The method can also be used more generally to "guide" the interpolation as it provides additional constraining data for interpolating D. The method consists in a "preprocessing" step performed before the interpolation of D. We extract a point set that is then used as constraining data during the interpolation.

Input data We start from the uncertainty envelope boundaries, and the probability p that we want to impose along the envelope stem axis (p represents the probability of generating disconnected salt bodies).

Imposing equal probabilities along the envelope medial axis We consider for the moment that we want to impose $p = 0.5$ (which is a simplified case). To define the point set to extract, we compute the two Euclidean distance fields: the distance D_{int} to the internal envelope boundary, and the distance D_{ext} to the external envelope boundary (figure 3.12, top left). We only consider these fields within the uncertainty envelope. They can be computed using e.g., an Euclidean distance transform.

We define the point set to extract as the maximum value edges in the field D_{min}, defined as $D_{min} = min(D_{int}, D_{ext})$. For the specific case of $p = 0.5$, these points form the envelope medial axis (figure 3.12, bottom, case $D_{min,0.5}$). The point set can then be extracted using the watershed transform (section 3.4.1). To ensure that the resulting point set does not contain irregularities (due to the sensitivity of the watershed transform), it is necessary to perform beforehand a local minima filtering step (section 3.4.2) to preserve only the four most significant local minima (corresponding to the salt base layer, the salt bulb, and the two weld blocks). Note that a small post-processing step is required to remove the unwanted vertical edge present between the two weld blocks above the salt bulb. This step can easily be implemented in the point extraction process, by using inclusion relations and depth conditions (similarly to the blob filtering strategy presented in section 3.3.1).

Imposing an arbitrary probability of generating welds A difficulty arises when we want to impose a probability different from 0.5 using the above method. Indeed, the point set we extract corresponds to the uncertainty envelope medial axis. We therefore constrain values not only in the envelope stem, but also everywhere else (e.g., between the top of the *Salt* bulb and the top of the envelope). Imposing a value different from 0.5

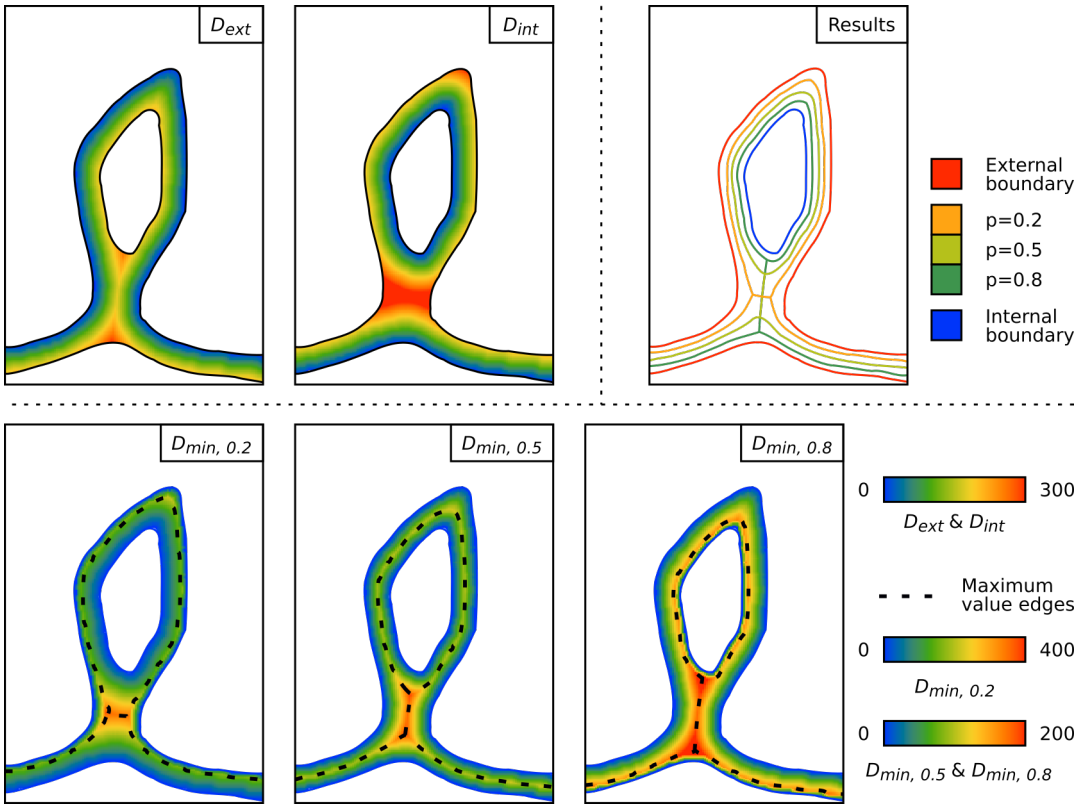

Figure 3.12 – Imposing the probability of generating disconnected salt bodies. Top left: the two initial distance fields D_{int} and D_{ext}. Bottom: the $D_{min,p}$ fields obtained for three different probabilities p (from left to right: $p = 0.2$, $p = 0.5$ and $p = 0.8$), and the maximum value edges to extract (dashed curves). Top right: the three constraining data sets superimposed on the same image with the uncertainty envelope.

along the medial axis would introduce a distortion of the D field, which is not desirable. To overcome this limitation, we use "variable speed" Euclidean distance transforms. We now consider the field $D_{min,p}$, depending on p and defined as (figure 3.12, bottom)

$$D_{min,p} = \min(p \times D_{int}, (1-p) \times D_{ext})$$

To explain with an analogy, it is equivalent to simulating the advance of two wavefronts, starting respectively from the internal and external envelope boundaries, and propagating at different velocities. The field $D_{min,p}$ then corresponds to the first wave arrival time. As previously, we extract the maximum edges in $D_{min,p}$ using a watershed transform and a local minima filtering strategy. The extracted point set contains all the points where two wavefronts enter in contact. This includes the case when the internal front meets the external front, but also when two parts of the external front (coming from each side of the envelope stem) enter in contact. So, we extract in the same time points within the envelope stem, and a "shifted" medial axis in the other envelope parts (figure 3.12, top right).

Chapter 4

Stochastic seismic interpretation for the characterization and sampling of imaging uncertainties

Contents

Abstract This chapter presents an application of the salt modeling workflow introduced in chapter 2. We investigate the characterization and the sampling of the uncertainties underlying the imaging of secondary salt diapirs in 2D. We use a rough *a priori* definition of the uncertainty to generate multiple equiprobable salt body interpretations, that we populate with velocities. One of the velocity models is extracted from the set and used to simulate a seismic acquisition. The other ones are used to migrate these seismic data, forming a set of distorted seismic images. The computation of some basic statistics over all the realizations, such as the mean and standard deviation, either directly on the seismic images or on derived seismic attributes, highlights the average image response to any input velocity model and the image parts which are most sensitive to velocity variations.

We apply this methodology to two different seismic data sets obtained by imaging respectively a salt stock and a teardrop diapir. The comparison of the statistics derived from both data sets shows that: (1) it is possible to infer the type of diapir from stochastically interpreted seismic data, and (2) these statistics significantly reduce the localization of the uncertainties as compared to the input prior used to generate the velocity models.

4.1 Introduction

Numerous advances in acquisition design and equipment, imaging algorithms and computing infrastructures now allow for the generation of high quality 3D seismic images in complex geological settings. Regular reviews of the existing technologies and practices [e.g., Leveille et al., 2011, Jones and Davison, 2014] highlight, however, that challenges still remain. These include the difficulty to suitably represent the geologic structures and anisotropy, to predict diagenesis and cap rock formation in salt, and to understand the wave behavior in the vicinity of salt (complex travel paths, reflection vs. refraction, mode conversion, etc.) [Jones and Davison, 2014]. One of the consequences of these different pitfalls is the presence of large lateral velocity variations in the vicinity of salt bodies. These variations are not handled by time migration methods. They require the use of a depth migration method, and thus the definition of a subsurface velocity model whose accuracy is essential to ensure producing a usable seismic image.

Due to the difficulties listed above and the necessity to define an accurate velocity model, seismic imaging in the presence of salt bodies is often an iterative time-consuming process involving successive phases of data migration and manual picking of the salt boundaries for updating the velocity model [e.g., Jones, 2015]. Dellinger et al. [2017] showed that, even in almost perfect conditions (i.e., knowing the true background sediment velocity model and the exact salt velocity), interpreting the actual salt boundary position remains subject to large uncertainties, especially in poorly illuminated areas.

The topic of structural uncertainty characterization during seismic imaging has been raised for a long time and discussed by numerous authors [e.g., Landa et al., 1991, Abrahamsen, 1993, Thore et al., 2002, Pon and Lines, 2005]. Various approaches have been considered. Some authors derive formulas to describe the positioning errors in simple model configurations. For example, Bube et al. [2004a,b] describe the impact of velocity and anisotropy modeling on structural uncertainties. Pon and Lines [2005] describe and quantify the effect of erroneous migration velocity on the resulting horizon shapes and depths. Other authors have proposed methods to estimate imaging uncertainties in concrete situations. Thore et al. [2002] propose a thorough review of the uncertainty sources along the imaging workflow to determine uncertainty envelopes around the structural model elements. Osypov et al. [2013] apply remigration to the model elements to determine such envelopes. Similarly, Weinzierl et al. [2016] use the concept of Fresnel zone to define uncertainty envelopes around faults. Fomel and Landa [2014] use the principle of velocity continuation [e.g., Fomel, 2003] to determine the sensitivity of structures to velocity variations, and use a range of migration velocities to determine time and position windows from this sensitivity around each seismic event.

Once the magnitude of the uncertainties has been determined, different strategies can be considered to estimate the structural uncertainties. For example, Thore et al. [2002] propose to use stochastic modeling to sample the structural uncertainties. Grubb et al. [2001] use a set of velocity models to perform multiple migrations and collocate the seismic events in the migrated images. Similarly, Protasov et al. [2017] use a focusing criterion to define a weighted sum of the different images and derive a final image.

In this chapter, we investigate the impact of salt-related structural uncertainties within the seismic imaging loop. We propose an approach to characterize how, at a given iteration of the imaging loop, the variability of the salt boundary interpretations that can be drawn from an ambiguous PSDM seismic image affect the velocity model updating and the resulting remigrated seismic image at the next iteration. The long term objective of this work is to move toward the integration of uncertainty quantification during automatic velocity model updating in seismic imaging.

The approach is inspired by the works of Grubb et al. [2001] and Thore et al. [2002] and is based on stochastic seismic interpretation. Rather than trying to define a "best possible" salt boundary geometry, we start from a rough *a priori* estimation of the uncertainties and we use the salt modeling method presented in chapter 2 to generate a set of equiprobable structural interpretations. We use this set of interpretations to define as many velocity models, that serve to remigrate the seismic data. We thus obtain a set of depth migrated seismic images, all of which being somehow distorted. To characterize the sensitivity of migration to structural variations in the velocity model, we perform a statistical analysis of various seismic image properties. The underlying idea is simple: a seismic image is the combination of two contributions: one from the seismic data and one from the migration velocity model. Considering a set of images obtained from the same data but different velocity models should thus allow to increase the data contribution as compared to the individual model contributions. The statistical analysis can be performed directly on the seismic amplitude, or on derived seismic attributes. It allows for the integration of multiple image properties in the analysis, and especially the position, the amplitude and the focus of the reflections. Among the interesting

statistical measures, the mean seismic image illustrates the "average" behavior of the data set to any input velocity model, and the computation of the standard deviation highlights which image parts are most sensitive to velocity migration changes.

The first section of this chapter presents the overall methodology: how we generate the structural models, how we populate them with velocities and the imaging strategy we use. The second section develops qualitative and quantitative results illustrating the impact of salt-related structural uncertainties on seismic imaging. It starts by introducing some qualitative indicators that can help link specific errors in the migration velocity model to specific image patterns, and then develops the results of the statistical analysis. The last section provides further elements of discussion and some perspectives for future works.

4.2 Methodology

4.2.1 Overview

The generation of a seismic image requires performing a migration of the seismic data. This step is computationally intensive, so generating a large set of seismic images requires performing a prohibitive quantity of migrations. For these reasons, we only work with 2D seismic images in this chapter. Moreover, we work with synthetic seismic data and images. It provides a better control when analyzing the results: the data are noise free, we control the overall imaging process, and we have the reference solution to compare our observations.

The depth migration requires to define a set of detailed parameter fields [Jones, 2015]. The nature of the parameter fields to consider depends on the selected migration algorithm. The migration scheme we use is detailed later (section 4.2.4.2), but it is important to note here that we only model the P-wave velocity. We assume isotropic velocity fields and a constant density independently of the rock nature. We thus estimate that the reflectivity model is controlled by the P-wave velocity. These are strong assumptions, but we consider them as acceptable as we are investigating first-order structural uncertainties. In addition, Dellinger et al. [2017] have shown that even such "simple" imaging conditions are challenging to handle.

4.2.2 Creation of a set of structural interpretations

Input data The modeling support is a 2D grid of 195 by 305 cells. The cells have a dimension of 20 m by 20 m. The overall studied section is thus 3.9 km long for 6.1 km deep. The uncertainty envelope describing the *a priori* uncertainty is defined by a manual picking of a general diapiric shape (figure 4.1.a). The associated *Salt* region contains a basal layer and an isolated bulb, allowing for the simulation of both salt stocks and teardrop diapirs. The pseudo-distance field D (figure 4.1.b) is interpolated as described in section 2.2.2, using the uncertainty envelope points as constraints, and a few additional points set to 0.5 between the two *Salt* volumes, to impose an approximately equivalent probability of generating connected and disconnected salt bodies.

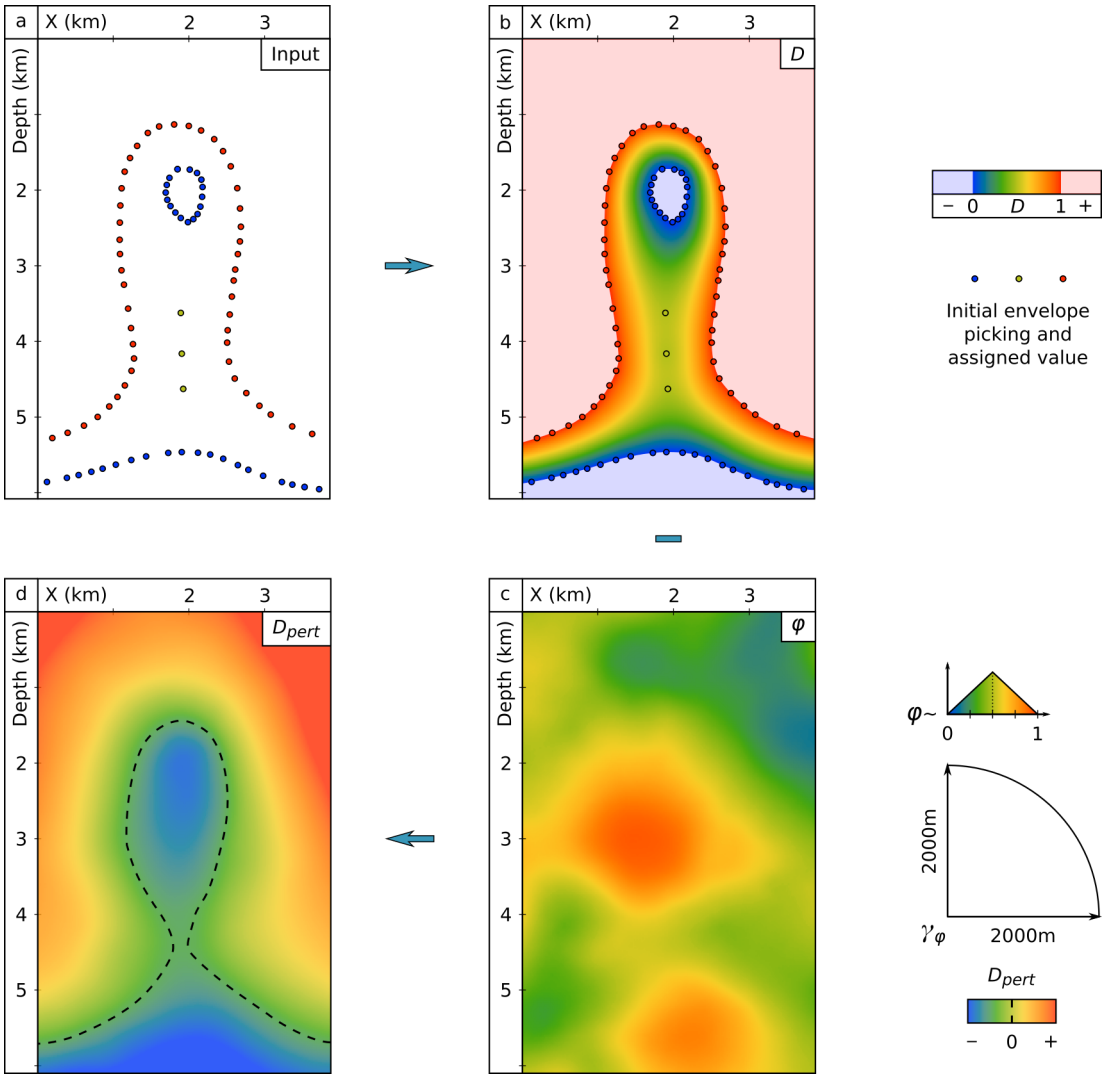

Figure 4.1 – Generation of the salt structural models. (a) Input manual picks used to define the uncertainty envelope. (b) Interpolated field D. (c) A perturbation field φ. (d) The corresponding perturbed distance field D_{pert} and simulated salt boundary (dashed curve).

Simulation parameters The perturbation fields φ_i (figure 4.1.c) are generated using a triangular distribution model with a mode at 0.5, and an isotropic Gaussian variogram model with principal ranges of 2 km. Such large ranges generate very smooth salt boundaries ($D_{pert,i}$, equation 2.1, figure 4.1.d). They were chosen to limit the complexity that rough boundaries locally introduce on the wavefield. We can therefore focus on the impact of the large scale salt structures.

4.2.3 Velocity modeling

We use two types of velocity models in this chapter. On the one hand, we use finely layered velocity models for seismic modeling. The aim is to reproduce a subsurface model as realistic as possible when generating the synthetic seismic data. On the other hand, the use of such detailed velocity models is not common when performing migra-

tion. Migration velocity models are most commonly smooth, resulting, e.g., from an inversion procedure. Therefore, we use smoothed approximations of the finely layered velocity models for performing the migrations. For the moment, we consider only the generation of the layered models, the smooth models will be detailed with the migration scheme (section 4.2.4.2).

4.2.3.1 General velocity model settings

As already stated, we only model the P-wave velocity, which is assumed isotropic. We consider that we know the exact background sediment velocity model V^{sed}. The sediment velocity ranges from roughly 1950 to 4350 m.s^{-1} and globally increases with depth. The salt velocity V^{salt} is assumed constant at 4480 m.s^{-1}. This implies that we assume a constant lithology within salt bodies (slightly impure halite). This is a strong assumption, as a wrong prediction of the salt lithology may drastically alter the resulting image (see e.g. the example presented in Jackson and Lewis [2012]), but we focus primarily on the impact of salt geometry rather than lithology. Dellinger et al. [2017] showed that even such simple configurations (i.e., with constant salt lithology) are already difficult to handle if the geometries are convoluted. To represent the simulated salt bodies, we overlay the background sediment velocity model with the salt velocity to obtain the final velocity model V. For any pixel x in the velocity model, its velocity is given by

$$V(x) = \begin{cases} V^{sed}(x) & \text{if } D_{pert}(x) > 0, \\ V^{salt} & \text{else.} \end{cases} \tag{4.1}$$

4.2.3.2 Velocity models for wave propagation

Building finely layered velocity models To generate realistic synthetic seismic data, we simulate a fine layering within the sediments (figure 4.2). This is done by creating a constant per layer velocity model V_l^{sed} (figure 4.2, second column), and applying a geostatistical perturbation ϕ to it (figure 4.2, third column). The perturbation is generated using an SGS, with a Gaussian distribution model following $\mathcal{N}(0, 0.01)$, and a Gaussian variogram model with very large ranges along the layer planes (2000 meters), and a very short range orthogonal to the layers (100 meters). The resulting finely layered velocity model V^{sed} is defined as (figure 4.2, last column)

$$V^{sed}(x) = V_l^{sed}(x) \times (1 + \phi(x)). \tag{4.2}$$

Handling random weld position A difficulty arises, however, when welds are present in the structural model. Indeed, a weld introduces a discontinuity in the velocity model, and the position of this discontinuity varies from one realization to another. To handle varying weld locations, we use three different background sediment velocity models (V_{cert}^{sed}, V_{+}^{sed} and V_{-}^{sed}) that we combine depending on the output of the structural modeling workflow.

The first model V_{cert}^{sed} manages the sediment velocity in the *Sediments* region of the seismic image (where the interpretation is considered certain). Each pixel belonging to this region will therefore always have the same velocity from one realization to the next (figure 4.2, top row). The two other models (the V_{+}^{sed} and V_{-}^{sed} models) are

complementary and manage the velocity values within the *Uncertain* region, on each side of the simulated weld or diapir (figure 4.2, middle and bottom rows). As the velocity values must be consistent at the contact between the *Sediments* and *Uncertain* regions, the model V_{cert}^{sed} is used to constrain the generation of the two others.

Creation of the background sediment models We start by manually picking horizon data representing the stratigraphy of the V_{cert}^{sed} model (figure 4.2, S_{cert}, black lines). We then use the *Structure and Stratigraphy* workflow of the SKUA-GOCAD software [Emerson E&P Software, 2019] to generate a curvilinear grid whose cells are aligned with the stratigraphic layers (figure 4.2, S_{cert}, colored regions). This grid is used to define the layered velocity model $V_{l,cert}^{sed}$ and to perform an SGS for generating the field ϕ_{cert}. The first background velocity model V_{cert}^{sed} is then obtained using equation 4.2.

To generate the V_{-}^{sed} and V_{+}^{sed} models, we use the same workflow with additional data. We first introduce an unconformity in their stratigraphic models to ease the simulation of the folded and upturned geometry of the strata near the weld (figure 4.2, thick red line in S_+ and S_-). This erosion is placed such that it is not visible in the final velocity model: the strata truncations only occur in the *Salt* region and on the opposite side of the weld. Then, we use some of the horizon data of V^{cert} to enforce the stratigraphic continuity across the *Uncertain* region boundary (figure 4.2, black lines in S_+ and S_-). In addition, we add manually picked horizon data specific to each model (figure 4.2, dashed lines in S_+ and S_-). The output of the workflow is again a curvilinear grid for each model, grids which are used to generate the layered velocity models V_{+}^{sed} and V_{-}^{sed}, and the perturbation fields ϕ_- and ϕ_+. To ensure that the different perturbation fields are continuous across the external *Uncertain* region boundary, the values of ϕ_{cert} are used as constraining data in the *Sediments* region. Finally, each background velocity model V_{cert}^{sed}, V_{-}^{sed} and V_{+}^{sed} is transferred back to the seismic grid by pointwise value transfer from the curvilinear grids.

Combination of the background sediment models Once the three background velocity models have been created, they must be assembled to generate the different velocity models we will use in practice. For a given realization, we segment the field D_{pert} to create a binary partition P^+/P^- as described in section 3.4. We then associate each pixel to a velocity model to define its value. The pixels belonging to the *Sediments* region take the value of V_{cert}^{sed}. Within the *Uncertain* region, the pixels take respectively the value of the V_{+}^{sed} or V_{-}^{sed} models depending on which partition they belong to. Finally, the pixels belonging to the simulated salt body(ies) are set to the salt velocity value V^{salt}. Figure 4.3 illustrates the creation of two velocity models, for the cases of salt stock and salt weld. The final velocity model V from equation 4.1 can thus be rewritten as

$$V(x) = \begin{cases} V_{cert}^{sed}(x) & \text{if } D(x) \geq 1, \\ V_{+}^{sed}(x) & \text{if } D(x) < 1 \wedge D_{pert}(x) > 0 \wedge x \in P^+, \\ V_{-}^{sed}(x) & \text{if } D(x) < 1 \wedge D_{pert}(x) > 0 \wedge x \in P^-, \\ V^{salt} & \text{else.} \end{cases} \tag{4.3}$$

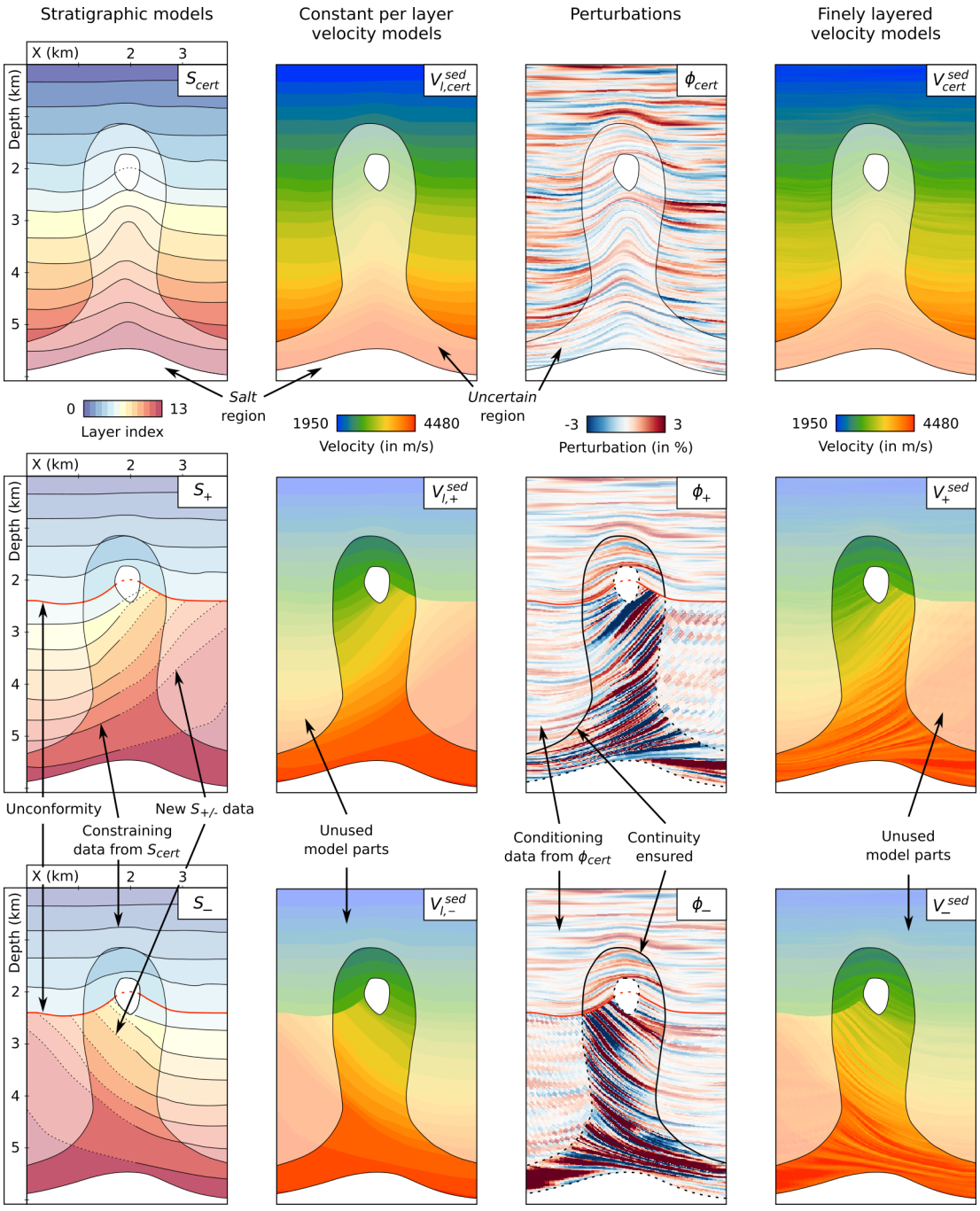

Figure 4.2 – Building of the different background sediment velocity models. Top: model used in the *Sediments* region. Middle and bottom: models used in the *Uncertain* region, on each weld side. Left: initial stratigraphic models. Middle left: constant per layer velocity models. Middle right: velocity perturbation. Right: final finely layered velocity models.

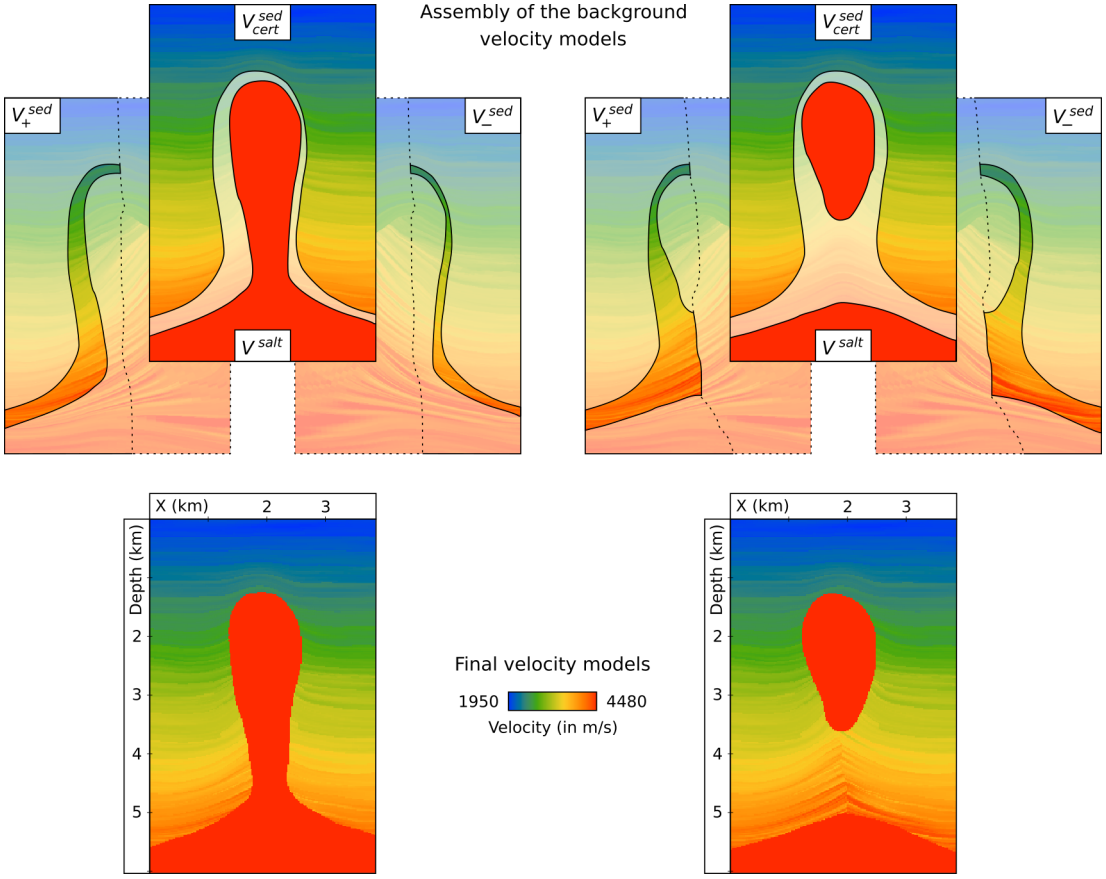

Figure 4.3 – Combination of the different velocity models. The velocity model associated to a given realization D_{pert} is the combination of four different ones: the three background sediment velocity models (figure 4.2, right column) and the simulated salt body velocity. Each pixel is associated to a given velocity model following equation 4.3. The dashed line separating the V_+ and V_- models indicates the limits of the P^+ and P^- partitions defined by the watershed transform of the field D_{pert}.

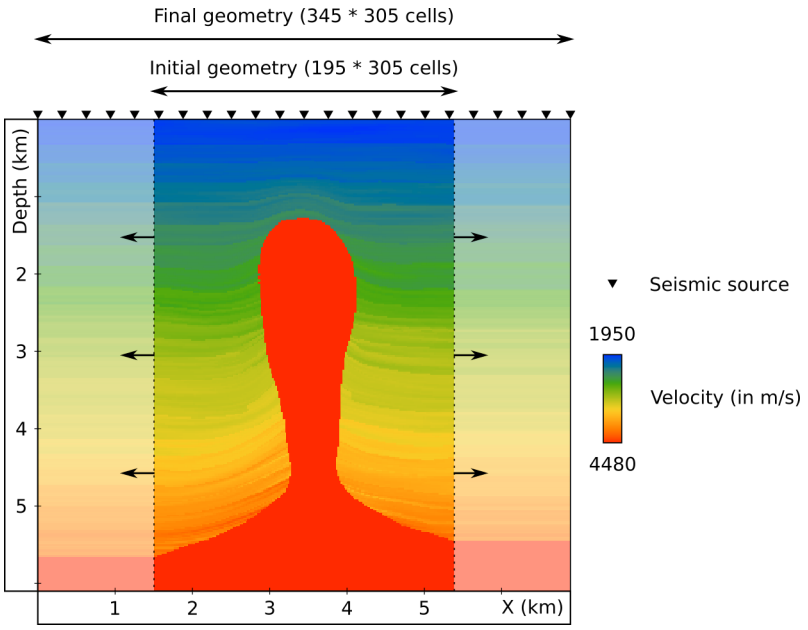

Figure 4.4 – Seismic modeling setup. The initial velocity model is extended to improve the illumination of the diapir flanks. We place 23 sources and 69 receivers (not shown here) evenly distributed at the surface.

4.2.4 Imaging strategy

4.2.4.1 Seismic modeling

In the next section of this chapter, we will use different sets of synthetic seismic data. We consider here the generation of one of these data sets. To perform the seismic modeling, we use the SIGMA software suite [ASGA, 2019] developed by Modeste Irakarama during his PhD within the RING team.

We perform an acoustic finite difference wave simulation assuming constant density, using the velocity-stress formulation described by Virieux [1984]. We use 8^{th} order difference operators in space and 2^{nd} order difference operators in time. We use perfectly matched layers boundary conditions [Collino and Tsogka, 2001] and the program runs on GPU [Micikevicius, 2009].

In order to ensure a proper illumination along the diapir flanks, we laterally extend the stochastically generated finely layered velocity model (figure 4.4). This is done by horizontally extrapolating the first and last traces. The final model geometry is 345 by 305 cells, with a spatial grid discretization h of 20 meters (both vertically and horizontally).

We use 23 seismic sources and 69 receivers, evenly distributed every 300 and 100 meters respectively. The source wavelet is a Ricker with a dominant frequency of 25 Hz. Each shot is slightly delayed (so that the wavelet is centered at 0.4 second) and is recorded at the receivers location for 5 seconds. The time discretization dt used for the wave simulation is determined by $dt = 0.2 \times \frac{h}{V_{max}} \approx 0.89$ millisecond. The result of the simulation is a set of 23 shot gathers. These gathers are resampled with a time step of 2 milliseconds and we mute the first arrivals (corresponding to direct waves, figure 4.5). This is done by defining a cone starting at $t_0 = 0.66$ second with a slope equal to the

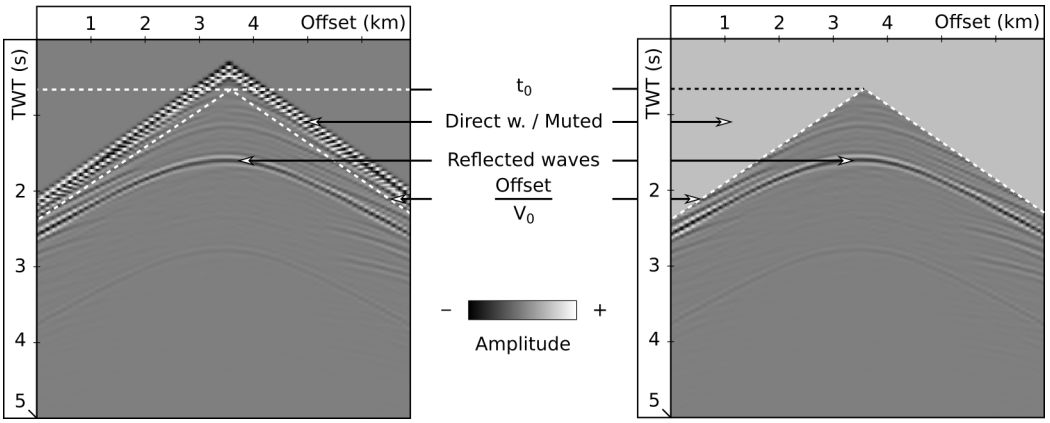

Figure 4.5 – Example of synthetic shot gather and direct wave muting. Shot gather from source 12 before (left) and after (right) first arrival muting.

offset divided by the minimum speed $V_0 = 2000$ m.s^{-1}, and muting any signal outside this cone.

4.2.4.2 Migration scheme

To generate a seismic image from the synthetic seismic data, we need to migrate these data. Due to the complex shape of salt bodies, we apply a pre-stack depth migration method. We chose the Reverse Time Migration [RTM, Baysal et al., 1983]. The RTM implementation follows the same rules as the wave simulation. We apply a post-processing to the RTM images to normalize the amplitude, which includes a high-pass filtering step and automatic gain control based on the illumination map. The different migration and processing algorithms we use are implemented in the SIGMA software suite [ASGA, 2019]. The RTM requires the definition of a velocity model that is given as input of the algorithm. As discussed previously, instead of using finely-layered velocity models we use smoothed approximations of these models for the application to be more realistic with current practices.

Definition of an equivalent velocity model The aim is to generate a new medium, whose response to seismic wave propagation is equivalent to the original one. A common way to do that consists in smoothing the elastic parameters defining the medium. In our case, the velocity is directly related to the Young's modulus E and the density ρ by

$$V = \sqrt{\frac{E}{\rho}}. \tag{4.4}$$

In the following, X^* denotes an equivalent medium of X. We are therefore looking for velocity model V^* equivalent to V, and we can use equation 4.4 to express V^* as

$$V^* = \sqrt{\frac{E^*}{\rho^*}}. \tag{4.5}$$

The density ρ is considered constant in our application, so $\rho^* = \rho$. Moreover, in 1D, we can approximate that $E^* = \langle \frac{1}{E} \rangle^{-1}$ [Backus, 1962], where the symbol $\langle \cdot \rangle$ denotes a

smoothing operator. Equation 4.5 thus becomes

$$V^* = \sqrt{\frac{1}{\rho\langle\frac{1}{E}\rangle}}. \tag{4.6}$$

By replacing E with equation 4.4 and using $\langle\rho\rangle = \rho$ (as it is constant), we finally obtain

$$V^* = \sqrt{\langle\frac{1}{V^2}\rangle^{-1}}. \tag{4.7}$$

Velocity model filtering The conclusion of equation 4.7 is that to define an equivalent velocity model V^* of V, we have to smooth $\frac{1}{V^2}$. In practice, we define the smooth (stochastically generated) velocity models exactly as their finely layered equivalents: as the combination of (smooth) background models. These background models V^{*sed}_{cert}, V^{*sed}_{-} and V^{*sed}_{+} are derived from V^{sed}_{cert}, V^{sed}_{-} and V^{sed}_{+} by smoothing them.

The smoothing is defined as a 1D (assumption of equation 4.6) vertical low-pass filter. This eliminates the high frequency variations and the sharp contrasts in the layered velocity models. We apply two successive first-order Butterworth filters (causal and anti-causal, e.g., Oppenheim et al. [1999], Hale [2009]). This is equivalent to applying a second-order Butterworth filter, but the forward-backward application ensures that the resulting filter has zero phase (and thus does not introduce delay). One of the advantages of the Butterworth filter is that its gain G is practically constant up to its cutoff frequency ω_c. The frequency spectrum of the filtered signal is thus (almost) unchanged in the filter bandwidth [Oppenheim et al., 1999].

Definition of the cutoff frequency We define the filter cutoff frequency as $\omega_c = \frac{1}{\lambda_{min}} = \frac{f_{max}}{V_{min}}$, with λ_{min} the shortest seismic wavelength we want to preserve in the model, V_{min} the lowest velocity in the model, and f_{max} the maximum seismic frequency we want to preserve when performing the seismic acquisition. A difficulty arises as the velocity increases with depth: the minimum wavelength λ_{min} to preserve is thus not constant in the model when the cutoff frequency of the filter is not adaptive.

In order to preserve the "exact" lowest wavelength everywhere in the model, we would need to use $V_{min} = 2000$ m.s^{-1} and $f_{max} = 50$ Hz (if we consider that the higher frequencies are negligible, given that the source Ricker wavelet has a dominant frequency of 25 Hz). However, given the sampling step of the velocity model (20 meters), we find that $\frac{1}{\lambda_{min}} = \frac{1}{f_{Nyquist}}$, where $f_{Nyquist}$ is the Nyquist frequency of the signal, i.e., the highest frequency that can be sampled in a signal given its sampling step. So there are no smaller wavelengths than λ_{min} in the model, and thus nothing to filter. As the depth increases, however, we know that λ_{min} increases and that we can filter using larger wavelengths.

The ideal solution would be to have an adaptive cutoff frequency for the filter, decreasing with depth, but we do not have the necessary tools to do so. In our application, we use a fixed cutoff frequency $\omega_c = 0.0125$ m^{-1}. For each velocity value (and thus more or less depth), we can compute the highest frequency preserved by the filter, e.g., 25 Hz at 2000 m.s^{-1}, 37.5 Hz at 3000 m.s^{-1}, and 50 Hz at 4000 m.s^{-1}. This introduces some bias for the near-surface part of the model, but we consider this approximation as

reasonable. It would require, however, to be tested by comparing the results obtained in the filtered and unfiltered media. This is a complex task that we do not perform here. Some elements to do so can be found in Irakarama et al. [2019], but as far as we know no "perfect" solution exists to date to perform this. Figure 4.6 illustrates the three smoothed background velocity models (central column) and their difference with the original layered models (right column).

4.3 Results

The previous section detailed the generation of the seismic images that we use in the following. In this section, we investigate how an erroneous interpretation of the salt boundaries in the migration velocity model affects a seismic image after remigration. We first investigate the uncertainties inherent to the imaging process (that is, independently from any migration velocity error). Then, we propose a qualitative description of the impact of specific interpretation errors on seismic images. Finally, we use stochastic seismic interpretation to compute quantitative indicators (in the form of statistics computed at the pixel scale) describing the sensitivity of seismic images to velocity migration errors.

4.3.1 Intrinsic seismic imaging limitations

Before investigating the impact of erroneous salt interpretations, it is necessary to characterize to which extent a seismic image can be interpreted, and the inherent underlying uncertainties. Indeed, seismic data processing faces challenges even in "ideal" conditions, due to different sources of physical limits. By "ideal", we mean that we know the exact velocity model and we assume the data are noise-free (conditions which are never verified in practice). Figure 4.7 illustrates such an example of ideal processing: the seismic modeling and the migration have been performed using the same velocity model (the one illustrated in figure 4.4). Despite this, some imperfections can still be characterized in the resulting seismic image.

The first reason is the limited seismic signal resolution, which is due to the limited recorded seismic bandwidth, intrinsic attenuation and varying degrees of illumination [e.g., Yilmaz, 2001]. It results in a limited image resolution, both vertically and laterally (figure 4.7, orange frames). In theory, migration is supposed to reduce the limit of resolution to a quarter of the dominant wavelength [e.g., Herron, 2011]. For a dominant source frequency of 25 Hz and a velocity range between 2000 $\mathrm{m.s^{-1}}$ and 4480 $\mathrm{m.s^{-1}}$, we find a limit of resolution ranging from 20 meters in the upper model part to 45 meters in the lower model part. In practice, we visually find, however, a limit of resolution ranging from about 70 meters to 120 meters. We do not explain the relatively large difference between theoretical and observed values for the moment. The second reason is related to the complex shapes that develop salt bodies (especially the steeply dipping structures and the allochthonous layers) and the resulting strong velocity variations. Coupled with poor illumination, these phenomena can produce artifacts such as shifted or tilted boundaries (figure 4.7, yellow frames). The last reason is more practical and is related to the non-uniqueness of the velocity model solution of the imaging problem and the simplifying hypotheses made by migration algorithms (even though this last

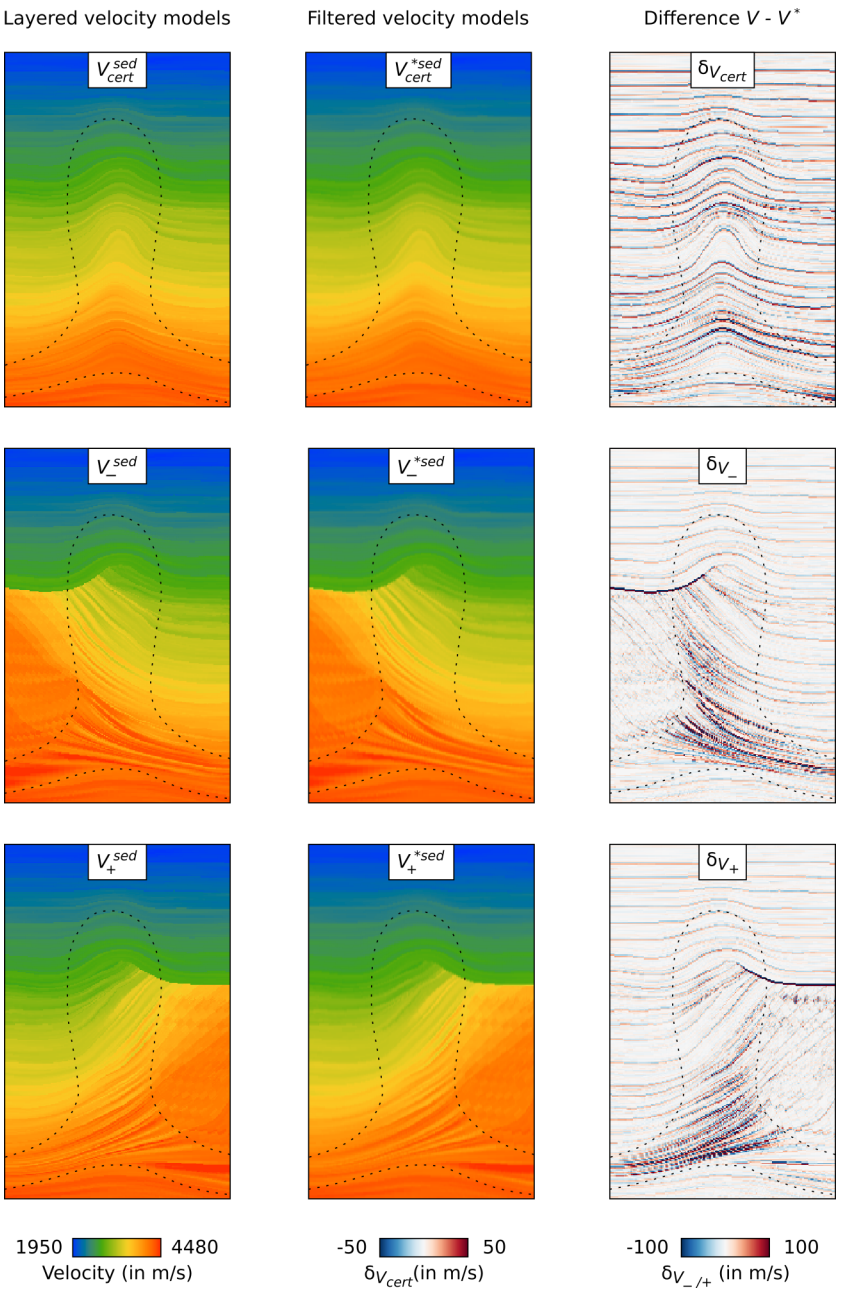

Figure 4.6 – Migration velocity models (central column), initial finely layered models (left column), and difference between both (right column).

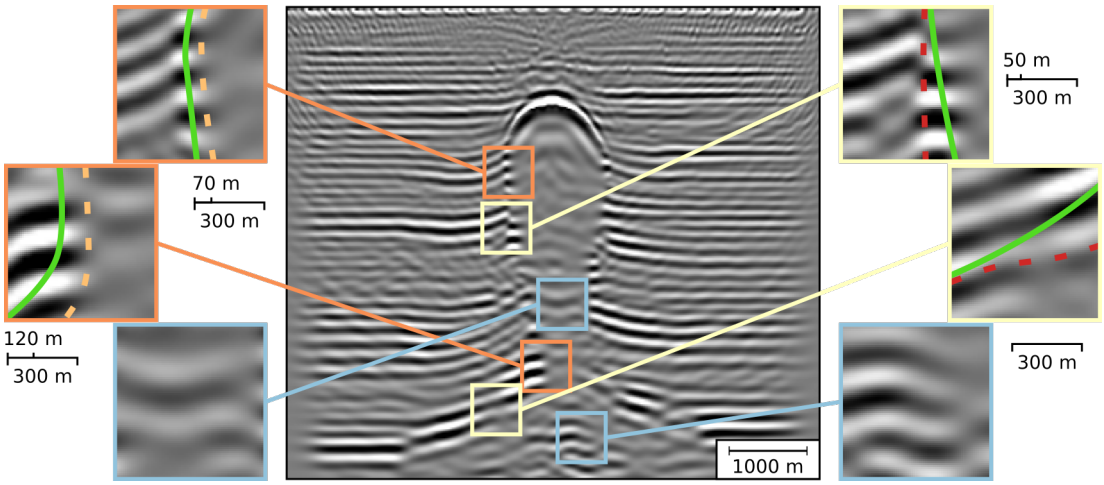

Figure 4.7 – Intrinsic imaging limitations. Seismic image obtained in "ideal" conditions (i.e., migrated using the exact, finely layered, velocity model from figure 4.4). Orange frames: limit of resolution. Yellow frames: shifted and tilted reflections. Blue frames: Spurious reflections resulting from incorrect energy repositioning.

point should have a 0limited impact in the cast of RTM). It may result in wrong energy repositioning during the migration, even when using the true velocity model (figure 4.7, blue frames) [e.g., Jones, 2015].

4.3.2 Qualitative impact of salt misinterpretation on seismic images

In this section, we try to characterize the impact of erroneous salt boundary interpretations on the quality of seismic images. The aim is to determine criteria that can be used later to detect interpretation errors on images.

4.3.2.1 Top of salt imaging

We first consider the impact of salt top boundary mispositioning on the resulting seismic images. This case is not very realistic for manual interpretations unless velocity errors exist above the salt top. It may happen, however, if the velocity models are stochastically generated. Moreover, it provides a first sense of the impact of salt interpretation errors in a simple reflection case. Two configurations can occur: the interpreter may either underestimate or overestimate the depth of the salt body. These two cases are illustrated in figure 4.8.

Predicting sediments instead of salt (figure 4.8.b) results in the presence of strong focused reflections (corresponding to the true salt boundary) that are not explained by the migration velocity model. These reflections appear at the true salt boundary position, as the migration velocity model is correct in all the domain crossed by the wave (figure 4.9, top). This means that even if we "forget" to put salt in the migration velocity model, we will observe these reflections in the seismic image. It is therefore easy to delineate the top of salt boundary on the image to update the migration velocity model. On the contrary, predicting salt instead of sediments (figure 4.8.c) leads to distorted images. The reflections corresponding to the true salt boundary location still appear on the images, however they are blurred and located deeper than their true

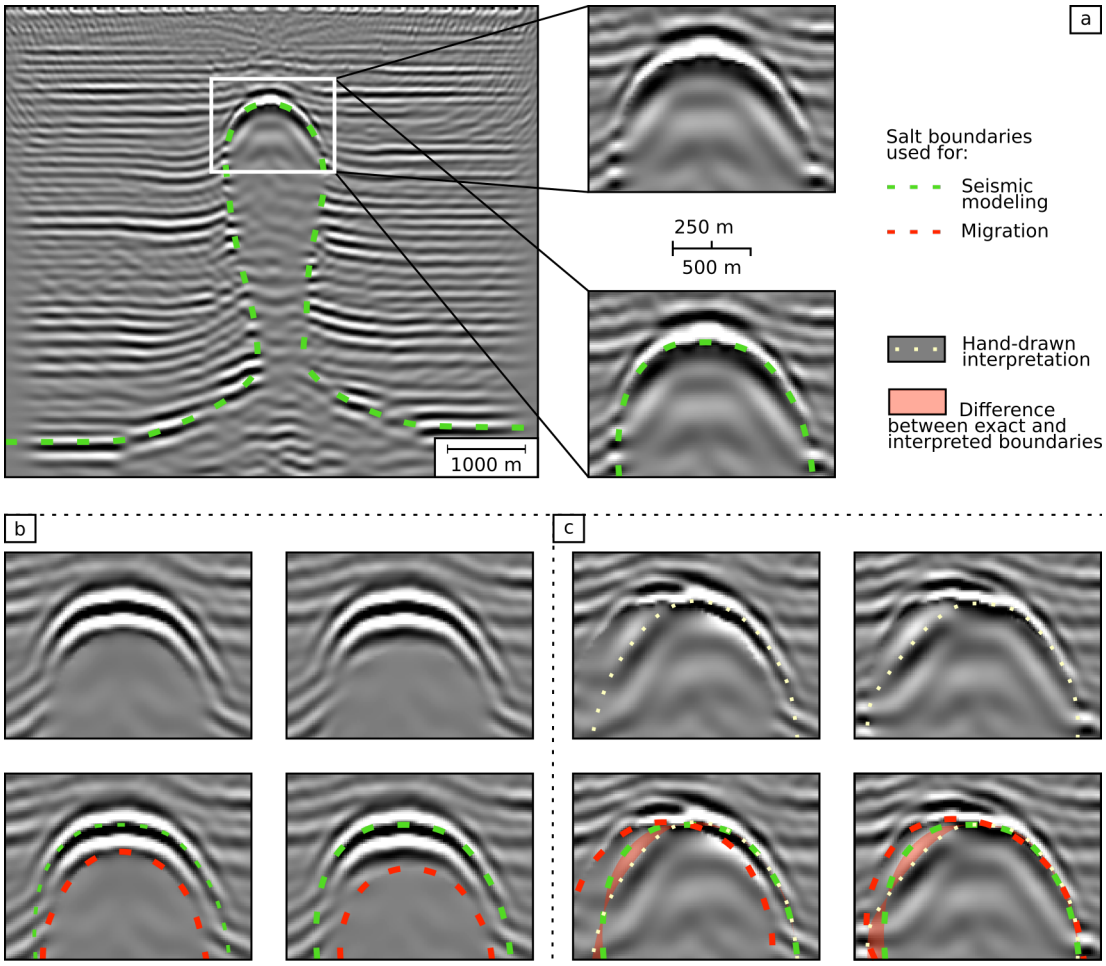

Figure 4.8 – Impact of errors on salt top boundary position on seismic images. (a) Reference image, obtained using the exact velocity model during migration. (b) Underestimating the salt volume results in "unexplained" (by the velocity model) strong focused reflections that are located at the true salt boundary position. (c) Overestimating the salt volume results in a distorted image, where the reflections corresponding to the salt boundary appear deeper than predicted by the velocity model.

position. This error is due to the overestimated velocity in the migration velocity model (figure 4.9, top). As the time arrival of the reflected wave is fixed, an overestimated velocity results in an overestimated traveled distance to compensate.

4.3.2.2 Diapir flanks and subsalt imaging

We now consider the impact of salt misinterpretation along steep diapir flanks, and on the base of the salt bulb in the case of teardrop diapirs. As we have seen that top of salt interpretation is not a major difficulty, we impose its position when generating the different velocity models, so we can focus on the deeper interpretation errors. Their impact is, however, less clear than in the case of salt top boundary misinterpretation.

Interpreting a weld instead of a salt stem usually results in the presence of spurious reflections beneath the bulb that reflect the sediment velocity model (figure 4.10.b). These reflections are often partly blurred and may not seem consistent with surrounding

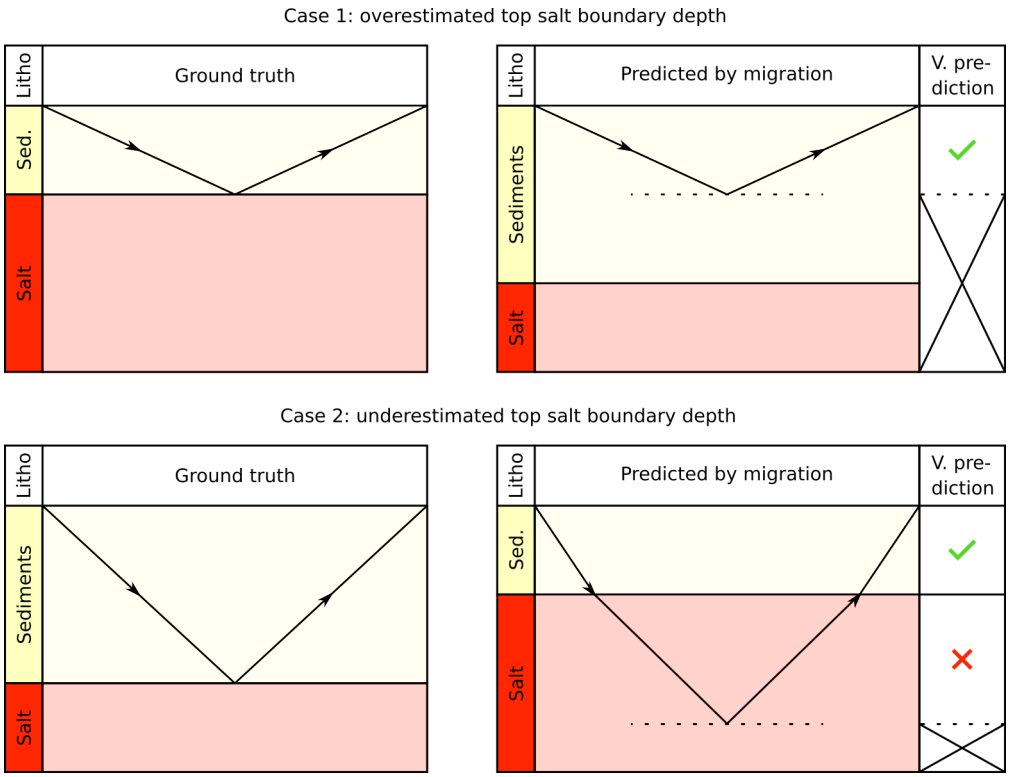

Figure 4.9 – Impact of salt top boundary position errors on migration depth prediction. (top) Overestimated salt boundary depth: the top of salt reflection has been registered in the seismic data. Thus, a reflection appears in the migrated image (even if it is unexplained by the migration velocity model). As the predicted velocity is exact along the wave path, the reflection is correctly repositioned. (bottom) Underestimated salt boundary depth: contrarily to the first case, the velocity prediction is not correct and the reflection is not correctly repositioned. As the velocity is overestimated (and the wave arrival time is fix), the traveled distance is overestimated, hence the reflection appears deeper in the migrated image.

sediments reflections. Underestimating the stem diameter usually results in a light blurring of the sediment reflections (figure 4.10.c). This is, however, not conclusive and such blurring could be attributed to many other sources of error. The overestimation of the stem diameter results in the strong attenuation of the sediment reflections located within the predicted diapir, making the actual diapir geometry impossible to distinguish (figure 4.10.d). Only the interpretation of a stem instead of a weld (and more generally the overestimation of the depth of the base of salt) has a significant effect (figure 4.10.e): a package of strong reflections, having an inverse polarity, appears in the image due to the strong impedance contrast between salt and the underlying sediments (despite the fact that it is not present in the migration velocity model). Provided that the migration velocity model is exact in the overlying image part, this base of salt reflection is correctly repositioned in the image during the migration.

4.3.2.3 Impact of apparent welds

As apparent welds are known to potentially impact the quality of seismic images [e.g., Jackson and Hudec, 2017], we can also test their impact on seismic images. We use the method presented in section 3.5.1 to generate an apparent weld on the velocity model of figure 4.3 (right). We use a triangular distribution ranging from -25 to 50 meters, with a mode at 25, and the same variogram model as used to generate the field D_{pert} (i.e., a Gaussian isotropic model with principal ranges of 2000 meters). The simulated salt volume (around the weld surface) is 20 to 80 meters thick and links the salt bulb and pedestal.

The only perceptible difference that can be noticed by visual comparison of the complete and apparent weld images is a very light horizontal smearing of the sediment reflections around the weld position. This smearing introduced by the apparent weld would, however, not be conclusive (even discernible) without having the complete weld image as reference. The very low impact of vertical welds on the image can be explained by considering its width as compared to the propagating wavelengths, and the relatively low illumination beneath the salt bulb.

4.3.2.4 Assessment

The above qualitative tests reproduce some known observations in the seismic reflection community. Underestimating the volume of a salt body in the migration velocity model usually deteriorates less the resulting seismic image than overestimating it [S. Jayr, 2019, personal communication]. In particular, the top of salt boundary does not present much difficulties to interpret on such simple diapir cases [e.g., Mosher et al., 2007] (although it may become drastically more complex when it presents overhangs or salt cap structures, e.g., Jones and Davison [2014]). Imaging steep diapir flanks and vertical welds is, however, much more complicated, and it is more difficult to determine causality rules between salt boundary misinterpretations and the resulting image distortions. The only really distinctive information that can be extracted comes from the base of salt reflection, that appears at the true location of the base of salt bulbs, even when it is placed too deep in the migration velocity model (given that the overlying velocity is correctly predicted).

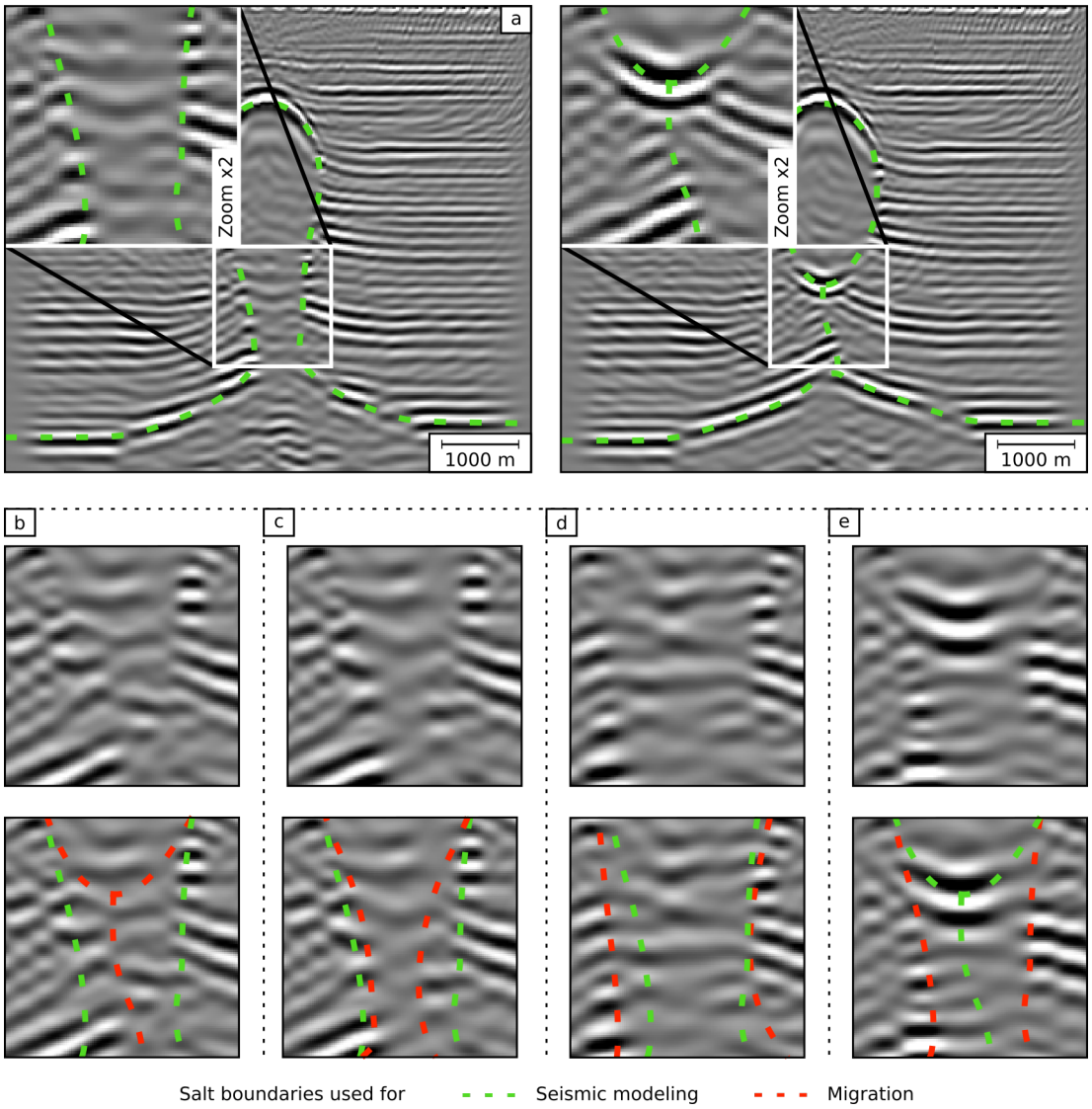

Figure 4.10 – Impact of errors on salt flanks and base boundary position on seismic images. (a) Reference images, obtained using exact finely layered velocity models during migration. (b) Interpretation of a weld instead of a stem. (c) Underestimation of the stem diameter. (d) Overestimation of the stem diameter. (e) Interpretation of a stem instead of a weld. The only truly informative interpretation element is the presence of a strong inverse polarity reflection when not interpreting the base of salt in (e). Provided that the velocity model is exact above the base of salt, the reflection is correctly relocated in the image.

4.3.3 Toward the quantification of imaging uncertainties

As a single erroneous salt boundary interpretation does not bring much information about the actual salt geometry, we now consider ways to use multiple stochastically generated interpretations. The underlying idea is pretty simple: a seismic image is the result of two contributions, one from the seismic data and one from the migration velocity model. Suppose we migrate multiple times the seismic data using different imperfect velocity models. If we can "stack" the different images into a single one, then we necessarily "increase" the contribution of the seismic data in comparison with the individual migration velocity models.

In this section, we investigate some ideas to perform this "stacking". The aim is to determine which parts of the image are the most sensitive to interpretation variations, to be able to focus on them later. We compare the response of two different synthetic seismic data sets, one obtained from a salt stock and one obtained from a teardrop diapir, when migrated using the same velocity models.

4.3.3.1 Creation of the data sets

The workflow used to create the two seismic image sets is illustrated in figure 4.11. We first create a unique set of 101 velocity models, imposing the position of the top salt boundaries (as described in sections 4.2.2 and 4.2.3). This set contains 40 salt stocks and 61 teardrop diapirs. Then, we select two of these models (a salt stock and a teardrop diapir) that we use to create two distinct synthetic seismic data sets (as described in section 4.2.4). Finally, for each seismic data set, we perform one migration per simulated velocity model (excepted the one used to create the data set). In the end, we have two sets of 100 seismic images corresponding to two different seismic data sets migrated using the same velocity models.

The variability of the simulated set of 101 structural models is illustrated in figure 4.12 using two indicators. The first indicator is the probability P_{sed} (figure 4.12.b) indicating for each pixel x the number of realization in which it belongs to the sediments over the total number of realization [cf. equation 11 in Wellmann et al., 2010]. In our example, it is defined as

$$P_{sed}(x) = \frac{1}{101} \sum_{real=1}^{101} \begin{cases} 1 & \text{if } x \in Sediments \text{ in } real, \\ 0 & \text{else.} \end{cases} \tag{4.8}$$

The second indicator is the information entropy H (figure 4.12.c) proposed by Wellmann and Regenauer-Lieb [2012] (cf. equation 2 in the paper), which in our example is defined for a given pixel as

$$H(x) = -P_{sed}(x) \times log(P_{sed}(x)) - (1 - P_{sed}(x)) \times log(1 - P_{sed}(x)). \tag{4.9}$$

Information entropy values can be interpreted (in our application) as the predictability of the output category of a pixel (i.e., *Salt* or *Sediments*) in a given realization. The higher the values, the lower the predictability of the category is. High information entropy values around the stem of the uncertainty envelope therefore indicate that the structural modeling method efficiently samples this model part without favoring specific

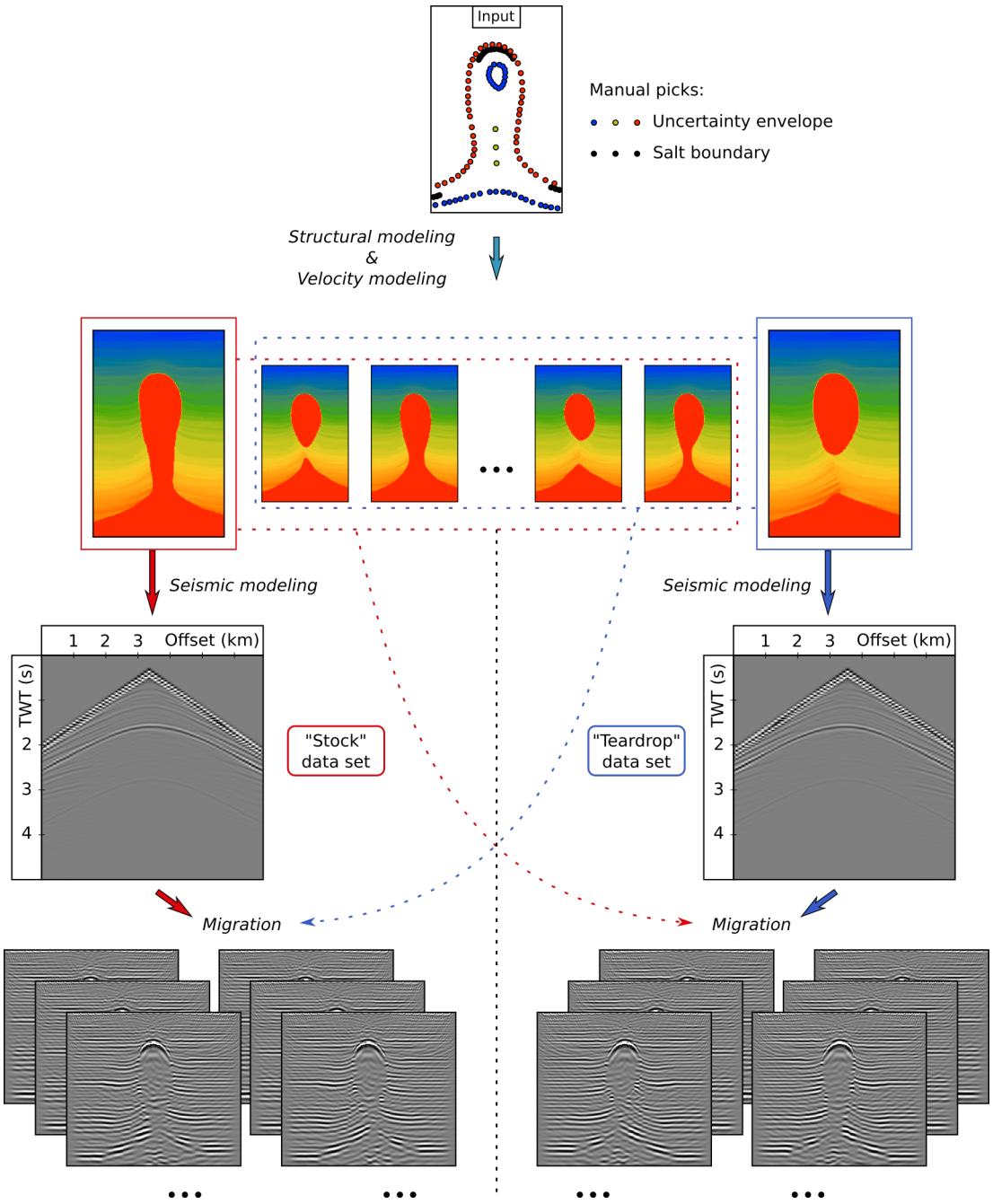

Figure 4.11 – Creation of the two sets of seismic images used for uncertainty quantification. The two sets are obtained using the same migration velocity models, but different synthetic seismic data.

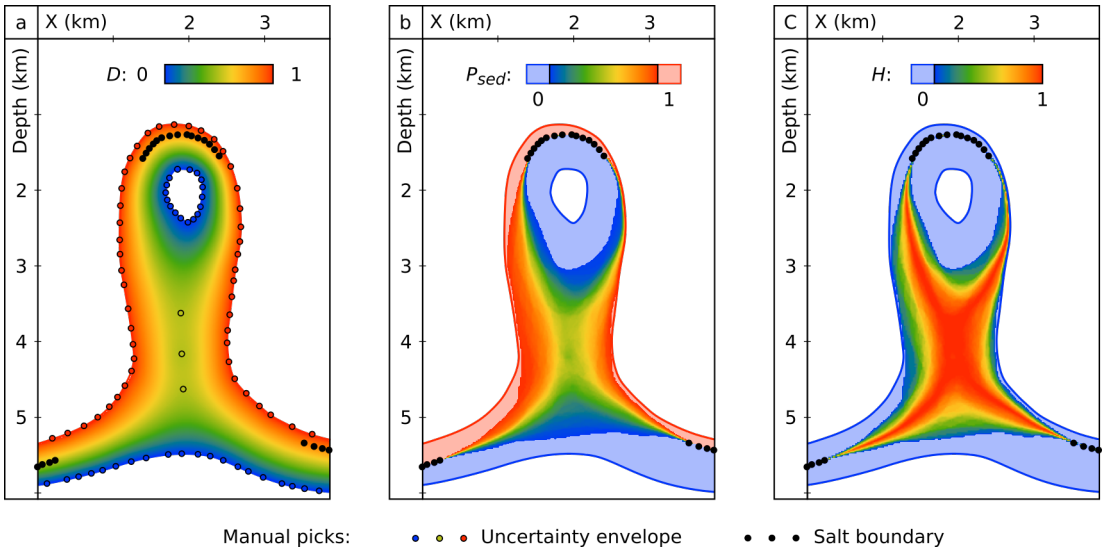

Figure 4.12 – Variability of the simulated structural models used for velocity modeling. (a) Pseudo-distance field D used to generate the structural models. (b) Indicator probability P_{sed} of the sediment facies (equation 4.8). Information entropy H (equation 4.9). Red and blue dots show the limits of the uncertainty envelope. The position of the salt boundary is imposed at the black dots location. The red and blue whitened areas indicate that the facies at the pixel location is constant over the realizations.

model geometries. It is interesting to note, however, that locally imposing the position of the salt boundary has a quite large impact on the possible salt geometries. For example, no salt bulbs are simulated close to the envelope "bulb". This is due to the very large ranges of the variogram model used for simulating the perturbation fields.

4.3.3.2 Statistical description of the image set

A first approximation to estimate the average seismic imaging response of a given seismic data set to different velocity models consists in computing basic statistics, such as the mean, the variance and the standard deviation between seismic images. The computation of such statistics is only possible when using a unique background sediment velocity model. Otherwise, the reflections would be repositioned independently from an image to the other, which would potentially result in a null average seismic image.

Mean of an image set We define the mean image I_{mean} of a set of N images $I_{k=1,\dots,N}$ as

$$I_{mean}(x,y) = \frac{1}{N}\sum_{k=1}^{N} I_k(x,y),$$

for any pixel (x,y). The mean amplitude describes the average response of the migration to any input velocity model. Computing the mean amplitude image works very similar to stacking common mid-point gathers. In the regions where all the velocity models have approximately the same response (i.e., where the signal of a given trace is in phase from one image to another), the resulting structures are preserved. On the contrary, for regions having disparate responses to velocity variations (i.e., where the signal is out of

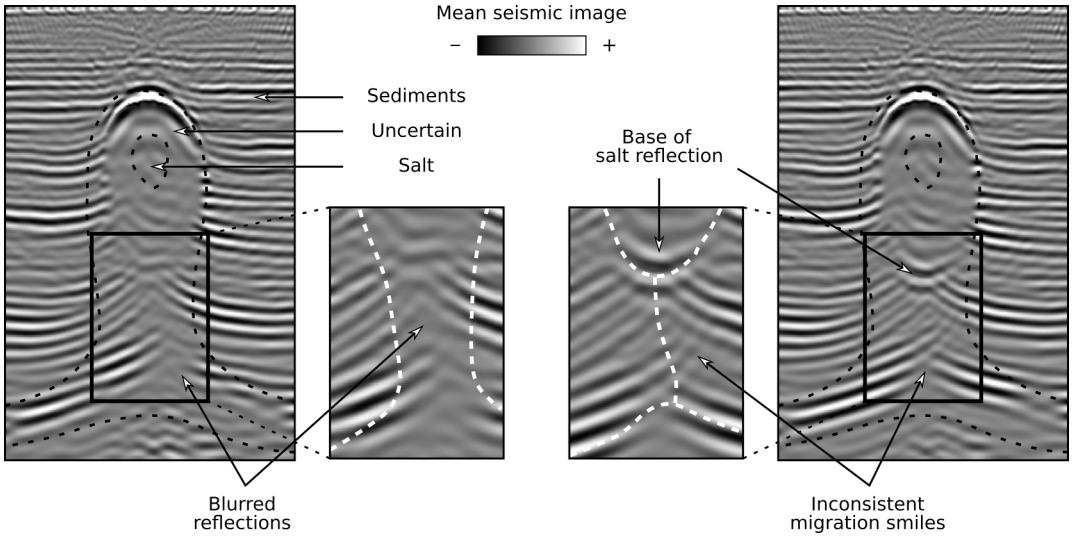

Figure 4.13 – Mean seismic images corresponding to the salt stock diapir (left) and the teardrop diapir (right) data sets. The dashed black lines are the uncertainty envelope boundaries. The dashed white lines are the salt boundaries used for seismic modeling. The reader is referred to section 4.3.3.2 for the full description.

phase from one image to another), their contributions interfere destructively, blurring the mean image and deteriorating the reflection packages which are not consistent from one realization to the other.

Figure 4.13 illustrates the mean seismic images computed for the two data sets (the "stock" and the "teardrop" examples). For the salt stock data, the seismic reflections are relatively attenuated in the stem of the diapir. We explain this by the absence of reflections in this part of the stock seismic data set (as salt is homogeneous). These "attenuated" reflections thus correspond to artifacts generated by the migration that are only present when the migration velocity model predicted the presence of sediments instead of salt. On the opposite, the reflections between the salt bulb and pedestal are better preserved in the image generated from the teardrop diapir data. Following the same reasoning as previously, we explain this by the fact that reflections have actually been recorded in the seismic data set and that energy is thus more "easily" relocated around its true position in the image. It is interesting to note, however, that the reflection packages on each side of the "weld" cross one through each other. It is an illustration of the destructive interference of incoherent reflections between images. Where high positive amplitude reflections intersect themselves they sum up positively, where high negative amplitudes intersect themselves they sum up negatively, and elsewhere they result in low to null amplitudes.

One major difference to note between the two mean images is the presence of a strong package of reflections in the teardrop mean image, having an inverse polarity, which is typical of a base of salt reflection. These reflections are correctly positioned in the image, which provides a good indication to place the base of salt boundary in the velocity model.

Standard deviation and variance of an image set We define the variance image I_{var} of a set of N images $I_{k=1,...,N}$ as

$$I_{var}(x,y) = \frac{1}{N}\left(\sum_{k=1}^{N} I_k^2(x,y)\right) - I_{mean}^2(x,y),$$

where x and y are the pixel coordinates. The standard deviation image I_{std} is defined as

$$I_{std}(x,y) = \sqrt{I_{var}(x,y)}.$$

These two measures indicate for each pixel how much its amplitude is subject to variations from one image to the other. As they are strongly related, we focus here on the analysis of the standard deviation (figure 4.14), which directly relates to the average dispersion of a pixel value around its mean between images. We use the variance (figure 4.15) only for visualization purposes, as it emphasizes more the highest amplitude variations, and thus the image parts which are most "sensitive" to variations in the migration velocity model.

In the two data sets, there are almost no variations observable near the top of the diapir and the top of the base layer away from the diapir pedestal. It is consistent with the imposed parts of the salt boundary and the spatial distribution of the simulated velocity models in the uncertainty envelope (figure 4.11). The high values are preferentially located close to the boundaries of the salt bodies used for seismic modeling. This can be easily explained as these are the image parts presenting the highest velocity variations from one realization to the other, depending on whether a given pixel belongs to salt or sediments.

The two data sets present similar and relatively low standard deviation values in the *Sediments* region, away from the salt boundaries. This is due to the fact that the two velocity models used for seismic modeling are identical in this region. In both data sets, the "uncertain" zone (i.e., the portion around the stem/weld) concentrates most of the high standard deviation values, which is consistent with the localization of most of the velocity variations. The teardrop data set presents higher values than the stock data set in this region. We explain it by the presence of higher amplitude reflections in the teardrop images (i.e., as we explained the larger mean amplitude values in this region). Another interesting piece of information in this zone lies in the organization of the high standard deviation values. In the first data set they are organized rather vertically in the peripheral parts whereas in the second data set they are more horizontal and vertically centered. These observations coincide with the diapir geometry differences between the two data sets: the vertical orientations match the steep stock boundaries and the horizontal orientations match the base of the teardrop diapir bulb and the top of its pedestal. The base salt layer part presents higher standard deviation values in the stock data set than in the teardrop data set. A potential explanation is that there must be more energy reaching this part of the domain in the stock data set (the seismic waves cross two more interfaces having a strong impedance contrast in the teardrop model, the base of the bulb and the top of the pedestal). Furthermore, such spurious reflections should not be present in the salt (as it is homogeneous). An element that may explain their presence is that the deepest model parts suffer from the accumulation

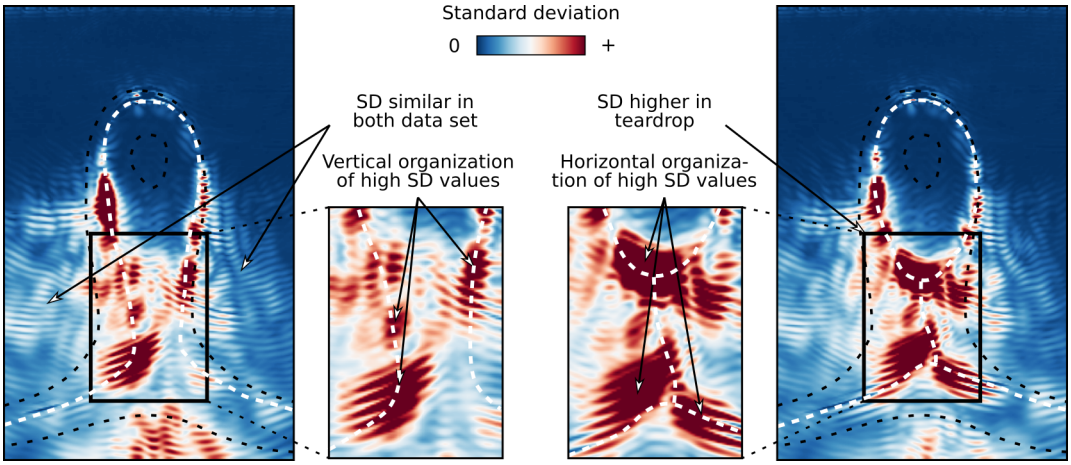

Figure 4.14 – Standard deviation images corresponding to the salt stock diapir (left) and the teardrop diapir (right) data sets. The high values are preferentially located around the salt boundaries used for seismic modeling (dashed white lines). They are organized vertically in the salt stock image, and more horizontally in the teardrop example. In the most "uncertain" region (in the black frame), the standard deviation values are sensibly higher in the teardrop data set, due to the amplitude "attenuation" observed in the stock data set. The dashed black lines are the uncertainty envelope boundaries.

of the migration errors that occurred above.

4.3.3.3 Use of seismic attributes

An alternative to the direct computation of statistics consists in using seismic attributes. As described in section 1.3, lots of work have focused on developing such measures and quantities dedicated to the description of seismic images. Their main advantage as compared to the direct statistics computation is that seismic attributes are natively designed to handle the specificities of the seismic signal (i.e., a strongly anisotropic oscillating signal). Among the different attributes that have been proposed in the literature, we focus here on some of the attributes derived from the GLCM [Haralick et al., 1973]. As stated in section 1.3.2, they are widely used and provide a suitable statistical description of the images.

Attribute and parameter selection We select four GLCM attributes in this application: the contrast (equation 1.2), the energy (equation 1.3), the standard deviation (equation 1.5) and the variance (equation 1.4). They cover the three categories of GLCM attributes (section 1.3.2). The variance is computed in addition to the standard deviation mainly for visualization purposes.

The attributes were computed on each individual seismic image, using 32 gray levels and a neighborhood of 21 by 21 cells. Due to boundary effects, we cannot properly define the GLCM neighborhood on the first 10 rows and columns of the seismic images. We simply ignore these pixels when computing the attributes (it corresponds to the blank lines on the borders of the images presented thereafter). To avoid compression effects when transforming the seismic image into a discrete grayscale, we "truncate" the extreme amplitude values to reduce the amplitude range (it is similar to, but simpler

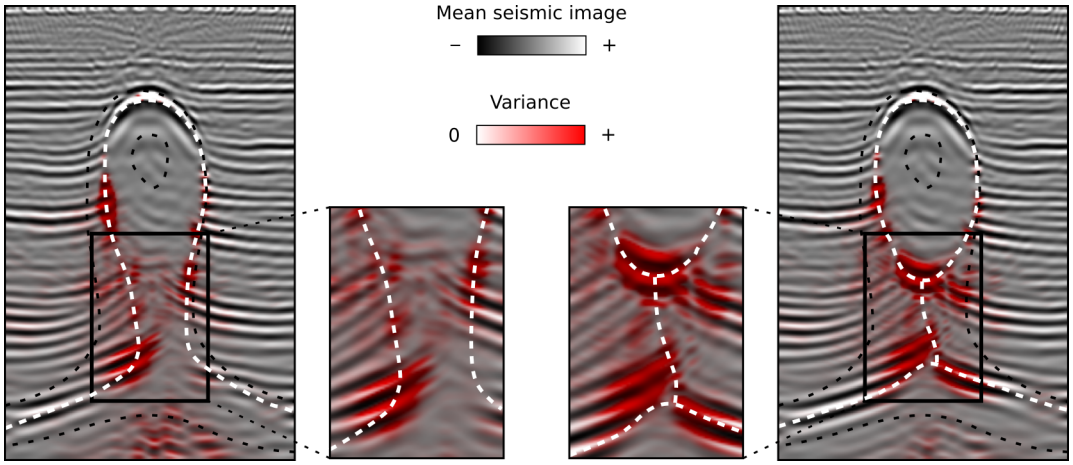

Figure 4.15 – Variance images overlaying mean images for the salt stock diapir (left) and the teardrop diapir (right) data sets. This display permits to visualize the image parts which are the most sensitive to variations in the migration velocity model. The dashed black lines are the uncertainty envelope boundaries. The dashed white lines are the salt boundaries used for seismic modeling.

than, applying a low-pass filter or some mathematical transformation). It also presents the advantage that all the seismic images have exactly the same amplitude range in the end, and are therefore comparable once transformed into a discrete grayscale. Once we have computed the different GLCM attributes for each seismic image, we compute and analyze their mean and standard deviation images (as explained in section 4.3.3.2).

Statistical description of the image set using the GLCM The first important thing to note is that we do not consider the same standard deviation and variance as in the previous section. In section 4.3.3.2, these terms referred to the variations of a given pixel value from one image to the other. Here, we are looking at the variations of the pixel values in the neighborhood of a given pixel in one image (equations 1.4 and 1.5). We thus have one GLCM standard deviation image per seismic image and we compute the mean GLCM standard deviation image for each seismic data set. Figure 4.16 illustrates these mean images (plus the associated mean variance images).

The first observation we can do is that, as the GLCM standard deviation emphasizes the large amplitude variations in a given neighborhood, it especially highlights the strong sediment reflection packages and the (sub-)horizontal salt boundaries. On the opposite, the steep salt boundaries correspond to sudden attenuations of the reflections and thus of the standard deviation. We focus on the analysis of the same region as previously (around the salt stem and between the salt bulb and the pedestal). We observe that the average standard deviation values are relatively low all along the stem in the salt stock (figure 4.16, left), when two high value events are clearly visible in the case of the teardrop diapir (corresponding to the base of the salt bulb and the top of the pedestal, figure 4.16, right). This confirms the observations made on the amplitude mean images (figure 4.13). Therefore, the GLCM standard deviation seems to be a good quantitative indicator to support the interpretations about the nature of the salt body that can be drawn from amplitude mean images. Especially, it is more robust

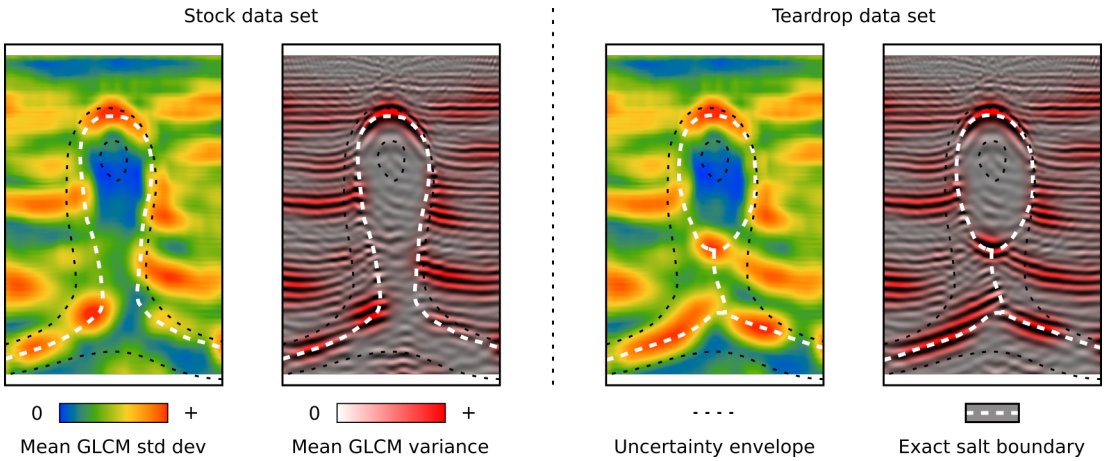

Figure 4.16 – Mean GLCM standard deviation and variance images for the salt stock diapir (left) and the teardrop diapir (right) data sets. The seismic images used as background for the variance images are the reference images. The high variation values are located along the horizontal salt boundaries and the strong reflection packages. This allows to clearly distinguish between the stock stem on the left and the bulb base and the pedestal on the right.

to velocity variations in the sediments than the standard deviation images computed directly from the amplitude.

Use of GLCM attributes to characterize the image set The GLCM contrast (equation 1.2, figure 4.17, left) highlights the high gray level variations between contiguous pixels. It is thus especially sensitive to the presence of large amplitude variations in a pixel neighborhood, and the result is relatively similar to the GLCM standard deviation. As the (square) difference of gray level is scaled by the number of occurrences M_{ij}, the ratio of low values over moderate values is higher in the contrast image than in the standard deviation image, providing a more accurate delimitation of the salt boundaries in both data sets. Figure 4.17 illustrates the mean contrast image (top left), and the contrast standard deviation image (bottom left). The mean images are relatively similar to the GLCM standard deviation images, but exhibit thinner high value events. The contrast standard deviation images do not provide much more information, except that they highlight the presence of much more variable amplitude signals in the teardrop data set than in the stock data set. It is interesting to note, however, that they are quite similar to the standard deviation images computed directly from the seismic amplitude (figure 4.14).

The GLCM energy (equation 1.3, figure 4.17, right) highlights the image parts having preferential gray level values associations (e.g., the salt bodies, which have a very homogeneous texture). The results are more difficult to interpret than for the contrast, but an interesting property that is visible on the mean energy image (figure 4.17, top right) is the presence of larger energy values all along the salt stem in the stock data set as compared to the teardrop example, which denotes the presence of salt. Once again, this seems to be a good indicator of the salt body nature. The standard deviation images computed from the GLCM energy (figure 4.17, bottom right) seem, however, more complex to interpret and it is difficult to extract any information from it.

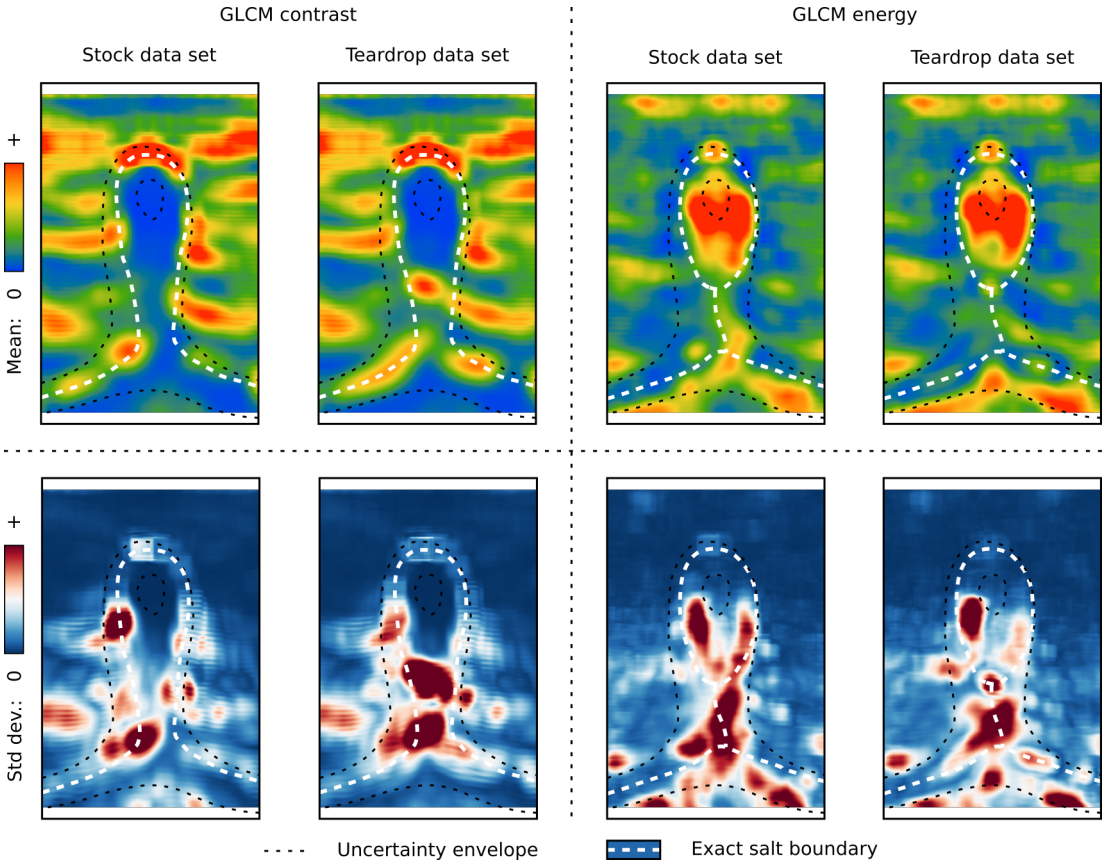

Figure 4.17 – GLCM contrast (left) and energy (right) mean images (top) and standard deviation images (left). The contrast highlights approximately the same properties as the GLCM standard deviation, but more finely. The energy highlights the presence of salt and is thus higher in the stem of the salt stock than along the weld in the teardrop data set. See section 4.3.3.3 for full details.

4.4 Discussion and perspectives

4.4.1 Experimental conditions

We have performed a series of imaging tests to investigate the sensitivity of seismic image quality to migration velocity errors. During these tests, we have only considered, however, the impact of the salt boundary position, and we kept all the other parameters fixed. This includes, particularly, the seismic modeling parameters (e.g., grid resolution, source wavelet), the sediment velocity, and the input salt modeling parameters which limit the variety of salt geometries.

Salt modeling parameters For multiple reasons, we have focused on the study of secondary salt structures (salt stocks and teardrop diapirs). The first reason is practical: the salt modeling method we have developed and presented in chapters 2 and 3 is specifically designed for these cases; whereas the same concept can be used to generate tertiary salt bodies, it still requires to work on the relationships between geology, uncertainty envelope definition and simulation parameters before being put into practice. The second reason is that even these "simple" structures present challenges with today exploration methods due to the large lateral velocity variations they introduce [e.g., Jackson and Lewis, 2012, Jones and Davison, 2014]. Note that the last developments in seismic acquisition designs (e.g., wide-azimuth and full azimuth) probably offer a much better illumination of the diapirs flanks and subsalt sediments, but they are used at larger scales [e.g., Dellinger et al., 2017]. The last reason is again relatively practical: we first focus on these structures as we can easily control the different simulated envelope geometries, and thus investigate specific structure impacts (e.g., top of salt, diapir flanks, base of bulb). This would not necessarily be the case with more complex initial structures. An important aspect which has not been investigating is the impact of salt internal heterogeneity and the potential formation of cap rock structures that can drastically modify the velocity field in and around salt bodies [e.g., Jackson and Lewis, 2012, Jones and Davison, 2014].

Sediment velocity model The impact of erroneous sediment velocity models has not been broached here, both by lack of time to perform the necessary tests and because the core of this work focuses on salt interpretation. This would be an interesting topic to investigate, as it is clear that it also plays a role in imaging uncertainties. As we have regularly mentioned it in this chapter, any error in the migration velocity model impacts all the underlying image parts [Biondi, 2006]. Sediment velocity errors (and especially shallow ones) therefore necessarily introduce uncertainties during the imaging.

The only (unpublished) tests we performed showed that different velocity perturbation fields ϕ_i sharing the same distribution model have a negligible impact on sediment imaging. This can be easily explained by the fact that the perturbation only introduces local vertical velocity shifts and that, as the perturbation field distribution is centered around zero, the travel time between a source and any location in the subsurface is "on average" the same from one realization to another. It would be more interesting to consider variable sediment layer geometries and variable velocities within the layers, as the differences between two models would be larger. To go further, the presence of struc-

tures such as faults or channels in the subsurface also introduces velocity uncertainties that should, ideally, be taken into account.

Seismic modeling parameters Another limitation of the presented study comes from the choices which have been made to perform the seismic modeling. Some of these choices were guided by material limitations (such as computer power requirements), and others appeared with the analysis of the results. One of the main limitations lies in the choice of the grid resolution and the source wavelet dominant frequency. The choices we made (i.e., 20 m and 25 Hz) were mainly guided by the necessity of limiting the overall resolution of the acquisition, as these parameters directly impact the time to perform the migration. Although we used an 8^{th} order spatial finite difference scheme, a spatial grid sampling of 20 meters might be a bit rough to prevent any numerical dispersion during the modeling and migration. This could partly explain the problem of spatial resolution observed in section 4.3.1. Furthermore, some early tests [Clausolles et al., 2019b] using a better grid resolution (10 meters) provided less deteriorated seismic images and more contrasted statistical images than illustrated in figures 4.13 and 4.15. Whereas these tests cannot be used to draw conclusions due to the limited amount of samples they used (10 images only), they however highlight the fact that the resolution effects probably have a non-negligible impact on the quality of the images we generate, and on the resulting statistics we draw.

Using a finer seismic grid would also be more consistent with the low-pass filtering we apply to the migration velocity models. It is important to keep in mind, however, that ideally it would require to prove that the difference between the response of the different media is not significant, which is still an open problem.

In summary Now that the overall methodology to generate the different seismic data sets and images is well set up and that we have some ideas about the different results we may obtain, we can seriously consider investigating more cases and parameters.

First of all, we may try to increase the grid resolution (e.g., 10 meters). This would be closer to the level of details we may resolve with the other imaging parameters. Then we may try to investigate the impact of sediment layer velocity uncertainty on top of salt imaging. The most interesting would be to test the method on real 2D seismic sections, to see if the use of a stochastic interpretation method can really help reduce the uncertainties underlying the seismic interpretation of salt. Testing on 3D seismic cubes would, however, require a prohibitive amount of computer power and would only be conceivable with an access to a computer cluster. The following section examines avenues to address this challenge.

4.4.2 Relation between statistics and model parameters

One major point has not been mentioned yet. The variability of the salt boundaries, and thus to some extent of the seismic images, is directly related to the model parameters used to simulate the interpretations (i.e., uncertainty envelope, distribution model and variogram model). The analysis of the statistics derived from the seismic image sets should, therefore, take into consideration this *a priori* variability and, ideally, be able to dissociate its contribution from the overall measured variability. This task is, however,

much complex as the relations between velocity model variations and seismic image variations are highly non-linear.

The most direct solution to investigate these relations would be to run multiple series of tests using variable salt modeling parameters, and to use machine learning to look at the relationships between model parameters and image variability. It is, however, probably not an option, as training the learning algorithm would already represent a prohibitive amount of seismic images to generate.

An alternative approach may consist, as a first-order approximation, in reducing as much as possible the high variability zones in the image. A solution which would not require going through the entire workflow (and especially the numerous migration phases) resides in the use of seismic attributes (as we have started to investigate in section 4.3.3.3). Indeed, each attribute has its own specificities (highlighting e.g., salt, sediment, or the boundary). A wise attribute selection can thus help during the statistical analysis to better characterize the most uncertain zones (i.e., the ones having the largest variability from one realization to the next) as each attribute focuses on a specific part of the seismic signal content. The cross analysis of the different attribute high variability regions then permits to determine more finely the overall sensitivity of a given model part to velocity variation.

4.4.3 Toward automatic velocity model updating

The long term objective of this work is to develop elements to move toward automatic velocity model updating during seismic imaging. The work presented in this chapter focuses on the development of indicators for characterizing the quality and the reliability of seismic images. Although these indicators have proven to have potential for highlighting the image parts being the most sensitive to migration velocity variations, their applicability to cases where more parameters vary remains to study. One of the most interesting perspectives of this work is related to the "additional knowledge" that such indicators can bring into the seismic imaging loop, in order to integrate the notion of uncertainty quantification in an automatic velocity model updating framework. This section develops some ideas about the completion of such an automatic imaging loop.

Updating the uncertainty envelope As the method we developed requires to define an uncertainty envelope at each iteration, a straightforward solution to "update" the initial velocity model consists in updating the uncertainty envelope from one iteration to the next one, with the objective of progressively shrinking it and thus converge toward a final salt boundary (i.e., when the external and internal envelope surfaces are collocated).

A first source of information that can be considered during the updating is the set of perturbed seismic images. An updating solution can consist in independently segmenting each image into *Sediments*, *Salt* and *Uncertain*, and then to compute the probability of each the three facies over the set of images to derive the new uncertainty envelope shape. Another source of information comes from the variability indicators which are computed from the perturbed images. We may consider using these scalar fields to deform the uncertainty envelope boundaries, in an approach similar to the level-set [e.g., Kadlec et al., 2009, Haukås et al., 2013] or surface wrapping [e.g., Carlson, 2010,

Haukås et al., 2017] methods. Methods from the topology optimization domain may also be interesting to investigate [see e.g., Rozvany, 2009, for a review].

Fast salt volume estimation Depending on the state of progress in the imaging loop, the questions we try to answer at a given iteration are not the same and other strategies can be considered to build and update the migration velocity model. At early stages for example, we may be more interested in estimating the bulk volume of the salt body rather than trying to place more or less precisely the boundary. A solution to do this consists in using a large uncertainty envelope with different distribution models to generate the salt bodies. By using models with narrow and increasing value ranges, it would be possible to quickly assess the impact of various salt volumes to determine the "breaking point" after which the salt volume is too large and the image is deteriorated. This bulk volume could then be used to define a "proper" uncertainty envelope and the following iterations can be performed as described in the previous paragraph.

4.5 Conclusion

We have presented an application of the salt modeling workflow introduced in chapter 2 to investigate the impact of erroneous salt boundary interpretations on the quality of seismic images. The first qualitative results of this application highlight well-known effects in the seismic imaging community, such as the relative ease to interpret the top of salt boundaries and the typical inverse polarity reflection which appears when flooding the subsalt domain with salt [e.g., Mosher et al., 2007]. Predicting the effects of salt boundary mispositioning remains, however, a complex task, and it seems difficult to define qualitative criteria that efficiently link interpretation errors and seismic images patterns.

To overcome these limitations we proposed a strategy to statistically quantify the structural uncertainties underlying the interpretation of a depth-migrated seismic image. It consists, from an initial image, to stochastically generate multiple interpretations and to remigrate them. From this set of images, the computation of the mean amplitude image illustrates the average response of the seismic data to migration velocity. It preserves the image parts in which the different images have similar structures, and exhibits inconsistent structures where the images differ significantly. The computation of the amplitude standard deviation emphasizes the image parts which are the most sensitive to migration velocity variations. Such statistics can also be computed from seismic attributes to emphasize specific image behaviors. The comparison of the results obtained from two different seismic data sets (a salt stock and a teardrop diapir) shows that this approach enables to clearly differentiate the two types of structures and to localize the most uncertain image parts when no uncertainty exists in the visible sediments.

This work is a step toward automatic velocity model updating integrating structural uncertainty management. Future works should focus on the development of a method to automatically update the initial uncertainty envelope consistently with the estimated uncertainty location and magnitude. This would finally close the seismic imaging loop. Concurrently, it is important to investigate the impact of sediment velocity uncertain-

ties, especially in the shallow model parts, as it may seriously alter the conclusions of this chapter. Once the uncertainty envelope updating will be performed, it would also be interesting to investigate the feasibility of the automatic velocity model updating workflow on real seismic data sets. Last but not least, limiting the number of necessary remigrations to perform at each iteration is mandatory to move toward 3D applications.

Conclusions

Seismic interpretation is often seen either as a geophysical problem, where the subsurface is a set of unknown parameter fields obtained by inversion or segmentation of the seismic data, or from a geological point of view, where the subsurface is composed of objects that are manually interpreted based on assumptions about their genesis and history. In this thesis, I was interested in conciliating these two approaches in the specific case of the assessment of the structural uncertainties underlying the interpretation of salt bodies from ambiguous seismic images. This includes their characterization, their sampling and the assessment of their impact on seismic imaging. In the following, I summarize the main contributions of the thesis, and the research prospects that seem to me the most promising.

Main contributions

Simulation of variable 3D shapes of salt bodies and their connectivity

A necessary step when assessing the impact of structural uncertainties is to sample the uncertainty space, that is, the space of all the possible structural interpretations given the uncertainties. Most existing uncertainty methods are based on the perturbation of a best-guess model or on independent data perturbations. These approaches can be limited for sampling variable model topologies, which is a crucial facet about salt uncertainty. I proposed a numerical method for stochastically modeling variable shapes of salt bodies and their connectivity. The input of the method is a buffer zone, which encompasses the salt boundary and defines the maximum spatial extent of the uncertainty space. The salt boundary is a level set of the combination of a reference scalar field, computed from the buffer zone, and a spatially correlated random field that is used as a perturbation. This implicit formulation, which uses the seismic grid as support, allows for the simulation of both varying salt geometries and topologies while ensuring that the simulated boundaries do not present invalid features such as self-intersections. When the result of the simulation is a diapir whose bulb is detached from its pedestal, a weld is simulated to connect them. The weld position is determined from the scalar field representing the salt boundary, to ensure its consistency with the simulated salt bodies. The method is automatic and can integrate punctual information (e.g., well data or manual seismic picks) and, to some extent, prior geological knowledge about the regional structure orientations, the types of structures and their connectivity.

Impact of salt interpretation uncertainties on seismic images

The building of a seismic image is an iterative process during which the subsurface parameter fields are progressively updated by creating and interpreting temporary versions of the image. Therefore, interpretation uncertainties at a given iteration are propagated throughout the imaging loop until the final image is produced. Their quantification is fundamental, especially with the development of automatic interpretation methods that generally deliver a unique, deterministic solution of the salt boundaries. I presented an application of the proposed modeling method to the characterization of salt-related structural uncertainties underlying seismic imaging on a 2D synthetic data set. I discussed the use of various basic statistical measures over a set of perturbed seismic images to localize and quantify how the uncertainties related to the interpretation of an ambiguous seismic image propagate through an iteration of the imaging loop. The set of perturbed images is obtained by generating stochastic interpretations of the salt boundary and remigrating the seismic data using the corresponding velocity models. The statistics can be computed either from the seismic amplitude image or from derived seismic attributes. Mean amplitude and attribute images provide information about the "on average" behavior of the seismic data set to migration, emphasizing the contribution of the seismic data during the migration as compared the contribution of the individual migration velocity models. Standard deviation images allow for a quantification of the local sensitivity of seismic images to migration velocity variations, reflecting part of the structural uncertainties underlying seismic imaging.

Perspectives

The method developed in this thesis and its application have provided interesting results on relatively simple synthetic models of salt bodies. Their use on real field data would, however, require to alleviate some of their underlying assumptions. The following section introduces some lines of research toward a generalization of the proposed approaches.

Uncertainty characterization and automatic seismic interpretation

In chapter 1, I review the various approaches that have been proposed in the literature to automatically interpret salt on seismic images. I also discuss how they can be used to integrate geological knowledge and take uncertainties into account during the interpretation. A fundamental idea of this chapter that is used in all the following is the notion of uncertainty envelope, that is, the representation of interpretation uncertainties by a buffer zone around the salt boundary [e.g., Bistacchi et al., 2008, Li et al., 2015]. In practice, we propose to segment the seismic image into three regions: *Sediments*, *Salt*, and *Uncertain* [also proposed by Haukås et al., 2017]. The work performed in the frame of Capucine Legentil's master project [appendix A, Legentil, 2019] aimed at building on the conclusions of chapter 1 review to develop a method for automatically segmenting a seismic image into these three regions. Although the implemented method provided first encouraging results, this work requires to be finalized and further tests are required. The question of the automatic generation of an uncertainty envelope suitable to be used

as input of the proposed modeling method is, therefore, still opened.

Extension of the modeling workflow and applications

Modeling other types of salt bodies

In this manuscript, I have mainly discussed the simulation of salt walls and stocks. The workflow proposed in chapter 2 can, however, also be used to simulate other types of salt bodies, and especially salt sheets and canopies. It already permits to model such structures in its current state, but it may require to introduce quite a lot of additional input data to define an uncertainty envelope suited to the modeling purpose (e.g., to model the associated salt feeders). In addition, these structures have their own specificities that would be interesting to introduce into the modeling workflow to better guide the simulation and reduce the need for additional inputs. For example, as salt sheets spread over the sea floor, they are usually conformal with the subsalt sediments. A solution to integrate this observation into the modeling workflow could consist in using prior information about the sediment stratigraphy (cf. section 2.3.3) to truncate the base of the salt sheet, as it is already done for the management of unconformities in implicit stratigraphic modeling [Wellmann and Caumon, 2018]. Salt sheets and canopies also introduce specific associated structures which are not considered yet in the workflow.

First, they potentially introduce a variety of secondary and tertiary welds. Even though the weld modeling principle presented in chapter 3 may remain valid in some configurations (e.g., when tertiary welds correspond to stratigraphic surfaces), the visibility criteria used to define the weld extent need to be redefined (as they were specific to secondary welds). Moreover, if secondary subsalt welds were expected to lie within the uncertainty envelope (due to the difficulty to image subsalt regions), this assumption is much less relevant for subhorizontal tertiary welds, that may be invisible and thus be classified along with the surroundings sediments. Other strategies for modeling welds have, therefore, to be considered, depending on the nature of the weld. In the case of subhorizontal tertiary welds, a strategy could consist, again, in using prior sediment stratigraphy information (known or simulated) as the weld is expected to be aligned with a stratigraphic surface. Handling more complex welds involving faulting (cf. Rowan et al. [1999] classification, section 3.2.1) will probably prove, however, to be a much more complex task.

Second, the presence of an allochthonous salt layer implies the existence of a preexisting salt source to model, that is, a salt feeder. In addition, if the allochthonous layer is welded, this salt "source" may not be a salt feeder but the other part of the welded layer. In the case of salt canopies, the presence, number and nature (i.e., welded or not) of salt feeders cannot necessarily be inferred from seismic images. When no salt feeder is detected on seismic images (or when their number is uncertain) a solution can consists is simulating one or several feeders connecting the salt sheet or canopy to the salt base layer it originates from. As salt feeders are initially salt diapirs [e.g., Jackson and Hudec, 2017], a relatively simple solution to perform the simulation may consist in using the salt modeling workflow proposed in chapter 2.

Third, a salt suture forms between two salt sheets that have merged in a salt canopy. Similarly to salt welds, salt sutures may contain some trapped sediments, impacting

seismic imaging. When they cannot be detected on seismic images, a solution for determining their number and approximating their position could consist in using the number of (eventually simulated) canopy feeders to derive a modeling strategy inspired from the Voronoi tessellation, which would make the salt sheets grow (starting from the feeder positions) until they coalesce. The contact surfaces between salt sheets determine the geometry of the sutures.

Modeling associated sedimentary structures

In order to build a complete geomodel, it is not sufficient to model salt bodies. It is also necessary to model the surrounding sedimentary structures. Among these structures, minibasins present challenges for current geomodeling methods due to their internal architecture. Indeed, sediment layers within minibasins are conformal in the minibasin center, but can be locally unconformable at the minibasin edges, close to salt diapirs [Collon et al., 2016]. These unconformities define packages of sediment strata, the halokinetic sequences, that are locally folded upward, forming wedge and hook patterns (figure 2.4.a) [Giles and Lawton, 2002, Giles and Rowan, 2012].

Current geomodeling methods are not designed to handle these structures, as they define one scalar field per package of conformal reflection and interpolate them independently (whereas halokinetic sequences are supposed to be conformal in the center of the minibasin). A solution to model halokinetic sequences can consist in first modeling the halokinetic sequence external boundaries, and second modeling the internal architecture of the sequences. Using two different levels of detail would permit to separate the questions of the overall sequence conformity and the local unconformity introduced by the hook and wedge patterns. In this frame, modeling the external sequence boundaries is reduced to modeling a concave layer cake model of sediment strata, which is already possible with current geomodeling methods. The internal architecture of each sequence can then be interpolated locally, independently from the other sequences, consistently with the external sequence boundaries. Such method would require to be able to integrate discontinuities into the interpolation of the scalar field [e.g., Renaudeau et al., 2018], and to have information about each internal sequence geometry. In the absence of such information, we may consider adapting predefined internal patterns of tabular and tapered sequences (e.g., Giles and Rowan [2012], and figure 2.4.a) to the geometry of the modeled sequences.

As described by Giles and Rowan [2012], the cusp-shaped patterns of the interpreted salt boundaries are related to the nature and architecture of the associated halokinetic sequences. The modeling of the halokinetic sequence boundaries should, therefore, be performed consistently with the geometry of the simulated salt boundaries (figure 2.4.b).

Impact on physical process simulation

Building a geomodel is seldom an end in itself. It is often part of a larger application aiming at simulating some physical process of interest. A major perspective that will be at hand once the overall modeling workflow will be set up (and especially the modeling of sediments) is its application to the characterization of salt impact on the various physical processes occurring at basin scale [e.g., fluid migrations, geomechanics, or heat transfers, Jackson and Hudec, 2017]. Some basic case studies can already be considered,

such as the application presented in chapter 4 about the impact of salt structures on seismic imaging or, for example, the impact of weld uncertainties on reservoir sealing.

Toward uncertainty assessment during automatic velocity model updating

The study presented in chapter 4 is a first step toward an automatic quantification of structural interpretation uncertainties during seismic imaging. It opens numerous perspectives that I think worthwhile to investigate, and that would be necessary for applying the method on real cases.

Updating of the uncertainty envelope

The first topic to work on is the updating of the uncertainty envelope. It is currently the missing piece to close the velocity model updating loop. Two main approaches can be considered to perform this step. It can be computed either from the set of perturbed seismic images or from the image variability estimations (or as combination of both).

The most direct way to update the envelope using the perturbed seismic images is to use automatic seismic interpretation methods (as discussed in sections 1.5 and 2.4.2). The interpretation can be performed for example on the mean amplitude image. Another solution can consists in interpreting independently each perturbed seismic image, and to compute facies probabilities (that is, *Sediments*, *Uncertain* and *Salt* probabilities) for each pixel from these interpretations. A classification rule can then be defined based on these probabilities.

The alternative is to update the uncertainty envelope using the estimated image variability. As this variability is defined as one or several scalar fields (that is, mean and standard deviation images), we can consider using an approach inspired from level-set [e.g., Kadlec et al., 2009, Haukås et al., 2013] or surface wrapping [e.g., Carlson, 2010, Haukås et al., 2017] methods to deform the initial uncertainty envelope boundaries. There may also be some interesting elements to prospect in the domain of topology optimization [see e.g., Rozvany, 2009, for a review], provided that we can define an optimization criterion from these scalar fields.

Limitation of the computational cost

A major limitation of the study proposed in chapter 4 is the necessity to perform a large number of migrations of the seismic data. It currently limits the applicability of such studies to 2D data sets. Applying it to 3D data sets would require to drastically reduce the number of required migrations. A first solution can consist in selecting a representative subset of the simulated velocity models [e.g., Suzuki et al., 2008, Scheidt and Caers, 2009]. In addition, the diversification of the indicators used to characterize the structural uncertainties and their cross analysis can help extracting more information out a given set of images. We have only considered some GLCM attributes in this first study, but the literature about the use of seismic attributes for structural interpretation is rich and would be worth to explore. Furthermore, this would allow for the application of this study to geological contexts different from salt tectonics.

Impact of sediment velocity uncertainty

A major assumption in chapter 4 is that we know the exact background sediment velocity model. It helps us focus on the salt structural uncertainty impact, but this condition is never met with field data. In order to use the workflow of chapter 4 on real data sets, an important line of research that should be investigated is the assessment of the impact of sediment velocity uncertainty on seismic imaging. This requires to investigate how varying sediment layer geometries and velocities affect seismic images. This perspective is therefore related with the necessity of developing tools to model the sediment geometries associated with salt bodies (i.e., halokinetic sequences, megaflaps, etc.). Such a sensitivity analysis would require, however, to perform a large amount of tests (and thus, again, of migrations). A way to limit this number may consists in using smooth sediment velocity models, as in conventional imaging applications. On the one hand, it would attenuate the impact of errors about the exact geometry of layers and faults. On the other hand, it helps to limit the internal reflections introduced by sharp reflectors, which can introduce artifacts during RTM [Biondi, 2006]. Last but not least, a similar assumption was made about salt homogeneity. Cap rock formation and internal salt heterogeneity are, however, frequent and important to take into account during imaging [Jones and Davison, 2014]. Therefore, their impact should also be investigated during the sensitivity analysis.

Appendix A

Seismic image segmentation for detection of salt bodies using multiscale attributes and unsupervised classifier

This appendix develops the MSc work of Capucine Legentil. It was presented at the 2019 RING Meeting [Legentil et al., 2019].

Abstract The manual interpretation of seismic data is a time-consuming process and automation is more efficient to extract information from various types of data. We propose a workflow to semi-automatically segment seismic data into regions: salt, sediments and "uncertain". The latter contains the transition between sediments and the salt bodies. This region is created to avoid over-interpretation and localize interpretation uncertainties. To increase the robustness of the method, we combine multi-attribute classification and multi-scale representation. We choose to handle seismic attributes at coarser scales which are closer to those of the salt domes that we want to interpret. The creation of multi-scale segmented images implies combining them to build a single interpretation. The interscale fusion combines strengths from both large and small scale detections: robustness and detail preservation. Our workflow consists of four steps. First, we choose a set of seismic attributes whose answers are different enough to separate the three regions. Second, each attribute is computed at coarser scales using Gaussian pyramid decomposition. Third, a k-means clustering is applied at each scale using the previously chosen attributes to build a map. This map contains the probabilities for each pixel to be in each region. Finally, an image fusion, based on Markov random Fields and interscale dependencies, is performed to obtain a single segmented image at the finest scale. We have tested the workflow on several seismic data sets. The results demonstrate good match between seismic images and interpreted regions, and the contribution of multi-scale approach for noise reduction.

Introduction

Salt geobodies possibly form stratigraphic traps for hydrocarbons because of their impermeability. An understanding of salt tectonics and detection of salt bodies are therefore critical to effective exploration for oil and gas. When submitted to stress, the salt moves upward in a ductile manner through the overlying sediments. A wide variety of three-dimensional forms reflects different stages in the upward migration of salt as shown in figure A.1.

The manual interpretation of seismic data is a time-consuming process and the type of highlighted structures depends on the interpreter and its experience [Bond et al., 2007]. For the last decades, automatic and semi-automatic seismic interpretations have been a relevant research topic to reduce both influence of manual detection and interpretation time. Automatic seismic interpretation implies two main steps: the first one aims

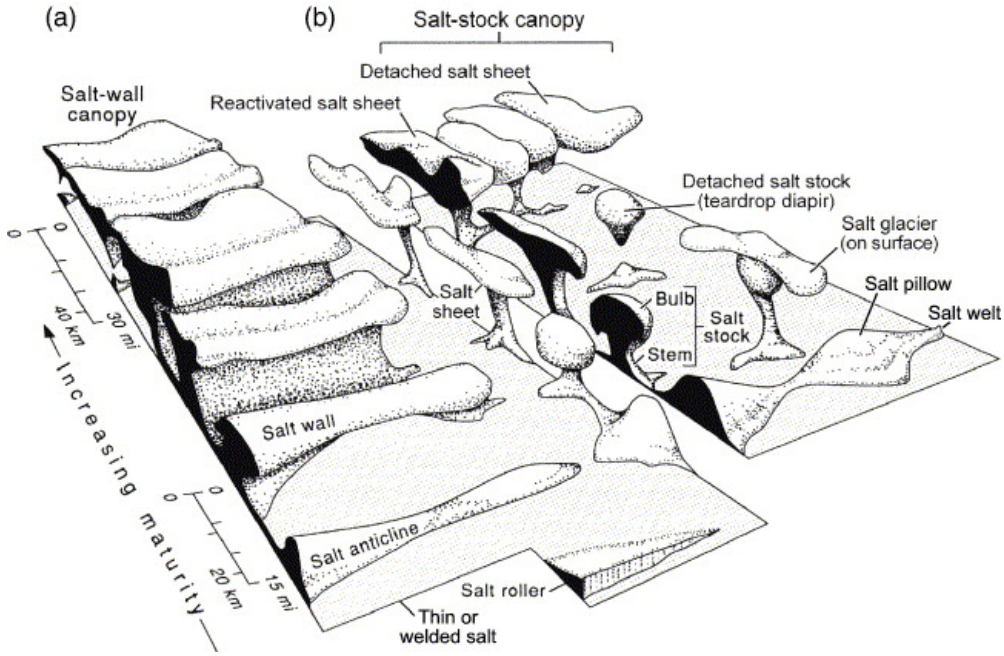

Figure A.1 – Block diagram showing schematic shapes of salt structures. Structural maturity and size increase toward the composite, coalesced structures in the background. (a) Elongated structures rising from line sources. (b) Structures rising from point sources. Image from Hudec and Jackson [2007].

at highlighting the objects (often thanks to seismic attributes); the second step consists in the object extraction (thanks for example to image segmentation methods). Image segmentation is a decomposition of an image into regions that make sense. Numerous works have already been carried out on automated salt interpretation [e.g., Berthelot et al., 2013, Wu, 2016, Waldeland et al., 2018, Di and Gao, 2017, Alfarraj et al., 2018]. The aim of all these works is to find the boundary between the salt and the sediments i.e., a surface.

A lot of works have been done on automatic or semi-automatic detection of salt geobodies from seismic data, and especially from seismic attributes. Chopra and Marfurt [2005] define seismic attributes as all quantities obtained by measurement, computation or mathematical transformation from seismic data. They provide the interpreter with new images that enhance descriptions of the subsurface. The aim of many of the automatic detection methods is to highlight edges of salt domes and then extract the information to segment images. To spot discontinuities between salt and sediment, authors compute texture attributes [Berthelot et al., 2013, Wu, 2016] and others that highlight the boundary [Di and Gao, 2017, Shafiq et al., 2017]. They often use attributes that have a different response to salt and sediments.

After the attribute computation, extraction becomes a classic problem of image segmentation. There are several methods of segmentation used in salt detection : Normalized Cuts for Image Segmentation (NCIS) [Lomask et al., 2007, Hale and Emanuel, 2003, Halpert and Clapp, 2008], k-means and stochastic clustering [Di et al., 2018a, Hale and Emanuel, 2003], and active contours based methods [Zhang and Halpert, 2012, Haukås et al., 2013].

Seismic data are, however, very noisy and results of automated detection methods are not always geologically consistent. The objects we are interested in are large scale structures. This implies a larger spatial correlation of interpretations than can be obtained at small noise-sensitive scales such as pixel scale in seismic images. In order to improve the spatial correlation (and thus the continuity) of the interpreted structures, one a common solution consists in using multi-scale representations. Common applications of multi-scale representations can be found in image processing, such as image enhancement, visualization and analysis of medical data, as well as remote sensing, automated cartography, data compression or denoising. It is also commonly used in seismic interpretation, as numerous methods use the frequency decomposition of the seismic signal. These approaches are based on the wavelet theory. Similar multi-scale representations also exist in the spatial domain, based on the scale-space theory, but they are much less studied in seismic interpretation.

We propose a workflow to semi-automatically segment seismic data into regions as suggested by Haukås et al. [2017]: "sediment", "salt" and "uncertain". The latter contains the transition between sediments and the salt bodies. The goal of this classification is to model directly volumes (the geological layers) rather than surfaces (horizons that are bounding these layers). As seismic image segmentation based on a single attribute is not always sufficient to produce an accurate result [Halpert and Clapp, 2008], we use a multi-attribute classification approach based on an k-means classifier [e.g., Di et al., 2018a]. To overcome the lack of spatial continuity that can be encountered when using unsupervised classification methods, we propose to combine the k-means classifier with the a multi-scale representation. We use Gaussian pyramids [Lindeberg, 1994], which are widely spread in the image processing domain.

Whether with several attributes or with multiple scales, the use of multiple attributes and scales implies creation of a set of images that must be combined to build a single interpretation. This unique interpretation has to combine the information provided by all the images. The higher number of sources of information, the higher the risk of conflicting interpretations is; combination of all the interpretations is therefore a major challenge of this project.

The solution we retained to integrate both the multi-attribute and the multi-scale information consists in four steps. First, the interpreter carefully selects a set of seismic attributes that segregates the different categories to interpret. Then, each attribute is decomposed at several coarser scales using Gaussian pyramids. At each scale, all the attributes are given as input of k-means classifier, in order to obtain a single interpreted image per scale. The last step consists in combining each scale interpretation into a single, final interpretation at the finest scale. This process is known as image fusion. As the fine scales are more sensitive to noise, classification at fine scale has to depend on the coarser scales to increase the spatial correlation of the interpretation and thus its geological consistency. The interscale dependencies are formulated as a Bayesian inference problem based on Markov random fields (MRF).

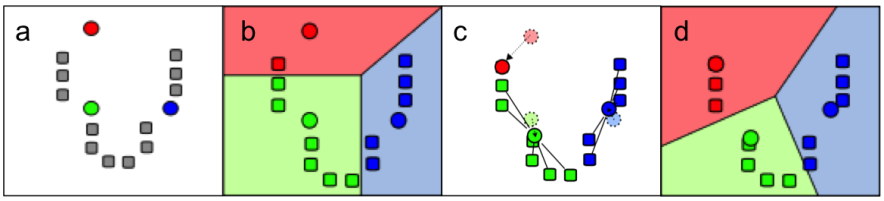

Figure A.2 – Illustration of k-means clustering of 12 points. (a) Initialization of three clusters (centroids are represented by circles). (b) Each point is affected to the closest cluster. (c)Update of cluster centroids by calculating the barycenter of the new cluster. (d) Step (b) and (c) are repeated until convergence is not reached [Wikipedia contributors, 2019]

Methodology

Multi-attribute K-Means clustering

Principle

K-means clustering [MacQueen, 1967] is a partitioning method initially used for signal processing. It is very popular in cluster analysis and data mining. It aims to partition n observations into k clusters in which each observation belongs to the cluster with the nearest mean. This method consists of four steps. First, the clusters are randomly initialized, *i.e.* the centroids coordinates are defined (figure A.2 (a)). Second, each observation is affected to the nearest cluster. The choice of the belonging cluster is guided by the computation of the Euclidean distance between observation and each centroid (figure A.2 (b)). Third, centroid positions are updated by computing the mean of observations which belong to the cluster (figure A.2 (c)). Finally, the second and third steps are repeated as long as the convergence criterion is not reached (figure A.2 (d)), *i.e.* when the centroid coordinates do not change between two iterations.

Algorithm

Attribute pre-process As we are using seismic attributes rather than Cartesian coordinates, it is not possible to define an "Euclidean distance to centroids". If we want the attributes to have the same weight when computing the distance between the points and the centroids, the different attribute range of values must be similar. Attributes are therefore centered and reduced, but it is not sufficient to restrict attribute values to the same interval (Di et al. [2018a]). According to the empirical three-sigma rule, in a normal distribution 99.73% of the values lie within a band around the mean (μ) with a width of six standard deviations (σ). For 99% of the values ($\simeq 6\sigma$) to be centered between -0.5 and 0.5 we apply this normalization:

$$\frac{x-\mu}{6\sigma} \tag{4.10}$$

Use of manual picking The result of k-means clustering depends on the initialization of centroids coordinates. To integrate geological knowledge and enhance the classification results, we decided to initialize the centroid positions from interpreted data [e.g., Di et al., 2018a]. We manually picked on a seismic section three sets of

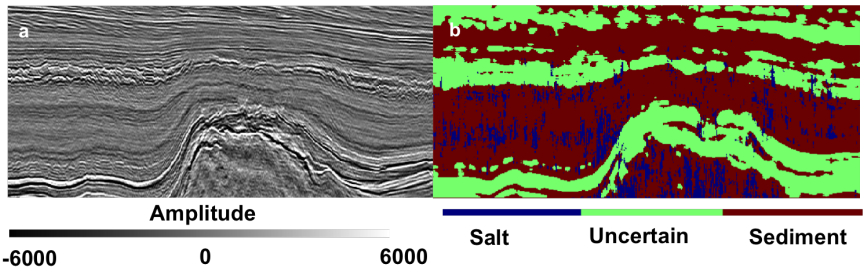

Figure A.3 – Results of the k-means clustering on the F3 block data set. (a) Initial seismic image. (b) Classification result using four attributes: GLCM angular second moment, GLCM sum of squares, dip variance, semblance.

points which represent the three classes (salt, sediments and uncertain), examples are given in figures A.17 (a) and A.18 (a). The three cluster centers are then initialized using the statistical means of their associated point set. Point sets can also be used during the clustering to help guide automated data interpretation or after the classification for results verification.

Probability Map The k-means output is categorical: each cell is associated to a given cluster. The method we use to perform the image fusion requires, however, to know for each cell the probability of belonging to each cluster. We consider that the probability p_i for a cell to belong to a cluster i is inversely proportional to its distance to each cluster. The probability p_i is estimated as follows:

$$p_i = \frac{\frac{1}{d_i}}{\sum_{j=0}^{k} \frac{1}{d_j}}, \text{ with } d_j \text{ the distance to cluster } j \tag{4.11}$$

Noise sensitivity The use of multi-attributes is very helpful for a more accurate automated interpretation, but due to the noise of the initial seismic data, classification results of k-means clustering can be noisy and insufficient for a good interpretation. The interpreted geological objects can be discontinuous such as in the figure A.3: it is difficult to recognize the shape of the salt body even if structures are recognizable. The uncertain areas contain the strong reflectors. The regions interpreted as sediments correspond to areas where reflections are more or less organized. The cells interpreted as salt are in regions where reflections are chaotic.

The classification at pixel scale is not sufficient to preserve the continuity of geological structures. To solve this problem, we propose to combine a multi-scale representation with the unsupervised classifier, to integrate more information about the spatial correlation of the structures during the interpretation.

Multi-scale decomposition using Gaussian pyramid

Objects are not identifiable at all scales. Human vision is really performing: if we move away from a scene, the eye is able to merge the small scales to constitute an object of larger scale. Seismic images are very noisy and an automatic interpretation at the pixel scale can cause artefacts or errors that a man could avoid. At coarser scales, noise

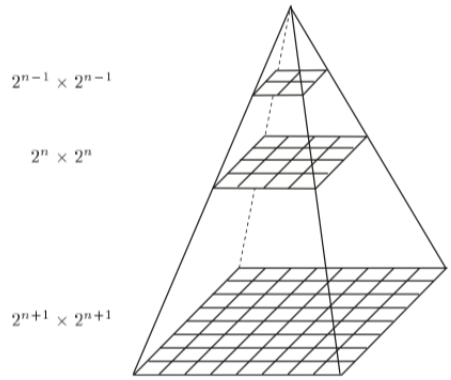

Figure A.4 – A pyramid representation is obtained by successively reducing the image size by combined smoothing and sub-sampling. Image from Lindeberg [1994]

is reduced and predictions can be more consistent because these scales are closer to the scales of the salt bodies that we want to interpret. Similar representations exist both in the spatial and frequency domains based on two main approaches: Scale space and wavelet Theory. We chose the spatial approach for this project for its ease of application. One of the most used multi-scale representations is the Gaussian pyramid [figure A.4, Lindeberg, 1994]. It combines a sub-sampling operation with a smoothing step (a low-pass filtering operation).

Smoothing To build the coarser level, the image is convolved with a Gaussian low-pass filter. A low-pass filter smooths contours and reduces noise. The smoothing filter is based on Gaussian function. Smoothing of signal is more important by increasing the size of the filter kernel. The Gaussian smoothing preserves low-frequency details and can produce a hazy effect. During the application of this filter, a kernel is computed from a Gaussian function and applied on each cell of the picture. In that way, a new value is computed for each cell by weighting the values of surrounding cells with the kernel coefficients. Information about the neighborhood of each pixel is preserved after the sub-sampling, thanks to this smoothing step.

Sub-sampling After the filtering, only one sample out of two is kept (figure A.5). The number of pixels decreases by a factor 2 at each scale as shown in figure A.4. The original image corresponds to the base level (level 0).

Scale parameter The Gaussian pyramid is characterized by the size of the Gaussian kernel and the sampling step used for suppressing fine-scale structures. In his works, Burt [1981] introduced the scale parameter t. In the case of Gaussian pyramid decomposition, the scale parameter $t = \sigma^2$ is the variance of the smoothing kernel. In the implementation of Gaussian smoothing filter, the kernel size is related to the variance value according the three-sigma rule. To estimate t, it is then sufficient to compute the equivalent kernel size k for each pyramid level. The equivalent kernel is the kernel that should be used to obtain a level directly from the original image. The size depends on

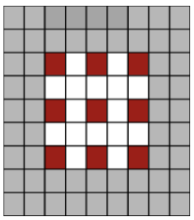

Figure A.5 – Sub-sampling principle, the red cells are kept and the gray ones are ignored because of the side effect of the Gaussian smoothing

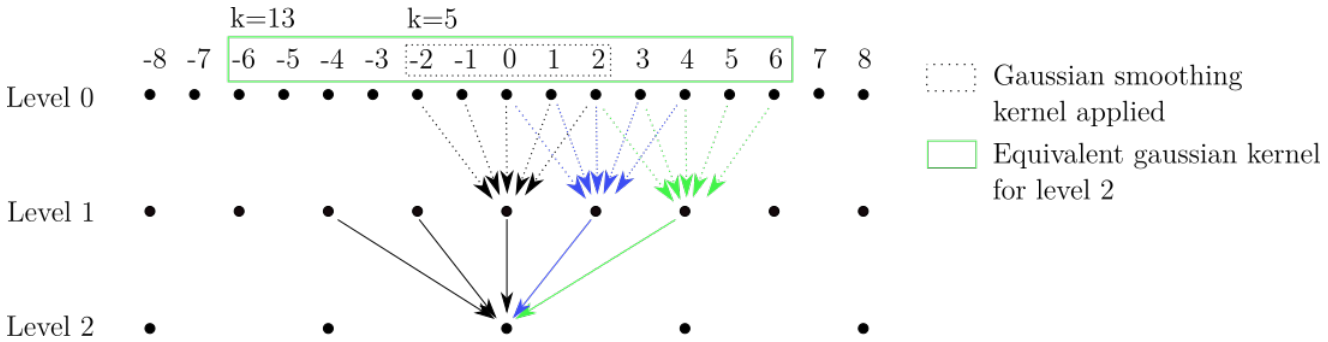

Figure A.6 – Concept of equivalent kernel, when the Gaussian smoothing kernel half-size $m = 2$ and sampling step $r = 2$. Modified from Burt [1981]

the level number l, the sampling step r and the half-size of the Gaussian kernel m, such as presented in figure A.6, following the relation:

$$k = 2\ (m\ \frac{r^l - 1}{r - 1}) + 1 \tag{4.12}$$

The scale parameter provides information about the structures that are still visible at each scale. In fact, image structures of spatial extent smaller than about $\sqrt{t}$ have largely been smoothed away in the scale-space level at scale t. For example, at the fifth level the structures with a spatial size smaller than 10 cells will be smoothed away.

Interscale Fusion

As previously stated, at finest scales classification results can be noisy due to the noisy seismic data and inherent misinterpretations of unsupervised classifiers. The Gaussian pyramid decomposition offers a way to relate each fine-scale cell to several blocks at coarser scales (figure A.7). The next step thus consists in bringing out a single interpretation from the information provided by each scale. This step is called interscale fusion.

Markov random field and Bayesian interscale decision fusion Kim et al. [2009] proposed an interscale fusion method based on Markov random field and Bayesian texture segmentation. To fusion two adjacent pyramid levels, we only use the outputs of the k-means clustering (probability map for adjacent parent scale and neighborhood classification).

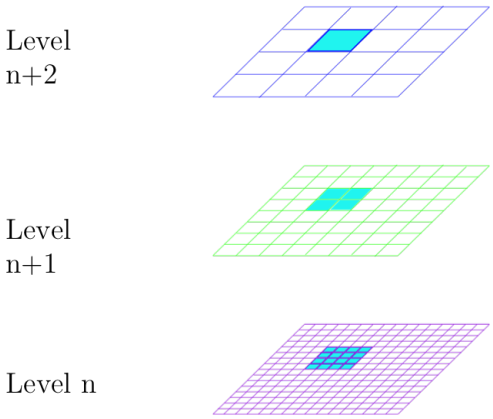

Figure A.7 – Dependency blocks of cells in the pyramid, represented in blue.

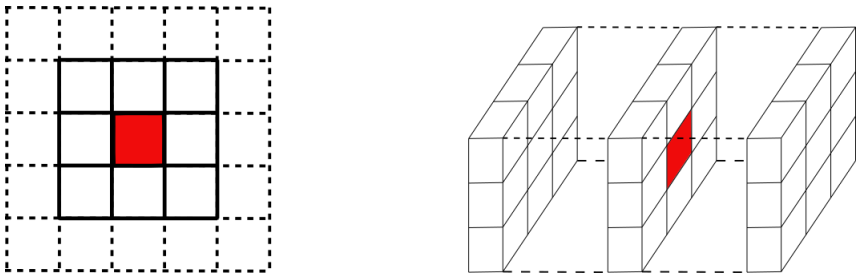

Figure A.8 – Neighbors used for the image fusion in 2D (left) or 3D (right) around a central cell in red.

For each cell i at a given scale s, Kim et al. [2009] define a context vector v_i^s which contains the class label of its parent cell and that of their neighbors. The set of context vectors at scale s forms a random vector field V^s defined as $V^s = \{v_i^s | \forall i \in M^s\}$, where M^s is the set of cells that the image contains at scale s. From the set of random fields (one is defined per scale), they define the "best" configuration C^{s*} (i.e. labeling) of V^s by using segmentation based on the naive Bayes rule:

$$C^{s*} = \text{argmax}_{C^s \in \Omega^s} \{p(V^{s+1}|C^s)p(V^s|C^s)p(C^s)\} \tag{4.13}$$

where Ω^s is the set of all possible segmentations. In our case, the probability $p(C^s)$ is computed from the probability map of k-means clustering. The probabilities $p(V^s|C^s)$ and $p(V^{s+1}|C^s)$ are computed from the random fields V^s and V^{s+1} which contain information about scale s and adjacent parent scale $s+1$. For the decision fusion rule, the computed probabilities relied on cell neighbors. The neighborhood is defined around the cell as a square in 2D or a cube in 3D such as presented in figure A.8.

Interscale dependency between class label Making the assumption that all v_i^s are independent, the probability $p(V^{s+1}|C^s)$ of the Eq. 4.13 can be rewritten as [Kim et al., 2009]:

$$p(V^{s+1}|C^s) = \prod_{i \in M^s} p(v_i^{s+1}|c_i^s) \tag{4.14}$$

The scale $s+1$ is closer to the scale of the object that we want to interpret, we assume that the classification is more geologically consistent and less noisy. We propose

to introduce an interscale dependency between two scales. It is a very important factor in the fusion rule. We estimate $p(v_i^{s+1}|c_i^s)$ as follows:

$$p(v_i^{s+1}|c_i^s) = \frac{\text{number of neighbors with the label } c_i^s}{\text{number of neighbors}} \tag{4.15}$$

Textural continuity prior The probability $p(V^s|C^s)$ represents the dependency of cell neighbors at scale s and can be written as follows [Kim et al., 2009]:

$$p(V^{s+1}|C^s) = \prod_{i \in M^s} p(v_i^s|c_i^s) \tag{4.16}$$

In the final interpretation, texture should be continuous as much as possible. To do that we use the same MRF smoothness prior as Kim et al. [2009], which is based on Gibbs distribution :

$$p(v_i^s|c_i^s) = \frac{1}{\sum_{c_i^s \in L} \exp\left(-\sum_{c_j^s \in v_j^s} V_2(c_i^s, c_j^s)\right)} \exp\left(-\sum_{c_j^s \in v_j^s} V_2(c_i^s, c_j^s)\right), \tag{4.17}$$

where

$$V_2(c_i^s, c_j^s) = \begin{cases} -\beta & \text{if i and j have the same label} \\ \beta & \text{otherwise} \end{cases} \tag{4.18}$$

where β is a positive constant. The exploitation of neighbors information is not the same for the scales s and $s+1$. The expression (4.17) is less restrictive than (4.15). In fact, probability $p(v_i^s|c_i^s)$ is strictly positive. None of the classes can be dismissed with this part of the decision rule.

Posterior probability from unsupervised classifier The classification was carried out at each scale of the pyramid. Probability map is used as a part of the decision fusion rule. It contains a posterior probability of belonging to each class for all cells. The term $p(C^s)$ becomes :

$$p(C^s) = \prod_{i \in M^s} p(c_i^s) \tag{4.19}$$

where $p(c_i^s)$ is obtained from the probability map of the k-means classification (using equation 4.11). In our case, from equations 4.13, 4.15, 4.17 and 4.19, the decision rule for each cell of scale s can be simply written as follows:

$$c_i^s = \text{argmax}_{c_i^s \in L}\{p(v_i^{s+1}|c_i^s)p(v_i^s|c_i^s)p(c_i^s)\} \tag{4.20}$$

where L is the set of possible class labels (salt, sediments or "uncertain").

Results

We tested the workflow on two seismic amplitude data sets. The first one is known as the F3 block, located offshore Netherlands and provided by dGB Earth Sciences B.V through the OpendTect software. The second one is the SEG Advanced Modeling

(SEAM) Phase I data set, provided by SEG Advanced Modeling Corporation. As a reminder, the objective is to segment seismic images into three regions : salt, sediments and "uncertain".

Multi-scale attribute choice

First, we choose a set of seismic attributes whose answers are different enough to separate the three regions. The choice has been made following criteria defined in Berthelot et al. [2013]. They define simple criteria to avoid redundancy with texture attributes for the problem of salt segmentation. The chosen attributes have to:

- allow to isolate one of the class.
- show homogeneity of values within each class.
- show different responses between classes.

Different tests have been realized and some examples of attributes that we chose, are presented in figure A.9. The semblance or dip variance (figure A.9) show different answers between the salt and the sediment, even if it is not the case everywhere in the sediment because of noisy initial seismic data. Sediments seem very homogeneous. Berthelot et al. [2013] and Di et al. [2018a] relied on several texture attributes such as attributes based on the Gray Level Co-Occurence Matrix (GLCM) introduced by Haralick et al. [1973]. GLCM angular second moment is a measure of homogeneity of an image. A homogeneous scene contains only a few gray levels, giving a GLCM with only a few but relatively high values. GLCM correlation and GLCM variance attributes show a low variance inside the salt but also in areas covered by sub-horizontal reflectors (figure A.9).

To verify that the chosen attributes are good enough and able to perform the classification, a cross-plot is used. The cross-plot between dip variance and GLCM angular second moment shows that the three clusters can easily be separated before classification (figure A.10).

However, some points are near the boundary between two classes, they can be misinterpreted by the automatic classifier. After the classification, clusters are given in figure A.11 and some misinterpretations are visible in the red circles. The obtained clusters are consistent with the picked initial data.

Multi-attribute classification

Figure A.3 illustrates the result of k-means clustering on the F3 block. To obtain these results, the initialization of the three clusters was made with an interpreted point set presented in figure A.17 with four attributes (GLCM angular second moment, GLCM sum of squares, dip variance, semblance).

After visual inspection, the results seem to be pretty good. The visible objects with the seismic amplitude are generally correctly classified but the geological continuity is not always respected. To evaluate classification results and to know if the model can make robust predictions, we use the point set previously presented to build a confusion matrix. From this confusion matrix, some evaluation markers are calculated such as

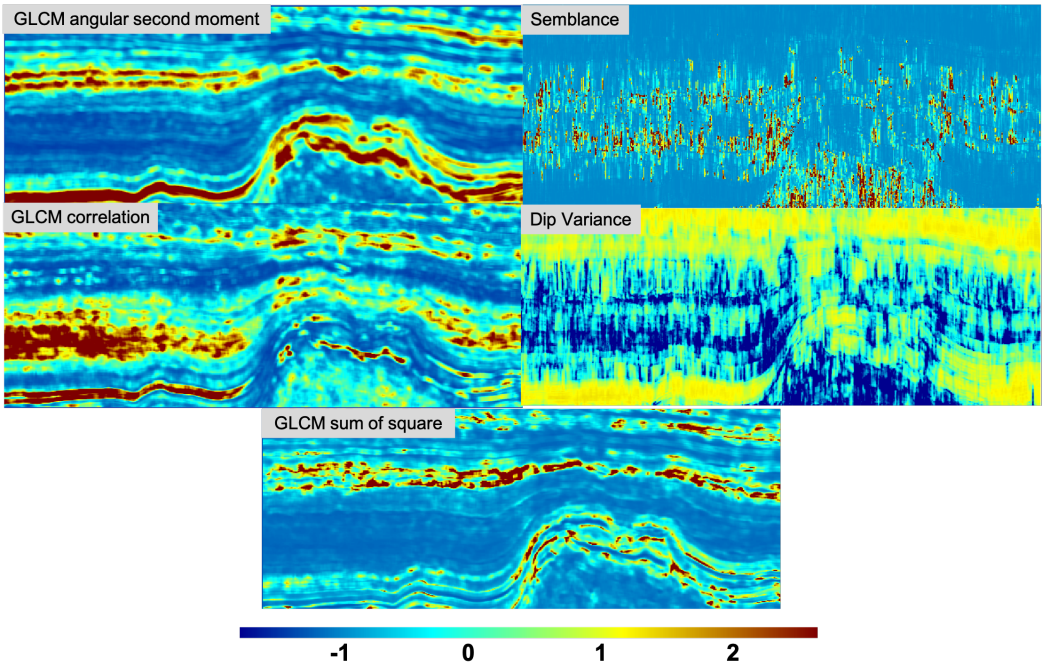

Figure A.9 – Examples of seismic attributes used in the segmentation process (computed from the F3 block amplitude cube).

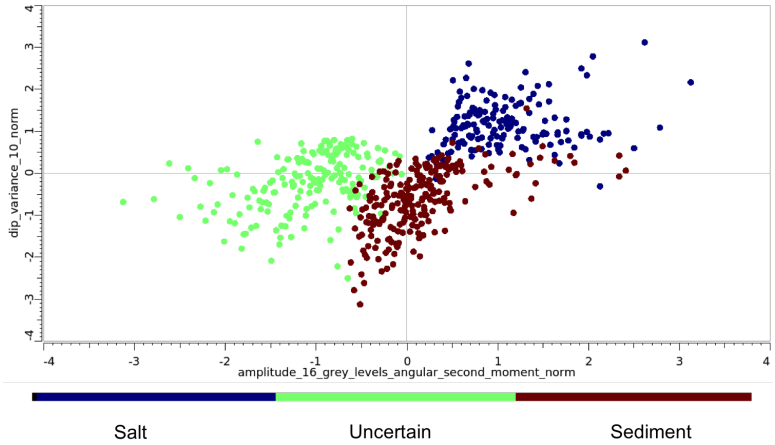

Figure A.10 – Cross-plot between dip variance and GLCM angular second moment shows a good possibility to define three clusters. Three attributes (dip variance, GLCM angular second moment and GLCM correlation) have been used for this cross-plot, the figure is a projection of the 3D space onto the (angular second moment; dip variance) plane.

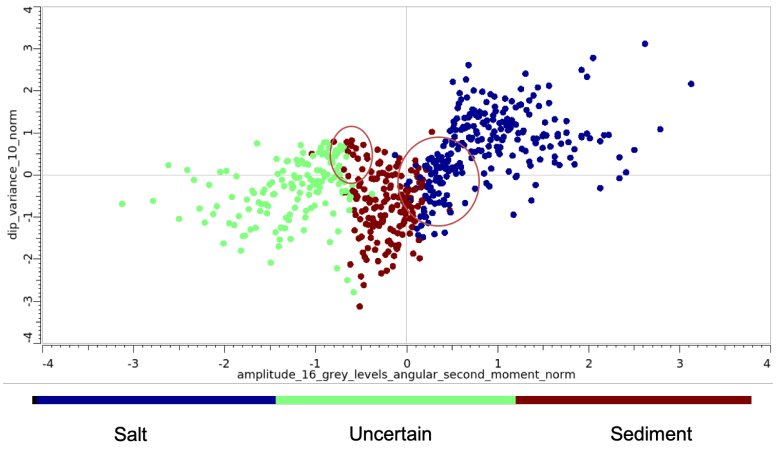

Figure A.11 – Cross-plot between dip variance and GLCM angular second moment after the classification shows that the obtained clusters are globally consistent with the picked initial data presented in figure A.10. The red circles indicate the location of the misinterpreted values, at the boundary between clusters.

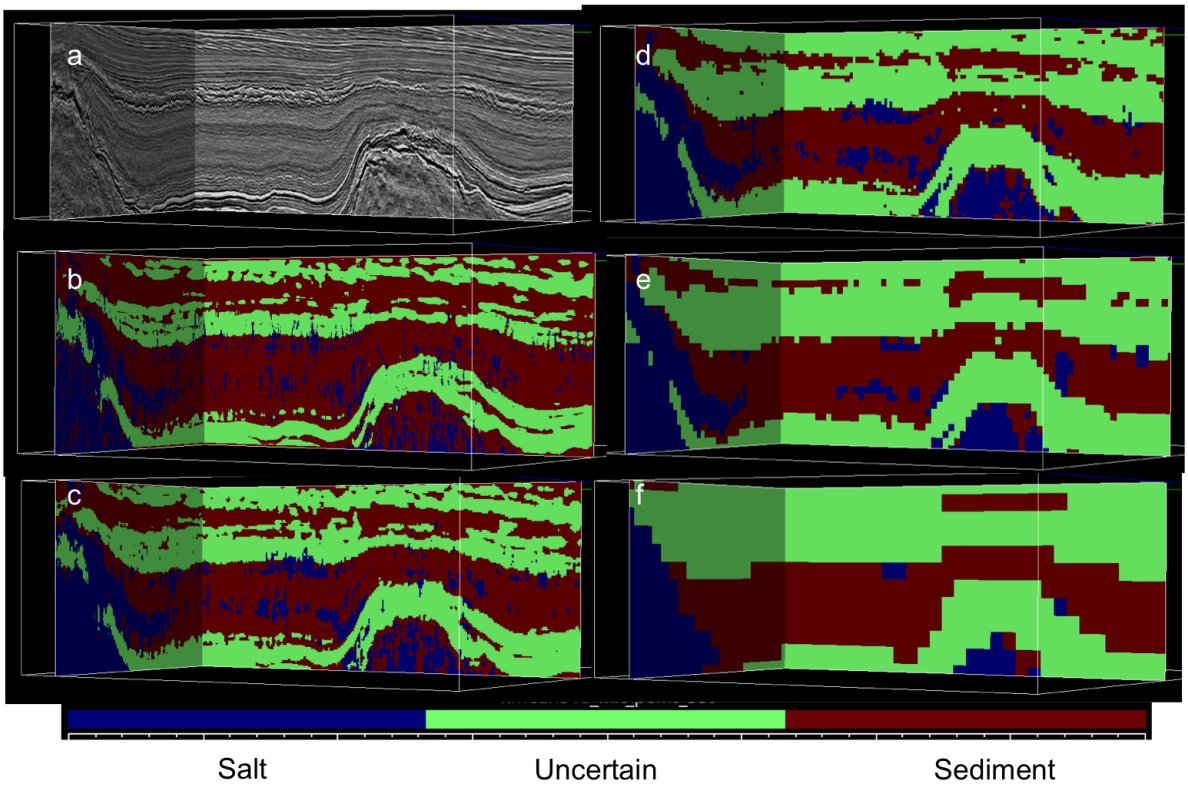

Figure A.12 – Classification results for the F3 block after Gaussian pyramid decomposition (levels 1 to 5 (b to f)) using four attributes (GLCM angular second moment, GLCM sum of squares, dip variance, semblance).

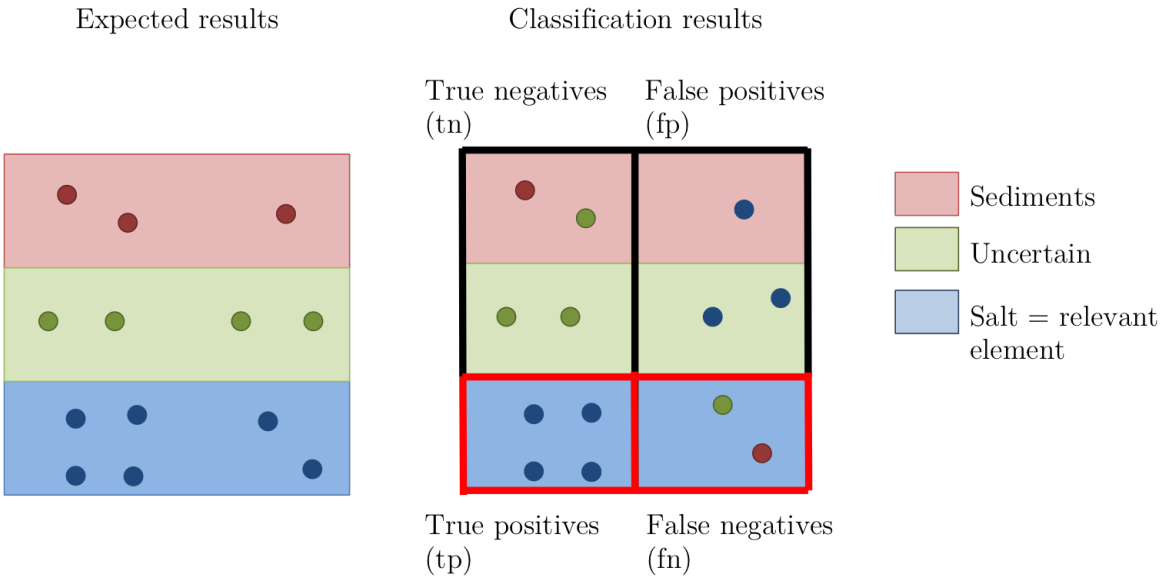

Figure A.13 – Evaluation of the classification results for the "salt" label. The circles are the data set, their colors correspond to the classifier prediction, the background color corresponds to the ground truth.

Precision	$\frac{tp}{tp+fp}$
Recall	$\frac{tp}{tp+fn}$
Accuracy	$\frac{tp+tn}{tp+tn+fp+fn}$

Table 4.1 – Evaluation markers for a classification, notations are explained in the figure A.13

precision, recall and accuracy (Tab. 4.1 and figure A.13). Accuracy is the proportion of correct predictions made by the model. Classification accuracy alone is typically not enough information to make this decision. Precision and recall answer the following questions, respectively: What proportion of positive identifications was actually correct? And what proportion of actual positive results has been identified correctly?

In the F3 seismic cube, our model has an accuracy of 80% and, however a precision of 62,5% and a recall of 34,4% for the salt. In other words, when the classifier predicts that a cell is salt, its prediction is right in 62,5% of cases and it correctly identifies 34,4% of the salt.

	Salt	Uncertain	Sediment	Overall
Precision	62.5%	79.8%	70.2%	70.9%
Recall	34.4%	92.2%	78.6%	68.5%
Accuracy	80.4%	91.6%	72.5%	81.5%

Table 4.2 – Evaluation of classification results on the seismic cube F3.

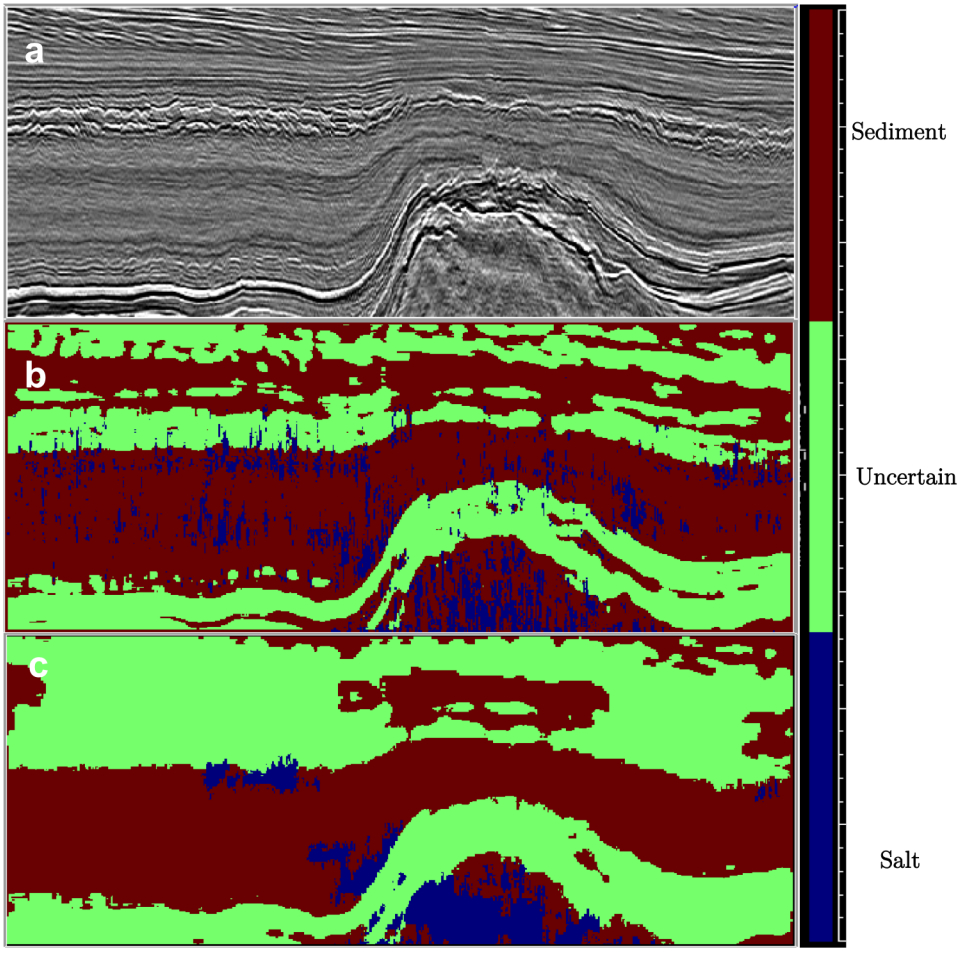

Figure A.14 – Fusion results on a section of the F3 block using four attributes (GLCM angular second moment, GLCM sum of squares, dip variance, semblance), (a) amplitude, (b) before fusion and (c) after fusion

Interscale fusion

From each attribute computed on the F3 block, we built a 5-level Gaussian pyramid. For each level, a k-means clustering is performed using the attribute images computed at this level. Figure A.12 illustrates the result of the classification at each level. At the finest scale (figures A.12 (a) and (b)), there is a lot of noise, especially in the salt, while noise is almost absent at the coarsest scale (figure A.12 (f)). The interpretation seems therefore to be more precise at the finest scale but more robust at coarse scale.

To combine the precision of interpretation of the fine scales and robustness of detection at coarse scale, we perform an image fusion. The results of the fusion are presented in Figs. A.14, A.15 and A.16. Figures A.14 and A.15 are time-slices extracted from the F3 block. Figure A.16 shows sections extracted from the SEAM data set. The initialization of the three clusters is made with a manually interpreted point set (Fig A.18). Unlike the F3 block, the classification on the SEAM model is carried out with only three attributes: GLCM angular second moment, GLCM correlation and dip variance.

For the two seismic cubes, the results are visually better after the interscale fusion operation. The classification results are much less pixelated when using a multi-scale

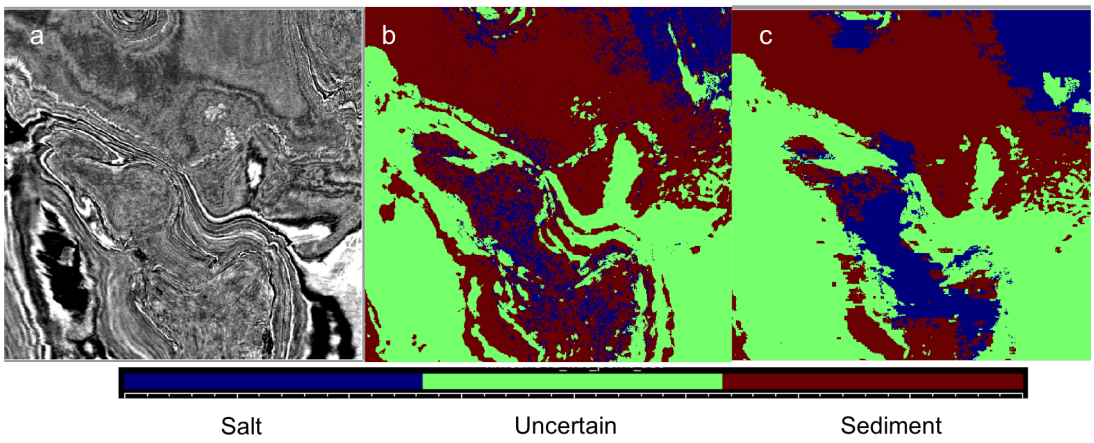

Figure A.15 – Fusion results on a time slice of the F3 block using four attributes (GLCM angular second moment, GLCM sum of squares, dip variance, semblance), (a) amplitude, (b) before fusion and (c) after fusion

approach (Figs. A.14, A.15 and A.16). This confirms that multi-scale representation and image fusion can bring more spatial correlation in the segmentation process. The results on the F3 block (Figs. A.14 and A.15) highlight, however, a major drawback of the application: the "uncertain" region represents about half of the data set and the fusion tends to increase this proportion. It can be explained by the fact that the classifier is strongly influenced by the choice of the input attributes, which are themselves sensitive to the input amplitude. After classification on the F3 block, the categories "sediments", "uncertain" and "salt" correspond more to "strong reflections", "moderate/low reflections" and "chaotic patterns", rather than to lithological categories. The same phenomenon is observable on the SEAM data set (figure A.16). The strongest reflectors (the sea floor and the top salt boundary) are classified as "uncertain". The salt is globally well identified. The sediment classification is, however, much more hazardous. Where good reflectors are present (in the upper third of the cube), the algorithm prediction is relatively reliable (especially after image fusion). In the rest of the cube (where the reflections are weaker, even nonexistent), the classifier only detect, however, salt as the signal is chaotic.

As for the evaluation after the classification, the initialization point set is used to build the confusion matrix and estimate the precision, recall and accuracy of the classifier (figures A.17 (b) and A.18 (b)). Figure A.17 (b) demonstrates the results presented in table 4.3, the classification for the salt is very precise, the prediction is right in 94.8% of cases. There are few areas interpreted as salt in the sediments. And the recall for the uncertain class is very good, the classifier correctly identifies 92.2% of the uncertain areas. On the other side, the recall for the salt objects is lower, in fact in the salt body it remains a lot of cells interpreted as sediments. The precision for uncertain area is also relatively low, the area interpreted as uncertain are correct in 63.3% of cases. This is due to the seafloor at the top of the seismic cube. The area is wider after the interscale fusion because of the misinterpretations of the coarser levels. Overall, after the interscale fusion, the classification results are better. Precision and recall are higher, there are fewer misinterpretations. For the seismic cube from the SEAM challenge, the impact of the interscale fusion is less visible. However, the used

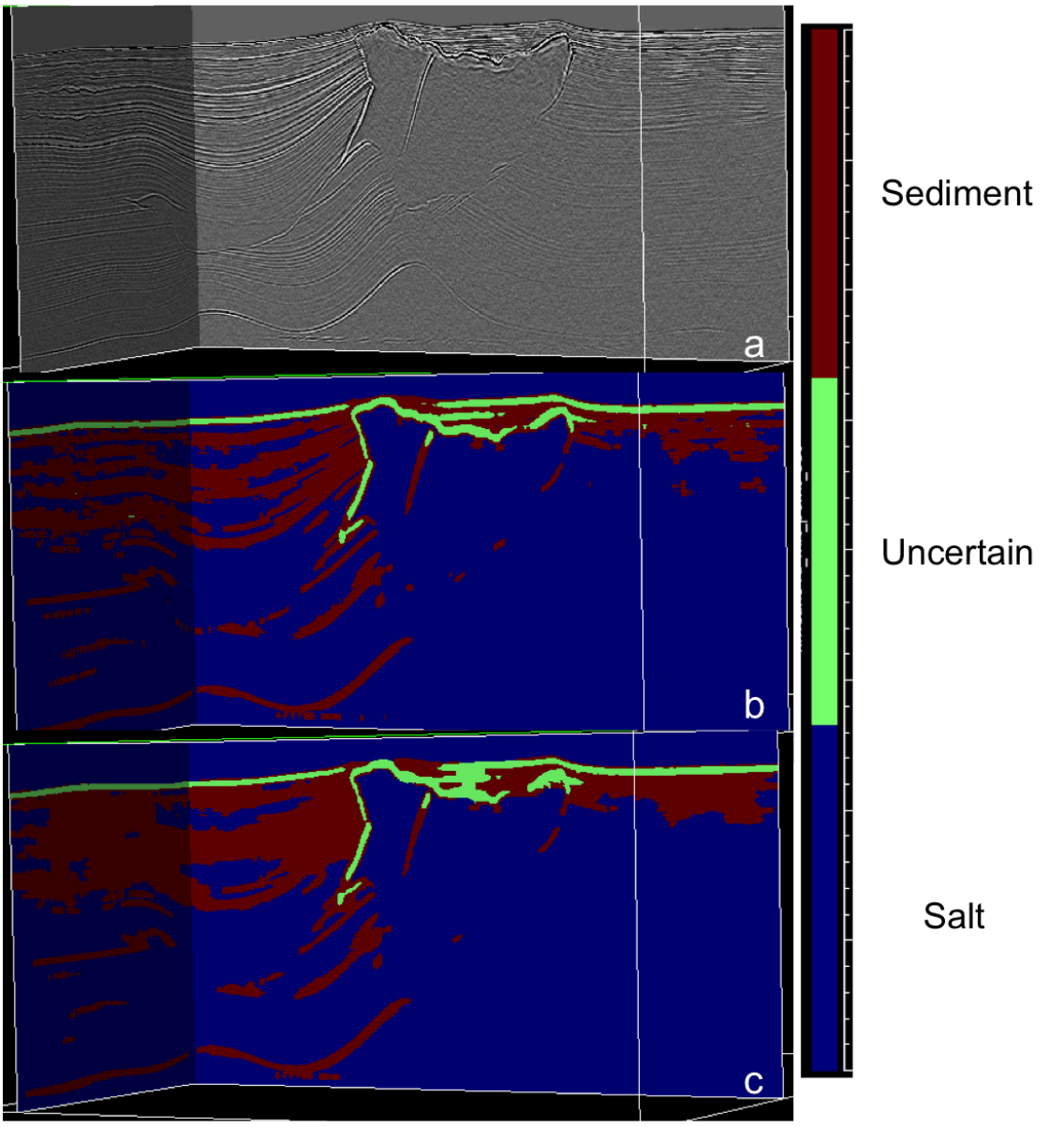

Figure A.16 – Fusion results for the SEAM seismic cube using three attributes (GLCM angular second moment, GLCM correlation, dip variance), (a) amplitude, (b) before fusion and (c) after fusion

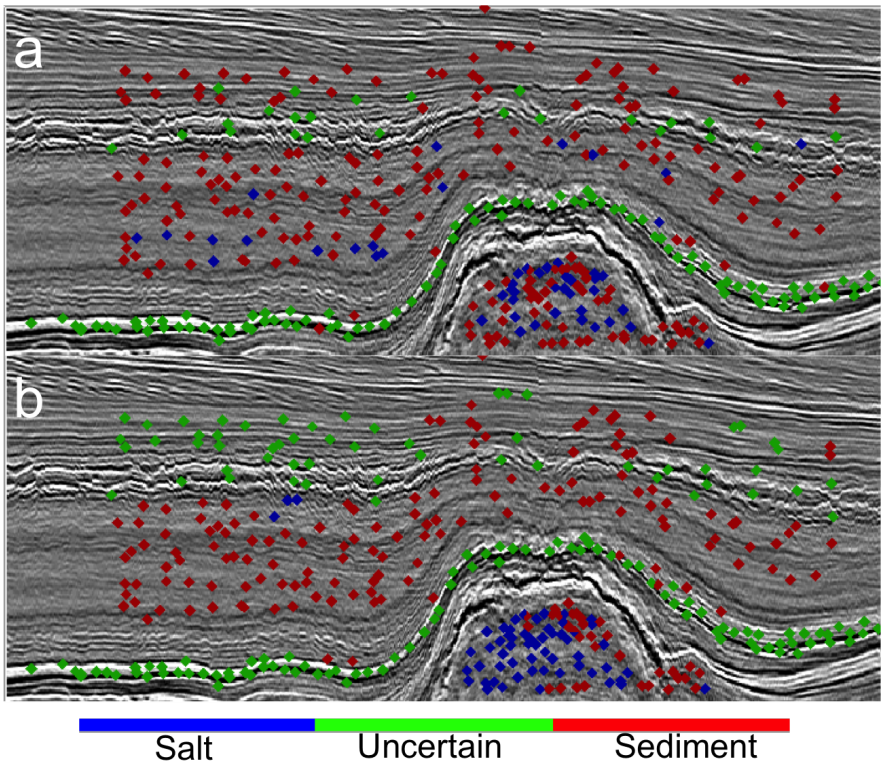

Figure A.17 – Results painted on the point set in the F3 seismic cube, (a) before and (b) after the interscale fusion

	Salt	Uncertain	Sediment	Overall
Precision	94.8%	63.3%	77%	78.4%
Recall	63.2%	92.2%	69.8%	75%
Accuracy	90.8%	83.5%	74.3%	82.9%

Table 4.3 – Evaluation of classification results on the seismic cube F3 after the interscale fusion.

point set presented figure A.18 did not take into consideration the bottom sediment part of the cube. But the global recall is better, the interpretation of the classifier are correct in 83.4% of cases in the top part of the slice.

Discussion and perspectives

Results depend on the choice of attributes, and some artefacts due to the computation of seismic attributes are still visible in the classification. So it will be very interesting to run this workflow with other attributes combinations to find the best attributes or just with more attributes. If more attributes are used for the classification, a principal component analysis (PCA) could be performed to avoid as much as possible the redundant information. It could also help the user to choose a simpler attribute combination (choose the most relevant attributes) to reduce the running time.

To decompose the different attributes with the Gaussian pyramid, we had two

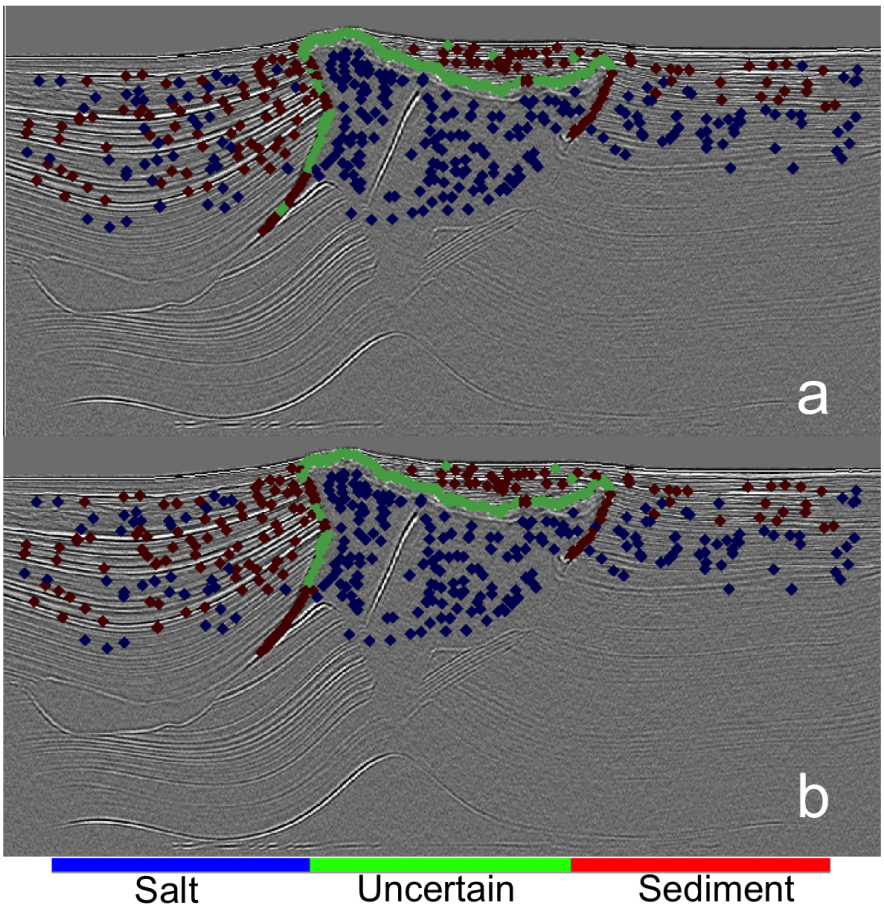

Figure A.18 – Results painted on the point set in the SEAM seismic cube, (a) before and (b) after the interscale fusion

	Salt		Uncertain		Sediment		Overall	
	Before Fusion	After Fusion	Before Fusion	After Fusion	Before Fusion	After Fusion	Before Fusion	After Fusion
Precision	98%	96.6%	61%	63%	76%	56.7%	78.3%	72%
Recall	79.8%	76.6%	100%	99.4%	53.6%	74.3%	77.8%	83.9%
Accuracy	92.8%	91.4%	82.3%	83.5%	75%	75.3%	83.4%	83.4%

Table 4.4 – Evaluation of classification results on the seismic cube from SEAM challenge before and after the interscale fusion.

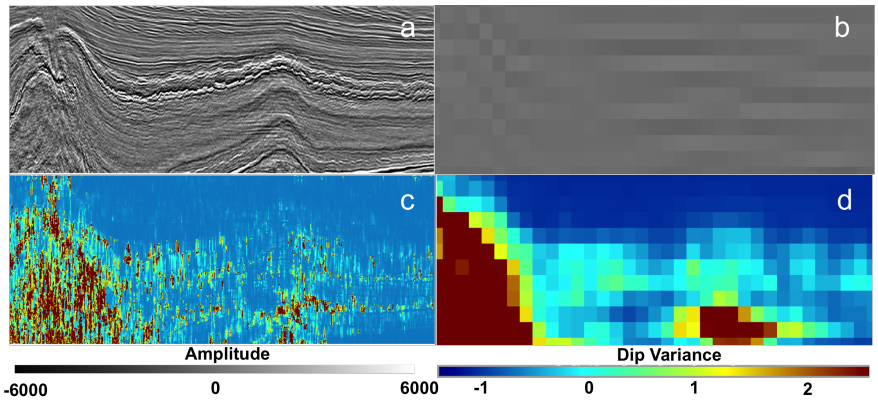

Figure A.19 – Results of the Gaussian pyramid decomposition on two seismic attributes: amplitude and dip variance at initial level (a) and (c), and fifth level

choices : first the amplitude is decomposed with the Gaussian pyramid (smoothing and sub-sampling steps) and the attributes are computed from this decomposed amplitude at each scale; second, the attributes are computed at the initial scale from the initial amplitude and then decomposed with the Gaussian pyramid. We chose the second possibility due to the amplitude properties: it is an oscillating signal with a small wavelength as compared to the smoothing kernel size. Successive smoothing and sub-sampling of the amplitude thus rapidly cancel the seismic signal, making it unusable. Figure A.19 (b) shows this canceling effect, at the fifth level, geological structures have almost disappeared. On the other hand, the decomposition does not have the same effect on the dip variance (figures A.19 (c) and (d)). Structures are highlighted in the coarser scales and they are more homogeneous. Noise due to the computation of this attribute is significantly reduced.

Conclusion

We proposed and implemented a workflow that allows to semi-automatically segment seismic data into regions: salt, sediments and "uncertain". It combines the strengths of the multi-attribute and multi-scale methods. The choice of attributes is the key to obtain relevant results with the k-means algorithm. A statistical procedure could help the user to find the best combination to highlight the three classes. The multi-scale approach improves the computer vision thanks to the robustness of large scale detection and precision of small scale detection. The interscale fusion is necessary to reduce noise and misinterpretations in the final results. The combination of multi-scale interpretations is the major challenge. The application of the workflow to realistic data sets has highlighted the difficulty to define segmentation criteria consistently with the target classes, but has proven its capacity to efficiently segment seismic data. Future work could focus on applying the workflow to directly extract the salt boundary (i.e. segmenting "boundary zone" and "salt or sediments") as the current results are very sensitive to strong reflections.

Acknowledgments

This work was performed in the frame of the RING project (http://ring.georessources.univ-lorraine.fr/) at Université de Lorraine. We would like to thank for their support the industrial and academic sponsors of the RING-GOCAD Consortium managed by ASGA. The software corresponding to this paper is available as the Goscope plugin of SKUA-Gocad geomodeling software. We also acknowledge Paradigm for the SKUA-Gocad Software and development kit.

Bibliography

P. Abrahamsen. Bayesian kriging for seismic depth conversion of a multi-layer reservoir. In *Geostatistics Tróia '92*, p. 385–398, 1993. doi: 10.1007/978-94-011-1739-5_31. (Cited p. 9, 40, 41, 83)

E. H. Adelson, C. H. Anderson, J. R. Bergen, P. J. Burt, and J. M. Ogden. Pyramid methods in image processing. *RCA engineer*, 29: 33–41, 1984. (Cited p. 27, 29)

M. Alfarraj, H. Di, and G. AlRegib. Multiscale Fusion for Improved Instantaneous Attribute Analysis. In *79th EAGE Conference and Exhibition 2017*, 2017. doi: 10.3997/2214-4609.201700530. (Cited p. 27)

M. Alfarraj, Y. Alaudah, Z. Long, and G. AlRegib. Multiresolution analysis and learning for computational seismic interpretation. *The Leading Edge*, 37(6): 443–450, 2018. doi: 10.1190/tle37060443.1. (Cited p. 25, 27, 123)

A. Amin and M. Deriche. A new approach for salt dome detection using a 3D multidirectional edge detector. *Applied Geophysics*, 12(3): 334–342, 2015. doi: 10.1007/s11770-015-0512-2. (Cited p. 22, 24, 39)

P. Anquez. *Correction et simplification de modèles géologiques par frontières: impact sur le maillage et la simulation numérique en sismologie et hydrodynamique.* PhD thesis, Université de Lorraine, 2019. (Cited p. 3)

A. Aqrawi, T. Boe, and S. Barros. Detecting salt domes using a dip guided 3D Sobel seismic attribute. In *SEG Technical Program Expanded Abstracts 2011*, p. 1014–1018, 2011. doi: 10.1190/1.3627377. (Cited p. 22, 39)

ASGA. SIGMA - Seismic Imaging for GeoModel Analysis. https://www.ring-team.org/software, 2019. (Cited p. 90, 91)

C. A. Baar. *Applied salt-rock mechanics 1: the in-situ behavior of salt rocks*, vol. 16. Elsevier, 1977. doi: 10.1016/B978-0-444-41500-4.X5001-0. (Cited p. 4, 61)

G. E. Backus. Long-wave elastic anisotropy produced by horizontal layering. *Journal of Geophysical Research*, 67(11): 4427–4440, 1962. doi: 10.1029/JZ067i011p04427. (Cited p. 91)

M. Bahorich and S. Farmer. 3-D seismic discontinuity for faults and stratigraphic features: The coherence cube. *The Leading Edge*, 14(10): 1053–1058, 1995. (Cited p. 21)

A. E. Barnes. Redundant and useless seismic attributes. *GEOPHYSICS*, 72(3): P33–P38, 2007. doi: 10.1190/1.2716717. (Cited p. 21, 23)

E. Baysal, D. D. Kosloff, and J. W. C. Sherwood. Reverse time migration. *GEOPHYSICS*, 48(11): 1514–1524, 1983. doi: 10.1190/1.1441434. (Cited p. 91)

A. Berthelot, A. Solberg, E. Morisbak, and L.-J. Gelius. Salt diapirs without well defined boundaries - a feasibility study of semi-automatic detection. *Geophysical Prospecting*, 59(4): 682–696, 2011. doi: 10.1111/j.1365-2478.2011.00950.x. (Cited p. 23, 25, 26, 39)

A. Berthelot, A. Solberg, and L.-J. Gelius. Texture attributes for detection of salt. *Journal of Applied Geophysics*, 88: 52–69, 2013. doi: 10.1016/j.jappgeo.2012.09.006. (Cited p. 21, 22, 25, 26, 27, 34, 39, 40, 123, 131)

S. Beucher and C. Lantuéjoul. Use of watersheds in contour detection. In *International Workshop on Image Processing: Real-time Edge and Motion Detection/Estimation*, 1979. (Cited p. 65)

B. L. Biondi. 3D Seismic Imaging. *Investigations in Geophysics*, 14: 1–247, 2006. doi: 10.1190/1.9781560801689. (Cited p. 109, 120)

A. Bistacchi, M. Massironi, G. V. Dal Piaz, G. Dal Piaz, B. Monopoli, A. Schiavo, and G. Toffolon. 3d fold and fault reconstruction with an uncertainty model: An example from an Alpine tunnel case study. *Computers & Geosciences*, 34(4): 351–372, 2008. doi: 10.1016/j.cageo.2007.04.002. (Cited p. vii, 28, 116)

C. E. Bond. Uncertainty in structural interpretation: Lessons to be learnt. *Journal of Structural Geology*, 74: 185–200, 2015. doi: 10.1016/j.jsg.2015.03.003. (Cited p. 1, 2)

C. E. Bond, A. D. Gibbs, Z. K. Shipton, and S. Jones. What do you think this is? "Conceptual uncertainty" in geoscience interpretation. *GSA Today*, 17(11): 4–10, 2007. doi: 10.1130/GSAT01711A.1. (Cited p. 2, 9, 16, 40, 122)

C. E. Bond, R. Lunn, Z. Shipton, and A. Lunn. What makes an expert effective at interpreting seismic images? *Geology*, 40(1): 75–78, 2012. doi: 10.1130/G32375.1. (Cited p. 2)

A. R. Brown. Seismic attributes and their classification. *The Leading Edge*, 15(10): 1090, 1996. doi: 10.1190/1.1437208. (Cited p. 19)

A. R. Brown. *Interpretation of Three-Dimensional Seismic Data*. Society of Exploration Geophysicists and American Association of Petroleum Geologists, seventh edition, 2011. doi: 10.1190/1.9781560802884. (Cited p. v, 16, 17, 18, 24)

K. P. Bube, J. A. Kane, T. Nemeth, D. Medwede, and O. Mikhailov. The influence of stacking velocity uncertainties on structural uncertainties. In *SEG Technical Program Expanded Abstracts 2004*, 2004a. doi: 10.1190/1.1851209. (Cited p. 83)

K. P. Bube, T. Nemeth, O. Mikhailov, D. Medwede, and J. A. Kane. The influence of uncertainties in anisotropy on structural uncertainties. In *SEG Technical Program Expanded Abstracts 2004*, 2004b. doi: 10.1190/1.1851210. (Cited p. 83)

P. J. Burt. Fast filter transform for image processing. *Computer Graphics and Image Processing*, 16(1): 20–51, 1981. doi: 10.1016/0146-664X(81)90092-7. (Cited p. 127, 128)

J. A. Carlson. *Surface Wrapping : A Deformable Mesh Approach to Semi-Automatic 3D Volume Segmentation*. PhD Thesis, University of Colorado, 2010. (Cited p. 25, 111, 119)

G. Caumon. Towards Stochastic Time-Varying Geological Modeling. *Mathematical Geosciences*, 42(5): 555–569, 2010. doi: 10.1007/s11004-010-9280-y. (Cited p. 2)

G. Caumon. Geological Objects and Physical Parameter Fields in the Subsurface: A Review. In *Handbook of Mathematical Geosciences*, p. 567–588. Springer International Publishing, 2018. doi: 10.1007/978-3-319-78999-6_28. (Cited p. 2, 9)

G. Caumon, A.-L. Tertois, and L. Zhang. Elements for Stochastic Structural Perturbation of Stratigraphic Models. In *EAGE Conference on Petroleum Geostatistics*, p. 10–14, 2007. doi: 10.3997/2214-4609.201403041. (Cited p. 2, 10, 41)

CeGP. LANDMASS:Large North-Sea dataset of migrated aggregated seismic structures. https://cegp.ece.gatech.edu/codedata/landmass/, 2015. (Cited p. 26)

T. C. Chamberlin. The method of multiple working hypotheses. *Science*, 15: 92–96, 1890. (Cited p. 2)

S. Chopra and K. J. Marfurt. Seismic attributes — A historical perspective. *GEOPHYSICS*, 70(5): 3SO–28SO, 2005. doi: 10.1190/1.2098670. (Cited p. 21, 123)

S. Chopra and K. J. Marfurt. Emerging and future trends in seismic attributes. *The Leading Edge*, 27(3): 298, 2008. doi: 10.1190/1.2896620. (Cited p. 21)

J. F. Claerbout. *Earth soundings analysis: Processing versus inversion*, vol. 6. Blackwell Scientific Publications Boston, 1992. (Cited p. 39)

N. Clausolles, P. Collon, and G. Caumon. Generating variable shapes of salt geobodies from seismic images and prior geological knowledge. *Interpretation*, 7(4): T829–T841, 2019a. doi: 10.1190/INT-2019-0032.1. (Cited p. 11, 38)

N. Clausolles, P. Collon, G. Caumon, and M. Irakarama. Stochastic salt modeling for characterizing seismic imaging uncertainties. In *2019 Ring Meeting*, p. 113–126, 2019b. (Cited p. 110)

F. Collino and C. Tsogka. Application of the perfectly matched absorbing layer model to the linear elastodynamic problem in anisotropic heterogeneous media. *GEOPHYSICS*, 66(1): 294–307, 2001. doi: 10.1190/1.1444908. (Cited p. 90)

P. Collon, A. Pichat, C. Kergaravat, A. Botella, G. Caumon, J.-C. Ringenbach, and J.-P. Callot. 3d modelling from outcrop data in a salt tectonic context: Example from the Inceyol mini-basin, Sivas Basin, Turkey. *Interpretation*, 4(3): SM17–SM31, 2016. doi: 10.1190/INT-2015-0178.1. (Cited p. v, vii, 10, 118)

J. Cousty, G. Bertrand, L. Najman, and M. Couprie. Watershed cuts: Minimum spanning forests and the drop of water principle. *IEEE Transactions on Pattern Analysis and Machine Intelligence*, 31(8): 1362–1374, 2009. doi: 10.1109/TPAMI.2008.173. (Cited p. viii, 65, 66)

R. M. Dalley, E. C. A. Gevers, G. M. Stampfli, D. J. Davies, C. N. Gastaldi, P. A. Ruijtenberg, and G. J. O. Vermeer. Dip and azimuth displays for 3D seismic interpretation. *First Break*, 7(3): 86–95, 1989. (Cited p. 21)

E. A. de Kemp. Visualization of complex geological structures using 3-D Bézier construction tools. *Computers & Geosciences*, 25(5): 581 – 597, 1999. doi: 10.1016/S0098-3004(98)00159-9. (Cited p. 75)

J. Dellinger, A. Brenders, J. Sandschaper, C. Regone, J. Etgen, I. Ahmed, and K. Lee. The Garden Banks model experience. *The Leading Edge*, 36(2): 151–158, 2017. doi: 10.1190/tle36020151.1. (Cited p. 7, 9, 22, 39, 82, 84, 86, 109)

dGB Earth Sciences B. V. Netherlands offshore F3 block, complete. https://www.opendtect.org/osr/Main/NetherlandsOffshoreF3BlockComplete4GB, 1987. (Cited p. 20, 30, 31, 33)

H. Di and D. Gao. Gray-level transformation and Canny edge detection for 3d seismic discontinuity enhancement. *Computers and Geosciences*, 72: 192–200, 2014. doi: 10.1016/j.cageo.2014.07.011. (Cited p. 22)

H. Di and D. Gao. Nonlinear gray-level co-occurrence matrix texture analysis for improved seismic facies interpretation. *Interpretation*, 5(3): SJ31–SJ40, 2017. doi: 10.1190/INT-2016-0214.1. (Cited p. 123)

H. Di, M. Shafiq, and G. AlRegib. Multi-attribute k-means clustering for salt-boundary delineation from three-dimensional seismic data. *Geophysical Journal International*, 215: 1999–2007, 2018a. doi: 10.1093/gji/ggy376. (Cited p. 25, 26, 34, 35, 39, 40, 123, 124, 125, 131)

H. Di, Z. Wang, and G. AlRegib. Real-time seismic-image interpretation via deconvolutional neural network. In *SEG Technical Program Expanded Abstracts 2018*, p. 2051–2055, 2018b. doi: 10.1190/segam2018-2997303.1. (Cited p. 25, 27)

T. P. Dooley, M. P. Jackson, and M. R. Hudec. Inflation and deflation of deeply buried salt stocks during lateral shortening. *Journal of Structural Geology*, 31(6): 582–600, 2009. doi: 10.1016/j.jsg.2009.03.013. (Cited p. 54, 59)

C. G. Eichkitz, J. Amtmann, and M. G. Schreilechner. Calculation of grey level co-occurrence matrix-based seismic attributes in three dimensions. *Computers and Geosciences*, 60: 176–183, 2013. doi: 10.1016/j.cageo.2013.07.006. (Cited p. 21, 33, 34)

Emerson E&P Software. SKUA-GOCAD Software Suite. https://www.pdgm.com/products/skua-gocad/, 2019. (Cited p. 12, 36, 87)

G. C. Fehmers and C. F. W. Höcker. Fast structural interpretation with structure-oriented filtering. *GEOPHYSICS*, 68(4): 1286, 2003. doi: 10.1190/1.1598121. (Cited p. 23, 35)

P. F. Felzenszwalb and D. P. Huttenlocher. Efficient Graph-Based Image Segmentation. *International Journal of Computer Vision*, 59(2): 167–181, 2004. doi: 10.1023/B:VISI.0000022288.19776.77. (Cited p. 25)

S. Fomel. Time-migration velocity analysis by velocity continuation. *GEOPHYSICS*, 68(5): 1662–1672, 2003. doi: 10.1190/1.1620640. (Cited p. 83)

S. Fomel. Velocity analysis using AB semblance. *Geophysical Prospecting*, 57(3): 311–321, 2009. doi: 10.1111/j.1365-2478.2008.00741.x. (Cited p. 25)

S. Fomel and E. Landa. Structural uncertainty of time-migrated seismic images. *Journal of Applied Geophysics*, 101: 27–30, 2014. doi: 10.1016/j.jappgeo.2013.11.010. (Cited p. 9, 52, 83)

H. Fossen. *Structural geology*. Cambridge University Press, second edition, 2016. (Cited p. 5, 39)

R. Frodeman. Geological reasoning: Geology as an interpretive and historical science. *GSA Bulletin*, 107: 960–968, 1995. doi: 10.1130/0016-7606(1995)107<0960:GRGAAI>2.3.CO;2. (Cited p. 1, 2, 16, 17)

D. Gao. Volume texture extraction for 3D seismic visualization and interpretation. *GEOPHYSICS*, 68(4): 1294–1302, 2003. doi: 10.1190/1.1598122. (Cited p. 19, 21, 39)

S. Geman and D. Geman. Stochastic relaxation, Gibbs distributions, and the Bayesian restoration of images. In *IEEE Transactions on pattern analysis and machine intelligence*, 6, p. 721–741, 1984. doi: TPAMI.1984.4767596. (Cited p. 50)

L. Gemmer, S. J. Ings, S. Medvedev, and C. Beaumont. Salt tectonics driven by differential sediment loading: stability analysis and finite-element experiments. *Basin Research*, 16(2): 199–218, 2004. doi: 10.1111/j.1365-2117.2004.00229.x. (Cited p. 6)

K. A. Giles and T. F. Lawton. Halokinetic sequence stratigraphy adjacent to the El Papalote diapir, northeastern Mexico. *AAPG Bulletin*, 86, 2002. doi: 10.1306/61EEDBAC-173E-11D7-8645000102C1865D. (Cited p. ix, 118)

K. A. Giles and M. G. Rowan. Concepts in halokinetic-sequence deformation and stratigraphy. *Geological Society, London, Special Publications*, 363: 7–31, 2012. doi: 10.1144/SP363.2. (Cited p. ix, 45, 47, 58, 118)

J. Giraud, E. Pakyuz-Charrier, M. Jessell, M. Lindsay, R. Martin, and V. Ogarko. Uncertainty reduction through geologically conditioned petrophysical constraints in joint inversion. *GEOPHYSICS*, 82(6): ID19–ID34, 2017. doi: 10.1190/geo2016-0615.1. (Cited p. 3)

G. Godefroy, G. Caumon, M. Ford, G. Laurent, and C. A.-L. Jackson. A parametric fault displacement model to introduce kinematic control into modeling faults from sparse data. *Interpretation*, 6(2): B1–B13, 2018. doi: 10.1190/INT-2017-0059.1. (Cited p. 76)

G. Godefroy, G. Caumon, G. Laurent, and F. Bonneau. Structural Interpretation of Sparse Fault Data Using Graph Theory and Geological Rules: Fault Data Interpretation. *Mathematical Geosciences*, 51(8): 1091–1107, 2019. doi: 10.1007/s11004-019-09800-0. (Cited p. 2)

H. Grubb, A. Tura, and C. Hanitzsch. Estimating and interpreting velocity uncertainty in migrated images and AVO attributes. *GEOPHYSICS*, 66(4): 1208–1216, 2001. doi: 10.1190/1.1487067. (Cited p. 83)

F. B. Guardiano and R. M. Srivastava. Multivariate geostatistics: beyond bivariate moments. In *Geostatistics Tróia '92*, p. 133–144, 1993. doi: 10.1007/978-94-011-1739-5_12. (Cited p. 21, 54)

P. Guillen, G. Larrazabal*, G. González, D. Boumber, and R. Vilalta. Supervised learning to detect salt body. In *SEG Technical Program Expanded Abstracts 2015*, p. 1826–1829, 2015. doi: 10.1190/segam2015-5931401.1. (Cited p. 25)

D. Hale. Structure-oriented smoothing and semblance. *CWP Report*, 635, 2009. (Cited p. 23, 35, 92)

D. Hale and J. Emanuel. Seismic interpretation using global image segmentation. *73rd Ann. Internat. Mtg.: Soc. of Expl. Geophys*, p. 2410–2413, 2003. doi: 10.1190/1.1817860. (Cited p. 123)

A. Halpert and R. G. Clapp. Salt body segmentation with dip and frequency attributes. *Stanford Exploration Project*, 136, 2008. (Cited p. 22, 24, 39, 123, 124)

A. D. Halpert, R. G. Clapp, and B. Biondi. Salt delineation via interpreter-guided 3d seismic image segmentation. *Interpretation*, 2(2): T79–T88, 2014. doi: 10.1190/INT-2013-0159.1. (Cited p. 24)

R. Haralick, K. Shanmugan, and I. Dinstein. Textural features for image classification. In *IEEE Transactions on Systems, Man and Cybernetics*, vol. 3, p. 610–621, 1973. doi: 10.1109/TSMC.1973.4309314. (Cited p. ix, 21, 39, 105, 131)

J. Haukås, O. Ravndal, B. Fotland, A. Bounaim, and L. Sonneland. Automated salt body extraction from seismic data using the level set method. *First Break*, 31(4): 35–42, 2013. doi: 10.3997/1365-2397.2013009. (Cited p. 25, 39, 111, 119, 123)

J. Haukås, A. Bounaim, and O. Gramstad. Automated salt interpretation, Part II : Smooth surface wrapping of volume attribute. In *SEG Technical Program Expanded Abstracts 2017*, p. 2076–2080, 2017. doi: 10.1190/segam2017-17739151.1. (Cited p. 25, 28, 39, 40, 41, 52, 112, 116, 119, 124)

V. Henrion, G. Caumon, and N. Cherpeau. ODSIM: An Object-Distance Simulation Method for Conditioning Complex Natural Structures. *Mathematical Geosciences*, 42 (8): 911–924, 2010. doi: 10.1007/s11004-010-9299-0. (Cited p. vii, 41, 50, 54, 70, 71, 74)

D. A. Herron. *First steps in seismic interpretation*. Society of Exploration Geophysicists, 2011. doi: 10.1190/1.9781560802938. (Cited p. vi, 16, 21, 23, 93)

L. Holden, P. Mostad, B. F. Nielsen, J. Gjerde, C. Townsend, and S. Ottesen. Stochastic Structural Modeling. *Mathematical Geology*, 35(8): 899–914, 2003. doi: 10.1023/B:MATG.0000011584.51162.69. (Cited p. 10)

Z. Huang, M. Zou, N. Carr, and T. Ju. Topology-controlled Reconstruction of Multi-labelled Domains from Cross-sections. *ACM Transactions on Graphics*, 36(4): 76, 2017. (Cited p. 52)

M. R. Hudec and M. P. A. Jackson. Terra infirma: Understanding salt tectonics. *Earth-Science Reviews*, 82(1-2): 1–28, 2007. doi: 10.1016/j.earscirev.2007.01.001. (Cited p. 3, 4, 6, 39, 123)

M. Irakarama, G. Laurent, J. Renaudeau, and G. Caumon. Finite Difference Implicit Modeling of Geological Structures. In *80th EAGE Conference and Exhibition 2018*, 2018. doi: 10.3997/2214-4609.201800794. (Cited p. 43, 74)

M. Irakarama, P. Cupillard, G. Caumon, P. Sava, and J. Edwards. Appraising structural interpretations using seismic data—theoretical elements. *Geophysics*, 84(2): N29–N40, 2019. doi: 10.1190/geo2018-0128.1. (Cited p. 10, 93)

C. A.-L. Jackson and M. Lewis. Origin of an anhydrite sheath encircling a salt diapir and implications for the seismic imaging of steep-sided salt structures, Egersund Basin, Northern North Sea. *Journal of the Geological Society*, 169(5): 593–599, 2012. doi: 10.1144/0016-76492011-126. (Cited p. 9, 39, 42, 86, 109)

C. A.-L. Jackson, Y. Zhang, D. A. Herron, and P. J. Fitch. Subsurface expression of a salt weld, Gulf of Mexico. *Petroleum Geoscience*, 25(1): 102–111, 2019. doi: 10.1144/petgeo2018-008. (Cited p. 59)

M. P. A. Jackson and C. Cramez. Seismic recognition of salt welds in salt tectonics regimes. In *Gulf of Mexico salt tectonics, associated processes and exploration potential: Gulf Coast Section SEPM Foundation 10th Annual Research Conference*, p. 66–71, 1989. doi: 10.5724/gcs.89.10.0066. (Cited p. 59, 60)

M. P. A. Jackson and M. R. Hudec. *Salt tectonics: Principles and practice*. Cambridge University Press, 2017. doi: 10.1017/9781139003988. (Cited p. 3, 4, 5, 19, 54, 59, 60, 61, 98, 117, 118)

M. P. A. Jackson and C. J. Talbot. *A glossary of salt tectonics*. Bureau of Economic Geology, University of Texas at Austin, 1991. doi: 10.23867/gc9104D. (Cited p. 58)

Z. Jing, Z. Yanqing, C. Zhigang, and L. Jianhua. Detecting boundary of salt dome in seismic data with edge-detection technique. In *SEG Technical Program Expanded Abstracts 2007*, p. 1392–1396, 2007. doi: 10.1190/1.2792759. (Cited p. 22)

R. A. Johnson and D. W. Wichern. *Applied multivariate statistical analysis*. Pearson Prentice Hall, sixth edition, 2007. ISBN 978-0-13-187715-3. (Cited p. 23)

I. Jones and I. Davison. Seismic imaging in and around salt bodies. *Interpretation*, 2 (4): SL1–SL20, 2014. doi: 10.1190/INT-2014-0033.1. (Cited p. 9, 38, 39, 82, 98, 109, 120)

I. F. Jones. Estimating subsurface parameter fields for seismic migration: Velocity model building. In *Encyclopedia of Exploration Geophysics*, p. U1–1–U1–24. Society of Exploration Geophysicists, 2015. doi: 10.1190/1.9781560803027.entry3. (Cited p. 7, 82, 84, 95)

C. Julio, G. Caumon, and M. Ford. Impact of the en echelon fault connectivity on reservoir flow simulations. *Interpretation*, 3(4): SAC23–SAC34, 2015. doi: 10.1190/INT-2015-0060.1. (Cited p. 3)

B. J. Kadlec, G. A. Dorn, and H. M. Tufo. Interactive visualization and interpretation of geologic surfaces in 3-D seismic data. In *SEG Technical Program Expanded Abstracts 2009*, p. 1147–1151, 2009. doi: 10.1190/1.3255055. (Cited p. 25, 111, 119)

M. Kass, A. Witkin, and D. Terzopoulos. Snakes: Active contour models. *International journal of computer vision*, 1(4): 321–331, 1988. doi: 10.1007/BF00133570. (Cited p. 25, 39)

M. Kazhdan and H. Hoppe. Screened poisson surface reconstruction. *ACM Transactions on Graphics*, 32(3): 1–13, 2013. doi: 10.1145/2487228.2487237. (Cited p. 25)

T. H. Kim, I. K. Eom, and Y. S. Kim. Multiscale Bayesian texture segmentation using neural networks and Markov random fields. *Neural Computing and Applications*, 18 (2): 141–155, 2009. doi: 10.1007/s00521-007-0167-x. (Cited p. 30, 128, 129, 130)

F. Lallier and N. Clausolles. Handling Fault Throw Uncertainty in Geological Modelling Study. In *79th EAGE Conference and Exhibition 2017*, 2017. doi: 10.3997/2214-4609.201700736. (Cited p. 75)

E. Landa, P. Thore, V. Sorin, and Z. Koren. Interpretation of velocity estimates from coherency inversion. *GEOPHYSICS*, 56(9): 1377–1383, 1991. doi: 10.1190/1.1443157. (Cited p. 83)

M. Lecour, R. Cognot, I. Duvinage, P. Thore, and J.-C. Dulac. Modelling of stochastic faults and fault networks in a structural uncertainty study. *Petroleum Geoscience*, 7: S31–S42, 2001. doi: 10.1144/petgeo.7.S.S31. (Cited p. vii, 2, 41)

D. Ledez. *Modélisation d'objets naturels par formulation implicite*. PhD thesis, Institut National Polytechnique de Lorraine, 2003. (Cited p. 25)

C. Legentil. *Seismic image segmentation for detection of salt geobodies using multi-scale attributes and unsupervised classifier*. MSc thesis, Université de Lorraine, 2019. (Cited p. vii, 11, 16, 17, 18, 25, 29, 30, 32, 34, 38, 116)

C. Legentil, N. Clausolles, and P. Collon. Seismic image segmentation for detection of salt geobodies using multi-scale attributes and unsupervised classifier. In *2019 Ring Meeting*, p. 355–373, 2019. (Cited p. 122)

J. P. Leveille, I. F. Jones, Z.-Z. Zhou, B. Wang, and F. Liu. Subsalt imaging for exploration, production, and development: A review. *GEOPHYSICS*, 76(5): WB3–WB20, 2011. doi: 10.1190/geo2011-0156.1. (Cited p. 82)

L. Li, J. Caers, and P. Sava. Assessing seismic uncertainty via geostatistical velocity-model perturbation and image registration: An application to subsalt imaging. *The Leading Edge*, 34(9): 1064–1070, 2015. doi: 10.1190/tle34091064.1. (Cited p. vii, 28, 116)

T. Lindeberg. Scale-space theory: A basic tool for analyzing structures at different scales. *Journal of Applied Statistics*, 1994. doi: 10.1080/757582976. (Cited p. 124, 127)

M. Lindsay, S. Perrouty, M. Jessell, and L. Ailleres. Inversion and Geodiversity: Searching Model Space for the Answers. *Mathematical Geosciences*, 46(8): 971–1010, 2014. doi: 10.1007/s11004-014-9538-x. (Cited p. 3)

M. D. Lindsay, L. Aillères, M. W. Jessell, E. A. de Kemp, and P. G. Betts. Locating and quantifying geological uncertainty in three-dimensional models: Analysis of the Gippsland Basin, southeastern Australia. *Tectonophysics*, 546-547: 10–27, 2012. doi: 10.1016/j.tecto.2012.04.007. (Cited p. 2, 3)

M. D. Lindsay, S. Perrouty, M. W. Jessell, and L. Aillères. Making the link between geological and geophysical uncertainty: geodiversity in the Ashanti Greenstone Belt. *Geophysical Journal International*, 195(2): 903–922, 2013. doi: 10.1093/gji/ggt311. (Cited p. 3)

J. Lomask, R. G. Clapp, and B. Biondi. Application of image segmentation to tracking 3D salt boundaries. *GEOPHYSICS*, 72: P47–P56, 2007. doi: 10.1190/1.2732553. (Cited p. 19, 22, 24, 39, 123)

Z. Long, Y. Alaudah, M. A. Qureshi, Y. Hu, Z. Wang, M. Alfarraj, G. AlRegib, A. Amin, M. Deriche, S. Al-Dharrab, et al. A comparative study of texture attributes for characterizing subsurface structures in seismic volumes. *Interpretation*, p. T1055–T1066, 2018. doi: 10.1190/INT-2017-0181.1. (Cited p. 21, 22, 25, 27, 34, 40)

T. Löfstedt, P. Brynolfsson, T. Asklund, T. Nyholm, and A. Garpebring. Gray-level invariant Haralick texture features. *PLOS ONE*, 14(2): e0212110, 2019. doi: 10.1371/journal.pone.0212110. (Cited p. 22, 24)

J. MacQueen. Some methods for classification and analysis of multivariate observations. In *5-th Berkeley Symposium on Mathematical Statistics and Probability*, p. 281–297, 1967. (Cited p. 25, 30, 125)

J.-L. Mallet. Discrete smooth interpolation in geometric modelling. *Computer-aided design*, 24(4): 178–191, 1992. doi: 10.1016/0010-4485(92)90054-E. (Cited p. 74)

J.-L. Mallet. *Geomodeling*. Oxford University Press, 2002. (Cited p. vii)

J.-L. Mallet. Space–time mathematical framework for sedimentary geology. *Mathematical geology*, 36(1): 1–32, 2004. doi: 10.1023/B:MATG.0000016228.75495.7c. (Cited p. 45)

T. Manzocchi, A. E. Heath, B. Palananthakumar, C. Childs, and J. J. Walsh. Faults in conventional flow simulation models: a consideration of representational assumptions and geological uncertainties. *Petroleum Geoscience*, 14(1): 91–110, 2008. doi: 10.1144/1354-079306-775. (Cited p. 3)

K. J. Marfurt, R. L. Kirlin, S. L. Farmer, and M. S. Bahorich. 3-D seismic attributes using a semblance-based coherency algorithm. *GEOPHYSICS*, 63(4): 1150–1165, 1998. doi: 10.1190/1.1444415. (Cited p. 29)

R. Martin and J. Boisvert. Iterative refinement of implicit boundary models for improved geological feature reproduction. *Computers and Geosciences*, 109: 1–15, 2017. doi: 10.1016/j.cageo.2017.07.003. (Cited p. 41, 52)

P. Micikevicius. 3D finite difference computation on GPUs using CUDA. In *Proceedings of 2nd Workshop on General Purpose Processing on Graphics Processing Units - GPGPU-2*, p. 79–84, 2009. doi: 10.1145/1513895.1513905. (Cited p. 90)

M. Mohr, J. K. Warren, P. A. Kukla, J. L. Urai, and A. Irmen. Subsurface seismic record of salt glaciers in an extensional intracontinental setting (Late Triassic of northwestern Germany). *Geology*, 35(11): 963–966, 2007. doi: 10.1130/G23378A.1. (Cited p. 45, 48)

C. Mosher, E. Keskula, J. Malloy, R. Keys, H. Zhang, and S. Jin. Iterative imaging for subsalt interpretation and model building. *The Leading Edge*, 26(11): 1424–1428, 2007. doi: 10.1190/1.2805763. (Cited p. 22, 98, 112)

N. Moës, A. Gravouil, and T. Belytschko. Non-planar 3d crack growth by the extended finite element and level sets-Part I: Mechanical model. *International Journal for Numerical Methods in Engineering*, 53(11): 2549–2568, 2002. doi: 10.1002/nme.429. (Cited p. viii, 65, 69)

L. Najman and M. Couprie. Building the component tree in quasi-linear time. *IEEE Transactions on Image Processing*, 15(11): 3531–3539, 2006. doi: 10.1109/TIP.2006.877518. (Cited p. viii, 66, 67, 72)

T. Ojala, M. Pietikainen, and T. Maenpaa. Multiresolution gray-scale and rotation invariant texture classification with local binary patterns. *IEEE Transactions on Pattern Analysis and Machine Intelligence*, 24(7): 971–987, 2002. doi: 10.1109/TPAMI.2002.1017623. (Cited p. 21)

A. V. Oppenheim, R. W. Schafer, and J. R. Buck. *Discrete-time signal processing*. Prentice Hall Signal Processing Series. Pearson, second edition, 1999. ISBN 978-0-13-754920-7. (Cited p. 92)

S. Osher and J. A. Sethian. Fronts propagating with curvature-dependent speed: algorithms based on Hamilton-Jacobi formulations. *Journal of Computational Physics*, 79(1): 12–49, 1988. doi: 10.1016/0021-9991(88)90002-2. (Cited p. 25, 39, 41)

K. Osypov, Y. Yang, A. Fournier, N. Ivanova, R. Bachrach, C. E. Yarman, Y. You, D. Nichols, and M. Woodward. Model-uncertainty quantification in seismic tomography: Method and applications. *Geophysical Prospecting*, 61(6): 1114–1134, 2013. doi: 10.1111/1365-2478.12058. (Cited p. 9, 52, 83)

S. Pon and L. R. Lines. Sensitivity analysis of seismic depth migrations. *GEOPHYSICS*, 70(2): S39–S42, 2005. doi: 10.1190/1.1897036. (Cited p. 83)

M. Protasov, D. Kolyukhin, S. Rostomyan, and E. Landa. Subsalt imaging in the presence of salt-body uncertainty. *The Leading Edge*, 36(2): 146–150, 2017. doi: 10.1190/tle36020146.1. (Cited p. 83)

M. Raguenel. *Modélisation des phénomènes thermo-hydrauliques dans des réservoirs fracturés sur des maillages non structurés : application au réservoir géothermique de Basse-Terre, Guadeloupe.* PhD thesis, Université de Lorraine, 2019. (Cited p. 3)

C. Ramirez, G. Larrazabal, and G. Gonzalez. Salt body detection from seismic data via sparse representation: Salt body detection from seismic data. *Geophysical Prospecting*, 64(2): 335–347, 2016. doi: 10.1111/1365-2478.12261. (Cited p. 25)

T. Randen, E. Monsen, C. Signer, A. Abrahamsen, J. O. Hansen, T. S\a eter, J. Schlaf, and L. Sonneland. Three-Dimensional Texture Attributes for Seismic Data Analysis. *SEG Technical Program Expanded Abstracts 2000*, p. 668–671, 2000. doi: 10.1190/1.1816155. (Cited p. 23)

J. Renaudeau, M. Irakarama, G. Laurent, F. Maerten, and G. Caumon. Implicit modeling of geological structures: a Cartesian grid method handling discontinuities with ghost points. In *WIT Transactions on Engineering Sciences*, vol. 122, p. 189–199, 2018. doi: 10.2495/BE410171. (Cited p. 118)

J. Renaudeau, E. Malvesin, F. Maerten, and G. Caumon. Implicit Structural Modeling by Minimization of the Bending Energy with Moving Least Squares Functions. *Mathematical Geosciences*, 51(6): 693–724, 2019. doi: 10.1007/s11004-019-09789-6. (Cited p. 74)

J.-C. Ringenbach, J.-F. Salel, C. Kergaravat, C. Ribes, C. Bonnel, and J.-P. Callot. Salt tectonics in the Sivas Basin, Turkey: outstanding seismic analogues from outcrops. *First Break*, 31(6): 93–101, 2013. doi: 10.3997/1365-2397.2013016. (Cited p. 54, 59)

A. L. Rojo, A. Escalono, and L. Schulte. The use of seismic attributes to enhance imaging of salt structures in the Barents Sea. *First Break*, 34(11): 49–57, 2016. doi: 10.3997/1365-2397.2016014. (Cited p. 40)

G. Rongier, P. Collon-Drouaillet, and M. Filipponi. Simulation of 3D karst conduits with an object-distance based method integrating geological knowledge. *Geomorphology*, 217: 152–164, 2014. doi: 10.1016/j.geomorph.2014.04.024. (Cited p. 41)

M. G. Rowan, M. P. Jackson, and B. D. Trudgill. Salt-related fault families and fault welds in the northern gulf of mexico. *AAPG bulletin*, 83(9): 1454–1484, 1999. doi: 10.1306/E4FD41E3-1732-11D7-8645000102C1865D. (Cited p. 60, 61, 75, 117)

M. G. Rowan, T. F. Lawton, and K. A. Giles. Anatomy of an exposed vertical salt weld and flanking strata, La Popa Basin, Mexico. *Geological Society, London, Special Publications*, 363: 33–57, 2012. doi: 10.1144/SP363.3. (Cited p. 58)

G. I. N. Rozvany. A critical review of established methods of structural topology optimization. *Structural and Multidisciplinary Optimization*, 37(3): 217–237, 2009. doi: 10.1007/s00158-007-0217-0. (Cited p. 112, 119)

A. Schaaf and C. E. Bond. Quantification of uncertainty in 3-D seismic interpretation: implications for deterministic and stochastic geomodeling and machine learning. *Solid Earth*, 10(4): 1049–1061, 2019. doi: 10.5194/se-10-1049-2019. (Cited p. 2, 9)

C. Scheidt and J. Caers. Representing Spatial Uncertainty Using Distances and Kernels. *Mathematical Geosciences*, 41(4): 397–419, 2009. doi: 10.1007/s11004-008-9186-0. (Cited p. 119)

J. Schlaf, T. Randen, and L. Sønneland. Introduction to seismic texture. In *Mathematical methods and modelling in hydrocarbon exploration and production*, p. 3–21. Springer, 2005. doi: 10.1007/3-540-26493-0_1. (Cited p. 16, 19)

M. A. Shafiq, Z. Wang, G. AlRegib, A. Amin, and M. Deriche. A texture-based interpretation workflow with application to delineating salt domes. *Interpretation*, 5(3): SJ1–SJ19, 2017. doi: 10.1190/INT-2016-0043.1. (Cited p. 23, 39, 123)

R. E. Sheriff. *Encyclopedic Dictionary of Applied Geophysics*. Society of Exploration Geophysicists, fourth edition, 2002. ISBN 978-1-56080-118-4 978-1-56080-296-9. doi: 10.1190/1.9781560802969. (Cited p. 19)

J. Shi and J. Malik. Normalized cuts and image segmentation. *IEEE Transactions on pattern analysis and machine intelligence*, 22(8): 888–905, 2000. doi: 10.1109/34.868688. (Cited p. 24, 39)

Y. Shi, X. Wu, and S. Fomel. SaltSeg: Automatic 3d salt segmentation using a deep convolutional neural network. *Interpretation*, 7(3): SE113–SE122, 2019. doi: 10.1190/INT-2018-0235.1. (Cited p. 10, 25, 26, 27, 40)

R. M. Srivastava. Reservoir Characterization With Probability Field Simulation. In *SPE Annual Technical Conference and Exhibition*, 1992. doi: 10.2118/24753-MS. (Cited p. vii)

S. Suzuki, G. Caumon, and J. Caers. Dynamic data integration for structural modeling: model screening approach using a distance-based model parameterization. *Computational Geosciences*, 12(1): 105–119, 2008. doi: 10.1007/s10596-007-9063-9. (Cited p. 119)

M. T. Taner, F. Koehler, and R. E. Sheriff. Complex seismic trace analysis. *GEOPHYSICS*, 44(6): 1041–1063, 1979. doi: 10.1190/1.1440994. (Cited p. 19, 35)

S. T. Thiele, M. W. Jessell, M. Lindsay, V. Ogarko, J. F. Wellmann, and E. Pakyuz-Charrier. The topology of geology 1: Topological analysis. *Journal of Structural Geology*, 91: 27–38, 2016a. doi: 10.1016/j.jsg.2016.08.009. (Cited p. 47)

S. T. Thiele, M. W. Jessell, M. Lindsay, J. F. Wellmann, and E. Pakyuz-Charrier. The topology of geology 2: Topological uncertainty. *Journal of Structural Geology*, 91: 74–87, 2016b. doi: 10.1016/j.jsg.2016.08.010. (Cited p. 3)

P. Thore, A. Shtuka, M. Lecour, T. Ait-Ettajer, and R. Cognot. Structural uncertainties: Determination, management, and applications. *GEOPHYSICS*, 67(3): 840–852, 2002. doi: 10.1190/1.1484528. (Cited p. 1, 9, 40, 52, 83)

L. J. Van Vliet and P. W. Verbeek. Estimators for orientation and anisotropy in digitized images. *Proceedings of ASCI*, p. 442–450, 1995. (Cited p. 23)

B. C. Vendeville and M. P. Jackson. The rise of diapirs during thin-skinned extension. *Marine and Petroleum Geology*, 9(4): 331–354, 1992. doi: 10.1016/0264-8172(92)90047-I. (Cited p. 6, 54)

J. Virieux. *SH*-wave propagation in heterogeneous media: Velocity-stress finite-difference method. *GEOPHYSICS*, 49(11): 1933–1942, 1984. doi: 10.1190/1.1441605. (Cited p. 90)

B. H. Wagner. *An analysis of salt welding*. PhD thesis, The University of Texas at Austin, 2010. (Cited p. 59, 61)

B. H. Wagner and M. P. Jackson. Viscous flow during salt welding. *Tectonophysics*, 510(3-4): 309–326, 2011. doi: 10.1016/j.tecto.2011.07.012. (Cited p. 59)

A. U. Waldeland, A. C. Jensen, L.-J. Gelius, and A. H. S. Solberg. Convolutional neural networks for automated seismic interpretation. *The Leading Edge*, 37(7): 529–537, 2018. doi: 10.1190/tle37070529.1. (Cited p. 25, 39, 40, 123)

Z. Wang, H. Di, M. A. Shafiq, Y. Alaudah, and G. AlRegib. Successful leveraging of image processing and machine learning in seismic structural interpretation: A review. *The Leading Edge*, 37(6): 451–461, 2018. doi: 10.1190/tle37060451.1. (Cited p. 16, 17, 19, 27)

R. Weijermars, M. P. A. Jackson, and B. Vendeville. Rheological and tectonic modeling of salt provinces. *Tectonophysics*, 217: 143–174, 1993. doi: 10.1016/0040-1951(93)90208-2. (Cited p. 6)

R. Weijermars, M. R. Hudec, T. P. Dooley, and M. P. A. Jackson. Downbuilding salt stocks and sheets quantified in 3-D analytical models. *Journal of Geophysical Research: Solid Earth*, 120(6): 4616–4644, 2015. doi: 10.1002/2014JB011704. (Cited p. 6)

W. Weinzierl, L. Schulte, and V. Aarre. Volumetric impact of fault perturbation in the first Fresnel zone. *Interpretation*, 4(4): T419–T426, 2016. doi: 10.1190/INT-2015-0192.1. (Cited p. 9, 83)

F. Wellmann and G. Caumon. 3-D Structural geological models: Concepts, methods, and uncertainties. *Advances in Geophysics*, 59: 1–121, 2018. doi: 10.1016/bs.agph.2018.09.001. (Cited p. v, 1, 2, 3, 9, 28, 41, 59, 117)

J. F. Wellmann and K. Regenauer-Lieb. Uncertainties have a meaning: Information entropy as a quality measure for 3-D geological models. *Tectonophysics*, 526-529: 207–216, 2012. doi: 10.1016/j.tecto.2011.05.001. (Cited p. 3, 100)

J. F. Wellmann, F. G. Horowitz, E. Schill, and K. Regenauer-Lieb. Towards incorporating uncertainty of structural data in 3d geological inversion. *Tectonophysics*, 490 (3-4): 141–151, 2010. doi: 10.1016/j.tecto.2010.04.022. (Cited p. 2, 3, 100)

Wikipedia contributors. k-means clustering, 2019. [Online; accessed 2-May-2019]. (Cited p. 125)

G. Winkler and V. Liebscher. Smoothers for Discontinuous Signals. *Journal of Nonparametric Statistics*, 14(1-2): 203–222, 2002. doi: 10.1080/10485250211388. (Cited p. 25)

X. Wu. Methods to compute salt likelihoods and extract salt boundaries from 3D seismic images. *GEOPHYSICS*, 81: IM119–IM126, 2016. doi: 10.1190/geo2016-0250.1. (Cited p. 10, 23, 24, 25, 26, 36, 39, 40, 52, 123)

X. Wu and G. Zhong. Generating a relative geologic time volume by 3D graph-cut phase unwrapping method with horizon and unconformity constraints. *GEOPHYSICS*, 77: O21–O34, 2012. doi: 10.1190/geo2011-0351.1. (Cited p. 45)

X. Wu, S. Fomel, and M. Hudec. Fast salt boundary interpretation with optimal path picking. *Geophysics*, 83: O45–O53, 2018. doi: 10.1190/geo2017-0481.1. (Cited p. 25, 39)

Z. Wu, H. Yin, X. Wang, B. Zhao, J. Zheng, X. Wang, and W. Wang. The structural styles and formation mechanism of salt structures in the Southern Precaspian Basin: Insights from seismic data and analog modeling. *Marine and Petroleum Geology*, 62: 58–76, 2015. doi: 10.1016/j.marpetgeo.2015.01.010. (Cited p. 59)

O. Yilmaz. *Seismic Data Analysis: Processing, Inversion, and Interpretation of Seismic Data*. Society of Exploration Geophysicists, 2001. ISBN 978-1-56080-094-1 978-1-56080-158-0. doi: 10.1190/1.9781560801580. (Cited p. 7, 18, 93)

Y. Zhai, D. L. Neuhoff, and T. N. Pappas. Local radius index - a new texture similarity feature. In *2013 IEEE International Conference on Acoustics, Speech and Signal Processing*, p. 1434–1438, 2013. ISBN 978-1-4799-0356-6. doi: 10.1109/ICASSP.2013.6637888. (Cited p. 21)

Y. Zhang and A. D. Halpert. Enhanced interpreter-aided salt boundary extraction using shape deformation. In *SEG Technical Program Expanded Abstracts 2012*, p. 1–5, 2012. doi: 10.1190/segam2012-1337.1. (Cited p. 25, 123)

Interprétation sismique stochastique des corps salifères : détection, échantillonnage et impact sur l'imagerie sismique

Résumé : La création d'un modèle numérique 3D du sous-sol nécessite d'intégrer des données éparses et ambigües. Les corps salifères développent des formes compliquées et des singularités topologiques spécifiques à la tectonique salifère. Modéliser leurs géométries est donc difficile, mais important puisqu'ils introduisent de larges contrastes de propriétés physiques dans le sous-sol. L'imagerie sismique est couramment utilisée pour cartographier le sel et obtenir des informations sur sa géométrie. Il s'agit toutefois d'un processus itératif long nécessitant de nombreuses phases d'interprétation. Ces interprétations sont sujettes à des incertitudes qui se propagent à travers le processus d'imagerie et impactent la compréhension du sous-sol et les modèles qui en sont faits. Prendre en compte ces incertitudes est donc crucial, et nécessite d'être réalisé automatiquement étant donné le caractère itératif de l'imagerie sismique. Dans cette thèse, je m'intéresse en particulier à l'estimation des incertitudes structurales liées à l'interprétation d'images sismiques ambigües dans des environnements de tectonique salifère.

La principale contribution de cette thèse est une méthode numérique de modélisation stochastique des enveloppes de corps salifères et de leur connectivité. La modélisation se base sur une définition *a priori* des incertitudes, sous forme d'une zone tampon autour de l'enveloppe du sel. L'enveloppe est définie par la combinaison d'un champ scalaire de référence, calculé à partir de la zone tampon, et d'un champ aléatoire spatialement corrélé servant de perturbation. Cette formulation implicite permet de simuler à la fois des géométries et des topologies variables, tout en assurant la validité des enveloppes simulées. Lorsque plusieurs corps déconnectés sont simulés, une suture est simulée pour les connecter. Sa position est déterminée à partir du champ scalaire représentant l'enveloppe de sel afin d'assurer sa cohérence avec les corps salifères simulés. La méthode est automatique et permet d'intégrer des informations ponctuelles (données de puits, pointés sismiques, etc.) et, dans une certaine mesure, des connaissances géologiques *a priori*.

Cette méthode est utilisée pour caractériser les incertitudes structurales liées à l'imagerie d'un jeu de données sismiques 2D synthétique. À partir d'une zone tampon grossière, un ensemble d'interprétations possibles de l'enveloppe du sel est simulé. Ces interprétations sont utilisées pour définir des modèles de vitesse de migration, qui servent à générer autant d'images sismiques. L'analyse statistique de ces images, directement ou via des attributs sismiques permet de mettre en évidence les régions les plus sensibles aux variations de vitesse de migration, et fournit des indications sur la nature des corps salifères imagés.

Ces contributions ouvrent de nouvelles perspectives pour la quantification des incertitudes dans le cadre de la mise à jour automatique du modèle de vitesse en imagerie sismique.

Mots-clés : géomodélisation 3D, quantification des incertitudes, interprétation sismique, tectonique salifère

---

Stochastic seismic interpretation of salt bodies: detection, sampling and impact on seismic imaging

Abstract: Building a numerical 3D model of the subsurface requires to integrate sparse and ambiguous data. Due to salt tectonics specificities, salt bodies have complex shapes and may present topological singularities. Modeling their geometries is, therefore, difficult, but important as they introduce large physical property contrasts in the subsurface. Seismic imaging is commonly used to map salt and get information about its geometry. Nevertheless, building a seismic image is a long and iterative process, which requires numerous interpretation phases. These interpretations are prone to uncertainties, stemming from the limits of data acquisition and resolution and the assumptions underlying their processing. These uncertainties propagate through the imaging process and impact our understanding and models of the subsurface. Taking them into account is, therefore, crucial during seismic interpretation and requires to be done automatically given the iterative nature of seismic imaging. In this thesis, I am interested in the assessment of structural uncertainties related to the interpretation of ambiguous seismic images of salt tectonics environments.

The main contribution of this thesis is a numerical method for stochastically modeling variable shapes of salt bodies and their connectivity. The modeling is based on an *a priori* definition of the uncertainties, represented as a buffer zone encompassing the salt boundary. The boundary is defined as the combination of a reference scalar field, computed from the buffer zone, and a spatially correlated random field that is used as a perturbation. This implicit formulation allows for the simulation of both varying salt geometries and topologies while ensuring the validity of the simulated boundaries. When the simulated diapir is a bulb detached from its pedestal, a weld is simulated to connect them. The position of the weld is determined from the scalar field representing the salt boundary, to ensure its consistency with the simulated salt bodies. The method is automatic and proposes to integrate punctual information (e.g., well data or manual seismic picks) and, to some extent, prior geological knowledge.

The second contribution of this thesis is an application of this method to the characterization of structural uncertainties underlying seismic imaging on a 2D synthetic data set. Starting from a rough buffer zone, I simulate a set of possible interpretations of the salt boundary. I use these interpretations to define a set of equiprobable migration velocity models, that are used in turn to generate as many seismic images. The statistical analysis of this image set, both directly and from derived seismic attributes, permits to highlight the image parts which are most sensitive to migration velocity variations, and provides insights on the nature of the imaged salt bodies.

These contributions open new perspectives for uncertainty quantification in an automatic velocity model updating framework in seismic imaging.

Keywords: 3D geomodeling, uncertainty quantification, seismic interpretation, salt tectonics